DIAS
Institiúid Ard-Léinn Bhaile Átha Cliath | Dublin Institute for Advanced Studies



Trinity College Dublin
Coláiste na Tríonóide, Baile Átha Cliath
The University of Dublin

Tracking Solar Electron Beams from the Corona to the Heliosphere using Bayesian Methods

Luis Alberto Cañizares
BA (TCD), BAI (TCD), BSc (DCU), MSc (Imperial)

April, 2025

A Thesis submitted in fulfilment
of the requirements for the degree of
Doctor of Philosophy

Supervisor: Professor Peter T. Gallagher

Declaration

I declare that this thesis has not been submitted as an exercise for a degree at this or any other university and it is entirely my own work.

I agree to deposit this thesis in the University's open access institutional repository or allow the Library to do so on my behalf, subject to Irish Copyright Legislation and Trinity College Library conditions of use and acknowledgement.

I consent to the examiner retaining a copy of the thesis beyond the examining period, should they so wish (EU GDPR May 2018).

Signed:  Date: April 16, 2025

"If you wish to make an apple pie from scratch, you must first invent the universe."
- Carl Sagan, Cosmos

Acknowledgements

First and foremost, I would like to extend my deepest gratitude to Peter Gallagher, for all the invaluable help and guidance you have provided throughout these years. I truly believe I would have never finished this PhD without you. Thank you for your endless patience and unconditional support. You motivated me during the tough times and were always there when I needed it. Thank you also for encouraging me when I had crazy or ambitious ideas and always saying 'we will figure it out'. I am profoundly grateful for everything you have done, and I will always be in your debt. I could not have asked for a better mentor and friend on this journey.

I would also like to thank Eoin Carley and Shane Maloney, for all the support you gave me during this PhD. Thank you for your continuous patience, for always keeping the door open and for all the invaluable help you gave me.

This PhD would have never been possible without the support of DIAS, thank you for the additional help you gave me, providing me with an extension. Also to the Irish Research Council, for supporting me during this PhD under the grant GOIPG/2019/2843. And of course to TCD, for the additional support, and to ESA for your support with the SURROUND project and for inviting me to the CubeSats Summer School in Belgium.

Of course, I would also want to extend my gratitude to all the people who helped me during this PhD, to Sam, Nicolina, Matt, Sophie, Shilpi, Philippe, Ciara, Aoife, Johnny, Jeremy, Dale, Pearse, Paul and David.

To my best friends Alan and George, thank you for always being there when I needed it, thank you for all the laughs and for helping me through engineering and physics.

To my siblings, thank you Alvaro, for always being there when we needed it, thank you Patricia for always having my back, and thank you Carlota for making me happy and making me 'un café'. To mum and dad, thank you for your support and encouragement. Thank you for everything you have done for me, thank you for all your sacrifices.

And to Giselle, thank you for putting up with me, thank you for supporting me, thank you for choosing me and sacrificing so much to be here with me. Thank you for making me laugh and thank you for making me happy.

Para mi familia

Abstract

The Sun is an active star that produces the most powerful phenomena in the solar system, particularly flares and coronal mass ejections (CMEs). These violent explosions accelerate electrons and other solar energetic particles (SEPs) to near-relativistic speeds. These particles eventually reach Earth, causing auroras but also damaging satellites, power grids, communication systems, and putting astronauts at risk. One way of studying these particles is by analysing the radio signatures they generate as they travel through interplanetary space.

Type III solar radio bursts (SRBs) are strong radio emissions associated with quasi-relativistic electrons travelling along open magnetic field lines. These bursts provide insight into the properties of accelerated electrons, the propagation of radio waves, and the plasma environments of the fully developed turbulent corona in which the electron beams travel. However, the physical interpretation of the discrepancies between the in-situ and remotely observed radio-emitting sources is still subject to debate. Here, I expand on our knowledge of localisation methods to understand the contributors to these discrepancies whether instrumental or physical. Furthermore, monitoring these bursts is essential for studying space weather (SW) phenomena and their potential impacts on Earth.

In this thesis I first introduce the BayEsian LocaLisation Algorithm (BELLA; Cañizares et al., 2024), a novel multilateration technique designed to track SRBs. BELLA uses Bayesian inference to generate probabilistic distributions of source positions and their uncertainties, allowing for comprehensive estimation of various uncertainties. Validation of BELLA was performed using both simulations and observations of a Type III SRB detected by STEREO A, STEREO B, and Wind on 7 June 2012. BELLA successfully tracked the SRB from approximately $10\,R_\odot$ to $150\,R_\odot$ (2 MHz to 0.15 MHz), revealing an apparent solar wind speed of around $400\,\mathrm{km\,s^{-1}}$ and a source longitude of $30\,^\circ$. These findings were consistent with established localisation methods and solar wind models, demonstrating BELLA's reliability and accuracy.

To enhance SW monitoring, a constellation of CubeSats aimed at observing SRBs to track CMEs and SEPs is proposed. This constellation named SURROUND would complement

missions like ESA's Solar Orbiter/RPW, NASA's Parker Solar Probe/FIELDS, and other. Through extensive analysis, nine use cases were established to define operational requirements. Goniopolarimetry and multilateration were shown to be suitable techniques for reliable routinary localisations. A conceptual design for the SURROUND system includes five spacecraft positioned at L1, L4, L5, Earth-leading (Ahead), and Earth-trailing points (Behind), with a three-spacecraft descope option.

Additionally, in this thesis, I investigate the contribution of scattering to the apparent location of the path of electron beams, using radio emissions from a solar event on 4 December 2021 which were observed by five spacecraft Parker Solar Probe, STEREO A, Wind, Solar Orbiter and Mars Express, as well as the Nançay Radioheliograph. These beams were found to follow an Archimedean spiral, and I present strong evidence that suggests that scattering caused a lensing-like effect, making solar wind velocities appear over $150\,\mathrm{km\,s^{-1}}$ faster than theoretical predictions. Finally, the quantitative measurements of radio scattering were found to align with current models, providing further insight into the complex interactions within the turbulent corona and inner heliosphere.

Overall, this research demonstrates the importance of advanced localisation techniques and dedicated monitoring missions towards improving our understanding of solar phenomena and their impacts on space weather.

List Of Publications

1. **Cañizares, L. A.**, Badman, S. T., Chrysaphi, N.,Bhunia, S., Sanchez-Cano, B., Maloney, S. A., and Gallagher, P. T., *Electron Beam Propagation and Radio-Wave Scattering in the Inner Heliosphere using Five Spacecraft.* In review, submitted to Astronomy & Astrophysics.

2. **Cañizares, L. A.**, Badman, S. T., Maloney, S. A., Owens, M. J., Weigt, D. M., Carley, E. P., and Gallagher, P. T., *Tracking solar radio bursts using bayesian multilateration.* Astronomy & Astrophysics, 684:A182, 2024. doi: 10.1051/0004-6361/202347747.

3. Weigt, D. M.*, **Cañizares, L. A.***, Maloney, S. A., Murray, S. A., Carley, E. P., Gallagher, P. T., Macario-Rojas, A., Crisp, N., and McGrath, C., *The science behind SURROUND: a constellation of CubeSats around the sun*. Proceedings of the 9th International Workshop on Planetary, Solar & Heliospheric Radio Emissions (in press). *these authors contributed equally.

4. Macario-Rojas, A., Crisp, N. H., McGrath, C. N., **Cañizares, L. A.**, Weigt, D. M., Maloney, S. A., Murray, S. A., Carley, E. P., and Gallagher, P. T., *Mission concept for SURROUND: Operational space weather detection and tracking using small satellites.* Acta Astronautica (in review).

5. Sánchez-Cano, B., Carter, S., Lester, M., Witasse, O., Musset, S., Cecconi, B., Siebenaler, L., Joyce, S., **Cañizares, L. A.**, Cicchetti, A., Fogg, A. R., Gallagher, P., Gerekos, C., Jackman, C., Jebaraj, I., Meggi, D., Orosei, R., Opgenoorth, H., Plaut, J., Regan, C., and Stergiopoulou, K., *Type-III Solar Radio Bursts at Mars: a catalogue of 16.5 years of observations from the Mars Express-MARSIS instrument between 0.1 and 5.5 MHz.* In preparation.

6. Verbeek, B., **Cañizares, L. A.**, Gross, H., Wischert, D., Vennekens, J., et al., *The Fire Localisation And Mitigation for Emergencies Satellites (FLAMES), a constellation of CubeSats in LEO for monitoring wildfires in near real-time.* 74th International Astronautical Congress, 2023. IAC-23,B4,4,6,x76466.

7. Crisp, N. H., Macario-Rojas, A., McGrath, C. N., Maloney, S., **Cañizares, L. A.**, Weigt, D. M., Murray, S., Carley, E., and Gallagher, P., *Technology challenges of SURROUND: A constellation of small satellites around the sun for tracking solar radio bursts.* Proceedings of the AIAA/USU Conference on Small Satellites, SSC23-WII-04, 2023.

8. Badman, S. T., Carley, E., **Cañizares, L. A.**, Dresing, N., Jian, L. K., Lario, D., Gallagher, P. T., Martínez-Oliveros, J. C., Pulupa, M., and Bale, S. D., *Tracking a Beam of Electrons from the Low Solar Corona into Interplanetary Space with the Low Frequency Array, Parker Solar Probe, and 1 au Spacecraft.* The Astrophysical Journal, 938(2):95, 2022.

9. Murphy, P. C., Callanan, P., McCauley, J., McKenna, D. J., Fionnagáin, D. Ó, Louis, C. K., Redman, M. P., **Cañizares, L. A.**, Carley, E. P., Maloney, S. A., Coghlan, B., Daly, M., Scully, J., Dooley, J., Gajjar, V., Giese, C., Brennan, A., Keane, E. F., Maguire, C. A., Quinn, J., Mooney, S., Ryan, A. M., Walsh, J., Jackman, C. M., Golden, A., Ray, T. P., Doyle, J. G., Rigney, J., Burton, M., and Gallagher, P. T., *First Results from the REAL-time Transient Acquisition backend (REALTA) at the Irish LOFAR station.* Astronomy & Astrophysics, 655:A16, 2021. doi: 10.1051/0004-6361/202140415

Software Publications

1. **Cañizares, L. A.**, **BELLA**, Tcdsolar/bella: Release v0.0.1, dec 2023a. https://zenodo.org/doi/10.5281/zenodo.10276814

2. **Cañizares, L. A.**, **SOLARMAP**, canizarl/solarmap: Release v0.0.7, dec 2023b. https://zenodo.org/doi/10.5281/zenodo.10262601

Acronyms

AIS Active Ionospheric Sounding. 53, 126

au Astronomical Unit. 43

BELLA BayEsian LocaLisation Algorithm. 23, 73, 74, 75, 76, 77, 78, 79, 80, 81, 83, 84, 85, 87, 89, 90, 91, 92, 93, 95, 96, 137, 139, 145, 148, 150, 151, 152, 153, 154, 155, 156, 157, 158, 159, 160, 163

CME coronal mass ejection. 1, 5, 10, 11, 12, 13, 14, 15, 16, 20, 43, 100, 101, 103, 105, 106, 107, 108, 109, 110, 118, 121, 122, 153, 167

DSN Deep Space Network. 45, 48, 56, 121

EM Electromagnetic. 39, 52

ESA European Space Agency. 39, 49, 53, 54, 56, 100, 122, 155, 156

FIELDS FIELDS. 48, 126, 127, 128

FoV Field of View. 51

GH Gauss-Hermite. 60, 61, 63, 64, 65, 87, 88, 127, 129, 159

GOES Geostationary Operational Environmental Satellite. 10, 129

GP goniopolarimetry. 19, 20, 21, 45, 46, 89, 96, 103, 106, 107, 114, 122, 160, 163

HiRAS Hiraiso Solar Observatory. 105

JAXA Japanese Aerospace Exploration Agency. 156

JUICE JUpiter ICy moons Explorer. 155

L1 Lagrange 1. 40

LEO Low Earth Orbit. 56

LOFAR LOw Frequency ARray. 73, 105

MARSIS Mars Advanced Radar for Subsurface and Ionosphere Sounding. 53, 126, 127

MEX Mars Express. 39, 53, 54, 59, 126, 127, 132, 150, 154, 157, 162

MHD Magnetohydrodynamics. 28

Mio Mercury Magnetospheric Orbiter. 156

MPO Mercury Planetary Orbiter. 156

NASA National Aeronautics and Space Administration. 39, 40, 43, 44, 45, 46, 49, 54, 56, 154, 165

NOAA National Oceanic and Atmospheric Administration. 14, 99

NRH Nançay Radioheliograph. 23, 58, 126, 129, 132, 137, 138, 145

PDF probability density function. 74

PSP Parker Solar Probe. 39, 46, 49, 59, 106, 107, 110, 126, 132, 134, 150, 162

PWI Plasma Wave Investigation. 156

RFI radio frequency interference. 63, 129

RFS Radio Frequency Spectrometer. 48

RPW Radio and Plasma Waves. 52, 126, 127

S/N signal-to-noise ratio. 21, 60, 91

SEP solar energetic particle. xvii, 10, 12, 13, 14, 19, 45, 100, 101, 103, 106, 108, 109, 122

SOAR Solar Orbiter Archive. 121

SolO Solar Orbiter. xvii, 39, 49, 51, 52, 59, 106, 107, 110, 122, 126, 131, 134, 150, 160, 161, 162, 163

SORBET Spectroscopie des Ondes Radio and du Bruit Electrostatique Thermique. 156, 157

SRB solar radio burst. 14, 15, 19, 36, 42, 45, 52, 88, 93, 94, 95, 96, 97, 101, 103, 104, 106, 109, 110, 114, 122, 126, 132, 147, 148, 153, 154, 155, 156

STEREO Solar Terrestrial Relations Observatory. 39, 43, 44, 45, 59, 103, 107, 119, 126, 150, 157, 162

STIX Spectrometer Telescope for Imaging X-rays. 129, 131

SW space weather. 12, 14, 99, 100, 102, 103, 105, 108, 118, 121, 122

TDOA Time-Difference-of-Arrival. 21, 66, 67, 68, 73, 75, 76, 96

TOA Time-of-Arrival. 66, 67, 75, 96, 123

TPS Thermal Protection System. 46, 48

TRL technology readiness level. 119, 167

WAVES Radio and Plasma Waves. 42, 84, 107, 114, 126, 127, 128

Wind The Global Geospace Science Wind satellite. 39, 40, 41, 59, 107, 114, 126, 134, 150, 157, 162

Contents

1 Introduction **1**

1.1 The Solar Corona . . . 3
1.2 Flares and Coronal Mass Ejections . . . 8
1.3 Space Weather . . . 12
1.4 Solar Radio Bursts . . . 14
1.4.1 Type III Bursts . . . 16
1.5 General Overview of Localisation Methods . . . 19
1.6 Thesis Outline . . . 22

2 Plasma Theory **25**

2.1 Plasma Physics . . . 25
2.2 The Magnetohydrodynamics (MHD) model . . . 28
2.3 Plasma Emission . . . 33
2.4 Radio Wave scattering . . . 36

3 Instrumentation **39**

3.1 A suite of solar dedicated spacecraft . . . 39
3.2 Wind . . . 40
3.2.1 Technical Aspects of the Wind Spacecraft . . . 40
3.2.2 The WAVES Instrument . . . 42
3.3 STEREO . . . 43
3.3.1 Technical Aspects of the STEREO Spacecraft . . . 43
3.3.2 The S/WAVES Instrument . . . 45
3.4 Parker Solar Probe . . . 46
3.4.1 Technical Aspects of the Parker Solar Probe Spacecraft . . . 46
3.4.2 The FIELDS Experiment . . . 48
3.5 Solar Orbiter . . . 49
3.5.1 Technical Aspects of Solar Orbiter . . . 49

3.5.2 Radio and Plasma Waves . . . 52
3.6 Mars Express . . . 53
3.6.1 MARSIS . . . 53
3.7 CubeSats . . . 54
3.8 Nançay Radioheliograph . . . 57

4 Methods **59**
4.1 Burst Characterisation . . . 59
4.1.1 Gauss-Hermite Polynomials . . . 60
4.1.2 The profile of a Type III . . . 65
4.2 Multilateration . . . 66
4.2.1 Time of Arrival (TOA) . . . 66
4.2.2 Time Difference of Arrival (TDOA) . . . 68
4.2.3 Bayesian Multilateration . . . 69

5 The BayEsian LocaLisation Algorithm (BELLA) **73**
5.1 Introduction . . . 73
5.2 Implementation of Bayesian Multilateration . . . 74
5.3 Simulations and Method Validation . . . 79
5.3.1 Confidence Maps . . . 79
5.3.2 Simulations to Validate BELLA . . . 80
5.4 Observations for the validation of BELLA . . . 84
5.5 BELLA Results . . . 87
5.6 Conclusion . . . 96

6 SURROUND: A constellation of CubeSats around the Sun **99**
6.1 Introduction . . . 99
6.2 The SURROUND Mission Concept . . . 100
6.3 Mission Requirements . . . 104
6.3.1 Mission Use Cases . . . 105
6.3.2 Use Case 1 - Detect and Track Type II radio bursts . . . 105
6.3.3 Use Case 2 - Detect and Track Type III radio bursts . . . 106
6.3.4 Use Case 3 - Localise Type II radio burst exciters in 3D . . . 107
6.3.5 Use Case 4 - Localise Type III radio bursts exciters in 3D . . . 107
6.3.6 Use Case 5 - Nowcast CME associated with Type IIs . . . 108
6.3.7 Use Case 6 - Nowcast SEP electrons associated with Type IIIs . . . 108
6.3.8 Use Case 7 - Forecast arrival of a CME at Earth using Type II radio burst . . . 108

6.3.9 Use Case 8 - Forecast the potential arrival of SEP protons associated with Type IIIs . . . 109
6.3.10 Use Case 9 - Scientific Analysis . . . 109
6.4 Measurement Requirements . . . 110
6.4.1 Frequency range . . . 110
6.4.2 Time resolution . . . 111
6.4.3 Spacecraft orbits/positions . . . 114
6.4.4 Spacecraft communications . . . 119
6.4.5 Frequency of downlinks . . . 121
6.5 Conclusion . . . 122

7 Measuring Radio Wave Propagation Effects 125
7.1 Introduction . . . 125
7.2 Observations of a Type III with five spacecraft . . . 126
7.3 Onset location of the Type III sources . . . 129
7.4 Spacecraft configuration assessment . . . 132
7.5 Propagation of the Type III sources . . . 137
7.6 Modelling the True location of Type III sources . . . 139
7.7 Measurements of Radio Wave Scattering . . . 140
7.8 Conclusion . . . 145

8 Conclusions 147
8.1 BELLA: Bayesian Localisation and Tracking of Type III Solar Radio Bursts 148
8.2 SURROUND: A Constellation of CubeSats around the Sun . . . 149
8.3 Measuring Radio Wave Propagation Effects . . . 150
8.4 Final Remarks . . . 151

9 Future Work 153
9.1 Making solar observations with eight spacecraft . . . 154
9.1.1 The Juno Waves investigation . . . 154
9.1.2 JUICE's Radio Plasma Waves Investigation . . . 155
9.1.3 BepiColombo's Plasma Wave Investigation . . . 156
9.1.4 Ulysses' Unified Radio and Plasma Wave Instrument . . . 157
9.2 BELLApy . . . 158
9.2.1 BELLA 3D . . . 160
9.2.2 BELLA+ . . . 163
9.3 SURROUND 2.0 . . . 163
9.4 Firefly . . . 165

List of Figures

1.1 Anatomy of the Sun. 2
1.2 Temperatures of the solar atmosphere. 4
1.3 The butterfly diagram and solar cycle. 4
1.4 Schematic of solar flux-transport dynamo processes. 6
1.5 The fast and slow solar wind measured by Ulysses. 7
1.6 Example of a flare shown at multiple wavelengths. 9
1.7 The standard flare model. 9
1.8 Example of a CME observed by SOHO. 11
1.9 Cartoon of the Earth's magnetosphere. 13
1.10 Example of SEPs interacting with the LASCO C3 coronagraph. 13
1.11 Cartoon of the different types of solar radio bursts. 15
1.12 Example of a Type III from Badman et al. (2022). 17
1.13 Schematic of the goniopolarimetry (GP) technique. 20

2.1 Plasma β model over an active region. 32
2.2 Flow diagram of the Plasma Emission Mechanism. 34
2.3 Simulations of the bump on tail instability made by Hou et al. (2024). . . . 34
2.4 Cartoon of the anisotropic scattering process. 37

3.1 Schematic of the Wind spacecraft and its orbit. 41
3.2 Schematic of the STEREO spacecraft and its orbit. 44
3.3 Schematic of the PSP spacecraft and its orbit. 47
3.4 Schematic of the SolO spacecraft and its orbit. 50
3.5 Artist impression of Mars Express. 54
3.6 CubeSats deployer and MarCO schematic. 55
3.7 Diagram of the Nançay Radioheliograph. 57

4.1 Examples of GH light-curves fittings. 64
4.2 Example of Type III leading, backbone and trailing edge fitting. 65

4.3 TOA vs TDOA comparison. 67

5.1 Example of the Bayesian trace plots. 78
5.2 BELLA confidence maps. 81
5.3 BELLA simulations of the STEREO-WIND constellation. 82
5.4 Summary of a full revolution of the STEREO-WIND simulations. 83
5.5 The event observed on 7 June 2012. 85
5.6 Images of the solar disk's features observed on 7 June 2012. 86
5.7 BELLA multilateration results compared with other localisation methods. . 88
5.8 BELLA multilateration results compared with GP inversions. 89
5.9 X and Y coordinate correlations of the posterior distribution. 90
5.10 Results of BELLA in polar coordinates. 92
5.11 Results of BELLA compared with the HUXt model. 94
5.12 Plasma frequencies observed by BELLA compared with in situ data. 95

6.1 Artist Impression of SURROUND. 101
6.2 SURROUND Constellation Overview. 102
6.3 Electron density models. 102
6.4 The SURROUND mission concept. 104
6.5 Cadence analysis for the proposed ecliptic spacecraft. 112
6.6 Summary of cadence analysis. 116
6.7 Comparison of the confidence maps between 3 and 5 spacecraft. 117
6.8 Comparison of 5-spacecraft confidence maps at different angles. 118
6.9 Stowed vs deployed configuration of the MarCO spacecraft and antenna gain vs area. 120

7.1 Double Type III radio burst observed on 4 December 2021. 127
7.2 Light travel adjusted and vertically stacked plot of the double Type III radio burst observed on 4 December 2021. 128
7.3 NRH imaging of the event and PFSS. 130
7.4 Combined e-Callisto and RPW spectra of the Type III event. 131
7.5 X-ray emission associated with the Type III event. 131
7.6 The effects on spacecraft configuration on the multilateration results. 133
7.7 The effects on spacecraft number on the multilateration results. 135
7.8 5-spacecraft multilateration of a Type III event. 138
7.9 BELLA results compared with electron density models. 140
7.10 ACE in-situ data. 141
7.11 BELLA results compared with theoretical model based source locations. . . 142

7.12 The observed scattering shifts between source location and theoretical model based sources. 143

9.1 Artist impressions of the Juno and JUICE spacecraft. 154
9.2 Artist impression of BepiColombo. 156
9.3 The orbit of the Ulysses spacecraft. 157
9.4 Cartoon of the intersection of the 3D multilateration spheres by 3 spacecraft. 161
9.5 Potential 8-Spacecraft configuration on 26 June 2028. 162
9.6 Spacecraft configuration of the Firefly mission. 166

List of Tables

1.1 GOES solar flare classification. 11

9.1 Summary of SURROUND's Mission Analysis results. 164
9.2 List of proposed Firefly instruments. 167

List of constants

All constants are in standard units as defined by the International System unless stated otherwise:

$c = 2.997\,924\,58 \times 10^{8}\,\mathrm{m\,s^{-1}}$

$\mathrm{R}_{\odot} = 6.957 \times 10^{8}\,\mathrm{m}$

$\mathrm{au} = 1.495\,978\,707 \times 10^{11}\,\mathrm{m}$

$k_B = 1.380\,649 \times 10^{-23}\,\mathrm{J\,K^{-1}}$

$e = 1.602\,176\,634 \times 10^{-19}\,\mathrm{C}$

$\mathrm{m}_e = 9.1 \times 10^{-31}\,\mathrm{kg}$

$\varepsilon_0 = 8.854\,187\,817 \times 10^{-12}\,\mathrm{F\,m^{-1}}$

$\mu_0 = 12.566\,370\,614\,4 \times 10^{-7}\,\mathrm{H\,m^{-1}}$

1 Introduction

In the past, civilisations like the Aztecs, Greeks or the Egyptians venerated our closest star and treated it like a god. However, modern society has stopped looking up towards the sky and is more interested in looking down at their phones. The truth is that the Sun is not a god, but that does not mean that our technologically dependent society cannot suffer from its wrath.

In 1859, a super-flare known as the Carrington event (Carrington, 1859; Hodgson, 1859) caused fires and disruptions across the telegraph network (Boteler, 2006). The magnitude of this event is unknown, and estimates vary between X14 and X80 (Hayakawa et al., 2023). Regardless of the event's exact magnitude, the flare was undoubtedly an extremely powerful event, and it is crucial to understand that a flare of that scale today would cause destruction to power grid transformers, satellites, and put astronauts at serious risk, among other risks. Fortunately, this event was a relatively rare occurrence, but not the last one. In 1989 the city of Quebec experienced a blackout that left thousands of people without power (Guillon et al., 2016). The cause of the blackout was reportedly a pair of coronal mass ejections (CMEs), associated with an X4.5 flare and M7.3 flare (Boteler, 2019).

Despite the potential to cause damage, the Sun is also responsible for all living creatures on Earth. It powers our society, the water cycle, winds, and nearly every energetic event in the solar system is ultimately linked to the Sun in one form or another. The Sun is nothing more than a medium-sized star, classified as a G2V main sequence star in the Hertzsprung-Russell diagram. It formed approximately 4.6 billion years ago and will continue to power our planet

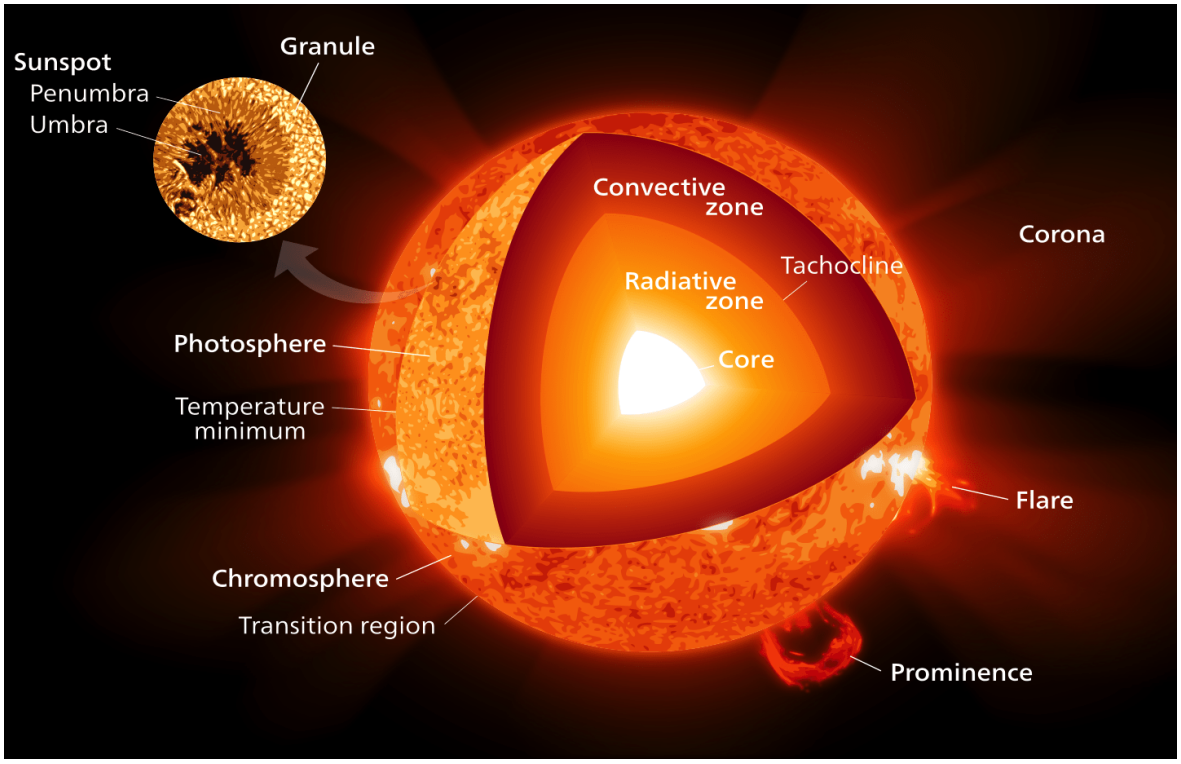


Figure 1.1: The Sun is structured in different layers. At its centre, the core is an active nuclear fusion reactor at 15 MK. As the energy escapes the core, it reaches the radiative zone at 7 MK, the plasma is then cooled down to 2 MK in the convection zone, where currents get generated causing the complex magnetic field of the Sun. The photosphere is the layer visible from Earth at a temperature of 4000 K to 6500 K. The chromosphere is the following layer and it has a temperature that starts at 4000 K and increases with altitude until reaching a temperature of 20 000 K. The outermost layer of the Sun is the corona, which extends gradually into the inner heliosphere reaching temperatures of up to 1.5 MK. This thesis will focus on events occurring on the corona. Source: Universe Today.

for another 5 billion years. After this period, it will become a red giant, continuing its journey for another billion years before transitioning into a white dwarf hidden behind the remnants of its outer layers, and likely displaying a beautiful planetary nebula for the universe to see.

The mass of the Sun is approximately 1.9889×10^{30} kg, and it has a radius ($R_{\odot}$) of 6.957×10^{8} m[1]. At its core (see Figure 1.1), the Sun is an active nuclear fusion reactor, turning hydrogen into helium at temperatures of approximately 15 MK. The photosphere is often considered a blackbody and emits radiation at all wavelengths. However, before this radiation gets emitted into the heliosphere, photons of light must endure a long journey from the

[1] `https://nssdc.gsfc.nasa.gov/planetary/factsheet/sunfact.html`

core, gradually cooling down until they reach the surface, passing through the radiation layer at 7 MK, the convection layer at 2 MK, the photosphere at 6500 K to 4000 K, the chromosphere at 4000 K to 20 000 K, and finally the corona, which reaches temperatures of 1 MK to 2 MK before cooling down again as it gradually extends into interplanetary space.

1.1 The Solar Corona

The sudden increase in temperature in the two outermost layers of the Sun, is shown in Figure 1.2, and is known as the coronal heating problem (Grotian, 1939; Edlén, 1943). This sudden exponential rise in temperature, known as the transition region between the chromosphere and the corona, remains one of the largest mysteries in astrophysics, seemingly violating the laws of thermodynamics. It all indicates that a series of processes and complex mechanisms, such as nanoflares and magnetic reconnection, might all be factors contributing towards this effect (Parnell & De Moortel, 2012); however, this is still the subject of investigation.

The solar surface is a complex region dominated by the magnetic fields generated as a consequence of the convection zone and tachocline (Kosovichev et al., 1997; Dikpati & Gilman, 2009). The convective currents generated, are visible on the photosphere as what is known as granules, which are relatively small areas of hot plasma moving towards the surface and are surrounded by cool plasma flowing down into lower layers. The convection zone exhibits a differential rotation, where the equator rotates faster than the poles and is separated from the radiation zone, which rotates as a solid body, by the tachocline. The two different rotational behaviours, result in a significant shear layer which is believed to play a crucial role in the solar dynamo, contributing to the amplification and organisation of magnetic fields (Spiegel & Zahn, 1992; Miesch, 2005).

The dynamo effect in the Sun results in a cycle known as the Solar cycle which was discovered by Schwabe (1844). During this cycle, the sun experiences peaks of violent activity, known as solar maximum, and periods of no (major) activity, where the solar surface remains

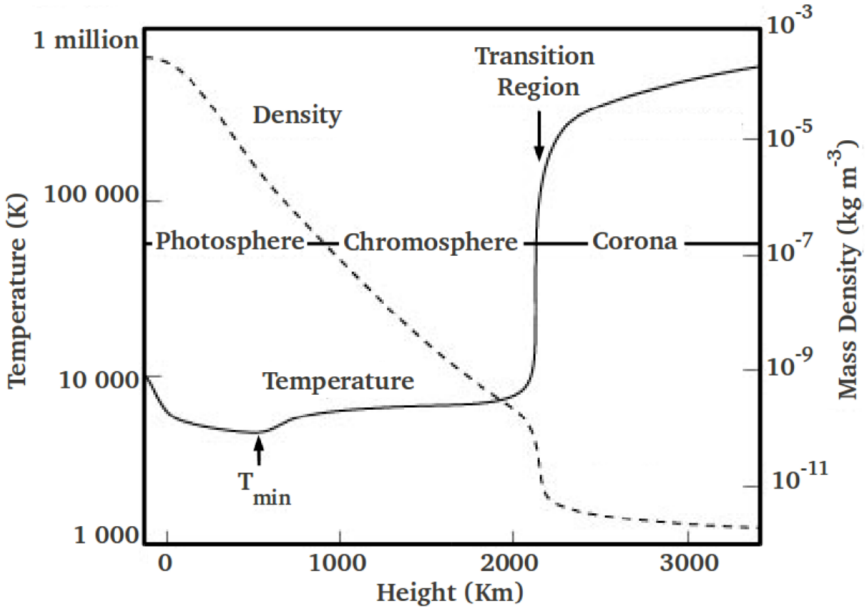


Figure 1.2: Temperature of the solar atmosphere compared to the surface height. The temperature decreases in the photosphere until approximately 500 km, after which it slowly increases in the chromosphere until a height of approximately 2000 km. At this point, the temperature rises exponentially within a few hundred kilometres, reaching temperatures of the order of 1 MK. This region, known as the transition region, separates the chromosphere from the solar corona. Source: Page 112 of Lang (2001).

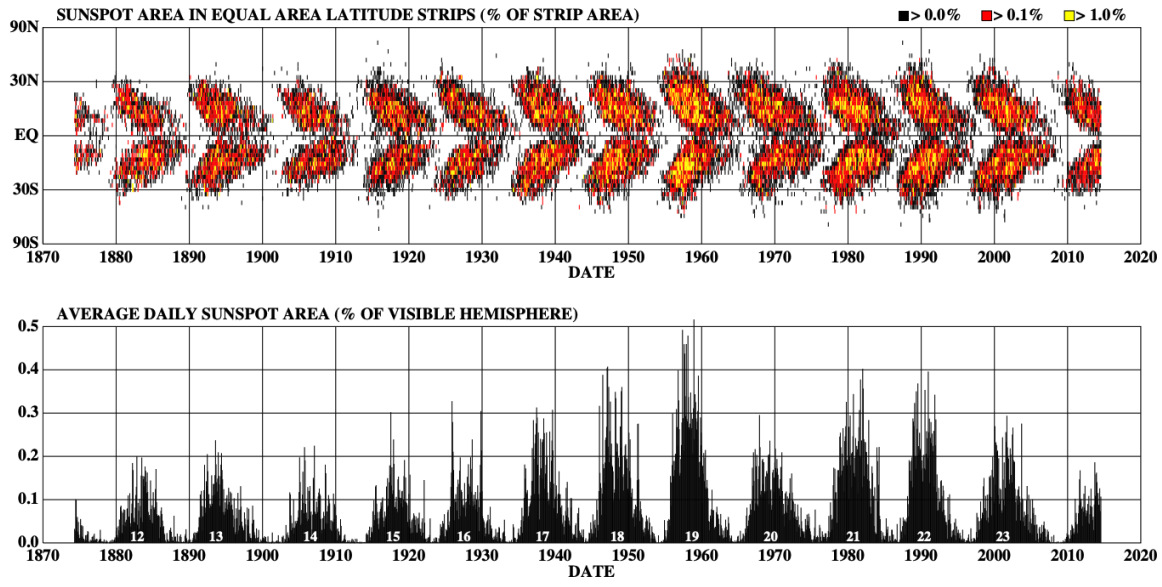


Figure 1.3: Sunspots as a function of latitude and time. *Top* shows the 'butterfly diagram' which maps the latitudinal location of sunspots over time. The characteristic pattern shown in this diagram shows the tendency of sunspots first appearing at higher latitudes and then towards the equator. It is also observed that the sunspots tend to appear at either side of the equator but do not typically cross it. *Bottom* shows the number of sunspots as a function of time, showing the solar cycle is an 11 year cycle. Source: Hathaway (2015).

mostly featureless. During solar maximum, a series of spots appear in the solar surface which appear dark in the photosphere. These 'sunspots' are cooler than the surrounding areas, thus giving the 'darker' appearance. However, sunspots are indeed regions that appear bright in other wavelengths of light, and are particularly bright when observing the chromosphere. Sunspots are of particular interest because they are associated with the two most powerful phenomena in the solar system, flares and CMEs.

Figure 1.3 (*top*) shows what is commonly known as the 'butterfly diagram'. This diagram shows the observed sunspots mapped in latitude strips as a function of time. The characteristic shape, is the result of the sunspots tendency to appear at approximately 30° to 45° latitude during the beginning of solar maximum and subsequent sunspots appear closer to the equator. This apparent drift was first noticed by Carrington (1858) and is commonly known as Spörer's Law (Hathaway, 2015). Additionally, Figure 1.3 (*bottom*) shows the number of sunspots taken each year, this revealed that the Sun's solar cycle has a period of 11 years. Furthermore, Hale et al. (1919) discovered what is now known as Hale's polarity laws, which states that in sunspot pairs, the leading and following sunspots in the Northern and Southern hemispheres exhibit opposite magnetic polarities. This pattern is mirrored across hemispheres and reverses with each solar cycle.

All these phenomena can be explained via the solar flux-transport dynamo process as described by Dikpati & Gilman (2009). In this process (see cartoon, Figure 1.4), the Sun first displays an organised poloidal magnetic field configuration, which gets sheared as a consequence of the differential rotation between the equator and the poles. This shearing changes the magnetic configuration of the Sun from poloidal to toroidal, which, as the magnetic field strengthens, forms buoyant loops that rise to the surface of the Sun. The footpoints of these loops on the photosphere form sunspots. These loops can become complex, and pressure from surrounding magnetic fields can twist them into a variety of intricate magnetic field loops, which can get reconnected, giving rise to solar flares and CMEs. As the magnetic flux keeps emerging, it causes dispersion both in latitude and longitude, which causes the

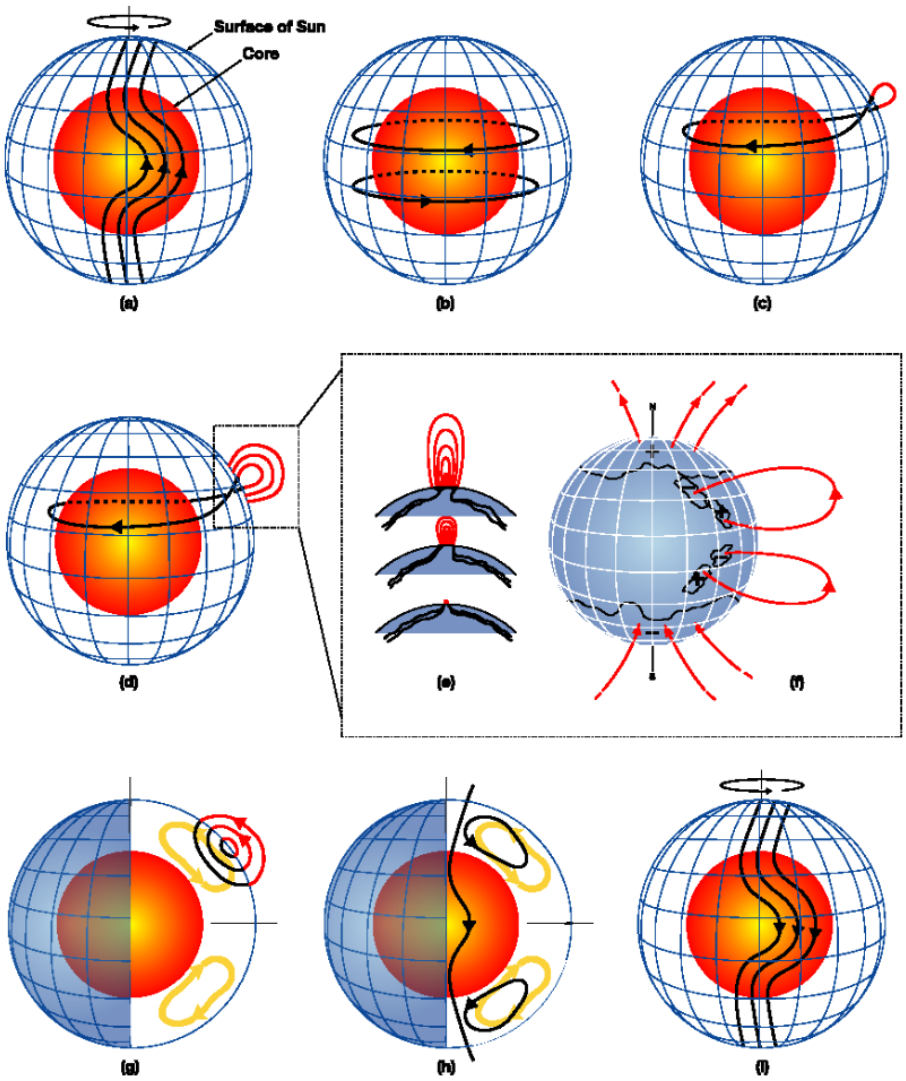


Figure 1.4: Diagram of the solar flux-transport dynamo processes. The radiative core shown in red and the solar surface shown as a blue mesh, with the space between them representing the solar convection zone where the dynamo operates. (a) The Sun's faster rotation at the equator compared to the poles generates differential rotation near the base of the convection zone, shearing the poloidal magnetic field. (b) This shearing creates a toroidal magnetic field, which (c) strengthens and forms buoyant loops that rise to the surface, twisting due to rotational forces and forming sunspots. (d, e) Additional magnetic flux emerges and spreads, causing (f) dispersion in latitude and longitude from decaying sunspots. (g) The meridional flow, depicted by yellow loops, transports the surface magnetic flux towards the poles, reversing the polar magnetic fields. (h) Some of this flux moves downwards to the base of the convection zone and towards the equator. (i) The reversed poloidal flux is sheared again by differential rotation at the base, creating a new toroidal field with an opposite sign than that of the original. Source: Dikpati & Gilman (2009).

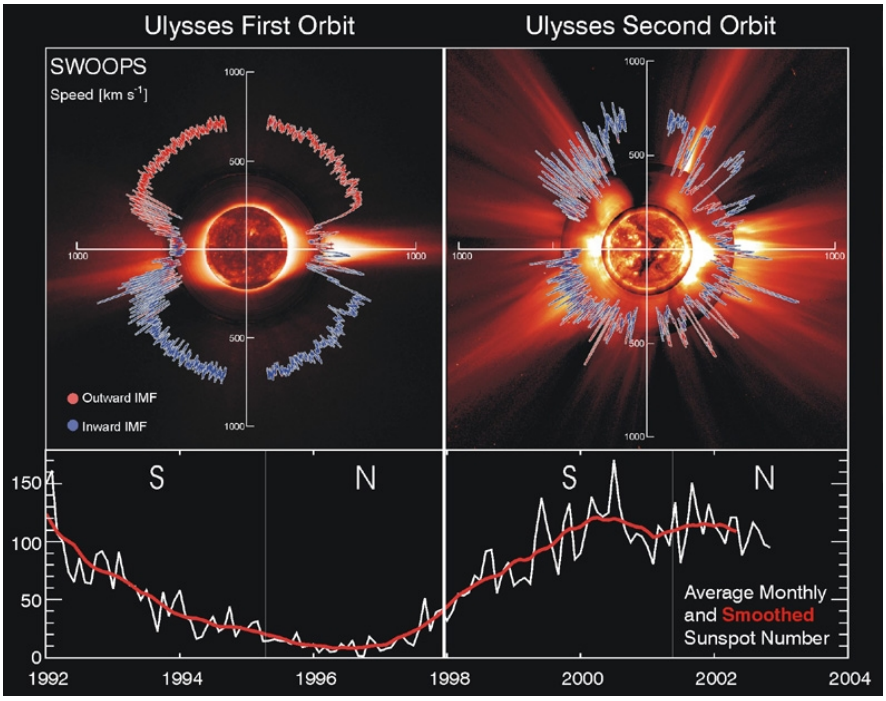


Figure 1.5: The fast and slow solar wind measured by Ulysses. *Left* shows the results obtained during solar minimum and *right* shows the results obtained during solar maximum. *Top* shows the velocity of the solar wind compared to the direction of the magnetic field lines. *Bottom* shows the sunspots number as a function of time for the period of the observations. It was shown that at solar minimum, the poles of the Sun produced most of the fast solar wind and the slow solar wind was produced at the equator. During solar maximum, the fast and slow solar winds were disorganised by the complex magnetic structures. Source: McComas et al. (2003).

sunspots to decay and the magnetic flux to spread. Eventually, the meridional flow transports the magnetic flux towards the poles, reversing their polarity and giving rise to a new poloidal configuration, which is reversed compared with the original poloidal configuration.

As mentioned, the Sun cycles through periods of violent activity at solar maximum and relatively quiet periods at solar minimum. However, this does not mean that the Sun ceases to emit other types of particles during solar minimum. The solar wind, first theorised by Eugene Parker (Parker, 1958, 1969), is a perpetual phenomenon resulting from the intense heat pressure exerted by the star on the outer layers of the solar atmosphere. The solar wind consists of electrically charged particles, such as electrons, protons, and alpha particles, streaming away due to the large pressure gradient between the hot corona and the cold interplanetary space. Magnetic confinement can prevent the plasma from escaping, but wherever the mag-

netic field is open, the plasma escapes. The solar wind typically flows at two different modes: the fast solar wind, travelling at $\sim 750\,\mathrm{km\,s^{-1}}$, and the slow solar wind, travelling at approximately $\sim 350\,\mathrm{km\,s^{-1}}$.

Figure 1.5 shows the data obtained by Ulysses during its first two orbits, which occurred during periods of solar minimum and solar maximum, respectively (McComas et al., 2003). During the period of solar minimum, it was observed that the solar wind is fastest at the poles and slowest at the equator, consistent with a poloidal magnetic configuration. However, during periods of solar maximum, the complex magnetic structure of the Sun allows for the fast solar wind to occur at all latitudes. Taking solar minimum as a benchmark, one can observe that the source of the fast solar wind is at the poles. This is due to the presence of coronal holes, which are large areas of open magnetic field lines that allow plasma to flow freely from the lower layers of the Sun's atmosphere. On the other hand, the slow solar wind is attributed in this case to the magnetic streamer formed at the equator. In this scenario, the plasma does not flow freely from the lower layers of the atmosphere and must flow from the corona. Therefore, the lower density of the source constrains the flow velocity (Fisk et al., 1998). During solar maximum however, coronal holes may appear at all latitudes, thus explaining Figure 1.5 which showed a highly disorganised velocity field with fast streaming solar wind sources at all latitudes of the Sun.

1.2 Flares and Coronal Mass Ejections

The Carrington event was a relatively rare event in magnitude, but flares are certainly not rare (e.g., see catalogue; Watanabe et al., 2012). Flares are rapid releases of energy (e.g., Figure 1.6) associated with active regions. The energy output of a solar flare varies widely depending on the magnitude of the flare where the largest measured flares can output $\sim 10^{25}$ J in minutes (Emslie et al., 2004). For context this is the equivalent of a combined 50 million Tsar bombs, the largest nuclear bomb ever detonated.

These solar explosions emit radiation across all wavelengths of the spectrum; however, they

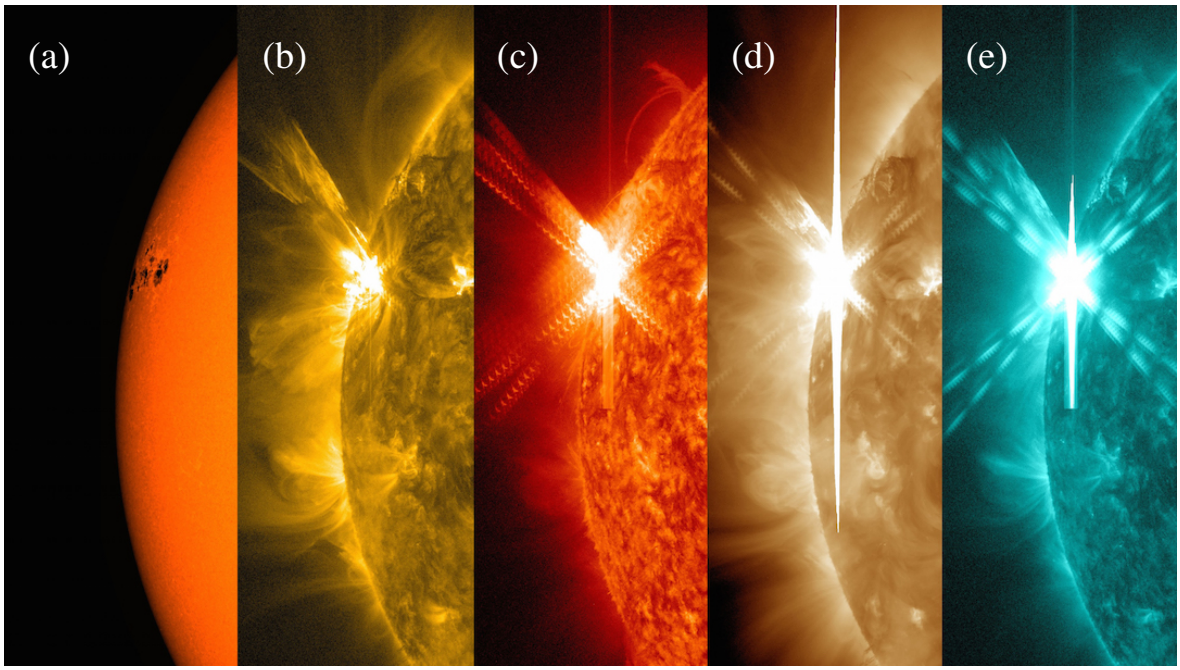


Figure 1.6: Example of a CME observed on 5 May 2015 at (a) visible light, (b) 171 Å, (c) 304 Å, (d) 193 Å, and (e) 131 Å. The flare, observed as a bright flash on the Sun's eastern limb, was classified as an X2.7-class flare. Source: NASA/SDO.

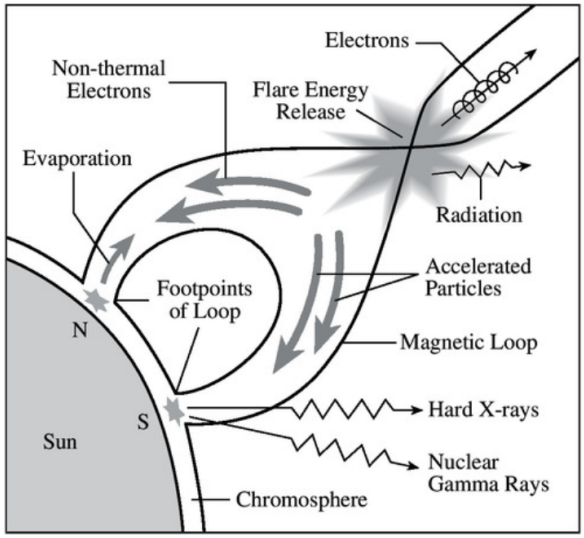


Figure 1.7: Cartoon of the standard model of a solar flare. Magnetic pressure leads to reconnection, which accelerates electrons to relativistic speeds. This acceleration produces radio emissions and soft X-rays along the loop, as well as hard X-rays and gamma rays at the footpoints. The accelerated electrons and protons heat up the chromosphere, causing chromospheric evaporation where hot plasma rises along the newly formed loop. Above the reconnection point, electrons and other particles are ejected, and if there is sufficient material, this can lead to a CME. Source: Page 142 of Lang (2001).

are particularly bright in the X-ray, EUV, and radio wavelengths, often outshining the rest of the Sun in its quiet state. The close proximity of flares to sunspots suggests that flares are energised by powerful magnetic events. While the flaring mechanisms are not fully understood and remain the subject of investigation, the standard flare model (see Figure 1.7) describes flares as the result of magnetic reconnection caused by the pressure exerted by processes such as flux emergence or complex magnetic field configurations.

Magnetic reconnection rapidly accelerates electrons and protons to relativistic speeds along the magnetic loops. When these accelerated particles reach the chromosphere at the footpoints of the magnetic loop, hard X-rays are produced via Bremsstrahlung emission. Additionally, nuclear reactions caused by the acceleration of protons and alpha particles generate gamma rays. The downward-moving electrons quickly heat the chromosphere, causing the plasma to expand along the magnetic field in a process known as chromospheric evaporation (Antiochos & Sturrock, 1978; Milligan et al., 2006a,b). The rising hot plasma results in soft X-rays and EUV emission.

Above the reconnection point, protons, electrons and heavier nuclei get accelerated to quasi-relativistic speeds and will travel along newly formed open magnetic field lines, causing intense radio emission, these are also referred to as solar energetic particles (SEPs). In some cases, if sufficient plasma has accumulated above the reconnection point, the plasma gets accelerated outwards and a CME occurs.

Flares are typically classified according to the Geostationary Operational Environmental Satellite (GOES; Mallette, 1982) classification, where the 1–8 Å measured peak flux (in W m^{-2}) determines the class. This classification is observed in Table 1.1.

CMEs are eruptions of plasma, ejected from the corona into the heliosphere. These eruptions were first detected by the seventh Orbiting Solar Observatory (OSO-7) and reported by Tousey (1973), although the term 'coronal mass ejection' was not coined until the late seventies (Munro et al., 1979)[2]. CMEs can be very violent explosions, and can rival the

[2] https://ntrs.nasa.gov/citations/20100030613

Class	Peak 1–8 Å flux (W m^{-2})
A	10^{-8} to 10^{-7}
B	10^{-7} to 10^{-6}
C	10^{-6} to 10^{-5}
M	10^{-5} to 10^{-4}
X	10^{-4} and above

Table 1.1: GOES solar flare classification. The peak flux in the 1–8 Å measurement determines the classification of the flare where A are the weakest and X are the strongest flares. Source: NOAA.

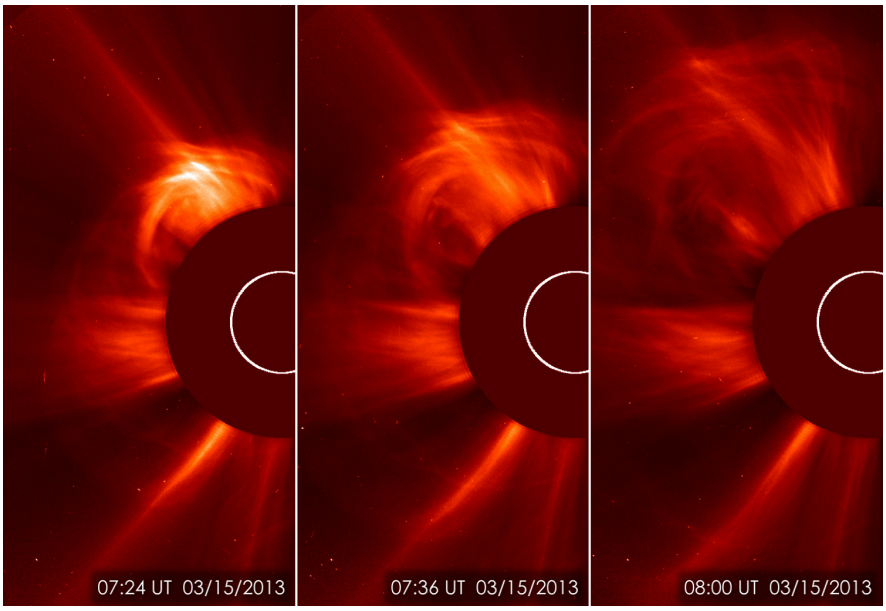


Figure 1.8: Example of a CME eruption on the northern-eastern limb of the Sun. The eruption occurred on 15 March 2013 and was captured by LASCO. This CME was associated with an M1.1 class flare (Beşliu-Ionescu et al., 2014). Source: ESA/NASA/SOHO.

solar disk in size (see e.g., Figure 1.8), although not in brightness. This means that in order to observe CMEs, coronagraphs are required. CMEs can be associated with flaring events, where if the initial magnetic confinement is strong enough, a plasmoid accumulates above the point that will become the reconnection point and gets ejected at reconnection. However, this is not always the case (e.g., filament eruptions) and there are multiple instances of CMEs occurring without flares and vice-versa (e.g., Vršnak et al., 2005). The ejected material is typically protons, electrons and traces of heavier nuclei such as alpha particles, which can cause significant damage if they reach Earth (e.g., the Quebec blackout). The velocity of a

CME can vary from a $100\,\mathrm{km\,s^{-1}}$ to $3500\,\mathrm{km\,s^{-1}}$ (Gopalswamy et al., 2009) and eventually reach the solar wind velocity as they propagate through interplanetary space.

1.3 Space Weather

Earth's magnetic field, provides a first line of defence against the perpetual flow of electrically charged particles in the solar wind and the arrival of CMEs and SEPs. Earth's magnetic fields in the absence of the solar wind would be dipolar, however, the pressure from the wind causes a tail at the night side of the Earth (see Figure 1.9). The magnetic fields from highly energetic events such as CMEs and SEPs can interact with Earth's magnetic fields, causing reconnection and triggering the acceleration of particles towards the poles. This causes beautiful displays of aurora at the poles but also devastating effects for our satellites, power grids, astronauts and more.

There are several mechanisms through which space weather (SW) events interact with technology. Figure 1.10 is an example of SEPs arriving to the SOHO/LASCO C3 instrument, interacting with the detector. The severity of the interaction will depend on the energy of the SEP, and can potentially overload the equipment and destroy it. A notable example of this occurred in 1994, where two telecommunication satellites known as Anik E1 and E2 suffered severe damage disrupting communications and television broadcast across Canada. Eventually the two spacecraft were recovered but at the estimated cost of $50 to $70 Million in recovery costs and lost business (Lam et al., 2012).

Another mechanism is the geomagnetically induced current (GIC), where the stream of magnetised particles along the Earth's magnetic fields, causes induced currents at Earth's power networks, potentially overloading the grid and causing transformer failure (Blake et al., 2016; Malone-Leigh et al., 2024). Apart from the Quebec blackout, another notable example is the damage of transformers in South Africa during the October 2003 geomagnetic storm (Gaunt & Coetzee, 2007).

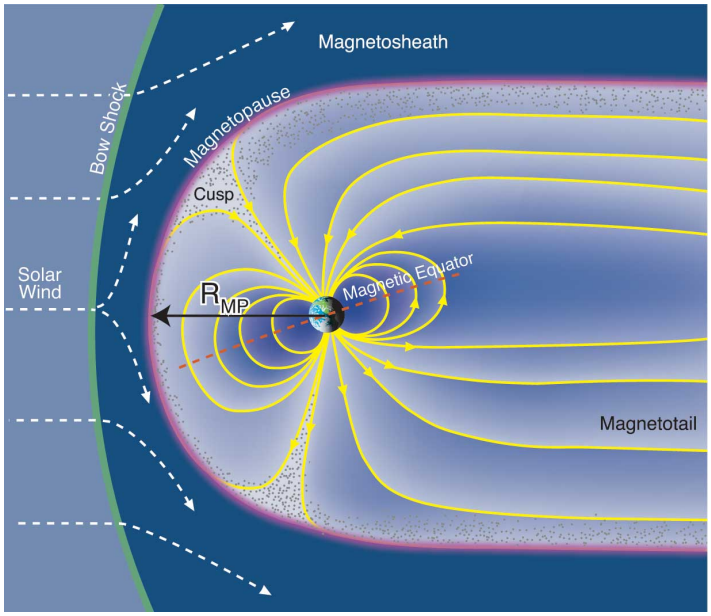


Figure 1.9: Cartoon of the Earth's magnetosphere. The solar wind interacts with the bow-shock and magnetopause re-directing harmful SEPs towards the poles and protecting Earth from harmful radiation. However, streaming particles can induce currents at Earth's power infrastructure causing potential overload and disruptions across the network. Credit: Fran Bagenal/Steve Bartlett.

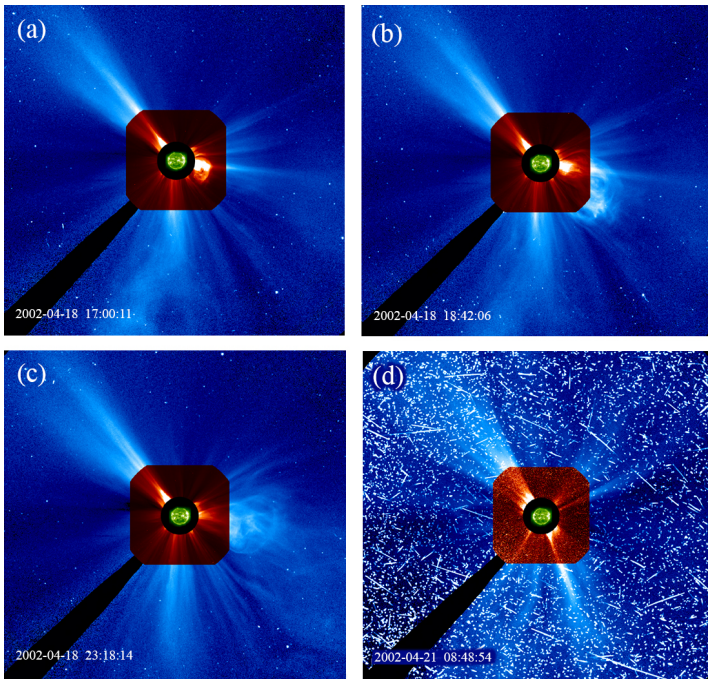


Figure 1.10: Example of SEPs interacting with the LASCO C3 coronagraph after the eruption of a CME. The arrival of SEPs can cause overload and significant damage to electronics. Credit: NASA/SVS.

Additionally, while Earth's magnetic fields do provide protection to humans on the ground, space-based astronauts do suffer increased exposure to radiation during SEP events. It is reported (Reames et al., 2001) that a $\sim$30 MeV proton penetrates spacesuits and a $\sim$130 MeV proton requires 20 g cm^{-2} of shielding. Reames et al. (2001) mentions that an SEP event that occurred on 4 August 1972 would have been fatal to astronauts had they been poorly shielded.

The dangers of SW has resulted in the creation of agencies such as ESA's Space Weather Service Network[3] and the Space Weather Prediction Center (SWPC)[4] which is part of the National Oceanic and Atmospheric Administration (NOAA). These agencies are focused on forecasting and nowcasting SW events with the aid of space and ground-based telescopes. By providing warning information, satellite operators can switch off sensitive equipment to prevent overloads, communication services can anticipate disruptions and electrical companies can reduce the load of the powergrids, potentially saving the expensive infrastructure.

1.4 Solar Radio Bursts

Of all the naturally occurring radio emitting sources in the universe, solar radio bursts (SRBs) associated with flares and CMEs rank among the highest power level received by radio spectrometers at Earth. They are powerful enough that a simple dipole antenna connected to almost every radio receiver will detect them, although the receiver must still be sufficiently sensitive. SRBs were first discovered in the early 1940s during the peak of World War II. Strange radio disturbances were being detected and were suspected to be an attempt at jamming radio signals transmitted by the Germans. James Stanley Hey discovered that these were in fact stellar in origin (Hewish, 2002), but due to the war secrecy, this discovery was not made public until the late 1940s.

Today we know that SRBs are generated during powerful solar phenomena, where non-

[3] `https://swe.ssa.esa.int/`
[4] `https://www.swpc.noaa.gov/forecasts`

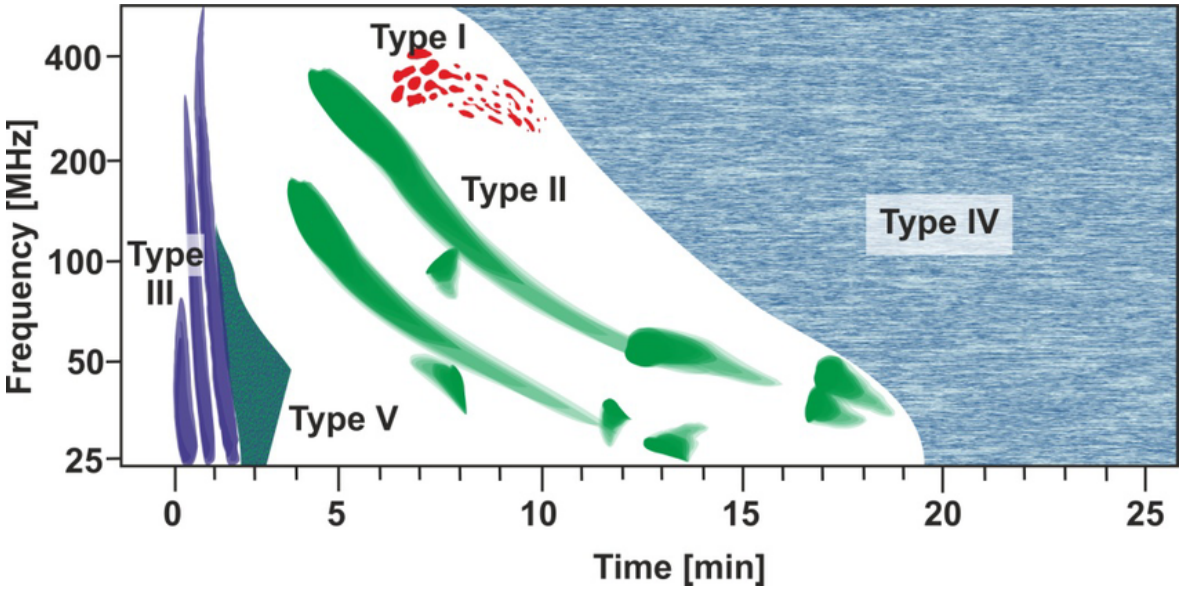


Figure 1.11: Cartoon showing the different types of SRBs. The different SRBs are classified by their morphology and are associated to different phenomena. This thesis focuses primarily on Type IIIs which are associated with electrons travelling along open magnetic field lines. Type IIs are briefly addressed in this thesis and these are associated with shock-driven CMEs Source: Ganse et al. (2012); Dabrowski et al. (2016).

thermal electrons emit radio waves via the plasma emission mechanism (discussed in Chapter 2). SRBs are classified into different types based on their morphology, each type being associated with different solar phenomena.

Type I radio bursts, also known as noise storms, are short narrow band bursts, that occur in large numbers and can last from minutes to days. Their frequency is in the meter wavelength range and their mechanism is attributed to small energy events such as nano-flares, micro-flares or magnetic flux emergence, that accelerate non-thermal electrons to produce emission strictly at its fundamental plasma frequency (Spicer et al., 1981; Mercier & Trottet, 1997; Cintra et al., 2020).

Type II radio bursts (Nelson & Melrose, 1985), are bursts that appear over a wide range of frequencies in the metric to decametric range, and drift relatively slowly ($\sim 0.1\,\mathrm{MHz\,s^{-1}}$) than other type of bursts. This drift rate is often used to compute the velocity of the radio driver, resulting in velocities of $\sim 1000\,\mathrm{km\,s^{-1}}$ to $3500\,\mathrm{km\,s^{-1}}$ which is faster than the Alfven speed, and the reason why Type II radio bursts are associated with shock-driven

CME. Type IIs are relatively narrow in bandwith, with $\Delta f_t \sim 100$ MHz. The typical duration of a Type II is in the order of 15 min. Morphologically, a Type II radio burst in the dynamic spectra contains two bands, one corresponding to the fundamental frequency and the second band is the harmonic emission located at twice the frequency of the fundamental. Type II are also observed to drift from higher frequency to lower frequencies as a consequence of the shock travelling outwards and the plasma frequency decreasing with lower densities.

Type IIIs are rapid drifting signatures, associated with electrons travelling along open magnetic field lines. Type IIIs are of particular interest for this thesis and will be described in more detail in Section 1.4.1.

Type IV radio bursts are composed of both broadband continua and fine structures appearing in the decimetric to metric range. Type IV radio bursts have been associated with gyrating particles (LaBelle et al., 2003) as a result of large fluxes of mildly energetic electrons being injected into a coronal loop. Type IVs are often associated with full halo CMEs (Gopalswamy, 2011) although it is not clear what part of the full Halo CME is responsible for the generation of Type IVs. Their duration is much longer compared to other bursts as these last from hours to days and they may or may not drift depending on whether the burst is stationary or moving.

Type V radio bursts are the last major type of radio burst. They are characterised for being broadband meter wavelength emission appearing strictly after a Type III radio burst has occurred (Stewart et al., 1965). Type Vs are closely associated with Type IIIs and is widely accepted that their origin is in electrons that initiated their journey as a Type III but got trapped in a closed magnetic field line in the corona.

1.4.1 Type III Bursts

Type III radio bursts (e.g., Figure 1.12) are probably the most abundant (see review; Reid & Ratcliffe, 2014) and a widely studied type of radio burst coming from the sun, being characteristic for their sharp drift rate. Type III radio bursts are usually very bright, with fast

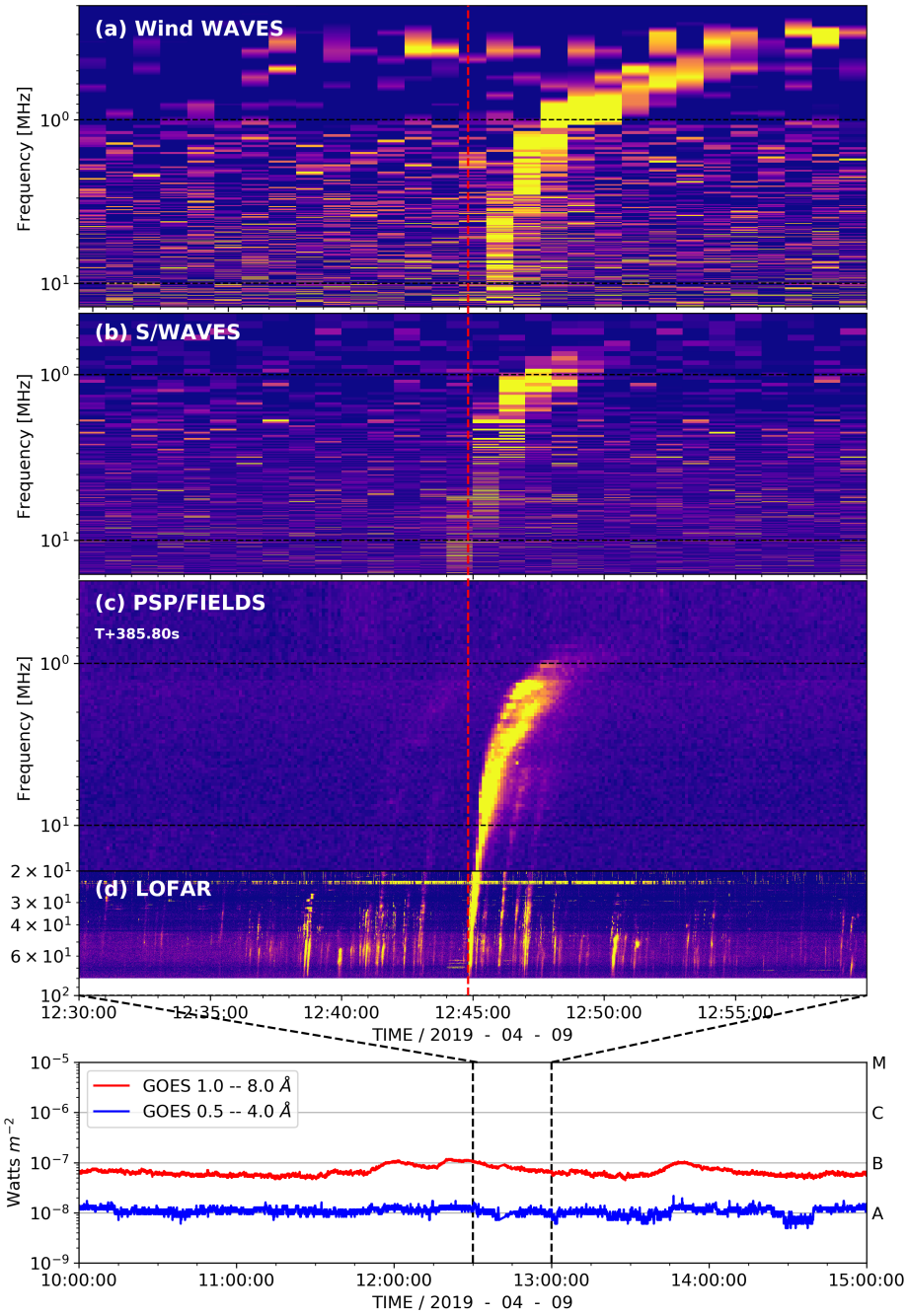


Figure 1.12: Example of a bright Type III radio burst observed by (a) Wind/Waves, (b) STEREO A/Waves, (c) PSP/Fields and (d) LOFAR. The LOFAR spectrogram shows that the Type III is embedded in a Type III noise storm. The *bottom* panel shows GOES X-ray flux, showing that the Type III noise storm occurred during a relatively calm period, in the absence of major flares. Source: Badman et al. (2022).

drift rates going from higher (1 GHz) to lower frequencies (10 kHz), and occur for a relatively short period of time ($\sim$ 5 min). Type IIIs are associated with electron beams travelling along open magnetic field lines, from the inner corona to the outer heliosphere.

Electrons can be accelerated to near relativistic speeds as a result of unstable magnetic field lines. The accelerated beams of electrons often results in the generation of Type III radio bursts as a consequence of the local plasma interaction of Langmuir waves being converted into electromagnetic radiation (Reid & Ratcliffe, 2014). Thanks to this interaction with local plasma and their abundance, Type III radio bursts are an ideal probe for investigating the different layers of the solar corona. An example of this is Reid & Kontar (2021) which showed that the fine structure of these bursts can often reveal information about small-scale turbulence in the corona. Additionally, the start frequency and the stop frequency of a Type III radio burst gives indication of what type of Type III it is. A Type III radio burst whose frequency starts in the GHz range is an indicator that an energetic event such as a flare has occurred (Reid & Ratcliffe, 2014), these bursts tend to be very bright due to a natural selection bias where it is believed that weak bursts get either absorbed by the corona or the higher density plasma background plays a bigger role in damping which will prevent weak bursts from happening at all. On the other hand there are the so called interplanetary Type III radio bursts that originate in the tens of MHz and their stopping frequencies are of a mere few KHz (Kou et al., 2020) which corresponds to a height of $\sim$1 au (Reid & Ratcliffe, 2014).

Type IIIs have a characteristic fast drift rate df/dt which is frequency dependent (Reid & Ratcliffe, 2014). This frequency dependency varies from study to study showing that $df/dt \propto f^{\alpha}$ where α ranges between 1 and 2.7. Measuring the drift rate, with the help of the appropriate density model, allows for the calculation of the velocity of the radio burst exciter. The general consensus is that the typical Type III corresponds to electron beam velocities that range between $v \approx 0.1$–0.3 c, although studies have shown that this number varies from Type III to Type III, with notable examples of Poquerusse (1994) which showed Type III exciters with associated relativistic speeds of 0.5–0.8 c and other studies such as

Meléndez et al. (1999) showed much slower speeds in the order of 0.14 c.

1.5 General Overview of Localisation Methods

Tracking SEPs using SRBs dates as far as the 1970s, where Baumback et al. (1976) and Kellogg (1976) used spacecraft from the Explorers program to track Type IIIs. However, there is not a large record of tracking Type IIIs until 1998, when Reiner et al. (1998) used the Wind spacecraft and Ulysses spacecraft to track a Type III along the path of a Parker Spiral. Since then, localising SRBs has proven to be a very prolific method of investigating Type IIIs (e.g. Cecconi et al., 2008; Magdalenić et al., 2014; Jebaraj et al., 2020).

Today, there are large interferometric facilities, that use multi-station ground-based telescopes and supercomputers capable of collecting terabytes of data for the purposes of imaging the location of these SRBs. One of these facilities, is the Low-Frequency Array (LOFAR; van Haarlem et al., 2013) which operates in the 10 MHz to 250 MHz range, and enables relatively precise tracking of radio sources low in the corona $<3\,R_{\odot}$. As an example, Morosan et al. (2014) tracked a Type III SRB at 30 MHz to 90 MHz using LOFAR tied-array observations with high temporal ($\sim$30 ms) and spectral (12.5 kHz) resolution. Moreover, LOFAR supports interferometric imaging as shown by Maguire et al. (2021), where a Type II radio source was imaged up to a height of $\sim 0.5\,R_{\odot}$. However, the Earth's atmospheric cutoff, prevents lower frequency emissions associated with interplanetary distances of being observed using ground-based telescopes. In order to observe at $\leq$10 MHz, space-based antennas are required.

Unfortunately, spacecraft have strict data budgets and strict instrument requirements that make them less sophisticated than their ground-based counterparts. However, there are a number of techniques and physical advantages that make observations at less than 10 MHz, particularly well suited to studying radio sources at great distances from the Sun.

A well-established method is the goniopolarimetry (GP) method, also known as the direction

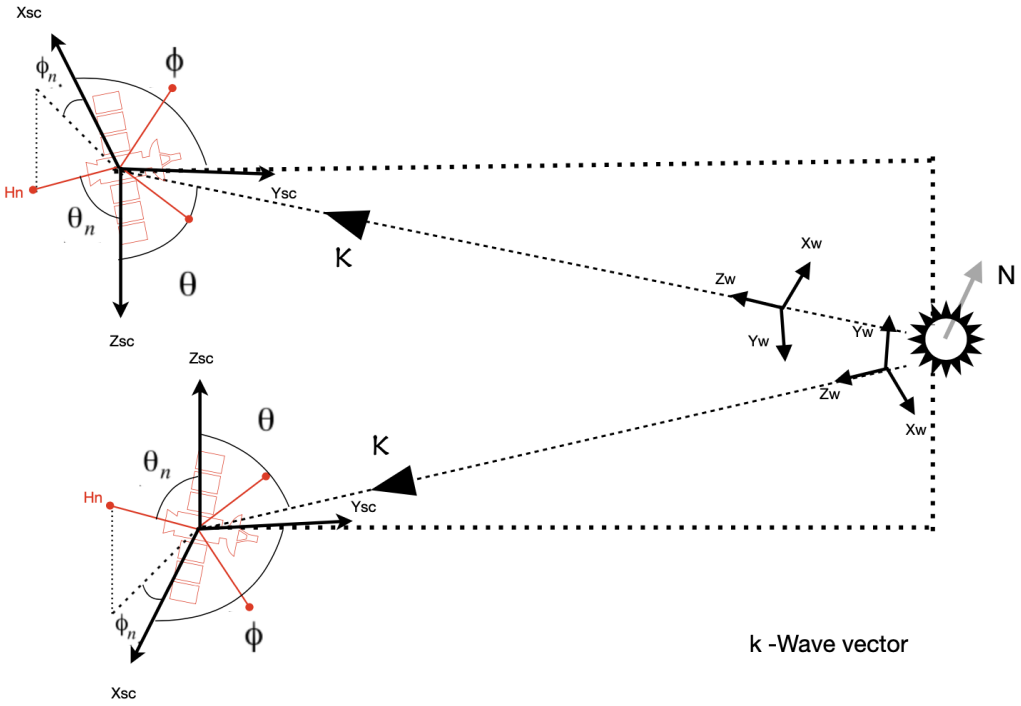


Figure 1.13: Schematic of the GP technique. Using two spacecraft equipped with three antennas each, the Poynting $\vec{k}$ vector can be obtained at each spacecraft. Back propagating these vectors until intersection will result in the localisation of the emission source. Source: Adapted from Cecconi & Zarka (2005).

finding method or triangulation, (Manning & Fainberg, 1980). GP uses the polarisation of radio waves to find the Poynting $\vec{k}$ vector (see Figure 1.13). Finding the direction of the $\vec{k}$ vector with different spacecraft allows for the back propagation of these vectors, which eventually intersect at the location of the source (e.g. Reiner et al., 1998). Some notable examples of using this method is described in Oliveros et al. (2012), Magdalenić et al. (2014), and Krupar et al. (2016), all of which used direction finding to track a Type II associated with a CME. Furthermore, examples of using GP to localise the sources of Type IIIs can be found in Fainberg et al. (1972), Reiner et al. (1998), and Krupar et al. (2024).

Weber et al. (1977), Steinberg et al. (1984), and Hoang et al. (1998) showed that time delay measurements with two spacecraft could potentially be an alternative to the GP method. Time delay methods, also known as Multilateration, consists in analysing the time at which the signal is received by different detectors to infer the location of the sources using geometry. These methods are feasible using two spacecraft but would require additional assump-

tions (e.g., the use of density models). The addition of a third spacecraft to the fleet of solar spectrograms meant that the Time-Difference-of-Arrival (TDOA) method was possible as a stand-alone approach (Alcock, 2018) allowing Badman et al. (2022), to track a Type III from 0.1–16 MHz. Multilateration is an integral method of this thesis and will be further examined in more detail in Chapter 4.

An alternative method of positioning using arrival times is the Solar radio burst Electron Motion Tracker (SEMP; Zhang et al., 2019), which fits a Type III to a Parker spiral using a forward modelling method. However, SEMP is constrained by the use of density models and the assumption of constant solar wind speed and field line.

Another innovative method of positioning is shown in Reiner et al. (2009) and Musset et al. (2021), where they used the intensity of the Type III radio sources in order to calculate the directivity of the radio emissions and density models to obtain the radial distance from the Sun. Lastly, Chen et al. (2023) have combined simulations of density fluctuations with several of these methods to account for scattering of the radio waves as they escape their source.

These localisation methods make different assumptions that result in having various advantages and disadvantages. For example, the main advantage of GP is that obtaining a solution requires a minimum of two spacecraft. TDOA, on the other hand requires three spacecraft. However, GP is limited, as it requires extensive knowledge of antenna geometry, signal-to-noise ratio (S/N), and spacecraft attitude state; for example, Wind is spin-stabilised and STEREO is three-axis stabilised. These differences result in different techniques to obtain the Poynting vectors, which might have additional errors associated to them (Manning & Fainberg, 1980; Krupar et al., 2012). It also has the disadvantage that when a pair of spacecraft is at a large angle of separation (e.g., $\sim 180^{\circ}$), the Poynting vectors might point at each other, and therefore would not yield a solution. Furthermore, GP is very susceptible to antenna failure. For example, an anomaly to antenna 3 of Solar Orbiter's radio instrument that occurred on 13 November 2023 left the spacecraft without direction-finding capabilities

(Bonnin et al., 2024). Currently it is unknown whether the antenna will be recovered or not.

In contrast, multilateration only requires one antenna per spacecraft, making the method less susceptible to antenna failures. Additionally, as it will be shown in Chapter 5, multilateration works best at large separation angles. However, the free-streaming assumption is intrinsic to the TDOA method via the assumption of light travelling at the speed of light (c), and as a consequence, the most relevant source of physical error could be radio scattering (Chen et al., 2023; Kontar et al., 2019). Other sources of errors could be the low temporal resolution of the spacecraft, in particular instruments providing data at a 1-min cadence; or a poor spacecraft configuration (discussed in Chapter 7). Badman et al. (2022) estimated errors via repeating the TDOA process a specific number of times with different timestamps selected from an uncertainty range informed by instrument resolution ignoring all the error sources listed above except cadence. A more elegant solution is the application of Bayes' theorem for the purpose of applying a statistical method that would allow for a quantitative analysis of the multiple error sources. That, is the subject of this thesis.

1.6 Thesis Outline

The research contained in this thesis aims to re-examine and expand the current understanding of the propagation of electron beams from the solar corona to interplanetary space. In order to do this, Chapter 1 introduced all the relevant physical phenomena associated with electron beams and the solar corona.

In Chapter 2 the relevant background theory is outlined focusing on plasma theory and radio wave scattering.

The work of this thesis heavily relies on the contributions of a multitude of instruments and spacecraft. Chapter 3 provides a summary of all the main instrumental characteristics of the instruments used in this thesis.

This thesis focuses on a newly developed method for studying the propagation of Type III

radio bursts exciters using Bayesian statistics. Therefore, Chapter 4 sets the mathematical background for this new methodology, describing the methods used to automate data extraction as well as the methods of localisation employed in this work.

Having established the mathematical foundation of the Bayesian approach to localising Type III exciters in Chapter 4, Chapter 5 focuses on the development, description, and implementation of the BayEsian LocaLisation Algorithm (BELLA). This chapter compares a number of established methods to validate BELLA.

Chapter 6 focuses on SURROUND, a conceptual CubeSats mission funded by the European Space Agency (ESA) aimed at tracking and localising space weather phenomena, with the goal of nowcasting and forecasting potentially dangerous events. This chapter utilises BELLA to develop simulations that helped set the basis for the mission requirements and measurement criteria.

While Chapter 5 focuses on the validation of BELLA and Chapter 6 uses BELLA for developing simulations in a highly controlled environment, Chapter 7 showcases the true potential of using BELLA in multi-spacecraft missions with real data, as well as combining the BELLA process with ground-based interferometers such as the Nançay Radioheliograph (NRH). Chapter 7 will present the first 5-spacecraft multilateration to measure radio wave scattering at interplanetary distances.

Furthermore, Chapter 8 provides a summary of this thesis, and Chapter 9 explores the future prospects of BELLA, the possibility of performing multilateration with six spacecraft, possible developments of the SURROUND mission, and other potential scientific studies using BELLA.

2 Plasma Theory

2.1 Plasma Physics

The solar corona is a hot tenuous plasma that gradually extends into interplanetary space as it fades into the solar wind. A plasma is "A quasineutral gas of charged and neutral particles which exhibits collective behaviour" some of this collective behaviour is commonly described as a jelly like substance. The collective behaviour is a consequence of the fundamental characteristic of plasmas where charged particles generate local concentrations of positive and negative charges, giving rise to electric fields and currents. These electric fields are responsible for the collective response of a plasma which is influenced by electromagnetic forces. The quasineutrality of a plasma is a direct consequence of the so called Debye shielding where electric potentials are shielded by individual charges of opposite charge by forming a cloud surrounding the original charge concentration.

This shielding is dependant on many factors such as the density or temperature. Thermal energy has an influence specially on those particles at the edge of the cloud, where the electric field is weak, and the thermal energy might be sufficient for the particle to escape. The size of this sphere or rather a measure for the shielding distance is known as the Debye length defined as:

$$\lambda_D = \sqrt{\frac{\varepsilon_0 k_B T_e}{n e^2}} \tag{2.1}$$

where ε_0 is the permittivity of free space, k_B is the Boltzmann constant, T_e is the electron temperature, n is the plasma density, and e is the electron charge.

This parameter therefore shows the quasineutrality of plasmas as a test particle will be shielded if located outside of the Debye sphere, however if the test particle is located inside, it will not be in a neutral zone. This means that for a plasma to be considered a plasma, the scale length L needs to be much larger than the Debye length λ_D. This particular length is dependent on both Temperature T and density n. Consequently, the hotter the plasma, the larger its Debye length, and the denser the plasma, the smaller its Debye length.

Therefore, this shielding is only effective if there are enough particles to form the Debye sphere. In scenarios where merely a few particles exist, shielding does not occur. An effective metric for quantifying the number of particles within a Debye sphere is encapsulated by the plasma parameter:

$$\Lambda = 4\pi n \lambda_D^3 \tag{2.2}$$

This dimensionless number is a good measure of the type of plasma that is being investigated as a $\Lambda << 1$ suggests a sparsely populated plasma, usually strongly coupled, resulting in conditions where individual particle interactions are more significant, as opposed to a plasma that is densely populated $\Lambda >> 1$, weakly coupled, and dominated by collective behaviours.

Another particularity of plasmas is their oscillatory nature. When a plasma has been ionised, the charges of opposite sign are constantly trying to re-neutralise each other. However, due to their high energy, they keep overshooting and therefore oscillating. These oscillations are called plasma oscillations, and have a characteristic frequency defined by:

$$\omega_p = \sqrt{\frac{n_o e^2}{\varepsilon_0 m}} \tag{2.3}$$

or in linear frequency:

$$f_p = \frac{\omega_p}{2\pi} = \frac{1}{2\pi}\sqrt{\frac{n_o e^2}{\varepsilon_0 m}} \tag{2.4}$$

This equation gives a fundamental time scale inherent to the plasma species being studied. This means that plasma oscillations will only be observed if plasma is being studied for time

periods τ longer than

$$\tau_p = \frac{2\pi}{\omega_p} \tag{2.5}$$

Eqn. 2.3 shows how the plasma frequency is mostly dependent on the plasma density. This is because a denser plasma will have shorter Debye lengths and therefore higher frequencies.

Furthermore, a particle travelling along a magnetic field line moves in a spiral with velocity $v_\perp$ and radius r_L, this motion is provided by the Lorentz force,

$$\mathbf{F} = q(\mathbf{v} \times \mathbf{B}) \tag{2.6}$$

where the magnitude of the force perpendicular to the magnetic field ($v_\perp$) is,

$$F = qv_\perp B \tag{2.7}$$

This force is the centripetal force, $F = mv_\perp^2/r_L$ and therefore,

$$qv_\perp B = \frac{mv_\perp^2}{r_L} \tag{2.8}$$

which results in the Larmor radius r_L,

$$r_L = \frac{mv_\perp}{qB} \tag{2.9}$$

where m is the mass of the charged particle, $v_\perp$ is the component of the particle's velocity perpendicular to the magnetic field, q is the charge of the particle, B is the magnetic field strength and ω_c is the cyclotron frequency defined as:

$$\omega_c = \frac{v_\perp}{r_L} = \frac{qB}{m} \tag{2.10}$$

2.2 The Magnetohydrodynamics (MHD) model

In order to describe the dynamics of a macroscopic plasma, the most widely used model is the Magnetohydrodynamics (MHD) model. The MHD model is a development of fluid theory which incorporates Maxwell's equations. It describes the dynamics of an electrically conducting fluid in terms of its macroscopic parameters.

First, Maxwell's equations are the foundation of classical electrodynamics, defined as: **Gauss' law** of electrostatics which describe how charges generate electric fields,

$$\nabla \cdot \mathbf{E} = \frac{\rho}{\varepsilon_0} \tag{2.11}$$

Gauss' law of magnetism also known as the solenoidal equation describes how the magnetic fields are a divergence free vector field:

$$\nabla \cdot \mathbf{B} = 0 \tag{2.12}$$

Faraday's Law or induction equation which describes how changes in magnetic field will induce an electric field.

$$\nabla \times \mathbf{E} = -\frac{\partial \mathbf{B}}{\partial t} \tag{2.13}$$

And finally there is **Amperes law** which describes how changes in the electric field as well as electric current will generate magnetic fields.

$$\nabla \times \mathbf{B} = \mu_0 \mathbf{J} + \mu_0 \varepsilon_0 \frac{\partial \mathbf{E}}{\partial t} \tag{2.14}$$

where ε_0 and μ_0 are the electric permittivity and magnetic permeability of free space, respectively, and the product $\varepsilon_0 \mu_0 = 1/c^2$, where c is the speed of light. Furthermore, electrons in a plasma are typically non-relativistic, therefore the displacement current can be neglected

from Ampere's law, resulting in the simplified form:

$$\nabla \times \mathbf{B} = \mu_0 \mathbf{J} \tag{2.15}$$

Having established the fundamental equations of how magnetic and electric fields behave, the next step is to establish the kinematics of plasmas. Plasma Kinetic Theory describes the microscopic behaviour of a plasma, which consists of a large number of charged particles, in the case of the solar corona, mostly protons and electrons. The kinetic theory is described in terms of a Maxwell-Boltzman velocity distribution function $f(\mathbf{r},\mathbf{v},t)$ which describes the number density of particles, at a position $\mathbf{r}$, with velocity $\mathbf{v}$ at time t.

From this distribution, one can determine the number of particles,

$$N = \iint f(\mathbf{r},\mathbf{v},t)\, d^3r\, d^3v \tag{2.16}$$

the number density,

$$\rho(\mathbf{r},t) = \int f(\mathbf{r},\mathbf{v},t)\, d^3v \tag{2.17}$$

and the bulk velocity,

$$\mathbf{u}(\mathbf{r},t) = \frac{1}{\rho(\mathbf{r},t)} \int \mathbf{v} f(\mathbf{r},\mathbf{v},t)\, d^3v \tag{2.18}$$

Furthermore, the evolution of the distribution function leads to the Boltzman equation (Inan & Gołkowski, 2010),

$$\frac{\partial f}{\partial t} + \mathbf{v} \cdot \frac{\partial f}{\partial \mathbf{r}} + \frac{\mathbf{F}}{m} \cdot \frac{\partial f}{\partial \mathbf{v}} = \left(\frac{\partial f(\mathbf{r},\mathbf{v},t)}{\partial t} \right)_{\text{coll}} \tag{2.19}$$

where $f(\mathbf{r},\mathbf{v},t)$ is the distribution function, $\mathbf{F}$ is the force acting on the particles, m is the particle mass, and $(\partial f(\mathbf{r},\mathbf{v},t)/\partial t)_{\text{coll}}$ is the collision term, representing the rate of change of the distribution function due to collisions. In a collisionless plasma, this term is zero, and

the Lorentz force dominates, which in the presence of electric fields and magnetic fields is,

$$\mathbf{F} = q(\mathbf{E} + \mathbf{v} \times \mathbf{B}) \tag{2.20}$$

resulting in the Vlasov equation (Inan & Gołkowski, 2010),

$$\frac{\partial f}{\partial t} + \mathbf{v} \cdot \frac{\partial f}{\partial \mathbf{r}} + \frac{\mathbf{q}}{m}(\mathbf{E} + \mathbf{v} \times \mathbf{B}) \cdot \frac{\partial f}{\partial \mathbf{v}} = 0 \tag{2.21}$$

which is the equation that describes the plasma interactions with the electromagnetic fields, and its moments, allowing to evaluate the macroscopic properties of the plasma. The moment of a distribution $f(x)$ is defined as,

$$\mu_n = \int x^n f(x)\, dx, \quad n = 0, 1, 2, \ldots, n \tag{2.22}$$

Taking the zeroth moment of the Vlasov equation (Inan & Gołkowski, 2010),

$$\int \left(\frac{\partial f}{\partial t} + \mathbf{v} \cdot \nabla f + \frac{q}{m}(\mathbf{E} + \mathbf{v} \times \mathbf{B}) \cdot \frac{\partial f}{\partial \mathbf{v}} \right) v^0\, d^3\mathbf{v} = 0 \tag{2.23}$$

results in **mass continuity** equation,

$$\frac{\partial \rho}{\partial t} + \nabla \cdot (\rho \mathbf{u}) = 0 \tag{2.24}$$

stating that the rate of change of mass must be conserved.

The first moment of the Vlasov equation (Inan & Gołkowski, 2010),

$$\int \left(\frac{\partial f}{\partial t} + \mathbf{v} \cdot \nabla f + \frac{q}{m}(\mathbf{E} + \mathbf{v} \times \mathbf{B}) \cdot \frac{\partial f}{\partial \mathbf{v}} \right) v^1\, d^3\mathbf{v} = 0 \tag{2.25}$$

yields the **momentum equation**,

$$\rho \frac{d\mathbf{u}}{dt} = -\nabla P + \mathbf{J} \times \mathbf{B} + \rho \mathbf{g} \tag{2.26}$$

where the gravitational force $\rho\mathbf{g}$ is negligible compared to the electromagnetic forces and the acceleration $d\mathbf{v}/dt$ is zero at equilibrium,

$$0 = -\nabla P + \mathbf{J} \times \mathbf{B} \tag{2.27}$$

substituting $\mathbf{J}$ from Eq. 2.15, this equation becomes,

$$\nabla p = \frac{1}{\mu_0}(\nabla \times \mathbf{B}) \times \mathbf{B} \tag{2.28}$$

which can be re-written as

$$\nabla \left(p + \frac{B^2}{2\mu_0} \right) = \frac{1}{\mu_0}(\mathbf{B} \cdot \nabla)\mathbf{B} \tag{2.29}$$

The right hand side of the equation shows the forces caused by curvature of the field lines, and the left hand side of this equation shows the gas pressure $p = nk_BT$ and the magnetic pressure $B^2/2\mu_0$, which generate forces in the case of a gradient. These is an important consideration as depending on which of the two pressures dominates, the plasma will behave differently. This is usually quantified as the plasma β,

$$\beta = \frac{p}{\frac{B^2}{2\mu_0}} = \frac{nk_BT}{\frac{B^2}{2\mu_0}} = \frac{2\mu_0 nk_BT}{B^2} \tag{2.30}$$

A plasma $\beta >> 1$ indicates that the thermal pressure dominates, and the magnetic field lines can be distorted by the plasma fluid dynamics. On the other hand, a plasma $\beta << 1$ is a plasma that is heavily shaped by its magnetic field configuration, and the gas follows the field lines. Figure 2.1 shows the plasma β model (Gary, 2001) over the different layers

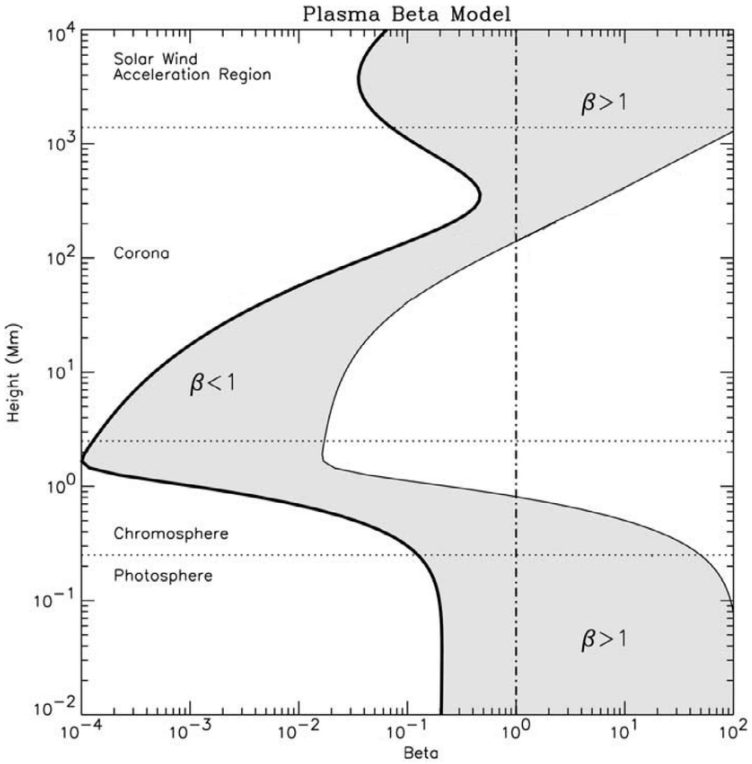


Figure 2.1: Plasma Beta Model Over an Active Region showing the plasma beta as a function of height with shading for open and closed field lines between a sunspot of 2500 G and a plage region of 150 G. Source: Gary (2001).

of the solar atmosphere. This figure shows that the plasma β changes with height, where at the photosphere, the plasma $\beta >> 1$ and therefore dominated by the thermal pressure. This is why buoyant loops are capable of emerging through the photosphere. However, as height increases the β parameter decreases to $\beta << 1$ and therefore the magnetic fields act as barriers for the surrounding plasma, for example in the case of plasma moving along a magnetic loop. As the height increases further, the plasma β parameter increases again to the region where the solar wind escapes.

The second moment of the Vlasov equation, is obtained by multiplying $\frac{1}{2}mv^2$ and integrating over the velocity space (Inan & Gołkowski, 2010),

$$\int \frac{1}{2}m\left(\frac{\partial f}{\partial t}+\mathbf{v}\cdot\nabla f+\frac{q}{m}(\mathbf{E}+\mathbf{v}\times\mathbf{B})\cdot\frac{\partial f}{\partial \mathbf{v}}\right)v^2 d^3v = 0 \tag{2.31}$$

which results in the **energy-conservation** equation,

$$\frac{\partial}{\partial t}\left[\frac{1}{2}m\rho\mathbf{u}^2\right]+\nabla\cdot\left[\frac{1}{2}m\rho u^2\mathbf{u}\right]-\mathbf{J}\cdot\mathbf{E}=0 \tag{2.32}$$

Furthermore, Ohm's law describes the variation of the current density **J** when the Lorentz force is applied in the presence of a **B** field,

$$\mathbf{J}=\sigma\left(\mathbf{E}+\mathbf{v}\times\mathbf{B}\right) \tag{2.33}$$

where σ is the plasma conductivity. Substituting **J** from Faraday's law (Eqn. 2.13) and Ampere's law (Eqn. 2.15) results, in the **induction** equation describing the evolution of a magnetic field in a plasma in terms of fluid flow velocity and magnetic diffusivity (Inan & Gołkowski, 2010),

$$\frac{\partial\mathbf{B}}{\partial t}=\nabla\times(\mathbf{v}\times\mathbf{B})+\eta\nabla^2\mathbf{B} \tag{2.34}$$

where $\eta=1/\sigma\mu$ is the magnetic diffusivity.

2.3 Plasma Emission

Plasma emission is the mechanism attributed to the generation of Type II and Type III radio emission (Reid & Ratcliffe, 2014). It consists of a multi-stage process (see Figure 2.2) first proposed by Ginzburg & Zhelezniakov (1958) which has since been the subject of thorough investigation (e.g., Melrose, 1987, 1991; Kontar, 2001; Ratcliffe et al., 2012). The first stage of the plasma emission mechanism consists of an electron beam being injected into a collisionless plasma. The electron beam can get accelerated via the magnetic reconnection model, and propagated along the magnetic field lines. Electron beams in a collisionless plasma exhibit adiabatic motion and are often non-thermal in nature. As a consequence, the velocity dispersion allows higher energy electrons to overtake the lower energy electrons. This generates a 'bump' on the velocity distribution commonly known as a 'bump-on-tail'

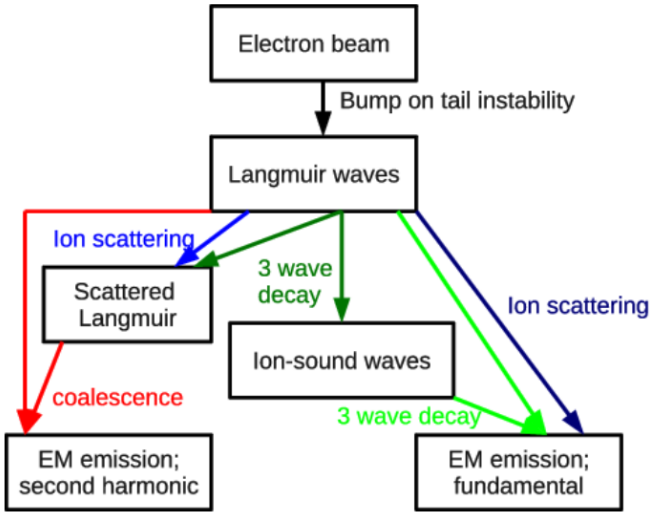


Figure 2.2: Flow diagram of the different stages of the Plasma Emission mechanism. Source: Reid & Ratcliffe (2014), adapted from Melrose (1991).

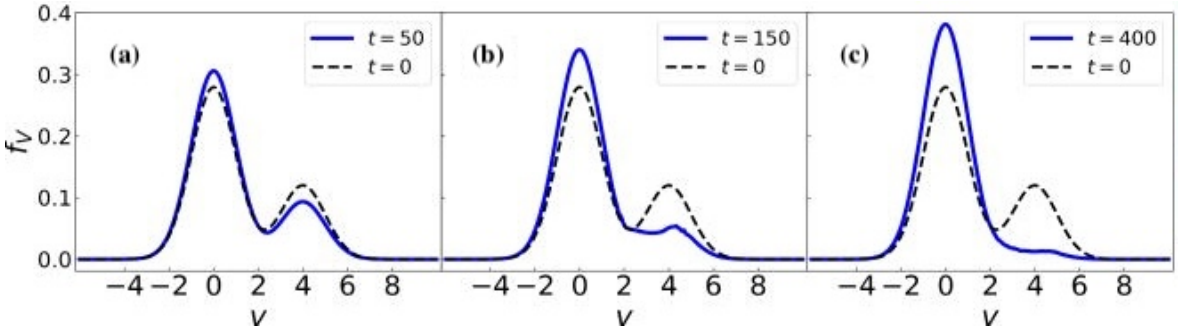


Figure 2.3: Simulations of the bump on tail instability showing the electron distribution function (y-axis) and velocity (x-axis). The simulation consists of (a) a 1D electron velocity distribution function of a background plasma and a low density and high velocity electron beam. (b) The positive gradient of the high speed bump on tail becomes unstable and can excite Langmuir waves in the background plasma. (c) Eventually, the bump dissipates as radio waves are produced by the Langmuir waves. Source: Hou et al. (2024).

(see Figure 2.3 (a)). The positive gradient of the 'bump' generates an instability known as the two stream instability or the bump-on-tail instability which causes Landau resonance and generates Langmuir waves (Tonks & Langmuir, 1929; Ginzburg & Zhelezniakov, 1959). As the Langmuir waves are produced, the bump-on-tail dissipates (see Figure 2.3 (b–c)), and at this point the Langmuir waves no longer grow. The Langmuir waves follow a dispersion relation (Aschwanden, 2004),

$$\omega_L^2(k) = \omega_p^2 + \frac{3}{2}k^2 v_{th}^2 = \omega_p^2 \left(1 + 3k^2 \lambda_D^2\right), \tag{2.35}$$

where λ_D^2 is the Debye length, ω_p is the plasma frequency, v_{th} is the thermal velocity of the electrons in the plasma and k is wavenumber.

The production of electromagnetic transverse (T) radio waves,

$$\omega^2(k) = \omega_p^2 + k^2 c^2 \tag{2.36}$$

comes as a consequence of wave coalescence processes of Langmuir (L) and ion acoustic sound (S) waves,

$$\omega_S = k v_s \tag{2.37}$$

Thus, the wave interactions to be considered are, first the production of the fundamental plasma emission,

$$L + S \rightarrow T \tag{2.38}$$

where the Langmuir and acoustic wave can also lead to Langmuir turbulence,

$$L + S \rightarrow L' \tag{2.39}$$

which leads to harmonic emission as,

$$L + L' \rightarrow T \tag{2.40}$$

Additionally, the radio emission can be absorbed if the density along the line-of-sight is not sufficiently small, thus

$$T + S \rightarrow L \tag{2.41}$$

which is the reason why SRBs such as Type IIIs are commonly observed with negative frequency drifts, but bursts with positive frequency drifts such as U bursts or J bursts, associated with electrons following a large closed loop, are relatively rare to observe. However this is outside of the scope of this thesis.

2.4 Radio Wave scattering

The absorption effect explored in the wave-wave interaction (Eq. 2.41) is not the only radio wave propagation effect. Scattering and refraction are widely observed effects (Chrysaphi et al., 2018; Kontar et al., 2019; Murphy et al., 2021; Chen et al., 2023) that are caused as a consequence of the electron density fluctuations,

$$\varepsilon = \sqrt{\frac{\langle \delta n^2 \rangle}{n^2}} \tag{2.42}$$

Krupar et al. (2020) analysed multiple Type III solar bursts observed by Parker Solar Probe in conjunction with some Monte Carlo simulations to obtain a prediction in the range 2.5 $R_\odot$ to 14 $R_\odot$of the density of fluctuations as a function of the radial distance to the Sun updating with certain agreement on previous predictions made with STEREO ($\varepsilon = 0.06 - 0.07$ at approximately 10–30 $R_\odot$) (Krupar et al., 2018),

$$\varepsilon = (0.36 \pm 1.02)\ r^{-(0.55 \pm 0.01)} \tag{2.43}$$

These electron density fluctuations can cause micro-refractions which cause the wave direc-

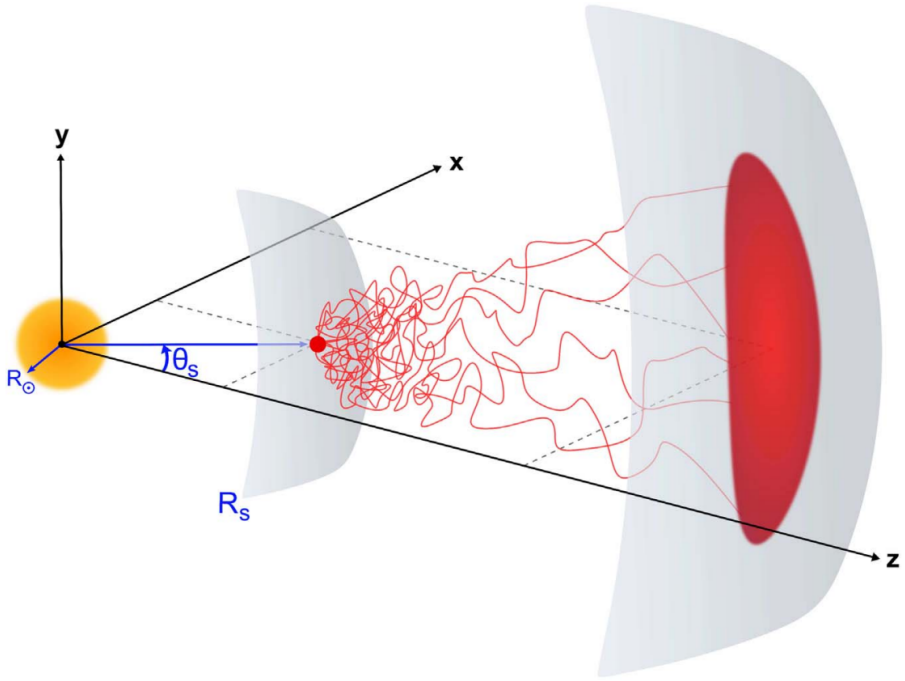


Figure 2.4: Cartoon showing the scattering of a source located at R_s which scatters until it reaches a point where the plasma is optically thin at which the radio emission propagates freely. The larger surface becomes the apparent source location. Source: Kontar et al. (2019).

tions to become randomised. By definition, the refractive index is,

$$\mu_{ref} = \frac{c}{v} = \frac{c}{\lambda f} = \frac{ck}{2\pi f} = \frac{ck}{\omega} \tag{2.44}$$

combining Eq. 2.36 with Eq. 2.44 gives the refractive index of an unmagnetised plasma,

$$\mu_{ref} = \sqrt{1 - \left(\frac{\omega_p}{\omega}\right)^2} = \sqrt{1 - \left(\frac{f_p}{f}\right)^2} \tag{2.45}$$

which implies that as the frequency of the radio emission approaches that of the local plasma frequency, the refractive index approaches zero. The consequence of this is that refraction and scattering are most pronounced at near the plasma frequency. Frequencies at $f >> f_p$, result in a refractive index $n \simeq 1$, allowing for free streaming propagation. However, frequencies where $f << f_p$, the refractive index becomes imaginary and absorption occurs.

Therefore, despite the production of radio waves being isotropic, the inverse relationship

between the distribution of the inhomogeneities and height, as well as their alignment with the surrounding magnetic field, plays an important role on the scattering process (Kontar et al., 2019). This results in an anisotropic large scale effect, shifting the apparent sources radially outwards and broadening the apparent size of the source (see Figure 2.4).

Chrysaphi et al. (2018) presented a simplified analytical model which quantises the scattering effect starting from an isotropic inhomogeneities distribution assumption from Steinberg et al. (1971),

$$\langle \delta n(\mathbf{r}_1)\delta n(\mathbf{r}_2)\rangle = \langle \delta n^2\rangle \exp\left(-\frac{(\mathbf{r}_1-\mathbf{r}_2)^2}{h^2}\right) \tag{2.46}$$

which describes the statistical correlation between density fluctuations at two different points $\mathbf{r_1}$ and $\mathbf{r_2}$, where h is the characteristic scale length. This causes an angular scattering effect as shown in Steinberg et al. (1971),

$$\frac{d\langle \Delta\theta^2\rangle}{dr} = \frac{\sqrt{\pi}}{2h}\frac{f_p^4(r)}{(f^2-f_p^2(r))^2}\frac{\langle \delta n^2\rangle}{n^2} \tag{2.47}$$

Finally, Chrysaphi et al. (2018) quantitatively estimated the effects of scattering by relating it to optical depth,

$$\tau(r) = \int_r^{1au}\frac{d\langle \Delta\theta^2\rangle}{dr}dr = \int_r^{1au}\frac{\sqrt{\pi}}{2}\frac{f_p^4(r)}{(f^2-f_p^2(r))^2}\frac{\varepsilon^2}{h}dr \tag{2.48}$$

where τ is the optical depth, f_{pe} is the plasma frequency as defined in Eq. 2.4, f is the frequency, ε is the density of fluctuations, h is the characteristic density inhomogeneity correlation scale and r is radial distance from the centre of the sun.

This scattering estimation is based on the analysis of optical depth for a particular frequency with respect to its heliocentric distance. In this model, the distinction between the optically thick regime $\tau(r) > 1$ where scattering is most pronounced, causing radio waves to diffuse, and the optically thin regime $\tau(r) < 1$ where scattering has no effect on radio waves. This allows for the transition region $\tau(r) = 1$, to act as the defining point where the radio waves are considered to propagate freely.

3 Instrumentation

3.1 A suite of solar dedicated spacecraft

The Sun, our closest star, has been the subject of scientific investigation since early human history. The relatively recent technological revolution has led to a series of groundbreaking discoveries with implications various scientific disciplines and everyday applications. Some of the most notable discoveries, such as the discovery of the solar wind or the famous coronal heating problem remain subjects of investigation.

As a result, NASA and ESA have shown interest in deploying solar-dedicated missions throughout the solar system, equipped with a variety of in-situ and remote instruments capable of studying the Sun across all wavelengths of the EM spectrum. This study uses data from four operative missions capable of studying the Sun in the radio spectrum from different vantage points. These are The Global Geospace Science Wind satellite (Wind; Acuña et al., 1995), Solar Terrestrial Relations Observatory (STEREO; Kaiser et al., 2008), Parker Solar Probe (PSP; Fox et al., 2016) and Solar Orbiter (SolO; Müller et al., 2020). Additionally, this study explores the capabilities of utilising data from a fifth spacecraft, Mars Express (MEX; Chicarro et al., 2004), which was not originally designed for solar observations.

3.2 Wind

Launched on November 1, 1994, the Wind spacecraft (see Figure 3.1 (a)) is part of NASA's Global Geospace Science (GGS) program (Hoffman & Hesse, 1996). The mission was designed to work in tandem with its sister spacecraft, Polar (Hoffman & Hesse, 1996), with the primary goal of studying the solar wind and its impact on Earth's magnetosphere. This significantly contributed to our understanding of the Sun–Earth system (Wilson III et al., 2021).

3.2.1 Technical Aspects of the Wind Spacecraft

Wind operates in a Halo orbit around the Lagrange 1 (L1) point (see Figure 3.1 (a)), allowing it to sample the solar wind before it reaches Earth. The spacecraft is spin stabilised, with a spin rate of 20 rpm (Acuña et al., 1995) meaning that specific corrections must be applied to its scientific measurements (Fainberg et al., 1985; Farrell et al., 1995). These corrections typically involve complex mathematical and computational techniques to account for the rotation of the spacecraft which can pose additional challenges. The data is recorded and temporarily stored in magnetic tape, which is relayed back to Earth during tracking passes. Additionally, the spacecraft is capable of transmitting data to Earth in real-time for limited periods (Acuña et al., 1995). The different scientific investigations on board the Wind spacecraft are as follow:

- Magnetic Field Investigation (MFI; Lepping et al., 1995) which measures the magnetic field structures, fluctuations and dynamics of the solar wind as it interacts with Earth's magnetosphere.
- Solar Wind Experiment (SWE; Ogilvie et al., 1995) which includes instruments such as two Faraday cup sensors for measuring the properties of the solar wind including velocity and density of ions and electrons.
- Three-dimensional plasma analyzer (3DP; Lin et al., 1995). This investigation is de-

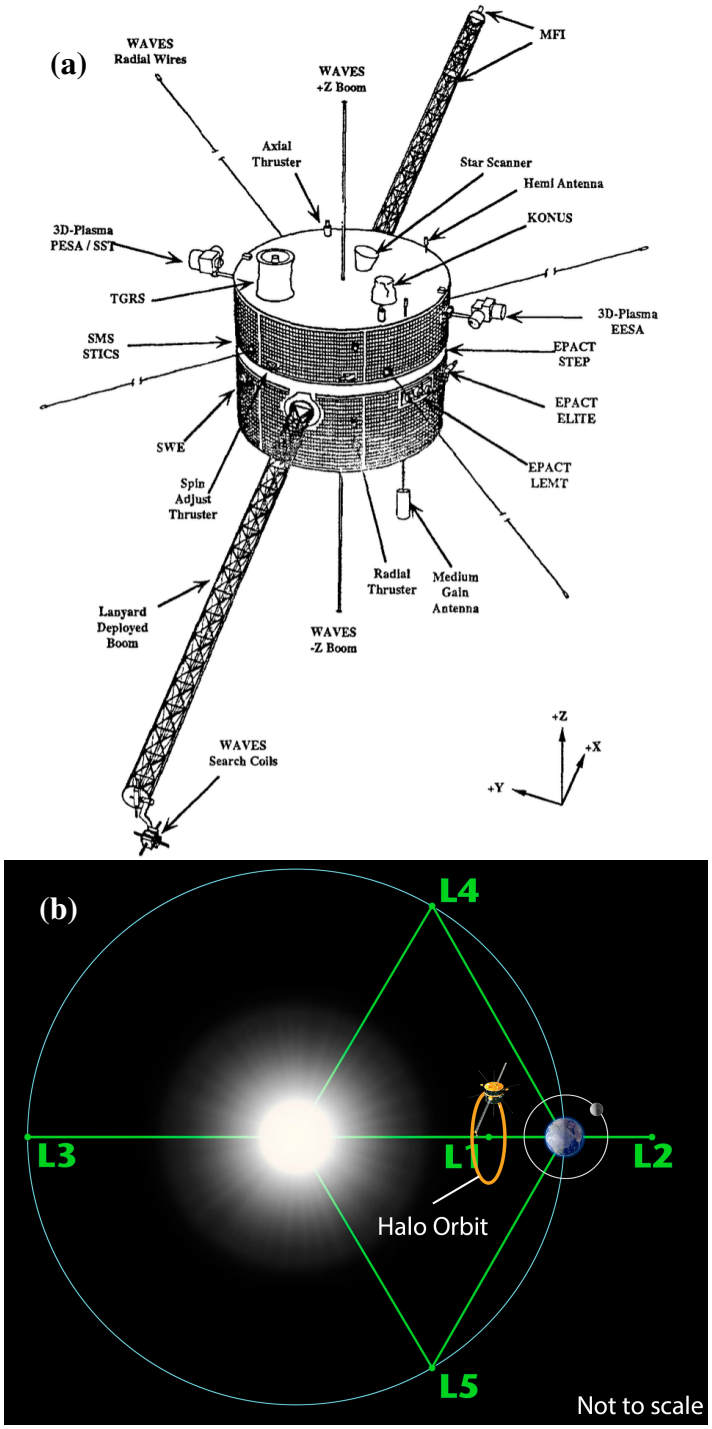


Figure 3.1: **(a)** Diagram of the Wind spacecraft showing its different instruments. The WAVES instrument is used throughout this study. Source: Harten & Clark (1995). **(b)** Wind is currently orbiting in a Halo orbit around the Lagrange 1 (L1) point. Wind's orbit is relatively stationary with respect to the Sun–Earth line making it a valuable asset for multilaterating sources travelling towards Earth. Source: Adapted from NASA.

signed to measure the three-dimensional distribution and energy of electrons and ions in the solar wind.

- The Solar Wind and Suprathermal Ion Composition Experiment (SMS; Gloeckler et al., 1995) which contains instruments designed to detect and analyse solar mass ejections.
- The Energetic Particles: Acceleration, Composition and Transport (EPACT; Von Rosenvinge et al., 1995) which contains eight particle telescopes in charge studying the composition, energy, and distribution of energetic particles in the solar wind.
- Two gamma-ray spectrometers, Konus-W (KONUS; Aptekar et al., 1995) and the Transient Gamma-Ray Spectrometer (TGRS; Owens et al., 1995). These are dedicated to observing gamma-ray bursts and hard X-rays associated with electrons accelerated by solar flares.
- Radio and Plasma Wave Investigation (WAVES; Bougeret et al., 1995). WAVES is a radio instrument that studies radio emissions and plasma waves in the solar wind, providing insights into solar flares, shock waves, and other interplanetary phenomena.

3.2.2 The WAVES Instrument

In this study we utilise data obtained by the radio receivers of the WAVES instrument. WAVES was designed to explore radio and plasma wave phenomena in the interplanetary medium, with a particular focus on SRBs. The WAVES instrument comprises of six antennas configured as three orthogonal dipoles and includes six preamplifiers. This configuration enables WAVES to capture a wide frequency range, spanning from 20 kHz to 13.825 MHz.

The main radio receivers are RAD1 and RAD2 covering frequency ranges of 20–1040 kHz and 1.075–13.825 MHz. Each receiver contains 256 frequency channels with frequency steps of 4 kHz for RAD1 and 50 kHz for RAD2. The data used in this study is 1 minute averaged data and it is available at Bonnin et al. (2023). Additionally, WAVES includes the

Thermal Noise Receiver (TNR), which operates in the 4 kHz to 256 kHz range across five logarithmically-spaced frequency bands.

3.3 STEREO

On October 26, 2006, NASA launched the STEREO mission (Kaiser et al., 2008), which consists of two twin spacecraft: STEREO A (Ahead) and STEREO B (Behind), as shown in Figure 3.2 (a). Their unique orbital configuration places STEREO A ahead of Earth and STEREO B trailing behind, as depicted in Figure 3.2 (b). The spacecraft separate at approximately $\pm 22^{\circ}/\text{year}$ relative to the Sun–Earth line. This arrangement was designed for coordinated solar observations, particularly to understand and track the propagation of CMEs (Kaiser et al., 2008). Unfortunately, on October 1, 2014, NASA lost communications with STEREO B after a series of hardware anomalies which likely caused the spacecraft to loss control of its orientation. Despite NASA's efforts to regain control STEREO B was never recovered[1].

3.3.1 Technical Aspects of the STEREO Spacecraft

The two STEREO spacecraft orbit the Sun along slightly different paths, providing a distinct stereoscopic perspective on solar phenomena. STEREO A is positioned in an orbit with a perihelion of 0.909 au and an aphelion of 1.022 au, while STEREO B follows an orbit with a perihelion of 0.983 au and an aphelion of 1.089 au (Dunham et al., 2009). As noted by Kaiser & Adams (2007), these orbits' near-circular eccentricities are designed to minimise variations in the observed solar diameter from the spacecraft. Figure 3.2 (b) *left* illustrates how these orbits are positioned slightly above and below Earth's orbit.

The spacecraft are three-axis stabilised (Mueller et al., 2003), which, as Sabroff (1968) suggests, leads to faster reaction times and greater precision compared to spin-stabilised space-

[1]NASA: STEREO-B Status Update. `https://stereo-ssc.nascom.nasa.gov/behind_status.shtml`

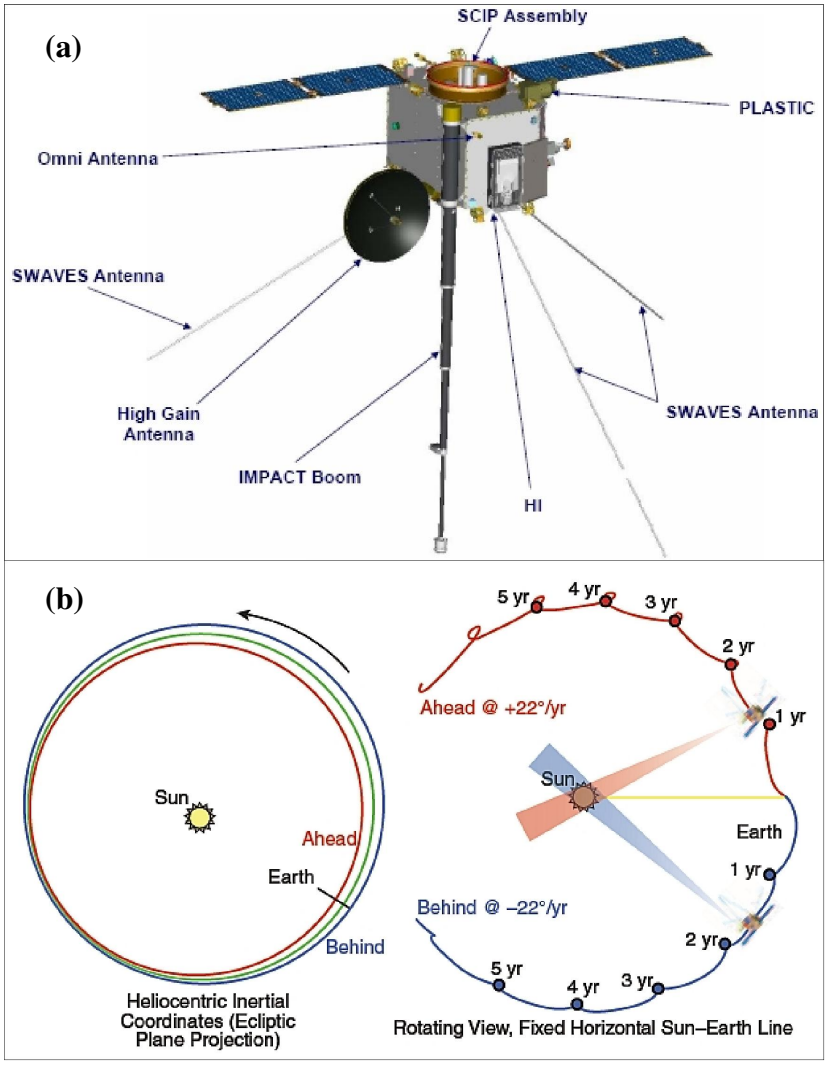


Figure 3.2: **(a)**: Diagram of one of the STEREO spacecraft highlighting its various instruments. The SWAVES instrument, which is central to this study, is indicated. **(b)**: The STEREO A/B spacecraft pair orbiting in a $\pm 22^{\circ}/year$ leading/trailing configuration relative to the Sun–Earth line. The *left* diagram presents the orbits in an inertial frame of reference, while the *right* diagram shows the same orbit in a Heliocentric Earth Ecliptic (HEE) frame of reference. Source: NASA/Kaiser & Adams (2007).

craft. The advantage of maintaining three-axis stabilisation includes simpler data processing, as de-spinning procedures are no longer required. Data is recorded on a solid-state recorder and downloaded daily through NASA's Deep Space Network (DSN) during regular operations. Kaiser et al. (2008) provides an overview of the diverse scientific investigations conducted aboard the STEREO pair.

- Sun–Earth Connection Coronal and Heliospheric Investigation (SECCHI; Howard et al., 2008). SECCHI includes two white light coronagraphs COR1 and COR2, an extreme ultraviolet imager (EUVI) and two white light heliospheric imagers (HI).
- In situ Measurements of PArticles and CME Transients (IMPACT; Luhmann et al., 2008). IMPACT has a number of instruments dedicated to the study in situ of the solar wind, detecting SEPs and measuring magnetic fields.
- PLAsma and SupraThermal Ion Composition (PLASTIC; Galvin et al., 2008). PLASTIC is dedicated to the study of the plasma characteristics of protons, alpha particles and heavy ions.
- STEREO/WAVES (S/WAVES; Bougeret et al., 2008). S/WAVES is the radio instrument which uses three antennas to detect the in situ electric field to track SRBs across interplanetary plasma. S/WAVES was designed along with the GP method described in Cecconi et al. (2008). Throughout this work, data from S/WAVES will be utilised.

3.3.2 The S/WAVES Instrument

S/WAVES (Bougeret et al., 2008) is a radio instrument designed to study solar radio emissions, with a focus on those emanating from solar storms, flares, and CMEs. The antenna system features three 6-metre-long monopole antennas, arranged orthogonally and mounted on the spacecraft's anti-sunward surface. This configuration allows for GP capabilities as described in Cecconi et al. (2008).

The main radio receivers are the Low Frequency Receiver (LFR) and the High Frequency

Receiver (HFR) with a frequency coverage of 2.5–160 kHz and 125 kHz–16.025 MHz respectively. Additionally, the Fixed Frequency Receiver (FFR) operates at 30.025 MHz or 32.025 MHz and is designed for coordinated measurements with ground-based detectors. The LFR receiver forms a total of 48 log-spaced frequencies with a spectral resolution of 8.66 %. The HFR receiver has a spectral resolution of 50 kHz. The direction finding capabilities of the instrument, paired with the stereoscopic configuration of the mission, makes S/WAVES the ideal instrument for the GP method with L3 GP inversions available at Krupar et al. (2022). This dataset provides 38 s cadence data which was used throughout this study.

3.4 Parker Solar Probe

PSP (see Figure 3.3), originally known as Solar Probe Plus (SPP), was launched by NASA on July 31, 2018. Its orbit around the Sun is highly elliptical (e $\sim$ 0.63), extending beyond Venus' orbit at aphelion and approaching closer to the Sun's surface than any previous mission during perihelion. This unique proximity allows PSP to offer unprecedented observations of solar phenomena, enabling both in situ and remote studies of the Sun's corona (Raouafi et al., 2023a).

3.4.1 Technical Aspects of the Parker Solar Probe Spacecraft

PSP's orbit is designed to reach a perihelion of 9.86 $R_{\odot}$, as described by Fox et al. (2016). Possibly the biggest challenge of a mission of this nature is surviving the harsh environment that PSP routinely experiences. PSP is capable of withstanding about 649 kWm^{-2}, which is $\sim$ 500 times the solar irradiance at Earth (Fox et al., 2016). The Thermal Protection System (TPS), a heat shield made of a carbon-carbon composite and carbon foam sandwich with an alumina coating placed on the sun-facing side of the spacecraft made this mission possible.

The close proximity of PSP to the Sun means that the solar panels need to angle back, having to be kept mostly in the penumbra of the TPS during close proximity with a relatively small secondary array getting illuminated (Fox et al., 2016). The data collected by the Parker

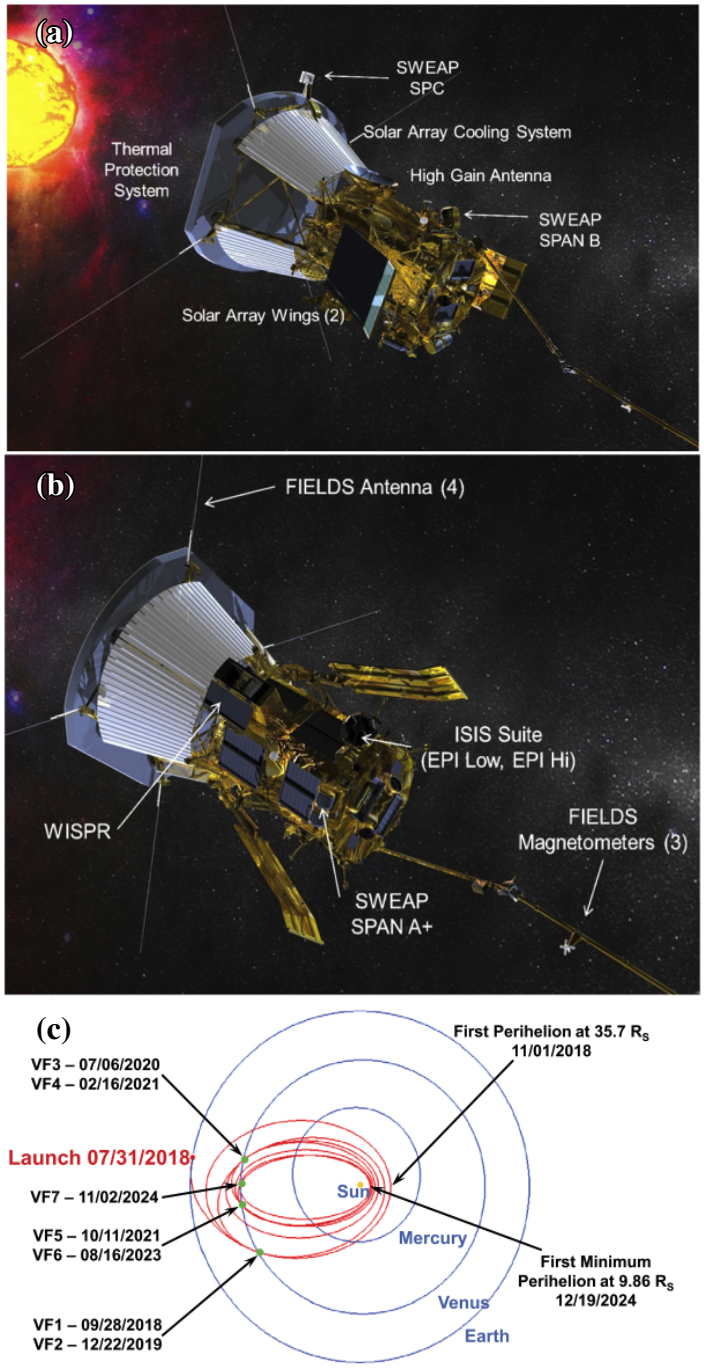


Figure 3.3: **(a)** Anti-ram orientation of PSP showing a number of different instruments. **(b)** Ram orientation of PSP showing a number of different instruments. **(c)** PSP is in a highly elliptical orbit (e $\sim$ 0.63) with aphelions that go beyond the orbit of Venus and perihelions under 10 $R_\odot$. Venus flybys offered the necessary gravitational assists to reach the low perihelions. Source: Fox et al. (2016).

Solar Probe is recorded and periodically transmitted back to Earth using NASA's DSN. The spacecraft's scientific payload includes four main in-situ and remote sensing instruments (Fox et al., 2016):

- Integrated Science Investigation of the Sun (IS⊙IS; McComas et al., 2014) designed to study energetic particles that are accelerated in the Sun's corona and in the inner heliosphere.
- Wide-Field Imager for Parker Solar Probe (WISPR; Vourlidas et al., 2016), an imaging instrument that captures images of the solar corona and inner heliosphere.
- Solar Wind Electrons Alphas and Protons (SWEAP; Kasper et al., 2016) investigates the solar wind and the Sun's corona by measuring electrons, protons, and helium ions.
- Fields Experiment (FIELDS; Bale et al., 2016) which measures electric and magnetic fields, the properties of in-situ plasma waves and plasma electron densities.

3.4.2 The FIELDS Experiment

The FIELDS instrument as described by Bale et al. (2016) is the instrument designed to investigate a multitude of phenomena including but not limited to the investigation of solar radio emissions. Among the many sensors of the FIELDS instrument suite there are four main electric field antennas (V1–V4) (see Figure 3.3 (b)) in two orthogonal co-linear pairs and placed in the sun-facing section of the spacecraft, just behind the TPS. These antennas are then connected to the Radio Frequency Spectrometer (RFS; Pulupa et al., 2017) which is a two channel digital spectrometer composed of the High Frequency Receiver (HFR) and the Low Frequency Receiver (LFR). Both channels operate simultaneously with frequency ranges corresponding to 10 kHz–1.7 MHz (LFR) and 1.3–19.2 MHz (HFR) with relative frequency spacing $\Delta f/f$ of $\sim 4.5\%$. Unfortunately, due to downlink limitations the raw spectra is limited to 64 selected frequencies.

3.5 Solar Orbiter

SolO (see Figure 3.4) was developed by ESA and launched by NASA on February 10, 2022 (Müller et al., 2020). It was designed for the purposes of studying solar activity and how it affects the heliosphere. SolO is a mission capable of imaging the Sun from the closest possible orbit. Unlike PSP, SolO is capable of taking images of the solar surface which has led to many discoveries such as the discovery of the so-called campfires (Berghmans et al., 2021) which are associated with micro-flares (Chen et al., 2021). Another feature that sets SolO apart is its unique trajectory, with each Venus fly-by, SolO will change its orbital angle with respect to the ecliptic plane, which will offer the first-ever direct images of the solar poles (Müller et al., 2020).

3.5.1 Technical Aspects of Solar Orbiter

SolO, as shown in Figure 3.4, is a three-axis stabilised spacecraft with an orbit that, although not as close to the Sun as PSP, is strategically positioned with a minimum perihelion of 60.21 $R_{\odot}$, falling just within Mercury's orbit. This distance is the minimum distance for which, given current technology, heliospheric imagers are safely capable of taking images of the Sun (Howard et al., 2020). With an aphelion of $\sim$ 1 au SolO has a relatively high eccentric orbit (e $\sim$ 0.57). The orbit's helio-latitude will reach a maximum of $\pm$ 33 ^{o} which will allow for investigation of the solar poles.

In order to withstand the 500^{o} surface temperature imposed by solar flux, SolO is equipped with a heat shield made of titanium foil with a coating of "SolarBlack" made of black calcium phosphate developed by Irish company ENBIO[2]. The solar panels, as shown in Figure 3.4 (c), are mounted along the Y-axis for a total wing-span of 18 m and are capable of rotating along the longitudinal axis for temperature control. The imaging instruments, as shown in Figure 3.4 (b), are placed internally and view the Sun through the heat shield via "feed-throughs" which have sliding doors for additional protection. The in-situ instruments are

[2] https://www.enbio.eu/solar-orbiter/

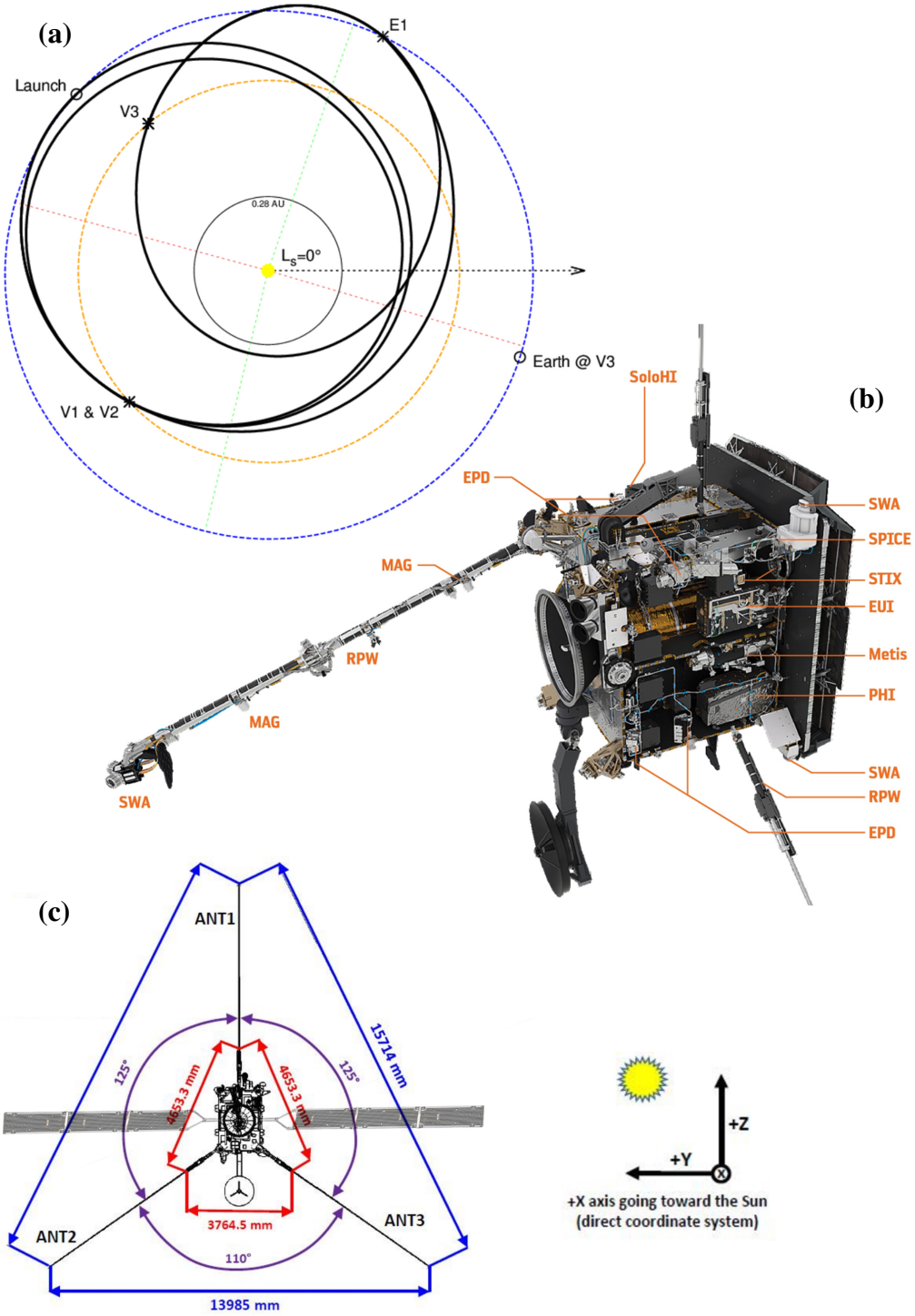


Figure 3.4: **(a)** The orbit of Solar Orbiter shown from above the ecliptic. Blue dashed line denotes Earth's orbit, orange dotted line denotes Venus' orbit and black solid circle shows the lowest perihelion that Solar orbiter will reach. Note that Solar Orbiter changes its orbital angle with each Venus flyby until it reaches a solar latitude of $\pm$ 30^o. **(b)** CAD render of Solar Orbiter showing all the different scientific instruments on board. **(c)** Solar Orbiter's dimensions showing the three antennas configuration arranged at $\sim$120^o from each other. Sources: Adapted from Maksimovic et al. (2020) and Müller et al. (2020).

placed externally, with some of the sensors placed on an anti-sun-facing boom. There is a total of ten instruments on board SolO, these are six remote-sensing:

- Heliospheric Imager (SoloHI; Howard et al., 2020), an imaging instrument that captures images of the solar corona and the heliosphere over a wide Field of View (FoV) in the visible spectrum.
- Extreme Ultraviolet Imager (EUI; Rochus et al., 2020), designed to provide high-resolution images of ultraviolet emission seen from the chromosphere to the corona.
- Spectral Imaging of the Coronal Environment (SPICE; Anderson et al., 2020), which performs extreme ultraviolet spectroscopic observations to study the plasma in the solar inner corona.
- Polarimetric and Helioseismic Imager (PHI; Solanki et al., 2020), aimed at studying the Sun's surface and its magnetic field.
- The Spectrometer Telescope for Imaging X-rays (STIX; Krucker et al., 2020), providing imaging spectroscopy of solar thermal and non-thermal X-ray emissions.
- Metis: Coronagraph (Metis; Antonucci et al., 2020), used for observing the solar corona in visible and ultraviolet light.

And four in-situ instruments:

- The Energetic Particle Detector (EPD; Rodríguez-Pacheco et al., 2020), designed to study energetic particles that are accelerated in the Sun's corona and in the inner heliosphere.
- Magnetometer (MAG; Horbury et al., 2020), which measures the magnetic field in the solar wind and contributes to the understanding of the Sun's magnetic influence in the solar system.
- The Solar Wind Analyser (SWA; Owen et al., 2020), which measures the solar wind's ions, electrons, and neutral particles.

- Radio and Plasma Waves (RPW; Maksimovic et al., 2020, 2021) which measures electric and magnetic fields for the investigation of radio EM radiation generated by solar activity and in-situ plasma properties.

3.5.2 Radio and Plasma Waves

RPW, as described by Maksimovic et al. (2020), is an instrument onboard SolO designed to investigate, among other phenomena, SRBs. RPW utilises three antennas, namely ANT1, ANT2, and ANT3, which are positioned just behind the heat shield in a single plane parallel to it. The configuration of these antennas is illustrated in Figure 3.4 (c). ANT1 is deployed in the +Z direction, while ANT2 and ANT3 are deployed at 125 degrees from ANT1 in the +Y-axis and -Y-axis directions, respectively. Each antenna, extending approximately 6.5 meters in length, is supported by a 1-meter deployable boom.

RPW is equipped with a number of subsystems dedicated to different frequency ranges of the radio spectrum. The Thermal Noise and High Frequency Receiver (TNR-HFR) is designed to study the radio spectrum in two bands. TNR measures the quasi-thermal noise in the range 4 kHz to 1024 kHz and HFR operates in the 0.4 MHz to 16.4 MHz range. TNR, used for the investigation of Langmuir waves, produces quasi instantaneous spectra divided in 4 bands of 32 log-spaced frequencies each at $\Delta f/f \sim 4.5\%$. HFR is a sweeping receiver capable of taking a sweep of 192 frequencies in 5.2 s during nominal operations. HFR is divided into two sub-bands HF1 operating in the 0.4 MHz to 3.6 MHz range with 64 selected frequencies at a frequency resolution of 50 kHz and HF2 operating in the 3.6 MHz to 16.4 MHz range with 128 selected frequencies at a frequency resolution of 100 kHz.

3.6 Mars Express

Unlike the other spacecraft mentioned in this work, Mars Express (MEX; Chicarro et al., 2004) is not a solar dedicated mission. MEX (Chicarro et al., 2004) was launched on June 2, 2003 by ESA to investigate the fourth rocky planet of our solar system, Mars. The MEX mission included an orbiter and a lander known as Beagle 2 which failed to communicate after its scheduled landing and was declared lost on February 6, 2004[3]. In contrast, the orbiter has been a success, with over 20 years of continuous operation and remains functional as of this writing.

3.6.1 MARSIS

The Mars Advanced Radar for Subsurface and Ionosphere Sounding (MARSIS; Picardi et al., 2004), is an instrument on board the MEX orbiter designed to study the Martian subsurface and ionosphere (see Figure 3.5). The instrument uses three antennas in a ⊤ configuration: two 20 m antennas in a dipole configuration and one 7 m monopole antenna. The monopole antenna is aligned with the Nadir axis and the dipole is aligned parallel to the surface.

Generally, a MEX orbit lasts 7 hours, out of which MARSIS is only operational for 40 minutes near periapsis. During this operational time, MARSIS can operate in one of the two available modes; an altimeter with ground-penetrating capabilities and a radar sounder. In subsurface mode, two simultaneous frequencies are chosen from 1.8, 3, 4, and 5 MHz. On the other hand, the Active Ionospheric Sounding (AIS; Jordan et al., 2009) mode transmits and receives radio waves in the 100 kHz–5.5 MHz range. AIS uses 160 frequencies with a frequency resolution of 10.937 kHz and a frequency sweep interval of 7.38 s.

Despite not being a solar dedicated spacecraft, radio emissions caused by solar activity have been observed to significantly impact MARSIS data (Sanchez-Cano et al., (in prep.))

and in Chapter 7 we will explore the possibility of utilising these “spoiled” martian observa-

[3] `https://www.esa.int/Science_Exploration/Space_Science/Mars_Express/Beagle_2_lander`

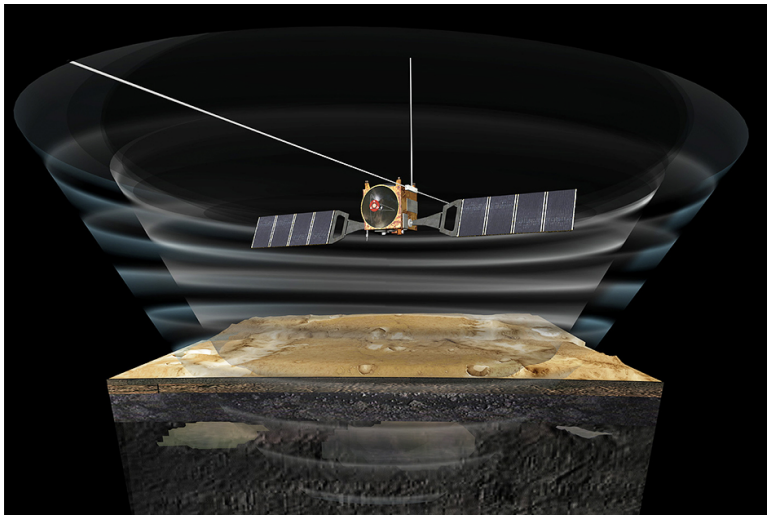


Figure 3.5: Artist's concept of the MEX MARSIS instrument in operation. MARSIS investigates the Martian ionosphere and subsurface by analysing the echoes of radar pulses. Solar activity can overload the measurements, preventing MARSIS from resolving the echoes. In Chapter 5, we will explore the use of MARSIS for coordinated solar observations. Source: NASA/JPL/ESA.

tions and repurposing them as data for solar observations.

3.7 CubeSats

CubeSats are small spacecraft designed to adhere to a standard specification[4], first developed in 1999 (Puig-Suari et al., 2000; Heidt et al., 2000). This standard primarily focuses on the launching platform which results in certain architectural constraints on the satellites. Over recent years, the popularity of CubeSats has increased (Swartwout, 2013; Villela et al., 2019), this is attributed to their relatively low cost and versatility. These characteristics make CubeSats an attractive option for educational purposes in schools, for small-scale research projects in universities, and as technology demonstrators for organisations like NASA and ESA (Villela et al., 2019).

CubeSats are typically engineered around a standard launching platform, which includes guiding rails for stable deployment and a spring-powered pusher plate as the deployment mechanism. Owing to these specifications, CubeSats are designed in standard cubic units

[4]CubeSat Design Specification: `https://www.cubesat.org/cubesatinfo`

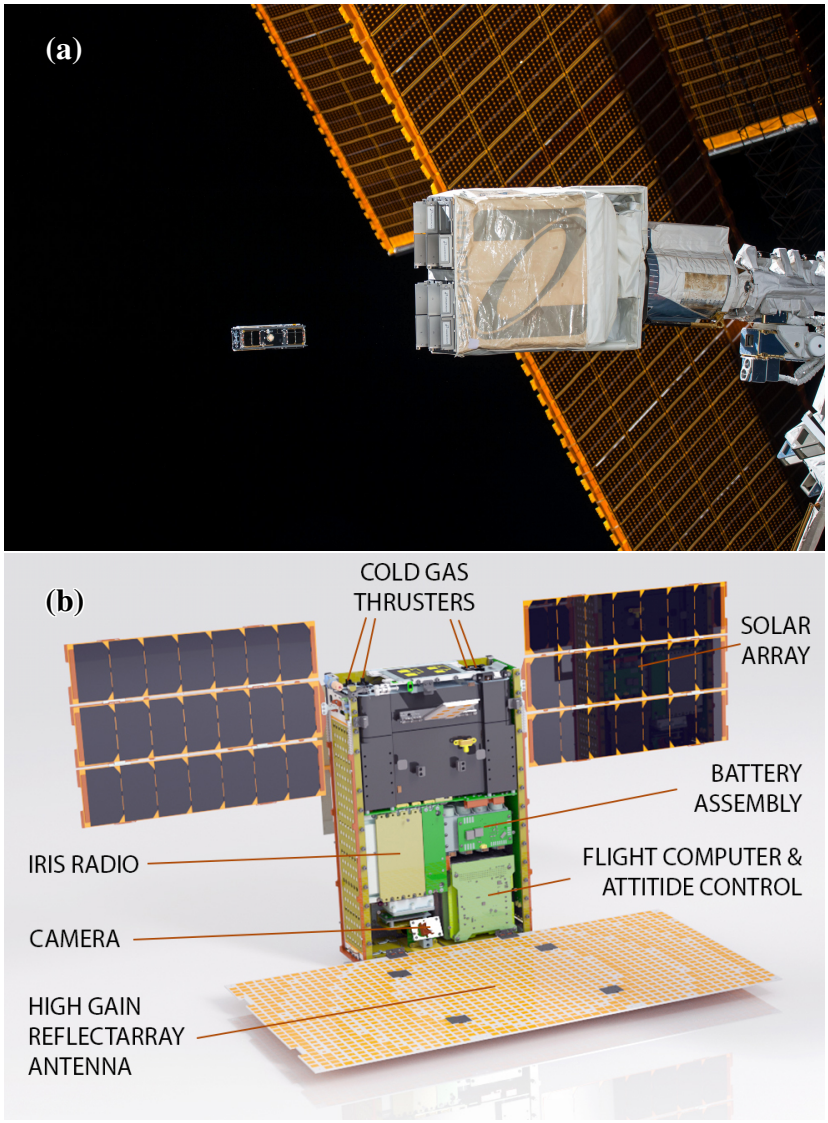


Figure 3.6: **(a)** 3U CubeSat being deployed from the International Space Station (ISS). **(b)** CAD render of the Mars Cube One (MarCO) showing some of its subsystems. Source: NASA/JPL.

"U" of approximately 10 cm in length that fit the launching pod seamlessly. Figure 3.6 (a) shows a 3U CubeSat being deployed from the International Space Station but it is also possible to launch CubeSats from rockets as secondary payload from larger satellite missions or even as standalone missions. CubeSats are typically designed as 1U, 2U, 3U, 6U or 12U and it is common practice to share a launching pod among different spacecraft.

Most CubeSats are inserted into Low Earth Orbit (LEO) primarily due to economic and feasibility constraints. Nonetheless, the challenges associated with interplanetary travel for CubeSats have been progressively addressed by pioneering missions. For instance, the Mars Cube One (MarCO Schoolcraft et al., 2017) mission, comprising two 6U CubeSats, demonstrated the capability to communicate with NASA's DSN using a high gain reflectarray antenna (Hodges et al., 2016) (see Figure 3.6 (b)).

MarCO has opened the door to deep-space CubeSat missions and currently ESA is developing the Miniaturised Asteroid Remote Geophysical Observer (M-ARGO; Topputo et al., 2021), a rendezvous mission to explore a near-Earth asteroid. M-ARGO will be a 12U CubeSat equipped with an electric propulsion system that will allow the spacecraft to independently navigate through deep-space. NASA's Sun Radio Interferometer Space Experiment (SunRISE; Kasper et al., 2021) is a solar dedicated mission under development at the time of writing, that will consist of six 6U CubeSats orbiting in a supersynchronous orbit. The CubeSats will be placed at 10 km from each other and will operate as a radio interferometer operating in the 0.1–20 MHz range.

In Chapter 6 we will explore the science and mission concept of ESA's SURROUND mission (Weigt & Cañizares et al. 2023; Crisp et al. 2023; Macario-Rojas, A. et al. (in review)), a CubeSat space weather monitoring mission currently at Phase 0 developmental stage designed to forecast and nowcast potentially damaging solar activity.

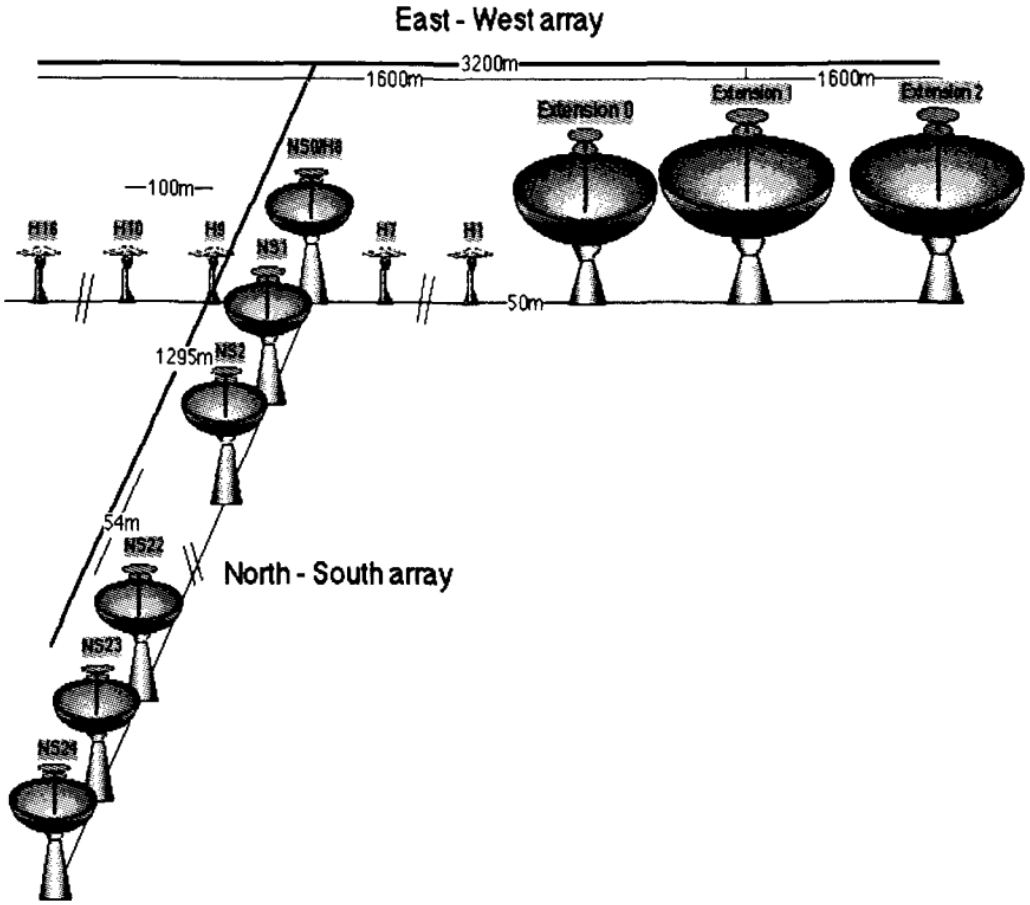


Figure 3.7: Diagram of the Nançay Radioheliograph (NRH). The instrument is composed of 44 antennas in T configuration, with 25 antennas distributed over a distance of 1.248 km in the North-South direction and 19 antennas distributed over a distance of 3.2 km in the East-West direction. The instrument operates in the 150 MHz to 450 MHz frequency range with a resolution of approximately $6'$ to $0.3'$, depending on frequency and direction. Source: Kerdraon & Delouis (2007).

3.8 Nançay Radioheliograph

The Nançay Radioheliograph (NRH; Kerdraon & Delouis, 2007) is a radio interferometer operated by the Observatoire de Paris and located in Nançay, France. The telescope operates as an array of radio antennas serving as a solar observatory during the day, tracking and making observations of the solar corona for approximately 7 hr a day, taking as many as 200 images of the solar corona per second. The antennas are designed to pivot over a base with a tracking accuracy of $1\,^{\circ}$.

NRH consists of 44 antennas, organised in a T configuration aligned North-South (NS) and East-West (EW) (see Figure 3.7). Along the EW array, 19 antennas are distributed over a range of 3.2 km, with the shortest baselines being approximately 50 m. The antennas along the EW array consist of two 10 m parabolas, one 7 m parabolas, one 5 m parabolas at the NS-EW intersection point and fifteen thick dipoles with no collector. Along the NS direction, the array consists of 5 m parabolic dishes distributed along a 1.248 km distance with the shortest baseline of 54.3 m.

NRH covers a frequency range of 150 MHz to 450 MHz with a time resolution of approximately 5 ms and spatial resolution of $0.3'$ to $6'$ which depends on frequency and direction. NRH allows for up to 10 observing frequencies which are typically 150.9, 173.2, 228.0, 270.6, 298.7, 327.0, 370.0, 408.0, 432.0, and 444.0 MHz.

At these frequencies, strong interference may occur due to the FM band at 88 MHz to 108 MHz and TV at $>$ 450 MHz and therefore each antenna is equipped with band pass filters. The system is calibrated via observations of intense radio sources such as Cygnus A fitted with a source model.

4 Methods

4.1 Burst Characterisation

Data from the radio spectrometers mentioned in Section 3.1 were available through different channels. The datasets for Wind were obtained from NASA Space Physics Data Facility[1] (Bougeret et al., 2021), STEREO data were available at MASER[2] (Krupar et al., 2022), PSP data were obtained through the NASA CDAWeb portal[3], the SolO data were obtained via the Solar Orbiter Archive (SOAR)[4] and the MEX data were obtained at ESA Cosmos[5]. All these datasets provide dynamic spectra data that were processed using the Python package Radiospectra (Mayer et al., 2024) which is part of the Sunpy (Barnes et al., 2020, 2023) suite of affiliated packages.

As it will be shown in Chapter 5, this work utilises time data extracted from the dynamic spectra at a given frequency. This is because multilateration requires only time differences (see Section 4.2.2). Given that the localisation of a source is frequency dependent (see Chapter 2), the timestamps of all spacecraft must be extracted from the same frequency channels. Furthermore, before extracting a timestamp from a frequency channel, one must first characterise and identify the detection point from the Type III light-curve. This involves a detailed analysis of the light-curve's morphological features. In order to process the data efficiently,

[1] `https://hpde.io/NASA/NumericalData/Wind/WAVES/DS/PT1M`

[2] `https://maser.lesia.obspm.fr/publications/doi/stereo-waves-lfr-hfr-l3-df-data.html`

[3] `https://cdaweb.gsfc.nasa.gov/pub/data/psp/fields/`

[4] `https://soar.esac.esa.int/soar/`

[5] `https://www.cosmos.esa.int/web/psa/mars-express`

a combination of automated detection algorithms and manual verification methods are employed. The detection algorithm uses strict rules to differentiate these features based on their distinct characteristics in the light-curve data.

The main identifying features of a Type III are the leading edge, the backbone and the trailing edge. The leading edge is determined by the arrival of the first photons, the backbone is the point of peak flux and the trailing edge is determined by the arrival of the last detected photons associated with the Type III. These are typically defined as the rise time, the peak time and the decay time respectively.

While the backbone of the Type III is normally used for methods of localisation such as GP, other methods (e.g., SEMP; Zhang et al., 2019) use the leading edge. The trailing edge of a Type III is typically discarded because of the diffuse gradient. The backbone of a Type III is employed in GP because the method requires high S/N in order to find the direction of the $\vec{k}$ vector. Multilateration is not limited by this and can therefore exploit the two main benefits of the leading edge, as it corresponds to the shortest possible path of the radiation from the source to the receiver and is morphologically well-defined as it has a relatively sharp gradient. Therefore, the use of the leading edge in multilateration provides an advantage in dynamic environments where the propagation conditions can change rapidly. By focusing on the leading edge, which is less influenced by subsequent scattering and attenuation effects, a more robust and precise localisation of the source is achieved.

In this work, a Gauss-Hermite (GH) polynomial method is used to characterise the shape of the Type III light-curves and obtain the required timestamps. These timestamps will later be introduced to a front fitting function that will characterise the morphology of the Type III.

4.1.1 Gauss-Hermite Polynomials

Determining a consistent point for the rising time of a Type III lightcurve for a particular frequency poses a number of challenges when the time resolution of an instrument is as low as 60 s, which is the case of the Wind/Waves data used in this thesis, and 38.05 s, as

in the case of STEREO/Waves. Additionally, studies such as Reid & Kontar (2018) and Jebaraj et al. (2023) have shown that the light-curves of Type IIIs are skewed, with the skewness being more pronounced at the low interplanetary frequencies. In the case of Reid & Kontar (2018) a Gaussian function and an exponential function were fitted to the relatively high cadence light-curves from LOFAR. However, following this approach on a skewed low cadence dataset will result in inconsistent results with large errors.

If the profile of a light-curve deviates from a Gaussian shape, Van Der Marel & Franx (1993) showed that a GH series can be used to derive a profile with skewness and kurtosis and Blinnikov & Moessner (1998) compared different methods that use Hermite polynomials noting that GH is a suitable method of fitting the profile of a skewed distribution in an economical way, which makes it a particularly attractive option when fitting a large number of light-curves. Some examples of the GH method being used are, Riffel (2010) who used the GH series to fit emission-line flux distributions in distinct astrophysical objects, and Dhungana et al. (2024) who used GH method to fit the light-curves of type-Ia supernovae.

Given that Type III light-curves are notoriously skewed, particularly at the frequency ranges studied in this thesis, and that the objective of this method is to fit a large number of light-curves, the usage of the GH method is explored in this thesis.

In order to obtain a consistent rise time for the lightcurve of a Type III, the GH model from Van Der Marel & Franx (1993) was fitted using the Python package Kapteyn (Terlouw & Vogelaar, 2014), and is defined by the following expression as shown in Vogelaar (1999):

$$\phi(x) = Ae^{-\frac{1}{2}y^2}\left\{1 + \frac{h_3}{\sqrt{6}}\left(2\sqrt{2}y^3 - 3\sqrt{2}y\right) + \frac{h_4}{\sqrt{24}}\left(4y^4 - 12y^2 + 3\right)\right\} + Z \tag{4.1}$$

where Z is a constant that represents the background, and:

$$y = \frac{x - \mu}{\sigma}$$

is a standardised variable with mean 0 and standard deviation of unity. The lowest term of Equation 4.1 is composed of a Gaussian:

$$Ae^{-\frac{1}{2}y^2}$$

and the higher order terms,

$$1+\frac{h_3}{\sqrt{6}}\left(2\sqrt{2}y^3-3\sqrt{2}y\right)+\frac{h_4}{\sqrt{24}}\left(4y^4-12y^2+3\right)$$

are related to the Hermite polynomials:

$$H_0(y)=1 \tag{4.2}$$

$$H_1(y)=2y \tag{4.3}$$

$$H_2(y)=4y^2-2 \tag{4.4}$$

$$H_3(y)=8y^3-12y \tag{4.5}$$

$$H_4(y)=16y^4-48y^2+12 \tag{4.6}$$

$$\vdots \tag{4.7}$$

$$H_n(y)=(-1)^n e^{y^2}\frac{d^n}{dy^n}e^{-y^2} \tag{4.8}$$

These polynomials, are used in statistics to approximate probability distributions. Each term in the expansion corresponds to corrections based on the cumulants of the distribution, allowing for the modelling of skewed distributions. In the context of a standardised normal distribution, the zeroth moment H_0 is 0. The first moment H_1 is the mean of the distribution and is also 0. The second moment H_2 is the variance of the distribution, which is 1. The third moment H_3 is related to the skewness, and the fourth moment H_4 is related to the kurtosis.

Skewness measures the asymmetry of the distribution where the scaling factor h_3 quantifies

the term in Equation 4.1 and is related to the third order Hermite polynomial as:

$$\frac{h_3}{\sqrt{6}}\left(2\sqrt{2}y^3 - 3\sqrt{2}y\right) = \frac{h_3}{4\sqrt{3}}H_3(y) \tag{4.9}$$

Kurtosis measures the "tailedness" of the distribution, describing the sharpness for which a PDF increases and decreases. In Equation 4.1, this corresponds to the h_4 term which is associated with the fourth moment H_4 of the Hermite Polynomials as:

$$\frac{h_4}{\sqrt{24}}\left(4y^4 - 12y^2 + 3\right) = \frac{h_4}{8\sqrt{6}}H_4(y) \tag{4.10}$$

The GH model (see Equation 4.1) is therefore an asymmetric Gaussian-like function that is written in terms of skewness and kurtosis. The criteria for the rise time of the lightcurve was defined in this case by the full width at quarter maximum (FWQM). Although, it is not a strict criteria, and other criteria such as a relative threshold value above background and half width at half max would also be acceptable.

Figure 4.1 shows various examples of fitting a GH model to different light-curves using the *kmpfit* module. In Figure 4.1 (a), a low-frequency lightcurve is observed with a relatively high data count, while Figure 4.1 (b) shows a high-frequency lightcurve with a low data count. Figure 4.1 (c) depicts a lightcurve with a low signal-to-noise ratio (S/N) and Figure 4.1 (d) is an example of an incomplete light-curve with some radio frequency interference (RFI) present. Figure 4.2 shows an example of the GH method in practice where the detection points shown as red circles, were obtained for the rise time, and for comparative purposes, the backbone and the decay time. The GH method proved to be a robust method that allowed for the automatic detection of the leading edge and the backbone. The trailing edge, showed some difficulty in the higher frequencies due to the low event rate. The low event rate also signify that the leading edge and backbone merged into one another.

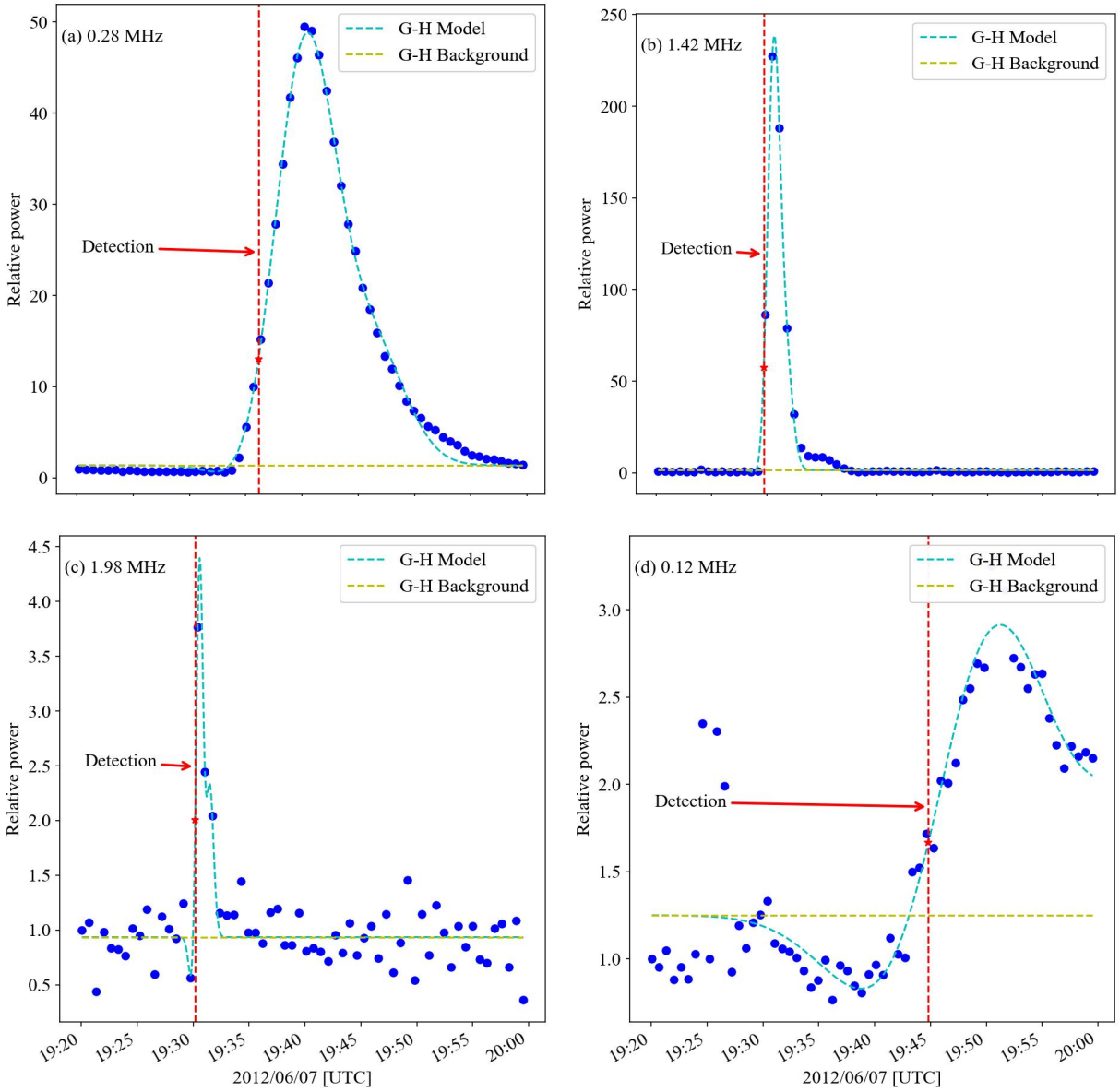


Figure 4.1: Examples of GH fitting of Type III light-curves. a) Shows a high S/N light-curve fit with a high data count. b) Shows a high S/N with a low signal data count. c) Shows an example of a light-curve with poor S/N and low data count. d) Is an example of an incomplete light-curve with RFI observed prior to the Type III. The GH algorithm proved to be a robust mechanism to characterise the profile of a Type III and consequently determine the rise time. Small discrepancies between the model and the data were observed at the trailing edge tails; this did not have a noticeable effect on the rise time results. Upon visual inspection of the detected points in the dynamic spectra (see Figure 5.5), the algorithm performed optimally and consistently detected the edge of the Type III within one cadence. Source: Adapted from Cañizares et al. (2024).

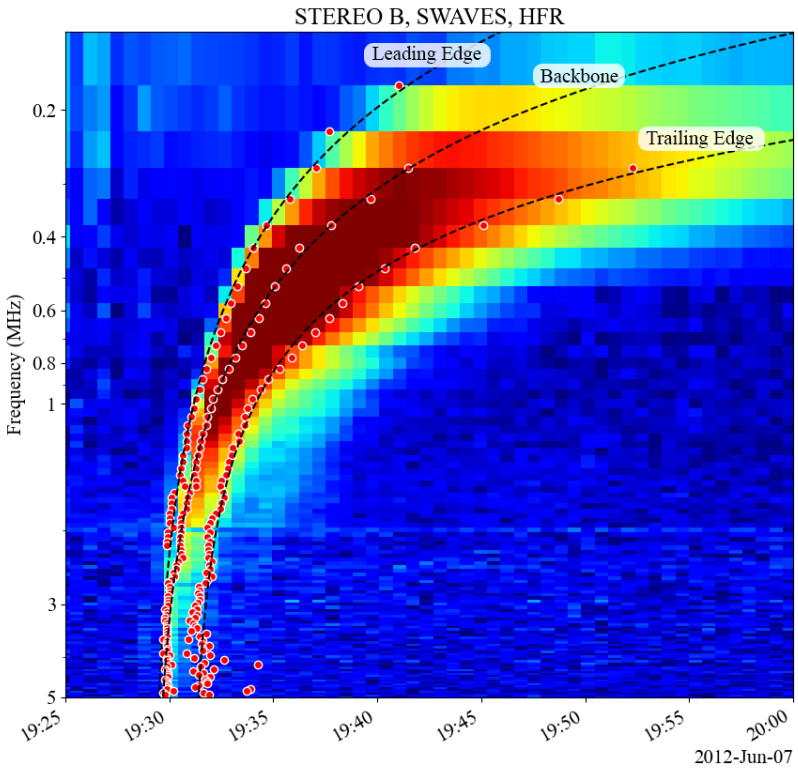


Figure 4.2: Example of a STEREO B dynamic spectra where the leading edge, the backbone and the trailing edge were detected using the GH method. The detection points were then fitted using an inverse polynomial Equation 4.11.

4.1.2 The profile of a Type III

Once the GH method has been used to obtain the rise, backbone and decay times, the data is fitted with a time evolution function. This time evolution function was parameterised using an inverse polynomial of the form

$$t(f) = a_2 \frac{1}{f^2} + a_1 \frac{1}{f} + a_0, \tag{4.11}$$

where t is the timestamp; f is the input frequency; and a_2, a_1, and a_0 are coefficients that represent the curvature, the drift rate, and initial position of the burst, respectively. These fits can be observed in Figure 4.2 as black dashed lines.

The time evolution function allows for the characterisation of the Type III and serves two

purposes. The first purpose is to make all spacecraft compatible for multilateration despite not sharing the same frequency channels. The second purpose is to average out any errors induced by the spectrometer receivers, such as zigzags due to frequency sweeps, low instrumental cadence, and outliers. Instrumental cadence, being the largest source of instrumental uncertainty, is later taken into account by the Bayesian solver priors (see. Section 5.2).

Before using the time evolution fits to extract data, the fits were subject to visual inspection to confirm some physical considerations. First, the polynomial fit had to be asymptotically stable and not show a characteristic polynomial U-shape near the fit of the Type III. Second, the leading edge, backbone and trailing edge fits must be asymptotically parallel to each other. If these two rules are broken, then manual adjustments were made to any outliers or to the last points of the array for the purposes of fine-tuning the Type III shape.

4.2 Multilateration

Multilateration is a localisation technique that relies on the intersection of geometrical functions based on the propagation times derived from measurements taken by different receivers. There are many types of multilateration (see review, Widdison & Long, 2024); however, the two most prominent types are Time-of-Arrival (TOA) and Time-Difference-of-Arrival (TDOA). Figure 4.3 shows a cartoon that illustrates both methods of localisation, highlighting the similarities and differences of these techniques. At first glance, each technique relies on a different geometrical shape: TOA uses circles, and TDOA uses hyperbolas. The main similarity is that both techniques require a minimum of three spacecraft in a 2D environment to achieve a solution.

4.2.1 Time of Arrival (TOA)

TOA is the method of multilateration used by global positioning systems such as Galileo and GPS, submarine sonar or speed cameras. The technique relies on a time difference Δt_{n0} resulting from the time difference between the emission time t_0 and the received time t_n

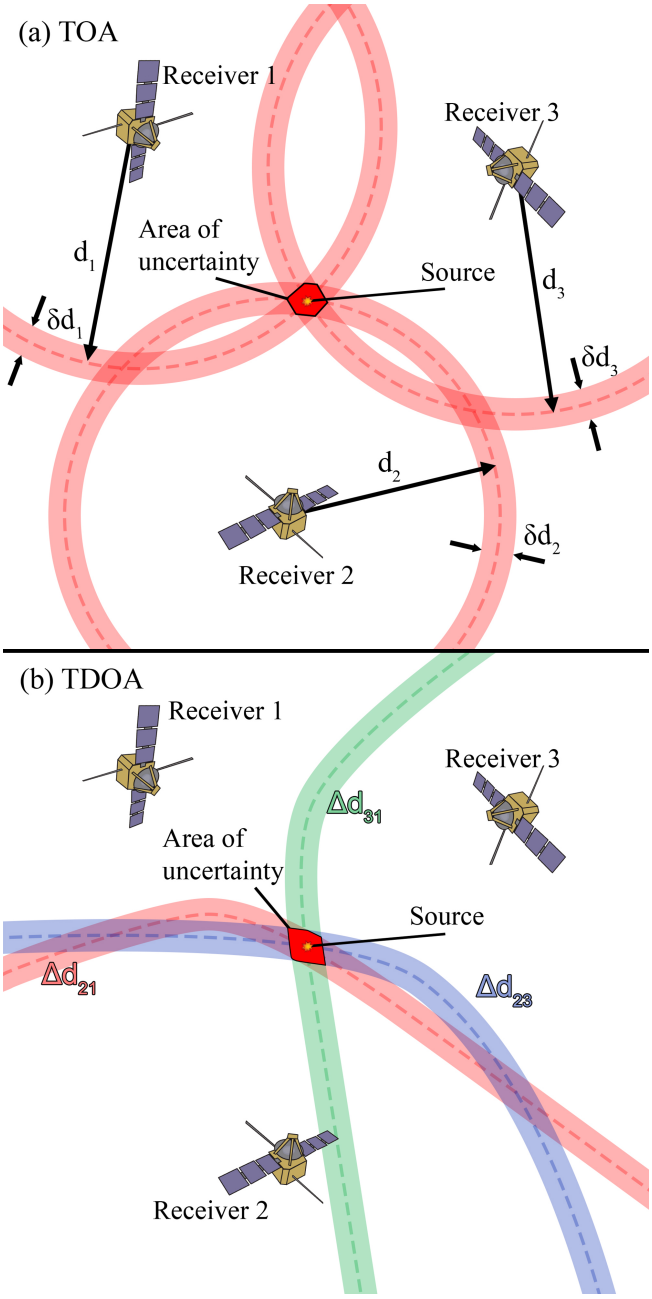


Figure 4.3: The two main multilateration methods. (a) TOA and (b) TDOA. TOA is defined by the time difference between the emission time and the received time to obtain circles. TDOA is defined by the time difference between arrival times to obtain hyperbolas. The point of intersection of all circles or all hyperbolas results in the location of the source. The resulting areas of uncertainty are determined by the instrumental cadence of the receiver and the angle of intersection of each circle/hyperbola. Source: Cañizares et al. (2024).

where $n = 1, 2, 3, ...$ depending on the number of receivers.

TOA is governed by the solution to the parametric equation of n circles with radius

$$d_n = c\ \Delta t_{n0} = c\ (t_n - t_0) \qquad n = 1, 2, 3, ... \tag{4.12}$$

and the equation of the circle

$$d_n^2 = (x_n - x)^2 + (y_n - y)^2 \qquad n = 1, 2, 3, ... \tag{4.13}$$

where (x_n, y_n) corresponds to the coordinates of each of the spacecraft receivers.

4.2.2 Time Difference of Arrival (TDOA)

Unfortunately, the time of emission is inherently unknown for astronomical applications, and requires a different approach. Alcock (2018) shows that TDOA uses the time difference between received signals, where the Δt_{ij} required is defined as $\Delta t_{ij} = t_j - t_i$.

$$\Delta d_{ij} = c\Delta t_{ij} \tag{4.14}$$

where i, j are subscripts for each of the receivers and $\Delta d_{ij} = d_j - d_i$, therefore if:

$$\Delta d_i = \sqrt{(x_i - x)^2 + (y_i - y)^2} \tag{4.15}$$

and

$$\Delta d_j = \sqrt{(x_j - x)^2 + (y_j - y)^2} \tag{4.16}$$

$$\Delta d_{ij} = c\Delta t_{ij} = \sqrt{(x_j - x)^2 + (y_j - y)^2} - \sqrt{(x_i - x)^2 + (y_i - y)^2} \tag{4.17}$$

This equation can be simplified by changing the frame of reference so that the receivers are aligned to the X-axis and the origin is centred between the spacecraft. The positions are

therefore defined as $x_i = x_j = 0$ and $-y_i = y_j = Y$

$$\Delta d_{ij} = \sqrt{x^2 + (Y - y)^2} - \sqrt{x^2 + (Y + y)^2} \tag{4.18}$$

According to Alcock (2018), Equation 4.18 is the equation of a hyperbola, which after a complex mathematical process, can be rearranged to the more recognisable form

$$\frac{x^2}{(\frac{c\Delta t_{ij}}{2})^2 - Y^2} + \frac{y^2}{(\frac{c\Delta t_{ij}}{2})^2} = 1 \tag{4.19}$$

where c is the speed of light in a vacuum and Δt_{ij} is the time difference between receivers located at each foci of the hyperbola. Unfortunately, hyperbolas have two branches, which means solving the parametric equation may lead to false positives. Thus, further assumptions or techniques must be utilised to reach a solution (Bishop et al., 2008). An example of this method being used for the localisation of Type IIIs is shown in Badman et al. (2022) and its implementation is available at Badman (2023).

4.2.3 Bayesian Multilateration

Combining Bayesian statistics with multilateration is widely used to track different objects in different fields. Some notable examples are underwater tracking (e.g., Watkins et al., 2024), Radio-frequency identification (RFID) nodes tracking (e.g., Zhou & Shi, 2009; Sanpechuda & Kovavisaruch, 2008), and tracking elephants in Africa using seismographs (Reinwald et al., 2021). The same Bayesian concepts and techniques used by Reinwald et al. (2021), which were previously introduced mathematically by Speagle (2019), are applied here to track solar radio bursts in the solar corona.

The posterior of a Bayesian statistics positional problem is defined as the probability of finding the position of a source ($\vec{x}$) and the speed of signal propagation (v) given an observable Δt:

$$P(\vec{x}, v \mid \Delta t) \tag{4.20}$$

According to Bayes' Theorem, this implies that

$$P(\vec{x}, v \mid \Delta t) = P(\vec{x}, v)\frac{P(\Delta t \mid \vec{x}, v)}{P(\Delta t)} \tag{4.21}$$

Noting that the conditional probability may be written in terms of the priors

$$P(\vec{x} \mid v) = \frac{P(\vec{x}, v)}{P(v)} \tag{4.22}$$

Rearranging Equation 4.22 and substituting into Equation 4.21 results in

$$P(\vec{x}, v \mid \Delta t) = \frac{P(\Delta t \mid \vec{x}, v)\ P(\vec{x} \mid v)\ P(v)}{P(\Delta t)}, \tag{4.23}$$

where each term is defined as:

- $P(\vec{x}, v \mid \Delta t)$ is the posterior distribution or the probability of finding the source at position $\vec{x}$ with a speed of propagation v given an observable Δt.
- $P(\Delta t \mid \vec{x}, v)$ is the likelihood function or the probability of observing a Δt given a position $\vec{x}$ and a speed of propagation v. This likelihood function is the physics model, and it is defined by the type of multilateration one wants to apply. In the case of TOA, $\Delta t = d/v$, where d is the distance between the source and the receiver.
- $P(\vec{x} \mid v)$ is the prior distribution of the source position given a speed of propagation v.
- $P(v)$ is the prior distribution of the speed of propagation of the photons. The main assumption made by traditional multilateration methods such as TOA and TDOA is that the speed of propagation of the electromagnetic radiation is c, which is valid asymptotically far from the radio source but may break down close to the emission site where the emitted radiation is at a frequency similar to the local plasma frequency (e.g. Thejappa & MacDowall, 2010; Kontar et al., 2019). The Bayesian solver does not make this assumption and allows for a distribution of the speed of propagation. The objective of this method is to accommodate the possibility that the ray from source to observer

may have a longer than expected time of arrival due to scattering or refraction near the source but without needing to introduce detailed ray-tracing simulations (e.g. Musset et al., 2021; Chen et al., 2023). This can be modelled as a truncated normal distribution with a maximum of c to restrict all solutions to physical solutions, or it can be modelled as a normal distribution with c as the maximum, allowing for the Markov chain Monte Carlo (MCMC) solver (see Sect. 5.2) to test if the solution is physical or not. Convergence is expected at $v \approx c$ or $v < c$ for a physical solution. The first one implying that the path of the light ray is along a straight line and the latter implying refraction is a considerable effect.

- $P(\Delta t)$ is the evidence probability shown as a distribution of the time difference between the time of emission t_0 and the time of arrival t_1. The time of arrival is observed by the spacecraft, and the time of emission is fitted by the MCMC solver, which finds a time of emission that would be consistent for all spacecraft.

5 The BayEsian LocaLisation Algorithm (BELLA)

5.1 Introduction

An example of applying TDOA for the localisation of Type IIIs is shown by Badman et al. (2022), where radio emission sources were tracked from low in the solar corona ($\sim$1.5 $R_\odot$) using LOFAR to interplanetary distances ($\sim$40 $R_\odot$) using TDOA. Badman et al. (2022) observed a small but noticeable discrepancy between the LOFAR-imaged sources and the location of the multilateration results. This discrepancy was analysed, and Badman et al. (2022) concluded that the difference in trajectory could be explained by the uncertainty of the multilateration results. However, the uncertainty was not measured quantitatively but rather by repeating the TDOA analysis thousands of times, using varying combinations of rise times sampled around the original onset times. This generated a relatively large "cloud" of results that engulfed the Sun and the LOFAR results. While this approach helped explain the results' discrepancies, it did not explain the sources of these uncertainties, whether instrumental, physical or as a consequence of the method used. Therefore, showing the need for a more rigorous statistical method that quantitatively analyses the uncertainty of multilateration. To address this issue, the BayEsian LocaLisation Algorithm (BELLA; Cañizares et al., 2024) was developed.

5.2 Implementation of Bayesian Multilateration

Fortunately, Bayesian inference is a well established method of performing statistics and there are a number of python packages available which help streamline the process. BELLA performs Bayesian multilateration (see Section 4.2.3) with the help of the PyMC package (Salvatier et al., 2016; Wiecki et al., 2023). PyMC allows for Bayesian inference based on probabilistic models and creates an environment where prior distributions can be defined intuitively within a model container that performs Bayesian statistics automatically. BELLA makes use of the normal distribution and uniform distribution functions embedded in PyMC. The probability density function (PDF) of a normal distribution is

$$f(x \mid \mu, \sigma) = \sqrt{\frac{1}{2\pi\sigma^2}} \exp\left(-\frac{1}{2\sigma^2}(x-\mu)^2 \right), \tag{5.1}$$

where σ is the standard deviation and μ is the mean. The other PDF used by BELLA is the uniform distribution

$$f(x \mid a, b) = \frac{1}{a-b} \tag{5.2}$$

where a and b are the upper and lower limits. Additionally, a truncated normal distribution is also compatible with BELLA. Although the use of the truncated normal distribution was substituted by the normal distribution for reasons that will be explained later, it is still available as an option. This distribution is defined as

$$f(x \mid \mu, \sigma, a, b) = \frac{\phi\left(\frac{x-\mu}{\sigma}\right)}{\sigma\left(\Phi\left(\frac{b-\mu}{\sigma}\right) - \Phi\left(\frac{a-\mu}{\sigma}\right)\right)} \tag{5.3}$$

where ϕ is the normal distribution (Equation 5.1) and Φ is the cumulative distribution function (CDF) evaluated at the truncated limits [a,b] and is defined as

$$\Phi(z) = \int_{-\infty}^{z} \phi(x)\, dx \tag{5.4}$$

The distributions defined above serve to generate a PyMC model context manager. This context manager defines the physical interpretations and the prior distributions that will be used for performing Bayesian inference (Equation 4.23). The main physical models to be considered are the two main types of multilateration shown in Section 4.2, TOA and TDOA. Both methods convert a measured time difference into a distance, via the $d = ct$ principle. However, TOA achieves this using circles, and TDOA uses hyperbolas. TDOA using hyperbolas is a disadvantage as hyperbolas contain two branches, and therefore false positives may appear. This can be mitigated by making further assumptions in order to choose one solution. However, TOA does not have this problem and provided that there are at least three spacecraft, it provides one solution only. Additionally, TOA is mathematically simple when compared to TDOA, further simplifying the computational process and can be easily extended to utilise multiple spacecraft. The main disadvantage of TOA remains that the emission time is unknown. Given that it is assumed that the received emission is point source, the PyMC engine can solve this by fitting for a common emission time. Because of these arguments, TOA was the chosen method of multilateration for BELLA. The priors are then set in the context manager as a series of stochastic variables and deterministic variables. The difference between these is that stochastic variables are random variables that have a probability distribution. These are defined with uncertainty, meaning that their value is not fixed but instead sampled from the specified distribution. On the other hand, deterministic variables are fully determined by other variables in the model. They are defined by a mathematical or logical relationship rather than by a probability distribution:

- $P(\vec{x} \mid v)$: The prior for the coordinate space of the source positions was implemented as a stochastic random variable sampled from a normal distribution with $\mu = 0$ and $\sigma = hR_{\odot}$, where h is an educated guess of the radial distance of the emission to the Sun in the range [-215, 215] $R_{\odot}$. The term h was chosen to be one-fourth of the space domain in one dimension, which is $\sim 80\ R_{\odot}$. This variable could also be defined as a uniform distribution with limits defined at 1 au.

- $P(v)$: The speed of propagation prior defined as a stochastic random variable sampled from a normal distribution with $\mu = c$ and $\sigma = 0.1c$.

- $P(\Delta t)$: The probabilistic evidence implemented by sampling from a uniform distribution with limits much larger than the light travel time corresponding to the coordinate space limits (for example, $t_{lims} = \pm 24$ x 60 x 60 s).

- The likelihood distribution is determined by the variable defined by $\Delta t = d/v$, where d is the distance between the location of the spacecraft $\vec{x_{sc}}$ and the source position $\vec{x}$. Note, $d = |\vec{x_{sc}} - \vec{x}|$, and v is sampled from the speed of propagation prior. PyMC then takes these values to define a normal distribution where $\mu = \Delta t$ and $\sigma = t_{sd}$, where t_{sd} is the cadence of the instrument. Another benefit of PyMC is that it allows to include the parameter 'observed' in the likelihood distribution. This feeds in the real data to the likelihood function making the model data-driven.

An important consideration is that the speed of propagation in the model is not c but determined by the distribution of propagation speeds $P(v)$. This is an advantage over the analytical TDOA method which inherently assumes the speed of light in a vacuum $v = c$ as the propagation speed. Additionally, the prior $P(v)$ was sampled from a normal distribution, thus allowing sampled values where $v > c$ with the purpose of testing if the Bayesian solver converges to a propagation speed that is physical (i.e. $v \leq c$). If the maximum of the posterior distribution shows that $v > c$, the results are no longer considered physical, and further investigation is necessary. Alternatively, the use of a truncated normal distribution (Equation 5.3) with $v = c$ as the upper limit of the distribution is compatible with BELLA. This would ensure that the results are sampled from a physical prior distribution but the system would lack the ability to flag unphysical solutions.

With the parameter space set up, the PyMC environment was ready for sampling. The PyMC package uses the No-U-Turn Sampler (NUTS; Hoffman et al., 2014) by default. NUTS is a self-tuning sampling method designed to prevent the sampler from retracing its steps, thereby efficiently exploring the target distribution. Given that BELLA uses relatively simple dis-

tributions, the NUTS sampler could be considered excessive and a significant contributor towards the large computational costs. PyMC also allows for the simpler 'metropolis' samplers and their implementation for the purpose of optimising BELLA computational costs will be subject of further investigation.

By default, the sampler uses four different sequences of samples, also known as chains. Each chain was initialised using 2000 tuning samples, and then an additional 2000 samples were drawn to achieve a singular stable solution (i.e. convergence). When convergence was achieved, the posterior distributions ($P(\vec{x}, v \mid \Delta t)$) were found to be approximate and discrete normal distributions. The mean of the distributions was then defined as $[\mu_x, \mu_y] = [x_x, x_y]$. This is the most probable source location with 1σ uncertainty for each coordinate. The results were then plotted in a BELLA map as an area of confidence depicted as an ellipse with axes $[\sigma_x, \sigma_y] = [\Delta x_x, \Delta x_y]$ where the centroid is located at $[x_x, x_y]$.

Figure 5.1 shows an example of the trace plots generated after one multilateration computation. BELLA uses four chains by default to ensure convergence. Each of the colours in the figure represents a different chain. The trace plots are made of two columns that show the distributions (*left*) and the sampled space (*right*). From top to bottom, (a) is the posterior distribution of the X coordinate, (b) is the posterior distribution of the Y coordinate, (c) is the distribution of the speed of propagation, and (d) is the distribution of the time of emission. Throughout this work, the peak of these distributions is defined as the most probable location of the source and 1σ as the uncertainty of the distribution. These points are identified in the trace plots as blue vertical lines (see Figure 5.1 *left*). The distribution of the speed of propagation also displays a red line corresponding to the $v = c$ limit. This was used as a quick view warning to test the $v \leq c$ criterion.

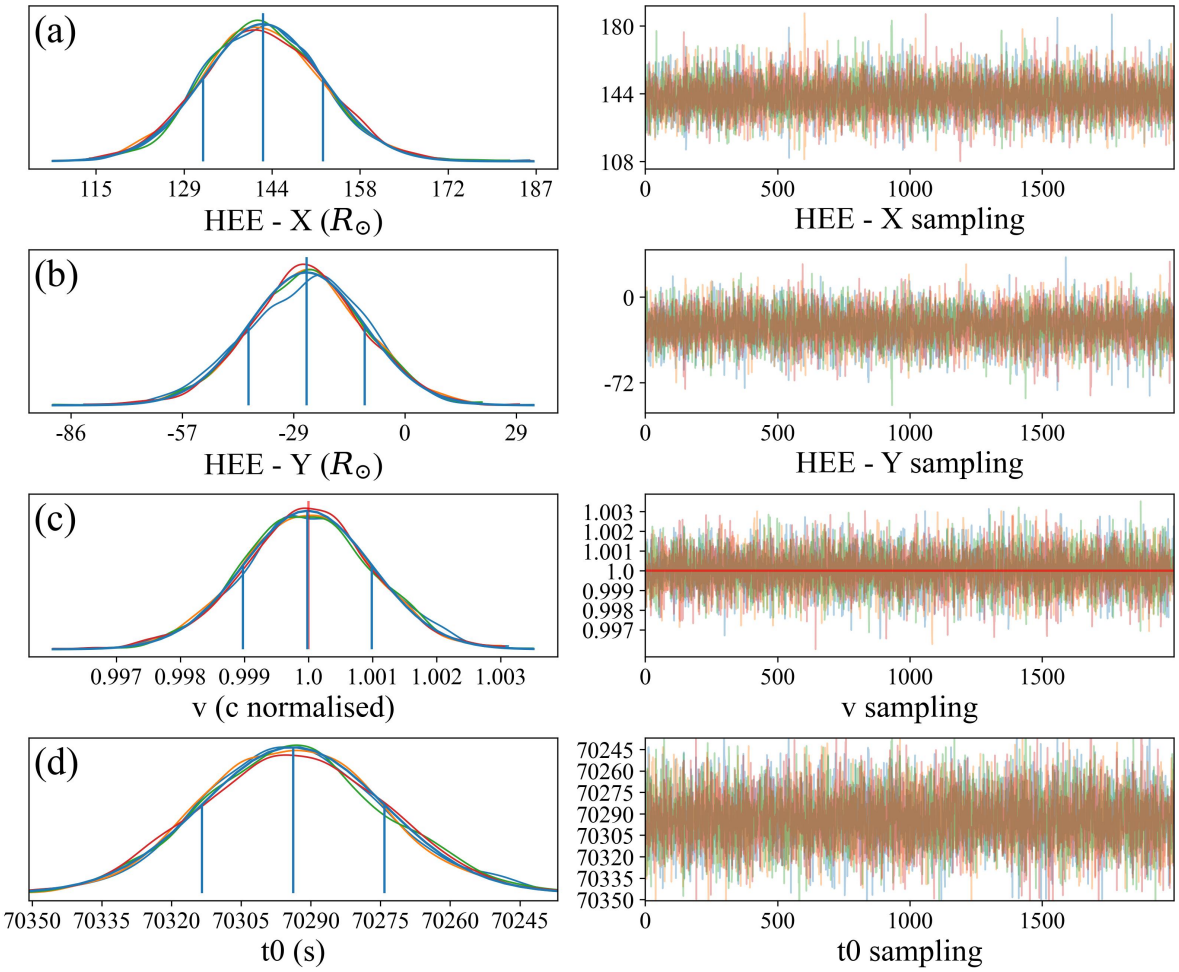


Figure 5.1: Example of the trace plots generated after one BELLA computation. (a) Is the X coordinate posterior distribution, (b) is the Y coordinate posterior distribution, (c) is the speed of propagation distribution and (d) is the emission time distribution. The right column shows the sampling space of each of the distributions shown on the left. At each of the distributions, four chains were computed and are shown in different colours. The blue vertical lines, show the peak of the distributions and 1σ which correspond to the solution and uncertainty, respectively. A vertical red line is shown in (c) as a visual reference of the $v = c$ limit which helps discard nonphysical solutions. Source: Cañizares et al. (2024).

5.3 Simulations and Method Validation

5.3.1 Confidence Maps

In order to investigate the effects of spacecraft geometry and instrument time resolution on the inherent uncertainty of multilateration, a mesh-grid of 500 x 500 nodes was established, and each node was treated as an emission source. By assuming free streaming and a propagation speed of $v = c$, synthetic arrival times were calculated as $t = d/c$ for each source-spacecraft pair. A small amount of Gaussian noise (on the order of <1%) was applied to the simulated data. The noisy data was then used as an input for the Bayesian procedure described in Section 5.2. Posterior distributions for the detected position at each node gave corresponding 1σ uncertainties in the X and Y directions. The maximum value of the X and Y uncertainties was taken as the value for the uncertainty map colour (e.g., Figure 5.2). These background maps serve to identify the regions of low and high confidence. The limit of low uncertainty is dictated by the instrumental cadence uncertainty, given by:

$$\Delta d_l = \frac{c\,\Delta t}{R_\odot} \tag{5.5}$$

where Δd is the uncertainty limit in $R_\odot$ and Δt is the cadence of the instrument. This corresponds to $\sim 3\,R_\odot$ for a cadence of 7 s and $\sim 25\,R_\odot$ for a cadence of 60 s. As a rule of thumb, confidence maps are made with the worst available cadence, that is 60 s. Therefore, the lower limit is established as $\Delta d_l = 25\,R_\odot$ and defines areas of high confidence. On the other hand, the upper tolerance limit is selected as an arbitrary conservative constant for which any larger of an uncertainty is deemed unacceptable. For this case $\Delta d_h = 100\,R_\odot$.

Taking Figure 5.2 as an example, these confidence maps show a relatively large area of high confidence in Figure 5.2 (a) (in dark blue) and a relatively large area of low confidence in Figure 5.2 (b) (in yellow). An event occurring in (a) will likely show sources of uncertainty due to factors agnostic to BELLA. However, the multilateration procedure will be significantly

affected in the case of (b). Therefore, the objective of these maps is to select configurations of spacecraft that minimise the uncertainty and to discard events occurring during time frames dominated by poor spacecraft configurations.

5.3.2 Simulations to Validate BELLA

In order to first validate BELLA and assess its capabilities, a simulation was set up under the controlled conditions of a known set of source positions and a known propagation speeds assuming no refractive or scattering effects. During these simulations, the ground truth signal was recovered to a better or worse extent depending on the spacecraft configuration. This approach allows to evaluate the impact of spacecraft configuration on the uncertainty of the localisation results. Figure 5.3 and Figure 5.4 illustrate the results of these simulations, where the first figure shows four different instances of the simulation and the second offers a summary. In order to observe the effects of instrumental cadence on the performance of the simulations, all cases were simulated twice: once at a cadence of 30 s (blue) and once at a cadence of 60 s (red). The background maps were all simulated at 60 s cadence. In addition to validating the methodology, these simulations allowed for the selection of a suitable Type III candidate by discarding spacecraft configurations that would guarantee uncertain results. The simulation was composed of the following: A three-spacecraft system analogous to the real STEREO A/B and Wind configuration was established. For simplicity, the Ahead and Behind spacecraft were kept at a constant distance of $\pm 1\%$ of 1 au, respectively. The Wind spacecraft was kept stationary at L1, while the Ahead and Behind spacecraft were synchronously separated from Wind in $\pm 10^{\circ}$ increments, respectively.

As shown in Figure 5.3, it is clear that when two or more spacecraft are close together, a source anywhere in the ecliptic plane has a large uncertainty (yellow regions), but when they are equidistantly spaced, the uncertainty is minimised (dark blue regions).

A test burst was also simulated by selecting a number of simulated sources along a notional Parker Spiral and performing the same procedure at two different cadences (60 s and 30 s),

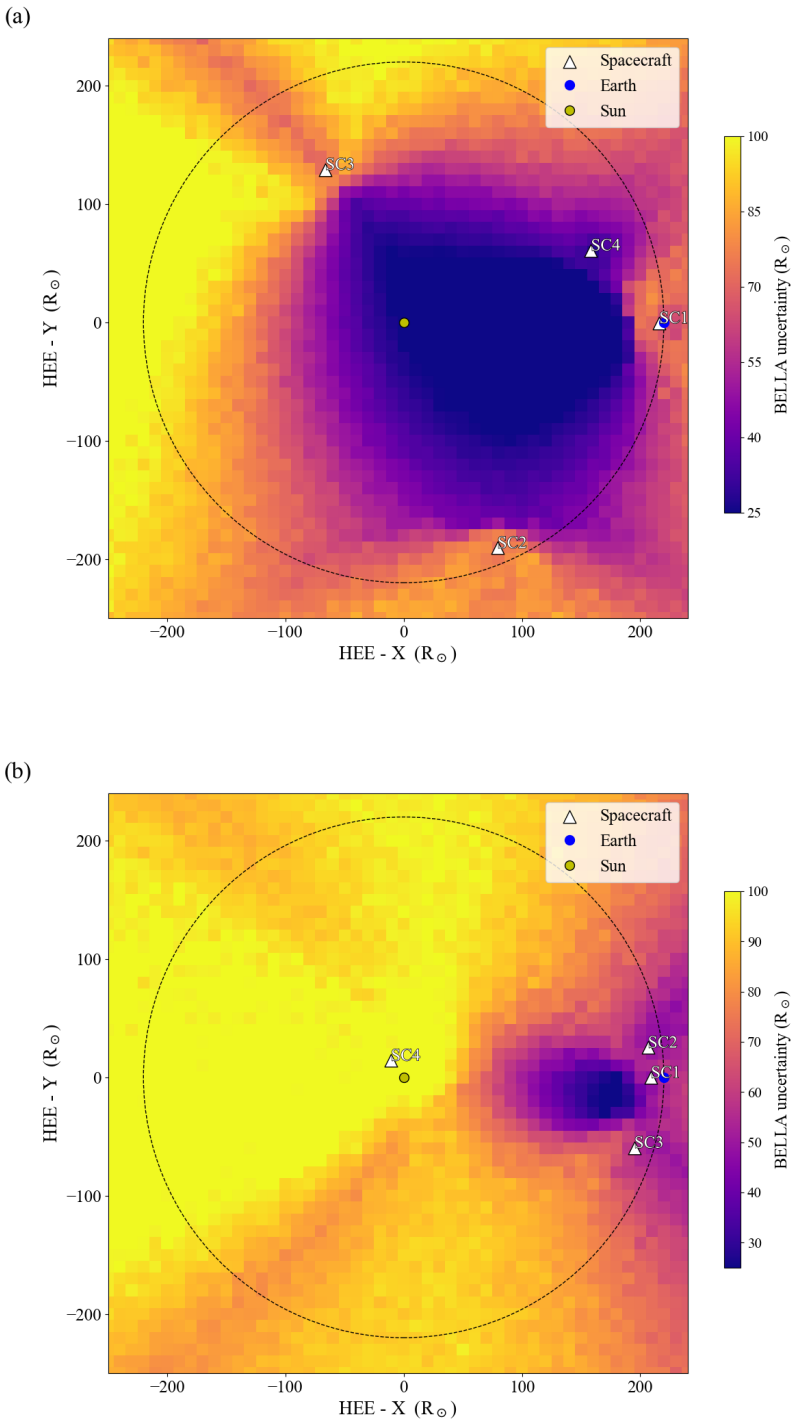


Figure 5.2: Examples of BELLA confidence maps showing maps dominated by (a) regions of high confidence (in dark blue) and, (b) regions of low confidence in (yellow). The background maps are developed by simulating emission at every grid pixel of the spatial domain and measuring the uncertainty of the localised posterior distribution. The pixels are then colourised based on this uncertainty.

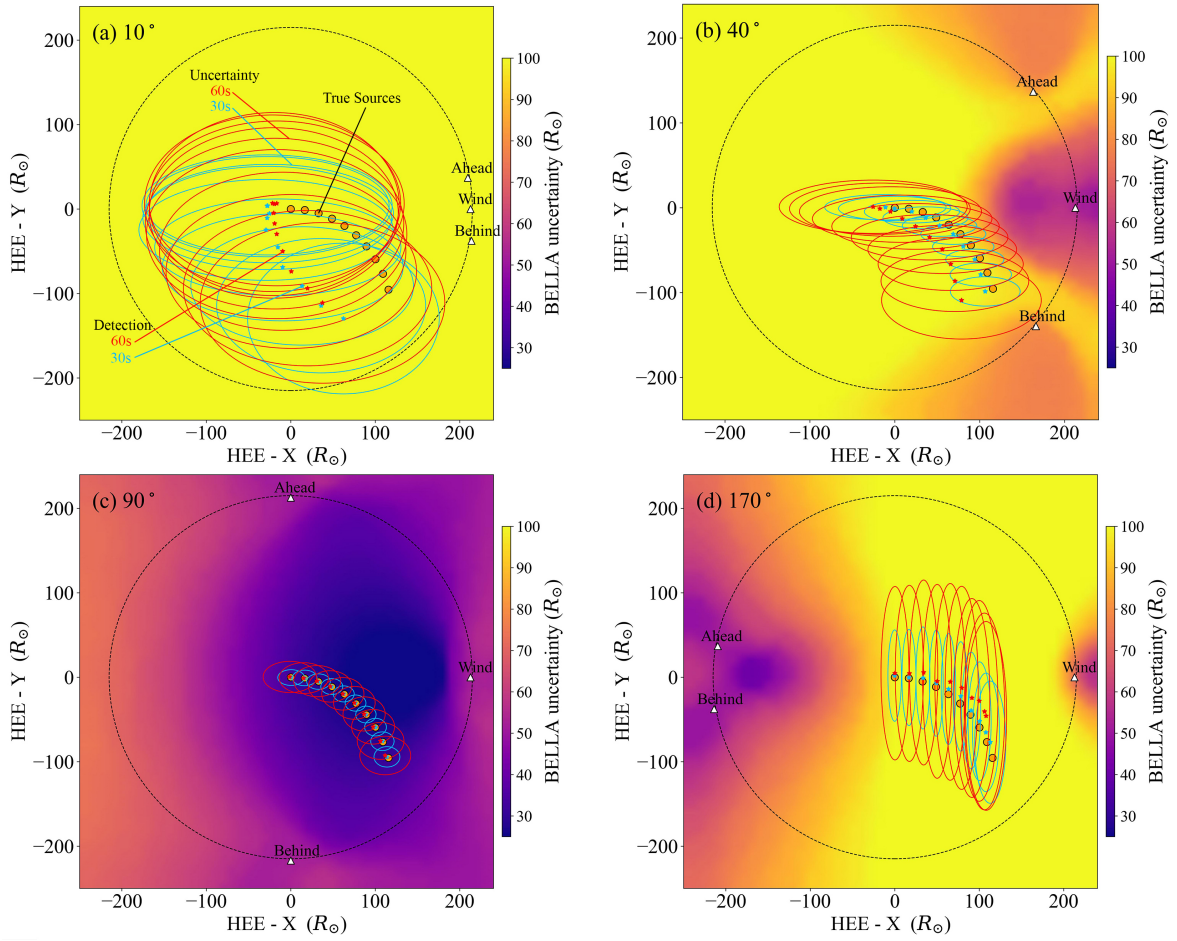


Figure 5.3: Simulation of radio sources with respect to spacecraft configuration where Ahead/Behind are located at (a) $\pm 10^{\circ}$, (b) $\pm 40^{\circ}$, (c) $\pm 90^{\circ}$, and (d)$\pm 170^{\circ}$ with respect to Wind. The background maps help distinguish between the regions of confidence (dark blue) and the regions of uncertainty (yellow). The orange dots represent the true sources, red/blue stars/ellipses show the localised sources. The instrument cadence was simulated by setting the standard deviation of the likelihood function. The simulation was repeated at different cadences showing red as 60 s cadence and blue as 30 s cadence. These simulations help understand the effects of spacecraft configuration on the localisation uncertainty and therefore, select events for multilateration. Note that in the (d) case, while the uncertainty in the Y-coordinate is relatively high, the centroids still follow the true sources with some degree of accuracy. This is likely because of the relative symmetry of the system and that the separation between the Ahead-Wind and Behind-Wind is large. This means that the solution might still be accurate but the confidence of this result is low. Source: Cañizares et al. (2024).

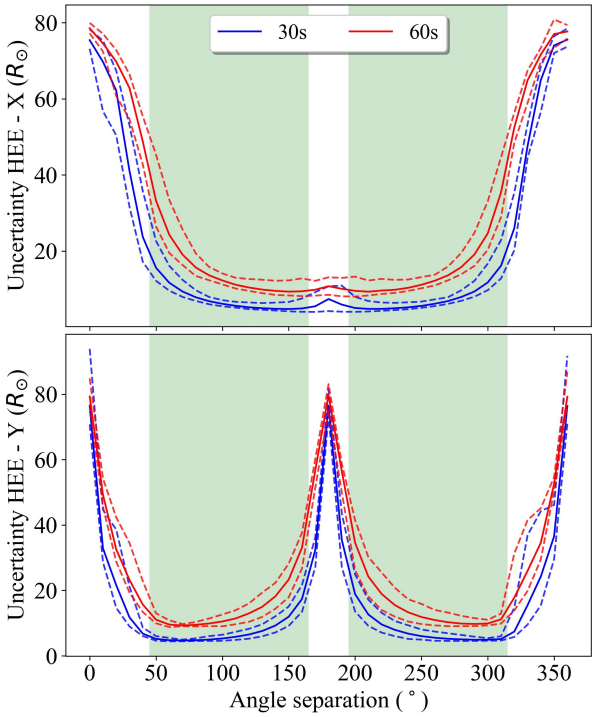


Figure 5.4: Summary of a full revolution of the simulations shown in Figure 5.3. This shows the uncertainty in the X and Y coordinates as a function of the separation between Ahead/Behind and Wind. The red and blue lines are the corresponding 60 s and 30 s cadence simulations, respectively. The solid lines represent the average uncertainty of all the sources in the simulation frame. The dashed lines show the maximum and minimum uncertainties observed. Green regions denominated as 'sweet spot' regions show the separation angles that will result in the lowest uncertainties. These simulations suggest that BELLA will have a minimal contribution to the localisation uncertainty if the angle of separation is in the range of $\pm[45°, 165°]$. Source: Cañizares et al. (2024).

where cadence is defined in the simulations as the standard deviation of the likelihood function. By recovering this known ground truth, the method was validated, and the validation allowed for testing of the effects of the instrument cadence on the performance of the multilateration. The test burst also allowed for a visual depiction of the discrepancy between the multilaterated source (shown as red and blue stars) and the ground truth counterpart (orange circles) as well as showing the difference in the X and Y uncertainties. Notice that the Figure 5.3 (d) shows that the multilaterated centroids follow the true sources with relatively accuracy despite being located in a yellow region. This is likely thanks to the large separation between Ahead/Wind and Behind/Wind, which give high confidence in the X-coordinate, and the small separation of Ahead/Behind is compensated by the sources falling

inside the virtual triangle made between all three spacecraft. It is likely that the symmetry of the configuration also works in favour of finding the true sources. However, the fact that these sources fall in a yellow area determined by the low Y-coordinate uncertainty means that this result is low confidence and if the true sources were unknown then it would be impossible to determine that this solution is relatively accurate.

Figure 5.4 shows the average uncertainties for the full test burst in solid lines, and the maximum and minimum uncertainties of the nodes are shown as dashed lines. The 'sweet spot' regions are highlighted in green and are the regions where both the X and Y uncertainties are under a user-defined threshold. Moreover, these regions served as a starting point for finding suitable candidates. The threshold in Figure 5.4 was defined as the largest of the midpoints of the decay and rise in uncertainty regions of the 60-s cadence simulation. This corresponds to the $\pm[45^\circ, 165^\circ]$ bands.

Figure 5.4 also shows that for the ideal case of nearly equidistant spacecraft, the ground truth is retrieved accurately, meaning at the expected uncertainty due to the light travel time corresponding to the cadence. However, as n number of spacecraft move closer together, they start to behave as a unique receiver. This is particularly evident for the 180° case, where the Ahead and Behind spacecraft are aligned with Wind. In this particular case, the system becomes one dimensional, and the X coordinate uncertainty remains stable as a minimum, while the Y coordinate becomes unstable, and the uncertainty becomes a maximum. The reason for this is that in a one-dimensional system, only two spacecraft are needed to multilaterate a source, and therefore the X coordinate still meets the minimum requirements for multilateration.

5.4 Observations for the validation of BELLA

To validate BELLA and test it on a real event, an individual Type III burst is examined in detail. The event chosen for this study occurred on 7 June 2012 from 19:30 UT and was observed by Wind/WAVES, STEREO A/WAVES, and STEREO B/WAVES (see Figure 5.5).

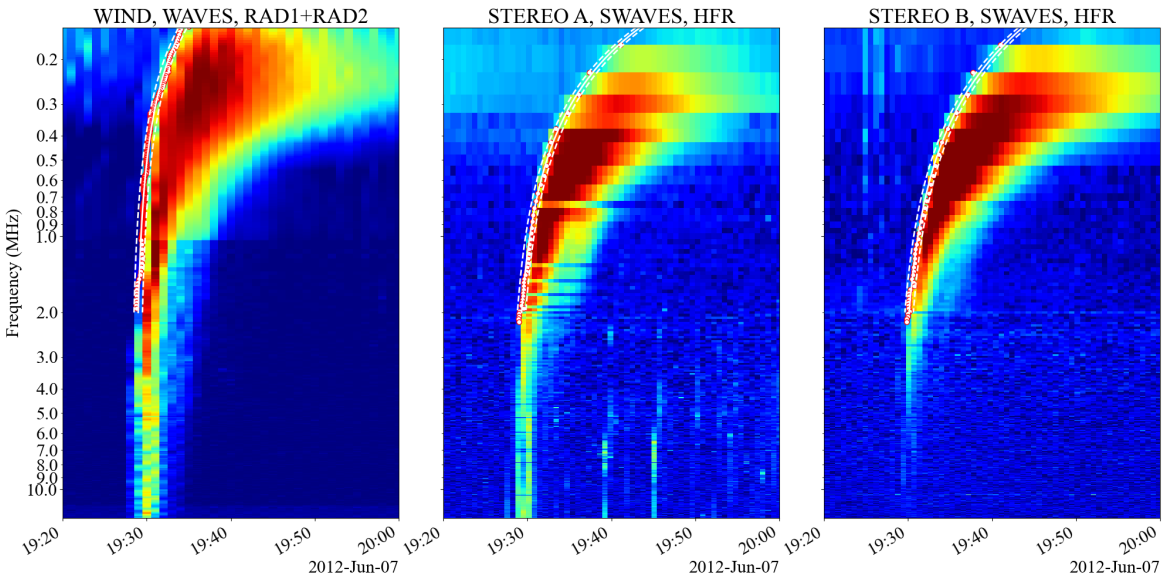


Figure 5.5: Type III radio burst observed by Wind (left), STEREO A (middle), and STEREO B (right) on 7 June 2012. The burst was an isolated event lasting approximately 20 minutes. The frequency range of the burst detected by each spacecraft was from 13 MHz to 0.1 MHz; however, STEREO B showed poor S/N at the higher frequency range, likely due to solar disk occultation. The white line represents the fit of the Type III bursts used for the multilateration in the range of 2 MHz to 0.15 MHz. Source: Cañizares et al. (2024).

During the date of the event, the coronal hole identification via a multi-thermal emission recognition algorithm (CHIMERA, Garton et al., 2018) reported a large coronal hole in the north-western quadrant of the Sun spanning $\sim 30°$, labelled as CH1 in Figure 5.6 (a). Figure 5.6 (b) shows over 10 active regions as observed by the SOLIS Vector Spectro Magnetograph (SOLIS VSM; Henney et al., 2006)) and labelled by NOAA. This makes this region a highly plausible Type III source region given the proximity of open field lines to active region loops. As will be shown, BELLA allows for a strong inference to support this hypothesis.

The Type III radio burst was observed by Wind from 0.06 to 13.825 MHz, by STEREO A from 0.15 to 16 MHz, and by STEREO B at a range similar to that of STEREO A but with signs of solar disk occultation, as the higher frequencies of the burst show a decay in brightness. This particular event was chosen for a number of reasons. The location of the spacecraft is optimal for multilateration techniques. The STEREO spacecraft are at $\pm 116°$ from the Wind spacecraft, which resulted in near-equidistant separation between all three space-

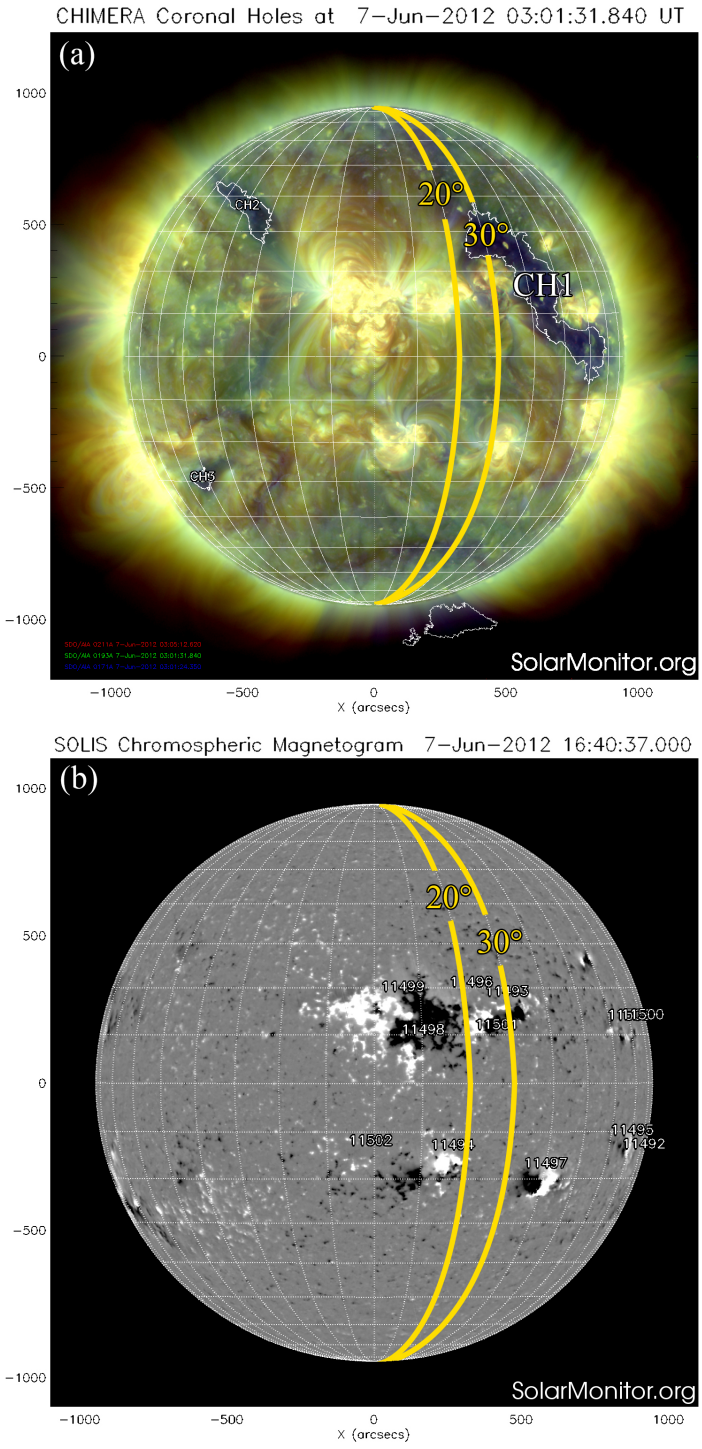


Figure 5.6: Images of the solar disk's features observed on 7 June 2012. (a) Coronal holes analysed by CHIMERA. Fast solar wind regions shown in Figure 5.11 are consistent with the location of CH1. (b) Magnetogram data from SOLIS indicate over 10 NOAA active regions, four of which are adjacent to the east of CH1. This alignment is later confirmed to be consistent with the location of the multilaterated Type III beam. Source: Cañizares et al. (2024).

craft. At this separation, Section 5.3.2 showed that the intrinsic uncertainty from BELLA is minimal and expected to be dominated by the cadence of the instrument and physical errors. Additionally, all spacecraft are at $\sim$1 au from the Sun, simplifying the system analysed. This allowed for the simplification of the simulations that led to finding this particular event.

Furthermore, the Type III radio burst is isolated. There is no other bursts or activity that could potentially cause confusion or uncertainty to the edge of the burst. The burst is bright, and the edges are well defined. The low cadence of the instruments was a limiting factor, and therefore, the burst picked for the validation of BELLA was chosen upon visual inspection to be as clean as possible and with as high S/N as it was possible.

Time stamps for the multilateration were extracted from the same frequencies following the procedure shown in Section 4.1, where the lightcurves of each spectrogram were analysed using the GH method to obtain rise times. These rise times were then fitted using the time evolution function (Equation 4.11). These fits can be observed in Figure 5.5 as white lines and show the data extracted for the multilateration. The white dashed lines represent the edges from where the PyMC sampler sampled for the time prior of the Bayesian calculation (see Section 5.2). Additionally, to assess the impact of the time evolution fitting, the rise times were also extracted as scattered data. To conserve the same number of data points and frequency channels, the data was linearly interpolated where needed.

5.5 BELLA Results

The results of BELLA are shown in Figure 5.7. Following the procedure in Section 5.3.1, the confidence map was obtained by simulating emission from every pixel in a [-250, 250] $R_\odot$ grid distributed in increments of 10 $R_\odot$ on both the X and Y coordinates. The blue regions of the background map are areas where BELLA is most confident and the yellow regions are regions where BELLA cannot position a source accurately. The large confidence region is a direct consequence of the optimal position of the spacecraft for that particular date. The spacecraft were equally spaced, and therefore a symmetrical output was expected. Simula-

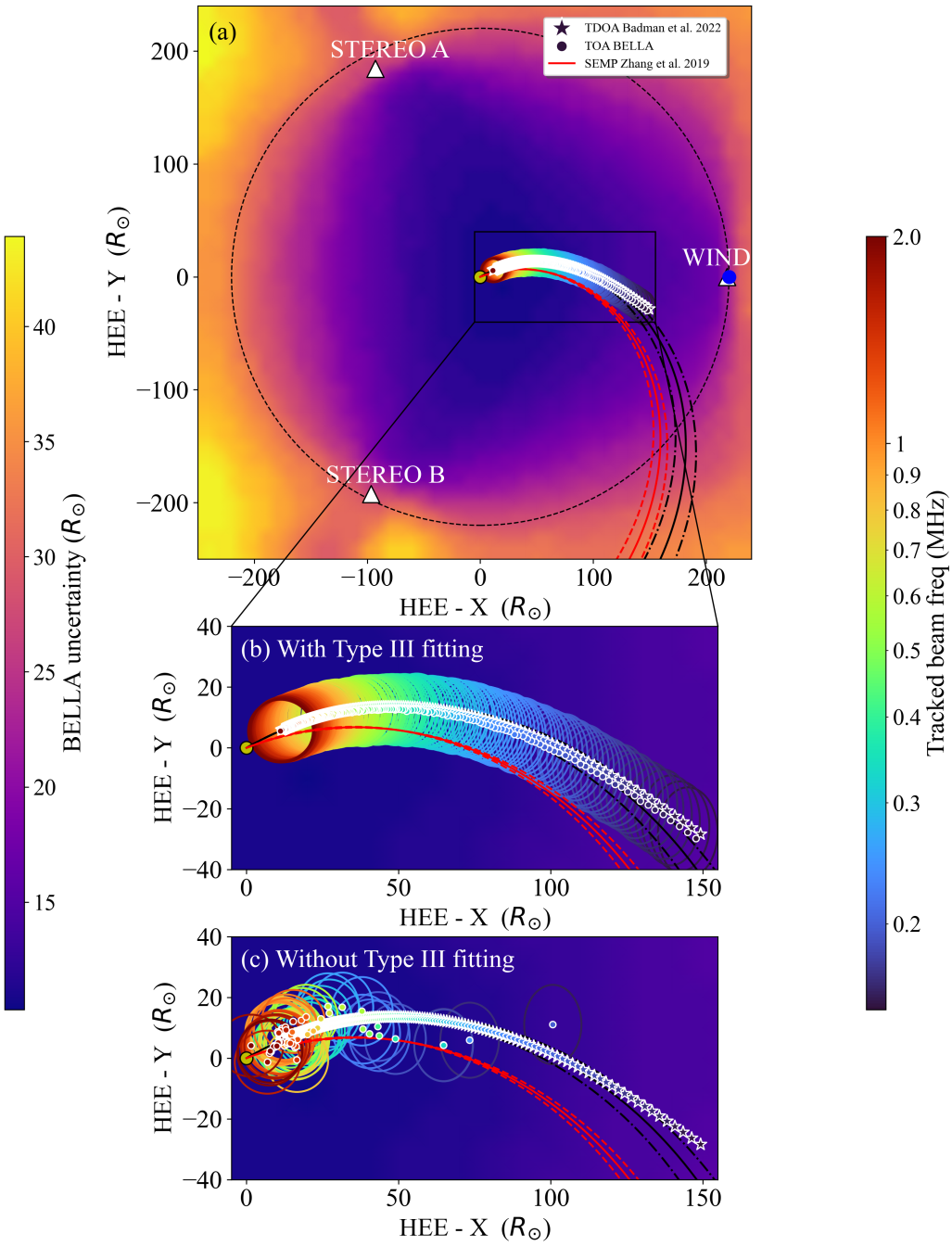


Figure 5.7: BELLA multilateration of the Type III SRB. (a) Top view of the ecliptic. (b) zoom-in of (a). (c) same zoom-in, but the multilateration was performed on the rise times extracted from the GH method without the final fit of the Type III. It was found that BELLA showed results with a confidence area of ∼15–20 $R_\odot$ in diameter. TDOA (Badman et al., 2022) and SEMP (Zhang et al., 2019) results are compared with BELLA for validation purposes. Parker Spirals show the results from fitted BELLA points (black) and SEMP (red) at 400±20km s^{-1}. The systematic differences between TDOA/BELLA ($\phi_0 \sim 30°$) and SEMP ($\phi_0 \sim 20°$), were consistent within the error bars of BELLA. Source: Adapted from Cañizares et al. (2024).

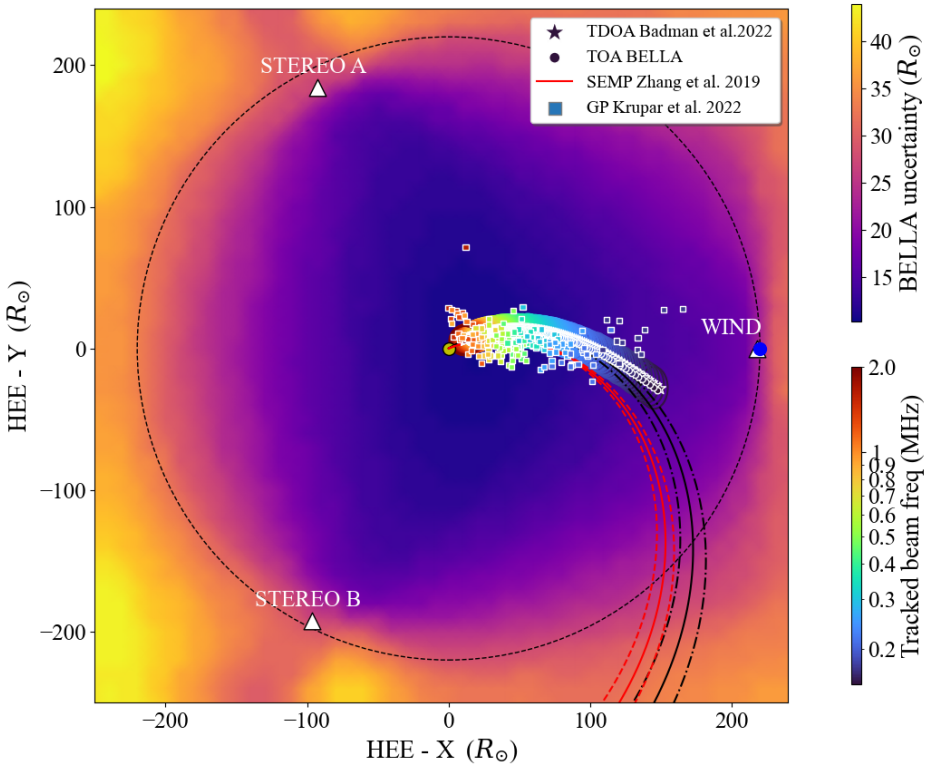


Figure 5.8: STEREO A/B L3 GP inversions (Krupar et al., 2022) overlaid on Figure 5.7 (a). The GP points show a clear trend that agrees with BELLA in both orientation and frequency distribution. The GP results have a larger spread, making the interpretation of an underlying spiral more difficult. All localisation methods are shown to be in agreement, illustrating that complementary but independent methods give approximately the same answer, further validating the BELLA methodology. Source: Cañizares et al. (2024).

tions of a similar burst with varying spacecraft positions shown in Figures. 5.3 and 5.4 show that the contribution of BELLA to the uncertainty of the measurements due to the position of the spacecraft is negligible for the position of the Ahead and Behind spacecraft during this event.

The map was generated using simulated data with a cadence of 38 s, which corresponds to a light travel time uncertainty of $\sim 15 R_\odot$. From the map, it is observed that the whole burst occurred in a region of $< 15 R_\odot$ in uncertainty. This means that BELLA has a negligible contribution to the uncertainty of the results, and any source of uncertainty is dominated by the cadence of the instruments and other (mostly physical) sources of uncertainty. This is

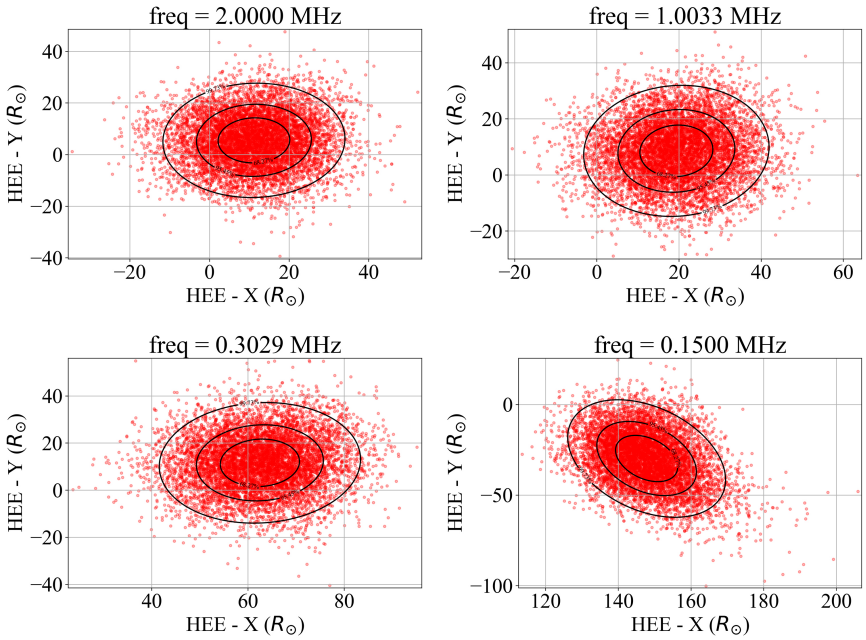


Figure 5.9: Examples of the correlations between the X-coordinate and Y-coordinate posterior distribution samples at different frequencies. The contours in the figures show the 1 σ (68%), 2 σ (95%), and 3 σ (99%) regions. The contours clearly reveal the correlations between the X and Y samples with their orientation determined by the relative spacecraft configuration around the source of the burst.

consistent with the dynamic spacecraft simulation shown in Figure 5.3.

Overlaid on this map is the BELLA output from the TOA multilateration performed on the Type III radio burst characterisation from Figure 5.5. The burst is colour-coded by the frequency of emission (see Figure 5.7 *right* colourbar). The ellipses around each of the source points are the 1σ uncertainties obtained from the BELLA posterior distributions. In order to further analyse these uncertainties, the correlations between the X and the Y coordinate posterior distributions were plotted. An example of this is shown in Figure 5.9, which shows a clear correlation between the X and Y posterior coordinate sampling. This figure also includes contours at 1 σ (68%), 2 σ (95%), and 3 σ (99%) regions where the orientation of the contours is dependent on the relative orientation of the spacecraft with respect to the source at that specific frequency.

Also overlaid on Figure 5.7 is the output from the TDOA multilateration (courtesy of Sam

Badman) using the method from Badman et al. (2022), and shown in red is the output from the Solar radio burst Electron Motion Tracker (SEMP, Zhang et al., 2019) at 400 ± 20 km s^{-1} solar wind speed. The three methods of positioning were found to be in agreement with each other within 1σ uncertainty. The TDOA method yielded results nearly identical to the TOA method used by BELLA. This is in agreement with Kaune (2012), which showed that simulations of TOA and TDOA have no discernible results in accuracy. The results indicate that if the TOA solution converges on the same solution as the analytical TDOA, producing an identical 'source beam', is likely because the signal propagation distribution of the BELLA results are close to $v = c$, which is the main assumption of analytical TDOA. Note that the line of sight of the radio waves propagation is for the most part unobstructed by the lower layers of the solar corona, which makes this burst ideal for the assumption of $v = c$. This convergence yields two possibilities: a) the effects of refraction and scattering can be neglected for this particular burst or b), in this case, BELLA has converged on an 'apparent' position of the burst shifted by propagation effects (Chen et al., 2023; Kontar et al., 2023). The effects of refraction and scattering will be discussed in Chapter 7, but as discussed later in this section, the evidence suggests that b) is more likely for this burst.

Additionally, Level 3 (L3) GP inversions from STEREO data available at Krupar et al. (2022) are shown in Figure 5.8. The GP triangulation was performed using the time of peak flux of the Type III as opposed to the leading edge because the GP inversions at the leading edge have low S/N. BELLA, on the other hand, is designed to utilise the leading edge of the Type III, making the two independent methods complementary to each other. A clear trend was observed between the results obtained by the triangulation and by the multilateration, with only a small number of points lying outside of the 1σ area of uncertainty. The agreement in orientation and frequency distribution along the spatial domain serves to validate BELLA as a suitable method of localisation.

Figure 5.7 also shows the results from SEMP, which assumed a pre-specified constant solar wind speed along the Parker Spiral. The SEMP longitude ϕ_0 parameter was found to be

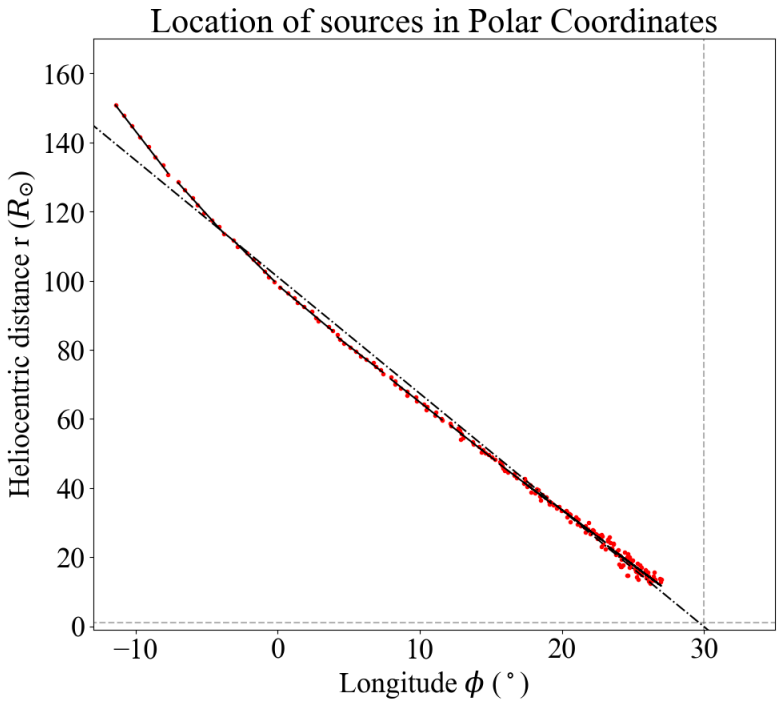


Figure 5.10: BELLA centroids in polar coordinates fitted with a Parker Spiral model. The linearised model allows to obtain an approximation of the solar wind and longitude ϕ_0 from the slope and intercept. This analysis suggests that the sources are located in a region of $v_{sw} = 400 \pm 20$ km s^{-1} and that the onset location of the beams is at $\phi_0 = 30^\circ \pm 2^\circ$. Source: Cañizares et al. (2024).

$\sim \phi_0 = 20^\circ$. A Parker Spiral, shown as a black dotted line in the figure, was also overlaid on the map. The parameters for this spiral were obtained by assuming a Parker Spiral to be an Archimedean spiral:

$$r(\phi) = \frac{v_{sw}}{\Omega_\odot}(\phi - \phi_0) + r_0, \tag{5.6}$$

where r is the distance from Sun, r_0 is the height at which the spiral starts, v_{sw} is the velocity of the solar wind, $\Omega_\odot$ is the angular velocity of the Sun, ϕ is the longitude, and ϕ_0 is the longitude at the base of the spiral.

Equation 5.6 shows that an Archimedean spiral is linear in polar coordinates. Using the slope and intercept of the linearised sources, as shown in Figure 5.10, leads to the derivation of the solar wind speed and longitude as $v_{sw} = 400 \pm 20$ km s^{-1} and $\phi_0 = 30^\circ \pm 2^\circ$. This implies that there was only a discrepancy of $\sim 10^\circ$ between the two methods. Comparing these results with Figure 5.6, a number of active regions in the 20° to 30° longitude are ob-

served. This suggests that these ARs are the source of the emission. Despite this uncertainty, both methods still suggest the coronal hole and active region boundary as the likely Type III source region. Closed active region loops may have access to neighbouring open field lines in order to give injected electron beams access to the solar wind. Figure 5.7 (c) also shows the results of performing the Bayesian multilateration of the Type III SRB data obtained using the GH algorithm but without the time evolution fit (Equation 4.11). The difference between Figures. 5.7 (b) and (c) show that the fitting of Equation 4.11 as a time evolution function to the Type III SRBs is responsible for the smooth Parker Spiral seen in Figure 5.7. This is consistent with the literature that shows that Type III exciters follow a Parker Spiral (Reiner et al., 1998; Reiner et al., 2009), and therefore Equation 4.11 is presented as a characterisation of the leading edge of a Type III SRB.

To further verify the plausibility of the inferred trajectory in the context of a realistic solar wind, Figure 5.11 shows the BELLA multilateration results overlaid on a solar wind model (courtesy of Mathew Owens) from the Heliospheric Upwind Extrapolation with time dependence (HUXt; Owens et al., 2020; Barnard & Owens, 2022). This model solution was obtained by assimilating the in situ solar wind speeds observed by ACE, STEREO A, and STEREO B to provide a data-constrained solution to the solar wind structure (Lang et al., 2021; Lang & Owens, 2019). This data assimilation was performed over a 27-day window centred on the time of the Type III burst.

The Parker Spiral obtained from the BELLA multilateration showed agreement with the HUXt output, suggesting that the electron beam of the emission follows a Parker Spiral with a solar wind velocity of 480 km s^{-1}. The HUXt output shows a region of fast solar wind caused by the coronal hole CH1 shown in Figure 5.6. This is consistent with the location of the cluster of active regions in Figure 5.6 (b), which is adjacent to the eastern region of the CH1 coronal hole region. This further suggests the interface between these active regions and the coronal hole are the origin of the electron beam. The discrepancy between the 480 km s^{-1}

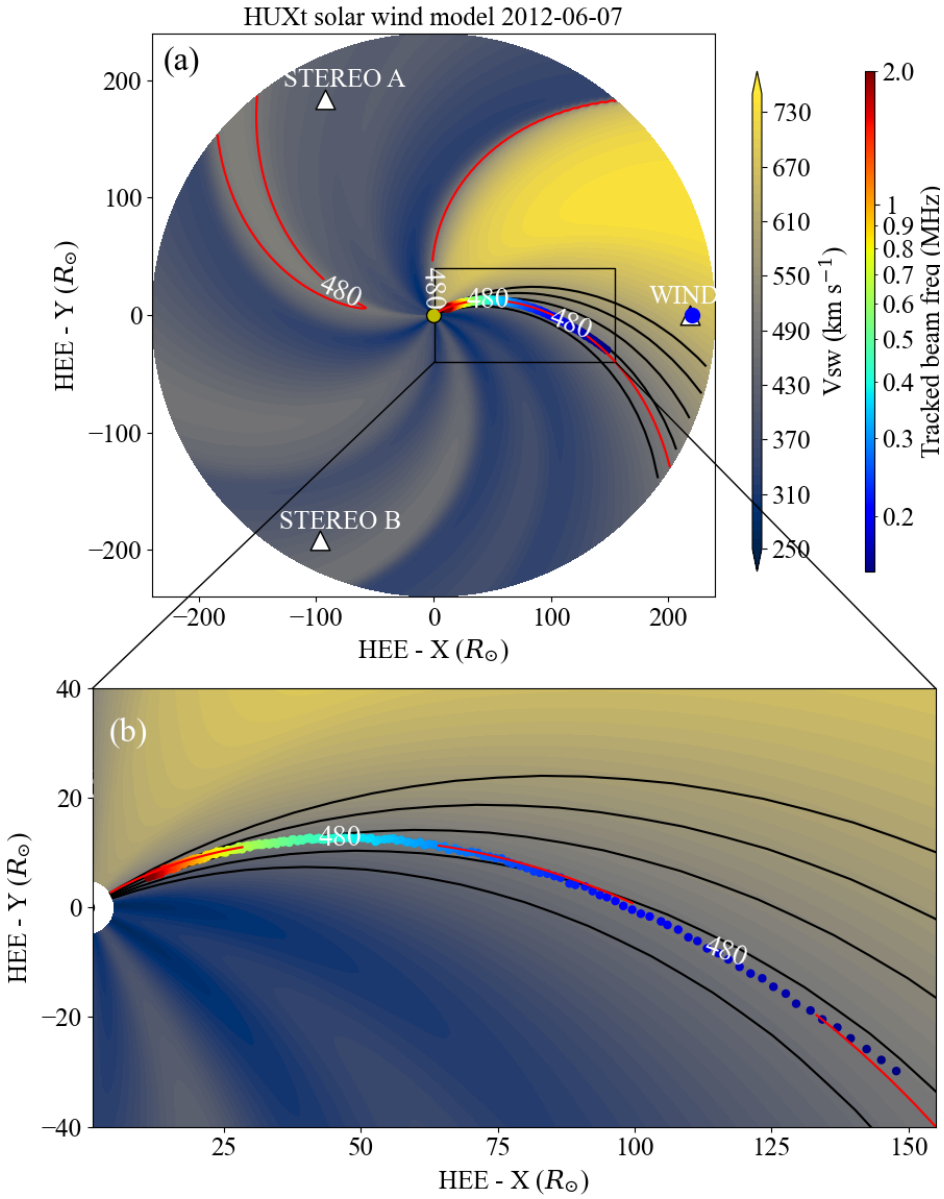


Figure 5.11: (a) Bird's eye view of the ecliptic showing the multilaterated BELLA centroids overlaid on the HUXt model. (b) A zoomed-in view highlighting the region of interest. The HUXt model identifies a fast solar wind region ($v_{sw} > 700$ km s^{-1}) in the +/+ quadrant, attributed to the coronal hole CH1 (see Figure 5.6 (a)). East of this high-speed region lies the multilaterated SRB path. The SRB sources follow the (red) 480 km s^{-1} field line with precision despite BELLA and HUXt being independent methods. The source locations relative to the high-speed solar wind region are consistent with a cluster of active regions visible in Figure 5.6 (b). Source: Cañizares et al. (2024).

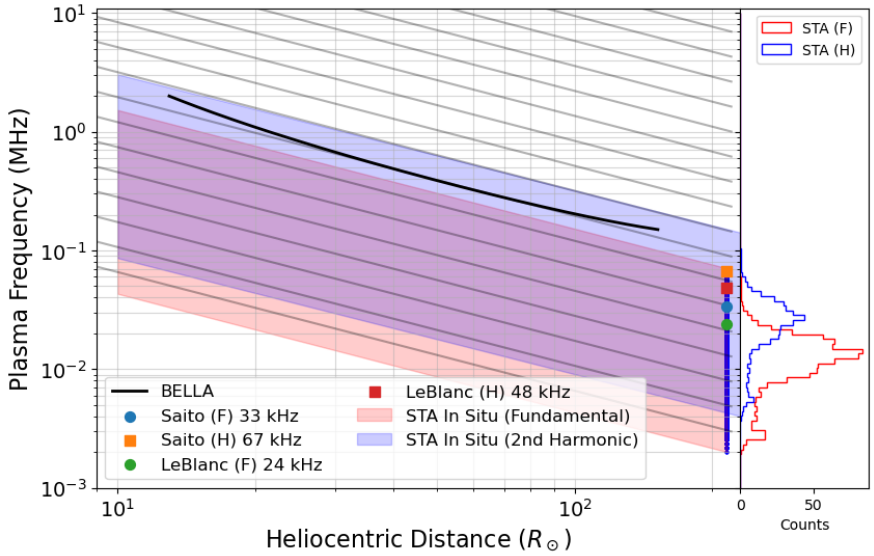


Figure 5.12: Plasma frequency as a function of heliocentric distance measured using BELLA's multilateration of the Type III SRB. These measurements were compared to a $1/R^2$ projection of in situ electron density data from STEREO A, presented in histogram form. Additionally, the harmonic and fundamental values from the Saito and LeBlanc density models at 1 au are included. BELLA's electron density readings are higher than those predicted by these models. The highest outliers of harmonic emissions from STEREO A in situ data align with BELLA's multilaterated sources. Scattering may explain these unexpectedly high electron densities. Source: Cañizares et al. (2024).

suggested by HUXt and the 400 ± 20 km s^{-1} result obtained by BELLA is attributed to the different assumptions and initial conditions made by the HUXt model compared to BELLA. HUXt is a one dimensional model that assumes that the solar wind moves radially outwards. The input parameter for the velocity of the solar wind comes from coronal models such as Wang-Sheeley-Arge (WSA; Arge & Pizzo, 2000) which will contribute to some degree of discrepancy if compared with BELLA.

Lastly, Figure 5.12 shows the results from plotting the radial distance from the Sun obtained from the BELLA posterior distributions with respect to the frequency of the emission. These frequencies are compared with the plasma frequencies obtained from density models Saito et al. (1977) and Leblanc et al. (1998) at 1 au and a $1/R^2$ fundamental and harmonic projection of STEREO A in situ electron density data. The slope of the BELLA electron density was observed to follow an expected $1/R^2$ trend. However, the densities obtained by BELLA compared to the different density models were seen to be significantly larger than expected

for either the fundamental or harmonic emission extrapolated inwards from the 1 au density measurements and from the typical density models. The STEREO A in situ data, which were collected over a Carrington rotation period (28 days) and centred on the time of the burst, could show that the observed source locations are consistent with harmonic radiation along a path at the upper end of the distribution of 1 au measured densities for this interval, but this would require the trajectory to lie along a 'much more dense than usual' region, which is statistically unlikely given that studies such as Steinberg et al. (1984) have suggested the opposite. This is, however, consistent with Chen et al. (2023) and Kontar et al. (2023), which state that radio wave scattering has an effect on the apparent position of SRB exciters, making them appear to be further than their true position. This would imply that the distribution of the speed of propagation v converging at $v = c$ is symptomatic of Type III SRB multilateration being susceptible to converging on the apparent location of the source as lensed by scattering effects. Chapter 7 will address this and explore the effects of scattering on the localisation of sources using BELLA.

5.6 Conclusion

This chapter presented the work published in Cañizares et al. (2024) known as BELLA. This novel method of localisation combines Bayesian statistics with TOA multilateration to analyse the localisation of Type III sources with an innate ability to quantify the uncertainties and distinguish between innate and instrumental uncertainties.

BELLA was first validated through simulations demonstrating its capability to recover ground truth locations with better or worse performance depending on the spacecraft configuration. BELLA was also tested on a real event, observed by Wind and the STEREO pair and showing strong agreement with TDOA, GP, and SEMP methods, as well as the HUXt solar wind model.

A Parker Spiral analysis revealed that the onset location of the beam was consistent with coronal hole and active region observations. Comparison with the HUXt model showed

BELLA's results conserve the morphology of the Parker Spiral but showed a non-trivial discrepancy on the suggested solar wind speeds. It was also shown that BELLA's derived electron densities indicated higher than expected altitudes, consistent with other studies, possibly due to scattering effects.

Overall, BELLA is a robust and powerful open-source tool designed for detailed multilateration analysis of Type III SRB, currently operating in 2D with planned 3D capabilities (see Chapter 9).

6 SURROUND: A constellation of CubeSats around the Sun

6.1 Introduction

On 3 February 2022, a minor geomagnetic storm caused the destruction of around 40 SpaceX Starlink spacecraft as a result of increased atmospheric drag (Kataoka et al., 2022). This event showed the significant impact, that even minor SW events can have. As technology advances and space exploration moves further away from Earth, missions such as ESA Heracles (Hiesinger et al., 2019), NASA Artemis (Smith et al., 2020), and SpaceX Interplanetary Transport System (Palmer, 2021), will require accurate SW monitoring and forecasting.

The main challenges of SW science are predicting events, assessing their impact on Earth, and determining potential damage to infrastructure. This has been acknowledged by some governments which now recognise extreme SW as a significant risk[1].

There are several space-based and ground-based forecasting centres (e.g., see NOAA[2]), but have limited observational capabilities within the heliosphere which make accurate predictions a challenging task. Furthermore, due to the elevated costs of a SW monitoring mission, the fleet of monitoring spacecraft are typically old, outdated scientific missions that are close to their end-life (e.g., SOHO[3]).

[1] e.g., The UK government included 'severe space weather' as a risk in their 2020 Risk Register
[2] National Oceanic and Atmospheric Administration: `https://www.noaa.gov/spacecraft`
[3] Solar and Heliospheric Observatory

Certain SW phenomena, like SEPs, are detectable through in situ measurements and radio spectrometry, specifically Type II bursts associated with CMEs and Type III bursts associated with SEPs. These are crucial for monitoring SW and improving forecasting systems. However, despite the effort of various SW organisations, each mission depends on the other for an accurate assessment of hazardous solar events, needing constant planning and additional data processing for compatibility.

Here, is shown my work on the SURROUND mission (see Figure 6.1), an alternative standalone mission which will monitor hazardous SW events using low-cost spacecraft. This mission concept, will focus on the radio bursts associated with two of the more hazardous SW phenomena: CMEs and SEPs. This Chapter will focus on the scientific requirements of SURROUND, using simulations that I developed in Weigt & Cañizares et al. (2023) and Macario-Rojas, A. et al., (in review). These publications are part of a more extensive ESA report, which include more details about the Engineering such as the spacecraft design and orbital mechanics. In this Chapter, Section 6.2 will discuss the mission concept, Section 6.3 will address the SURROUND use cases that will lead to the mission requirements, and Section 6.4 will focus on the measurement requirements of a mission of this nature.

6.2 The SURROUND Mission Concept

SURROUND is a conceptual spacecraft mission funded by ESA, that I initially designed and submitted as a proposal to The Open Space Innovation Platform (OSIP)[4]. It has since become a much larger collaboration between the Solar group at the Dublin Institute for Advanced Studies (DIAS) and the engineering department at the University of Manchester. The mission is, at the time of writing, in Phase 0 of the ESA lifetime cycle[5]. The initial mission concept consists primarily of a constellation of six CubeSats located at strategic vantage points (see Figure 6.2) and equipped with radio spectrometers. These radio spectrometers are used for

[4] https://ideas.esa.int/servlet/hype/IMT?userAction=Browse&templateName=&documentId=e43950bfe409269aa915e782cb928711

[5] https://www.esa.int/Science_Exploration/Space_Science/Building_and_testing_spacecraft

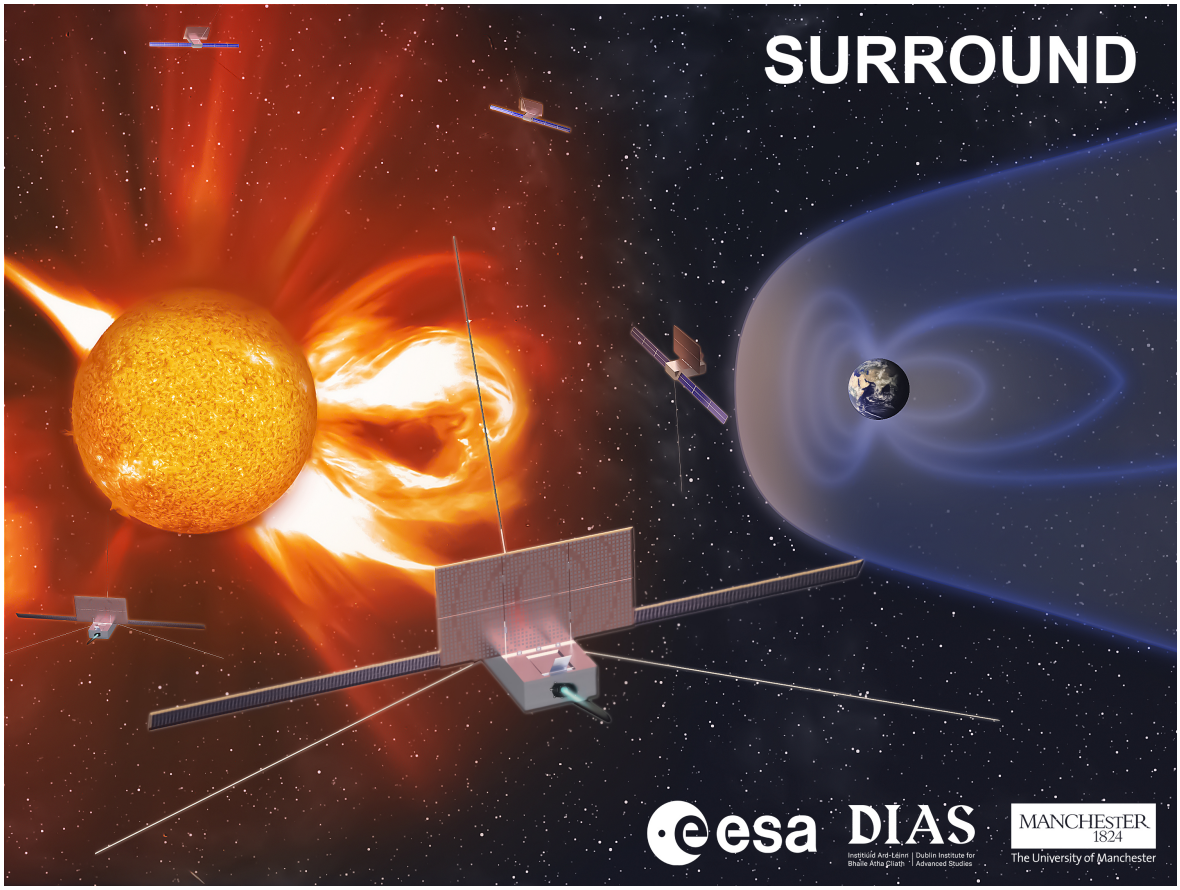


Figure 6.1: Artist's impression of the SURROUND mission. The SURROUND mission is a conceptual mission, currently at Phase-0, designed to monitor dangerous space weather events. If launched, the mission will use a number of CubeSats placed at strategic points around the inner heliosphere at 1 au for accurate tracking of CMEs and SEPs. Image adapted from ESA/A. Baker.

the detection of Type II and Type III SRBs associated with potentially dangerous CMEs and SEPs, respectively. The strategic vantage points of each SURROUND spacecraft are designed to track SRB sources and localise their position in 3D using multilateration (see Chapter 5) in combination with triangulation (see Section 1.5).

The aim is to track the burst exciters from close to the Sun at $\sim 2\ R_{\odot}$ to Earth like distances or $\sim 215\ R_{\odot}$. Figure 6.3, shows the Parker (Parker, 1958), Saito (Saito et al., 1977) and Leblanc (Leblanc et al., 1998) electron density models, which are theoretical, empirical, and observational density models used for the study of inner interplanetary plasma emission. This implies that in order to track SRBs from the desired coronal heights, SURROUND shall be capable of monitoring frequencies from 25 MHz down to 0.02 MHz.

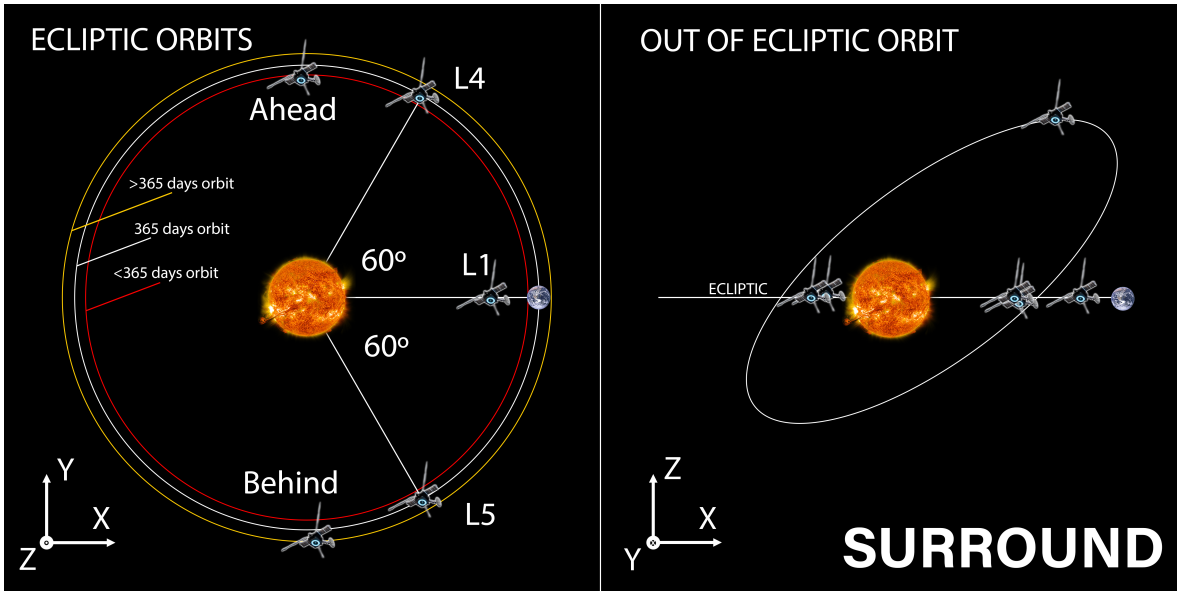


Figure 6.2: The proposed configuration of the SURROUND mission, composed of 6 CubeSats. The backbone of the mission consists of three Lagrange spacecraft located at L1, L4, and L5; these will remain static relative to the Sun-Earth line. An additional two spacecraft will orbit ahead and behind the Earth with synchronous drifts to allow much more accurate tracking. The final spacecraft would be located out of the ecliptic plane in order to allow for 3D tracking of SW activity.

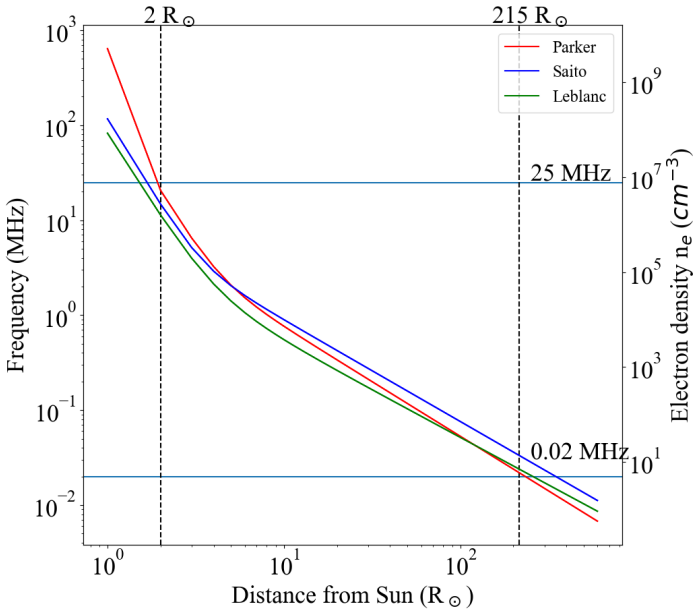


Figure 6.3: Parker, Saito, and Leblanc electron density models showing plasma emission at given heights. SURROUND's frequency range is determined by the desired monitoring range from 2 $R_\odot$ to 215 $R_\odot$ (or 1 au). This corresponds to a frequency range of 25 MHz to 0.02 MHz.

Chapter 5 showed that in order to achieve accurate tracking capabilities, SURROUND's spacecraft shall be located at positions of great angular separation. Additionally, SURROUND as a monitoring facility, shall be located in a stable configuration relative to Earth. The high level concept of SURROUND addresses these requirements by placing three spacecraft in the L1, L4 and L5 Lagrange points. The location of these three points is approximately 1 au and with $\sim 60^{\circ}$angular separation between each *L*4/*L*5 spacecraft and *L*1. This relatively static configuration, with respect to the Sun-Earth line, would allow SURROUND to consistently monitor Earth directed SW events.

The following two spacecraft known as *"Ahead"* and *"Behind"* will orbit the Sun in a similar manner as the STEREO mission. With the *Ahead* spacecraft orbiting a lower than Earth orbit, and the *Behind* spacecraft orbiting a higher than Earth orbit. The two orbits must be precisely calculated so that they both drift synchronously. The purpose of these two spacecraft is to provide support to the main three Lagrange spacecraft, specially when the spacecraft are located in the 'sweet spot´ regions (see Figure 5.4). The hypothesis that led to the inclusion of these two spacecraft is that with their support, the uncertainties associated with detecting the Type IIIs will be minimised, thus allowing for accurate and precise SW monitoring. This hypothesis will be investigated in this chapter via the usage of simulations.

The sixth spacecraft is known as the "Out-of-ecliptic" spacecraft which, for the purposes of this work, it will be referred to as SC6. As the "Out-of-ecliptic" name suggests, SC6 will be located outside of the ecliptic, in a highly elliptical orbit with its aphelion located Earthwards. The purpose of SC6 is to better constrain the localisation of the SRB exciters and allow for 3D reconstruction of their path.

Once the SURROUND spacecraft are positioned at their corresponding locations, each individual spacecraft would use radio spectrometers tuned to detect SRBs. This allows the use of GP and multilateration as localisation techniques (see Section 1.5 and Section 4.2). These two complementary methods will serve to localise and track potentially harmful CMEs or SEPs.

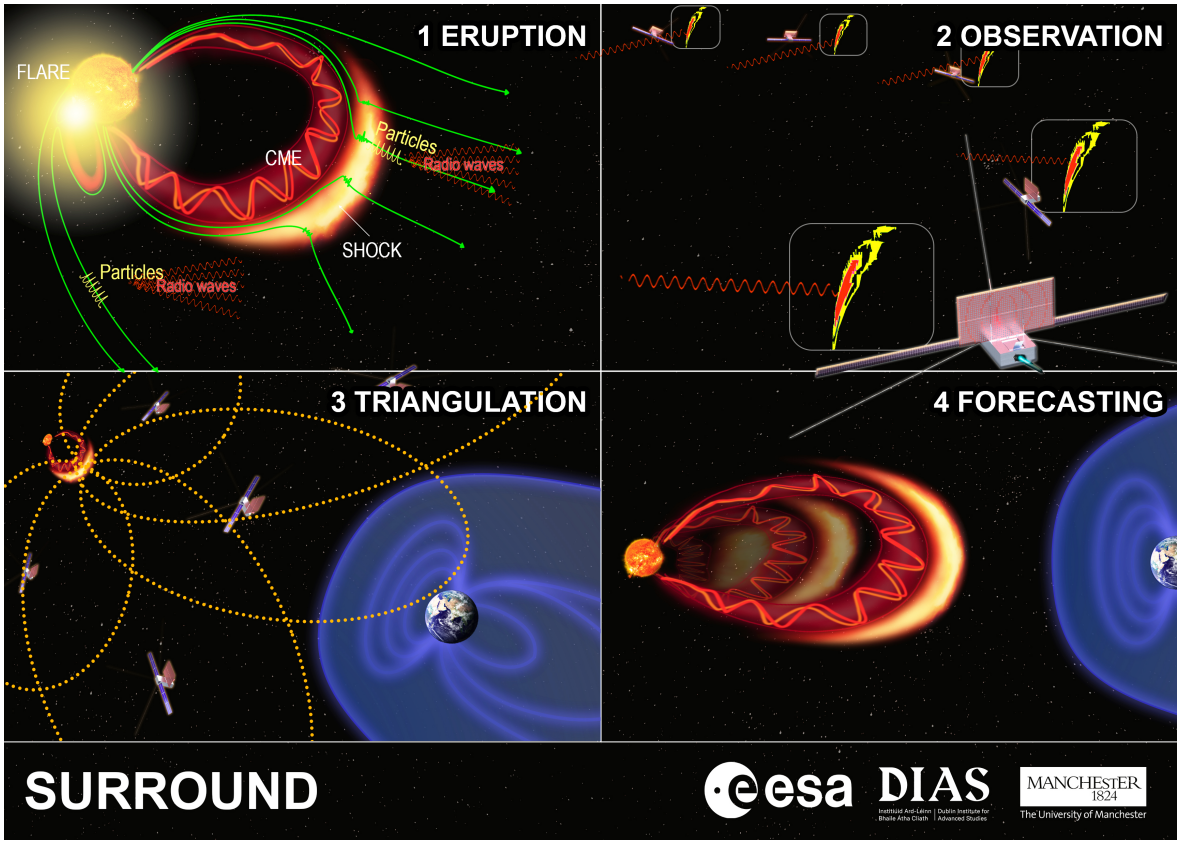


Figure 6.4: Conceptual design of the SURROUND mission. (1) An event such as a CME occurs, causing radio bursts. (2) SURROUND spacecraft detect the radio signatures. (3) Using the spacecraft data, the location of the event is triangulated/multilaterated. (4) The arrival time of the CME at Earth is forecasted.

6.3 Mission Requirements

The aim of the SURROUND mission requirements is to define a series of scenarios in which the mission must perform adequately, meeting certain established criteria. These requirements are designed to ensure the mission fulfils its intended objectives (see Figure 6.4), which are summarised as the following mission statement:

> "The SURROUND mission will detect, localise and track solar radio bursts in 3D using a constellation of radio spectrometers and to forecast the arrival of the radio bursts drivers at Earth or Earth like distances"

The primary use case of the SURROUND mission is the detection, tracking, and localisation of SRBs, enabling SURROUND to forecast the arrival of these events at the Earth. Further-

more, despite this being a solar monitoring mission, the scientific usage of the SURROUND data would offer great value to the solar and planetary science community. Researchers can utilise SURROUND's data to develop accurate models of solar emissions and effects, integrating data from other probes to refine these models and improve predictive capabilities for SW events. This will be explored in Chapter 7, which will serve as an example of what a mission like this could offer to the scientific community.

6.3.1 Mission Use Cases

In this section, a series of use cases will be presented to establish the scenarios for which the SURROUND mission is designed. Some scenarios may appear trivial, while others might seem impossible at the time of writing. The trivial scenarios are included to serve as a foundational basis for the mission. Conversely, scenarios that may seem unrealistic given current technological capabilities are also considered, as this is a concept mission aimed at pushing the boundaries of what is technologically possible. In essence, this phase sets the course for developing the technology required to meet the final mission requirements.

6.3.2 Use Case 1 - Detect and Track Type II radio bursts

Fast CMEs create shocks that perturb the magnetic field at the CME's forefront, where particles moving along these magnetic field lines emit radio waves at the plasma frequency (see Chapter 2). This emission leads to various morphologies, ranging from the infrequently seen narrow band noted in Vasanth et al. (2014) and observed by Hiraiso Solar Observatory (HiRAS), to the more commonly observed broader band Type II like the one seen by LOFAR and analysed by Maguire et al. (2021). By tracking the radio burst effectively, it is assumed that the driver is being tracked, which in this case is the CME.

Shock driven CMEs can travel at speeds of $1500\,\mathrm{km\,s^{-1}}$ and up to $3500\,\mathrm{km\,s^{-1}}$(Gopalswamy et al., 2009; Lamy et al., 2019). This means that a fast moving CME will arrive to Earth in around 12 h to 24 h, during which the radio bursts must be sampled multiple times.

CMEs generally form in the lower regions of the solar corona, thus their corresponding Type II radio bursts are found within the 10 MHz to 200 MHz frequency range. Because of this frequency range, it is relatively uncommon to detect Type IIs with space-based spectrometers, however GP studies, such as Jebaraj et al. (2020), demonstrate that direction-finding techniques have been previously employed to successfully triangulate a Type II radio burst. Additionally, SURROUND's proposed 25 MHz to 0.02 MHz covers a higher frequency range than the typical radio spectrometers on board solar dedicated missions. This will allow increase the frequency of observed Type IIs. It should also be considered that a higher spectrometer frequency range would be ideal for the detection of all Type IIs. This topic will be further examined in Section 6.3.4 - Use Case 3.

6.3.3 Use Case 2 - Detect and Track Type III radio bursts

Due to their prolific nature, Type III radio bursts have been key to understanding a series of physical processes occurring in the solar corona including, but not limited to, the warning of one of the most hazardous phenomenon to spacecraft, and modern infrastructure, SEP events. These radio bursts and the exciter of the emissions can be tracked from low corona out into the inner heliosphere (e.g., Badman et al., 2022; Cañizares et al., 2024). For the case of Type III SRBs, the driver is likely accelerated electrons from solar flaring.

Detecting Type IIIs is fully compatible with the detection of Type IIs, and therefore does not add any additional complexity to a radio spectrometer. In fact, Type IIIs are observed across broad frequency ranges and would be entirely visible within the proposed 25 MHz to 0.02 MHz range. However, the characteristic fast drift rate of Type IIIs makes them difficult to resolve without high cadence spectrometers. As discussed in Section 3, modern missions such as PSP and SolO are capable of measuring the radio spectrum at cadences of less than 10 s, which should mitigate this issue. Nonetheless, a compromise with the downlink budget might be necessary. This will be further explored later in this chapter and in Chapter 7, highlighting it as an important consideration.

6.3.4 Use Case 3 - Localise Type II radio burst exciters in 3D

Having successfully detected the Type II, the SURROUND mission must collect data from different spacecraft to localise the source of the emission in 3D. Localising Type IIs was demonstrated by Jebaraj et al. (2020), who used data from STEREO/WAVES and Wind/WAVES to triangulate a Type II radio burst associated with a CME. The results showed that, despite the benefit of GP only requiring two spacecraft for the localisation procedure, the positions of the two spacecraft are crucial for accurately localising the radio emission.

In their study, STEREO A and B were located approximately 130 ° from Wind; however, the two alone were incapable of producing a stable solution, making the GP procedure impossible without Wind. In reality, GP produced two different solutions, one for the Wind/STEREO A pair and another for the Wind/STEREO B pair. Multilateration, on the other hand, would have been the ideal method for this spacecraft configuration as it utilises all spacecraft simultaneously. Unfortunately, the complex morphology of Type IIs makes multilateration a challenging task, and as a consequence, it has never been performed before.

The loss of STEREO B, the solar minimum, and the lack of other operational spacecraft have all contributed to the need to look back to 2012 for a suitable candidate for Type II radio burst multilateration. However, with the new fleet of modern scientific spacecraft such as PSP and Solar Orbiter (SolO), and as we continue into the peak of Solar Maximum 25, it is only a matter of time before a suitable candidate for this type of study is found. This will be addressed in Chapter 9

6.3.5 Use Case 4 - Localise Type III radio bursts exciters in 3D

As it was shown in Chapter 5, the shape of Type IIIs makes the localisation of the radio sources a simpler procedure than the localisation of Type II drivers. There are multiple examples of the localisation of Type IIIs using spacecraft (e.g., Zhang et al., 2019; Badman et al., 2022; Chen et al., 2023; Cañizares et al., 2024) and therefore, the proposed SURROUND constellation should enable for a relatively low uncertainty localisation of Type III

sources.

6.3.6 Use Case 5 - Nowcast CME associated with Type IIs

CMEs can cause significant harm to spacecraft; however, they travel at a comparatively slower speeds than other SW events (Lamy et al., 2019), providing ample time to implement the required precautions before the harmful particle radiation reaches the spacecraft. By nowcasting the onset of a Type II radio burst, one can monitor and evaluate the intensity of the CMEs, including the shock front's velocity, its magnitude, and, using triangulation, its trajectory.

6.3.7 Use Case 6 - Nowcast SEP electrons associated with Type IIIs

Electrons travel along magnetic field lines at quasi-relativistic speeds of approximately 0.3 c, making the prediction of these particles after a Type III radio burst detection impractical. Thankfully, electrons are less harmful than the heavier protons (SEPs) (Malandraki & Crosby, 2018) that follow, which are observed to travel at significantly slower speeds of about 0.1 c (Simnett, 2017). Additionally, radio instruments can nowcast electrons through the detection of Langmuir waves. Consequently, nowcasting electrons at the $L1$ spacecraft indicates that SEPs might be targeting Earth and can serve as the final trigger for issuing warnings of hazardous SEPs (Klein & Posner, 2005).

6.3.8 Use Case 7 - Forecast arrival of a CME at Earth using Type II radio burst

By analysing the Type II localisations, the arrival time of the CME can be forecasted. Ravishankar & Michałek (2019) demonstrates that CME events with $V > 1000\,\mathrm{km\,s^{-1}}$ have transit times of 40-60 hours. They also note that due to drag effects, CMEs typically decelerate until their speed matches that of the solar wind ($\sim 300\,\mathrm{km\,s^{-1}}$ to $400\,\mathrm{km\,s^{-1}}$), after which the CME velocity remains constant. SURROUND can be employed to track the position of

the CME shock front over time, providing insights into its velocity and acceleration. This information would allow to estimate when the CME reaches its terminal velocity, facilitating the calculation of an accurate arrival time prediction from that point onward.

6.3.9 Use Case 8 - Forecast the potential arrival of SEP protons associated with Type IIIs

Type III SRBs are associated with both electrons and heavier particles such as protons (i.e., SEPs; e.g., MacDowall et al., 2003; Kalaivani et al., 2021). Flares accelerate both protons and electrons but, due to their larger masses, protons and other heavier particles are accelerated to lower velocities. These lower velocities lead to larger Sun-Earth transit times. While the heavier particles do not emit radio emissions, they are strongly correlated with the radio-emitting electrons. Cane et al. (2002) examined several solar proton events with energies greater than 20 MeV and showed that almost all of these events were preceded by prolonged Type III bursts. Each proton event was associated with a preceding CME and, for events originating near the solar limb, by flaring signatures such as peaks in the solar soft X-ray spectrum. They found that an early warning of an SEP event was the onset of Type III storms occurring 5 min to 10 min after the related flaring signatures. This suggests that a soft X-ray detector on the $L1$ spacecraft could be highly advantageous. An increase in soft X-ray intensity, followed by a Type III storm, could serve as an early warning mechanism for SEPs. Implementing this system would significantly enhance the mission's capabilities in forecasting SEP events. SURROUND would use the detection of Type IIIs to forecast the potential arrival, due to the lack of direct observations, of SEP proton events at the Earth.

6.3.10 Use Case 9 - Scientific Analysis

As it will be shown in Chapter 7, the data from a multi-spacecraft mission equipped with high cadence radio spectrometers and located in well-spaced vantage points would be of particular interest for scientific purposes. The ability to use SRBs to probe the plasma of the

solar corona and interplanetary media makes this mission ideal for the study among other things, of radio wave propagation effects, plasma waves and turbulence, or shock waves caused by CMEs. Furthermore, the addition of SURROUND to the fleet of solar dedicated spacecraft (see Chapter 3) will result in a significant improvement of the localisation of radio sources and determining their properties to a high degree of accuracy.

6.4 Measurement Requirements

The Use Cases established the framework within which SURROUND will operate, thereby defining the mission requirements. To meet these mission requirements, a series of measurement requirements must be fulfilled. These measurement requirements will dictate the payload instrument specifications, which are crucial for the spacecraft system design and mission analysis (see for details; Crisp et al., 2023). The primary requirements for conducting the science and multilateration techniques necessary to track Type II and Type III SRBs are outlined below.

6.4.1 Frequency range

As shown in Figure 6.3, the current density models (Leblanc et al., 1998; Saito et al., 1977; Parker, 1958) suggest that tracking bursts from $2\,R_{\odot}$ to $215\,R_{\odot}$ equates to a frequency range of 0.02 MHz to 25 MHz. As a starting point, a budget-friendly mission like SURROUND would require taking off-the-shelve components or re-purposing radio spectrometer designs from modern missions. Chapter 3 showed that the RFS receiver in PSP/FIELDS operates at a frequency range of 10 kHz to 19.2 MHz and the TNR-HFR receiver in SolO/RPW operates in the 4 kHz to 16.4 MHz which would imply that the SURROUND spectrometer would have to have a wider frequency range than the latest solar missions. To do this, and taking these two instruments as a comparison, some modifications would have to be made. Increasing the frequency range implies that the antennas would need to be capable of receiving signals up to 25 MHz, and therefore this increase in frequency might imply re-designing of current

radio spectrometer antennas. The higher frequency range would also suppose that any filters, such as bandpass filters would have to be re-designed to meet the 25 MHz requirement. The Analog-to-Digital Converter (ADC) must have a sampling rate high enough to accurately digitise signals up to 25 MHz. Furthermore, according to the Nyquist theorem, this would require a minimum sampling rate of 50 MHz, and higher rates would be preferred to allow for oversampling and better signal processing. Finally, the ADC should have sufficient resolution and dynamic range to handle the increased bandwidth without introducing significant quantisation noise or distortion.

6.4.2 Time resolution

Figure 4.3 in Section 4.2 presented a cartoon illustration of the multilateration method, showing how the time cadence of an instrument directly impacts positional uncertainty. Chapter 5 supported this hypothesis through simulations conducted at 60 s and 30 s cadences. This section aims to further test this hypothesis by conducting a comprehensive analysis of the cadences that SURROUND might utilise. The analysis was carried out using simulations in a strictly controlled environment with known variables, such as source positions and propagation speeds, while making physical assumptions, including the absence of scattering effects, refraction effects, source size, or propagation of exciters. Additionally, these simulations justify the necessity of having more than three spacecraft and may suggest that descope configurations, such as four spacecraft, would be acceptable to meet mission requirements. For simplicity, the simulations were confined to the ecliptic plane, and therefore SC6 was not taken into consideration, this decision will be further addressed later.

Figure 6.5 (a) shows the positional uncertainties for the proposed 5-spacecraft configuration at 120 °, along with two other configurations, 4-spacecraft also at 120 ° (Figure 6.5 (b)) and 3-spacecraft (Lagrange only, Figure 6.5 (c)). On the left column, a bird's eye view of the ecliptic shows the spacecraft configuration as well as, the ground truth sources (orange dots) and in different coloured ellipses, the different cadences. The right column, shows the positional uncertainties in X and Y coordinates as a function of distance from the Sun. This

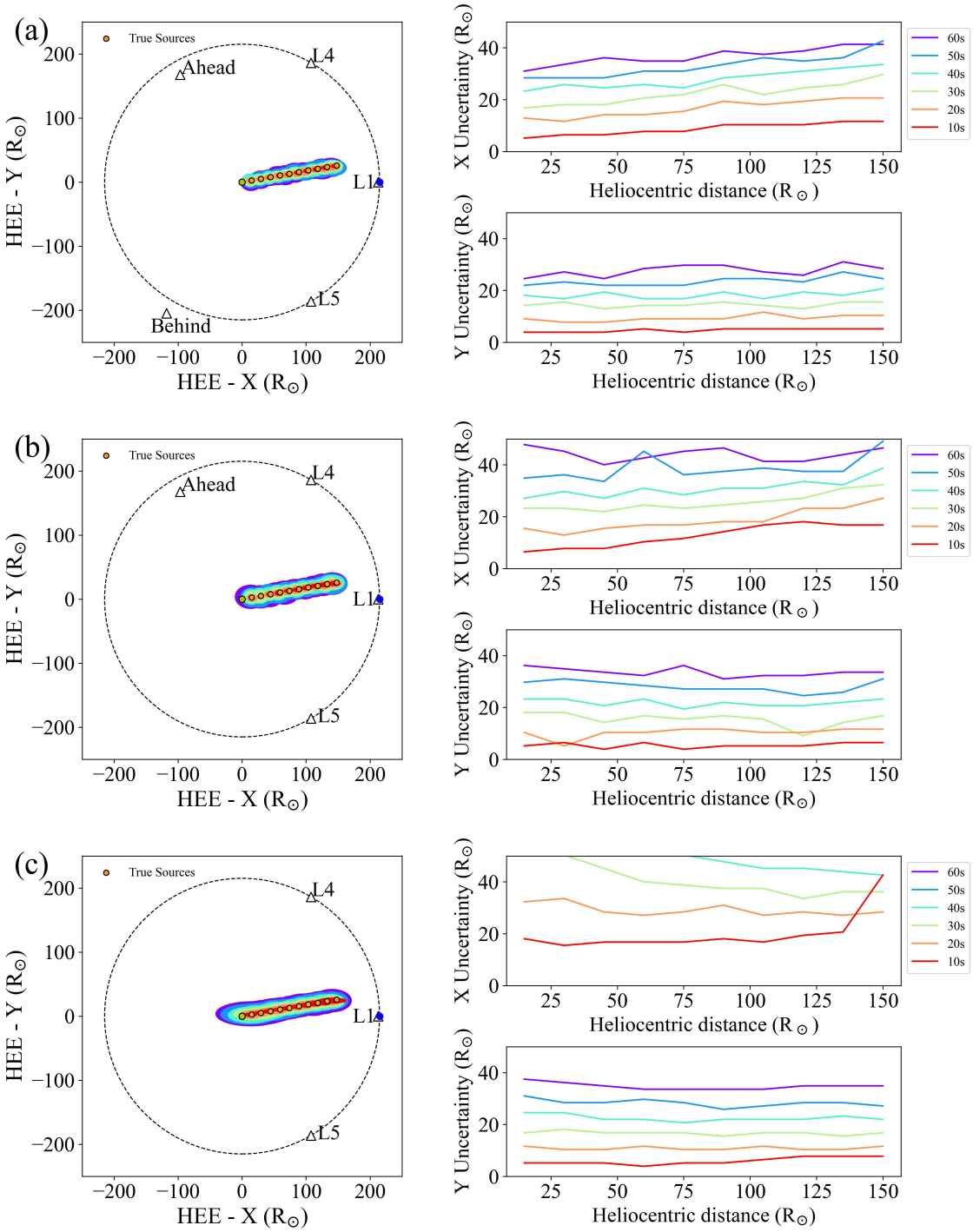


Figure 6.5: Cadence analysis for the proposed (a) SURROUND Ecliptic Spacecrafts: *L*1, *L*4, *L*5, *Ahead* and Behind, (b) case of 4 spacecraft and (c) a three spacecraft configuration at the aforementioned Lagrange points only. A source beam moving from $5\,R_\odot$ to $150\,R_\odot$ was simulated with *Ahead* and *Behind* were placed at $\pm 120°$. Analysis for full revolution of *Ahead*/*Behind* is also available. (*Left*) Map of the ecliptic showing beam and uncertainty ellipsoids for different cadences (see colours). (*Right*) X and Y 2σ uncertainty for different cadences as a function of height, each colour corresponds to the ellipsoids on the left maps.

analysis shows that, with the exception of a few outliers likely caused by anomalies in the Bayesian engine causing divergences, the lower instrument cadence resulted in reduced positional uncertainty of the source. Across all configurations, it is evident that the uncertainty difference between the 10 s and 60 s cadences differs by up to an order of magnitude.

Given that this is a monitoring mission, an upper uncertainty limit of 50 $R_{\odot}$ was chosen as the maximum acceptable threshold, although this is not the measurement requirement. A mission like SURROUND should aim for a much smaller uncertainty limit to act as a safety net in real-world scenarios. The 5-spacecraft configuration in the ecliptic plane showed the smallest uncertainties, followed by the 4-spacecraft configuration, with the Lagrange-only mission presenting the largest uncertainties, as expected. Both the 5 and 4-spacecraft configurations demonstrated positional uncertainties below the 50 $R_{\odot}$ threshold for all time cadences. The Lagrange-only mission performed poorly in the X-direction uncertainty, which is critical as it aligns with the Sun-Earth line. Despite the 3-spacecraft configuration showing uncertainties below the threshold at time cadences of 10 s to 40 s, it was still outperformed by the other configurations. Lower time cadences will produce results insufficient for accurately active monitoring of radio bursts. Additionally, a 3-spacecraft mission would offer very little margin for error, and other sources of uncertainty (such as scattering effects) would significantly affect localisation accuracy.

Based on this analysis, a 5-spacecraft configuration in the ecliptic plane, capable of achieving a low 10 s cadence, is highly desirable. To manage the high data transmission rates associated with higher cadences, 10 s data files can be prioritised and transmitted to the ground receiver during periods of heightened solar activity and increased risk of flaring events. During quieter periods, 60 s cadence datasets can be transmitted instead, as they will be of lower priority. This approach ensures that the most crucial data from SURROUND is delivered during the most significant time periods. Conversely, the Lagrange-only configuration faces a challenge, as it would require a consistent high data transmission rate to ensure the retrieval of useful data from all spacecraft at all times.

In addition to generating the most desirable results, a 5-spacecraft configuration will also reduce the risk of mission failure in the unlikely event of a spacecraft loss. This analysis shows that a 4-spacecraft mission is sufficient to achieve SURROUND's mission goals. Moreover, a 4-spacecraft mission accounts for the risk of losing a spacecraft, as SRBs can still be tracked with 3 spacecraft, though with lower-quality datasets. However, a mission with the bare minimum number of spacecraft, such as three, is considered high-risk, as the loss of one spacecraft would eliminate the mission's multilateration capabilities. Nonetheless, it is noted that GP methods can still be utilised with two spacecraft.

Finally, a high cadence dataset offers additional benefits beyond improved localisation performance. The dynamic spectra presented in this thesis indicate that Type III bursts become very narrow at high frequencies, particularly above 5 MHz. Figure 5.5 demonstrates that the Wind/WAVES lightcurves between 2 MHz to 13 MHz become indistinguishable from each other, with only one or two data points observed above the background, making it impossible for a data extraction algorithm to operate accurately. Ideally, in order to resolve Type III bursts at frequencies such as 25 MHz, SURROUND must operate using cadences comparable to those of ground-based telescopes (i.e., less than 10 s). However, given that the data transmission of a space-based mission is limited, a compromise of 10 s to 20 s should be considered.

6.4.3 Spacecraft orbits/positions

As it will be shown in Chapter 7, the effects of spacecraft configuration are critical for accurate source localisation. Fortunately, the symmetry of SURROUND and the inherently well-distributed design of the proposed 5-spacecraft configuration mitigate concerns related to spacecraft configuration compared to other sources of uncertainty. Despite this, the different combinations of spacecraft that can result from the proposed 5-spacecraft mission, including various 4-spacecraft and 3-spacecraft descope missions, are considered in this section.

In order to verify that the 5-spacecraft (*L*1-*L*4-*L*5-*A*-*B*: where *A* is "*Ahead*" and *B* is "*Behind*") configuration is the most accurate, a series of simulations were conducted considering all possible combinations of *L*1, *L*4, *L*5, *A*, and *B*. Similar to Section 6.4.2, the investigated cadences ranged between 10 s and 60 s for 3, 4, and 5 spacecraft configurations. The radio burst simulated was the same as in Figure 6.5. In order to quantify the performance of each spacecraft combination, the results were averaged for both over a full revolution of *Ahead*/*Behind* as well as the entire burst trajectory.

Figure 6.6 (a) shows the performance of each of the combinations of spacecraft available from a fleet of 5 ecliptic spacecraft. In Figure 6.6 (b), a close up look of the best-performing spacecraft configurations is shown. Each configuration was tested at cadences ranging from 10 s to 60 s, with different colours representing each cadence. This analysis shows that source localisation uncertainty is dependent on the spacecraft number and spacecraft configuration, with the smallest uncertainty associated with the 5-spacecraft configuration, as expected. However, when looking at the best performing of each spacecraft number, the improvements appear to be relatively small with each additional spacecraft. This suggests that spacecraft configuration is more determinant than spacecraft number.

For a 3-spacecraft mission, the localisation performance, using a 40 s cadence as a reference, can vary from 15 $R_\odot$ to 70 $R_\odot$. This wide range in positional uncertainty shows the importance of selecting the correct spacecraft configuration. The best-performing configuration was the Lagrange configuration (*L*1-*L*4-*L*5), followed closely by *L*4-*L*5-*A* and *L*4-*L*5-*B*, which showed nearly identical results. This suggests that a descope mission could be viable if deployment and manoeuvring to *L*1 prove to be unfeasible.

The best-performing 4-spacecraft configuration was *L*1-*L*4-*L*5 plus either *A* or *B*. Another acceptable configuration is *L*4-*L*5-*A*-*B*, indicating that the mission remains feasible even if *L*1 cannot be reached. Additionally, the configuration of *L*1-*A*-*B* plus *L*4 or *L*5 produced results below the threshold, though with noticeably lower performance compared to the other configurations.

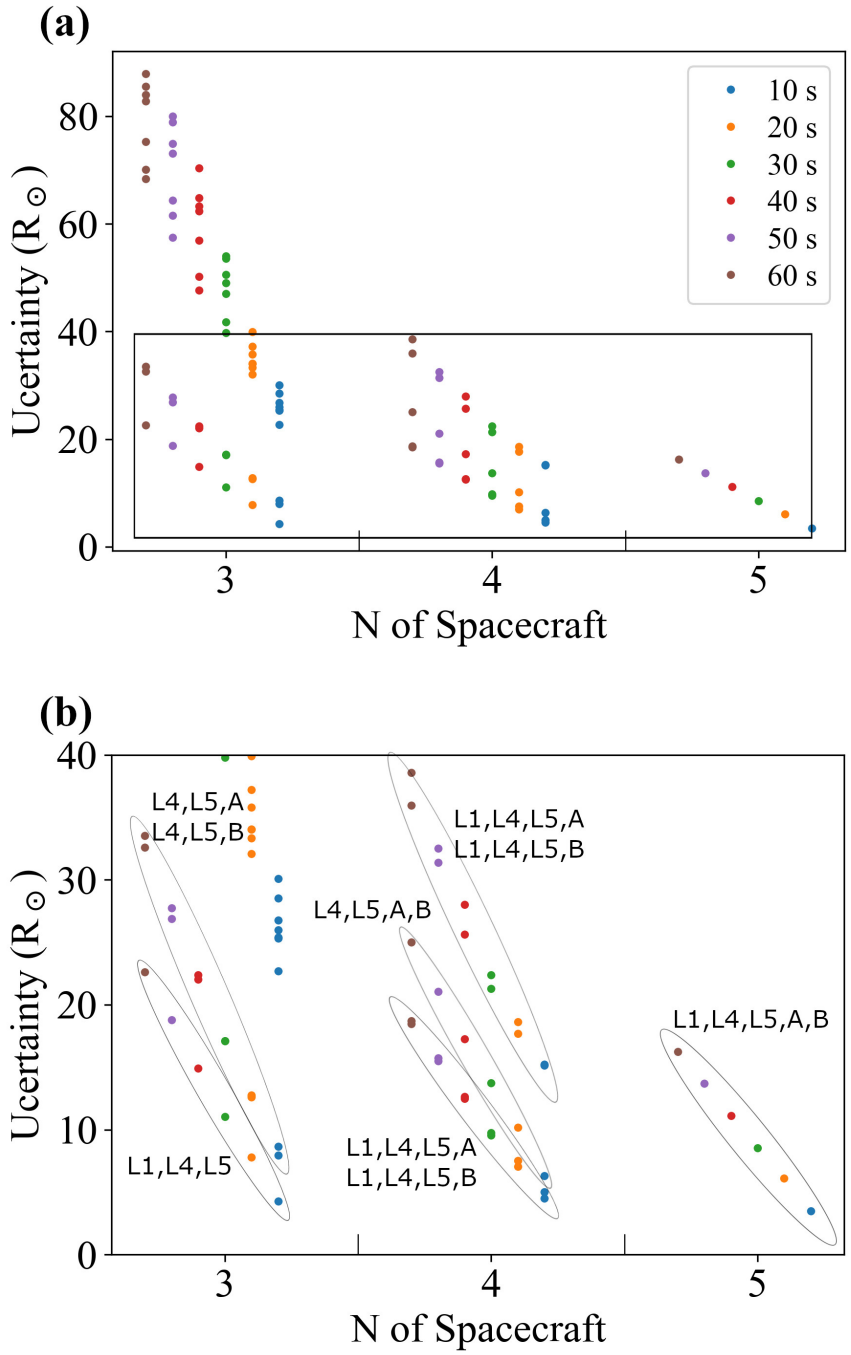


Figure 6.6: Summary of performing the cadence analysis over all the possible combinations of spacecraft configurations. (a) Shows averaged uncertainties expected for each combination of spacecraft between 3, 4, and 5 spacecraft and for different cadences. (b) Is a zoom of (a) focusing on the most accurate combinations. Labels and clusters are shown to indicate which combinations are most accurate. Note that combinations above 40 $R_{\odot}$ were not labelled for clarity, as these combinations of spacecraft were discarded as options.

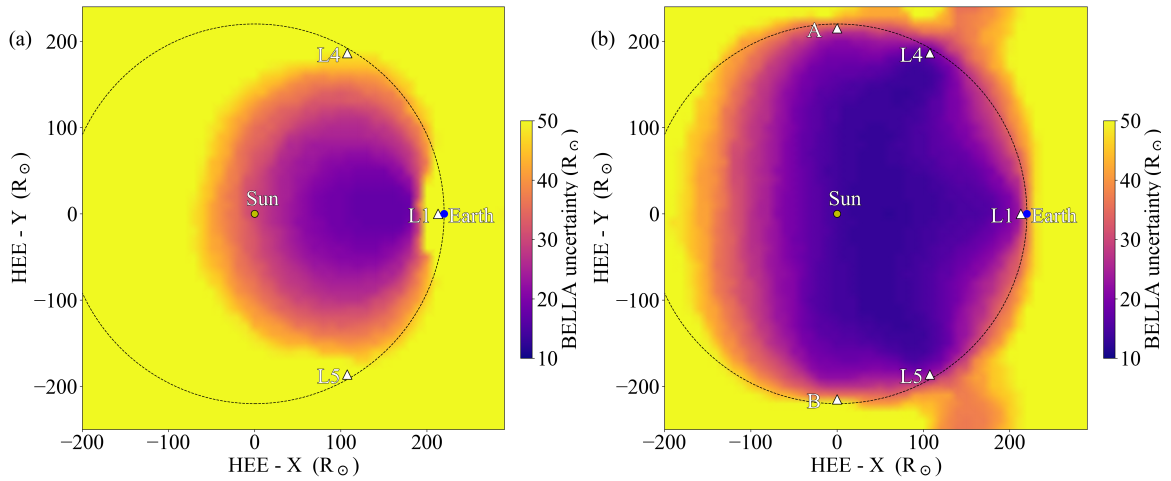


Figure 6.7: Comparison of the expected confidence maps for a 3 and a 5 spacecraft configuration. (a) Shows the Lagrange-only spacecraft, *L*1-*L4*-*L5*, and (b) is the proposed 5-spacecraft configuration with *A*/*B* at 90 deg. Blue denotes areas of confidence, and yellow denotes areas where the uncertainty is above the specified threshold of 50 $R_{\odot}$.

Throughout this section, three variables affecting positional uncertainty were identified: spacecraft configuration, instrumental cadence, and the number of spacecraft. The 5-spacecraft configuration, with *Ahead*/*Behind* positioned at greater than 90°, was inherently well-spaced and well-distributed, making spacecraft configuration less critical in this case. However, for the 3 and 4-spacecraft configurations, different combinations of spacecraft resulted in significant performance variations. Furthermore, the analysis consistently demonstrated that lower cadences lead to lower uncertainties, as expected. Finally, while increasing the number of spacecraft did improve performance, it was not as critical as the other two factors.

This analysis suggests that an *L*1-*L4*-*L5* configuration with a cadence of 20 s could be more precise than the 5-spacecraft configuration with 60 s cadence. However, this conclusion is specific to the particular simulated burst. A burst with a different trajectory will result in larger uncertainty differences, highlighting the importance of considering all factors in the mission design.

Figure 6.7 shows, using the uncertainty maps described in Section 5.3, that the *Ahead* and *Behind* spacecraft provide invaluable support to the accuracy performance of SURROUND. This figure compares the (a) 3-spacecraft and (b) 5-spacecraft configurations (at 90°). Here,

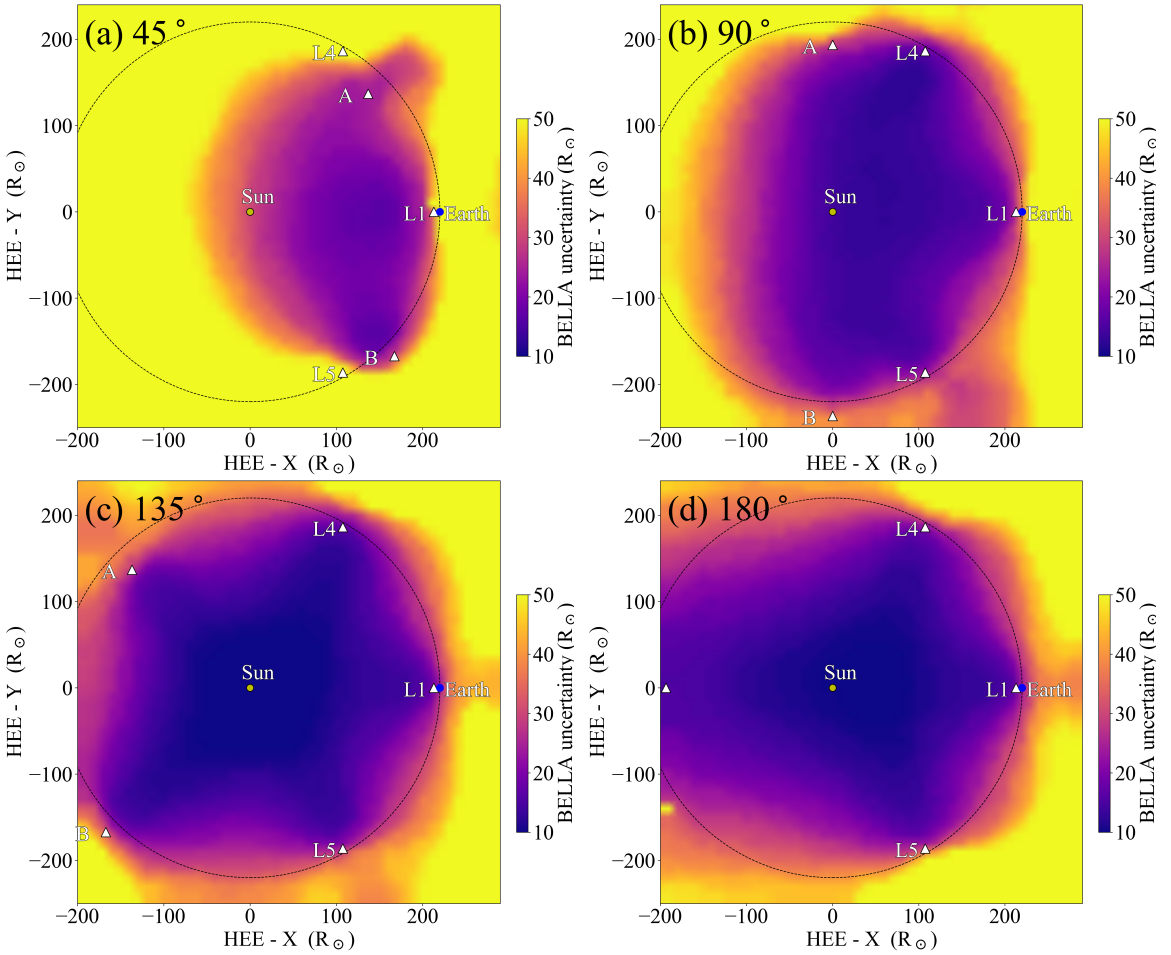


Figure 6.8: Confidence maps of the 5-spacecraft *L*1-*L*4-*L*5-*A*-*B* configuration, where *A* and *B* are at (a) 45 deg and (b) 135 deg. Blue denotes areas of confidence, and yellow denotes areas where the uncertainty is above the specified threshold of 50 $R_{\odot}$. Here it is shown that the boost performance of the 5-spacecraft configuration is only noticeable after the 45 deg point.

it is very clear that the three, Lagrange-only, spacecraft configuration results in low uncertainty exclusively for sources travelling towards Earth. While the primary focus of a monitoring mission such as SURROUND is protecting Earth, SW monitoring is also necessary in order to protect other assets around the solar system and will provide invaluable information in future human missions to Mars.

Additionally, the most critical areas to observe along the Sun-Earth line are those close to the Sun's observable surface, as these are the regions where CMEs are formed. Unfortunately, for the Lagrange-only configuration, this is a region of moderate uncertainty. Monitoring these areas can provide an essential time advantage for initiating trigger warnings when an

eruption occurs, thereby giving spacecraft-based and ground-based terrestrial communications and infrastructure more time to prepare.

Furthermore, Figure 6.8 presents the 5-spacecraft configuration with *Ahead*/*Behind* at (a) 45°, (b) 90°, (c) 135°, and (d) 180°. The comparison demonstrates that the 5-spacecraft configuration shows a performance improvement only when *Ahead*/*Behind* are positioned at an angle greater than 60°. Taking the STEREO mission as a proxy, a rate of 22 °/year would imply that the *Ahead*/*Behind* spacecraft would be operative after 3 years from launch. At that rate, the mission could operate nominally for a period of 10 years, after which, a CubeSat mission such as this one would be expected to be at the end of its mission.

6.4.4 Spacecraft communications

SURROUND's concept was motivated by the development of technologies that are currently considered unfeasible or at low technology readiness level (TRL), and SURROUND was funded for the purpose of advancing such technologies. Developing a constellation of CubeSats located at +1 au from Earth, poses a number of technological challenges that have to be addressed in order to make the mission feasible, particularly in the domain of communications. These technology challenges are the main reason as to why there are very few examples of deep-space CubeSats, even in development.

This subsection, focuses on summarising some of the developments made during the Phase 0 study conducted by the DIAS and the University of Manchester collaboration. The work shown in this subsection is not my own but has been included in this thesis to provide the reader with essential context and perspective on the mission's feasibility. Most of the work conducted in this subsection makes reference to Crisp et al. (2023) which describes the technology developments required to make SURROUND feasible.

Missions such as Hera and M-ARGO are being developed for use beyond Earth-orbit and currently developing the necessary technology that can make SURROUND feasible. The most notable example of a CubeSat communicating back to Earth from deep-space is MarCO

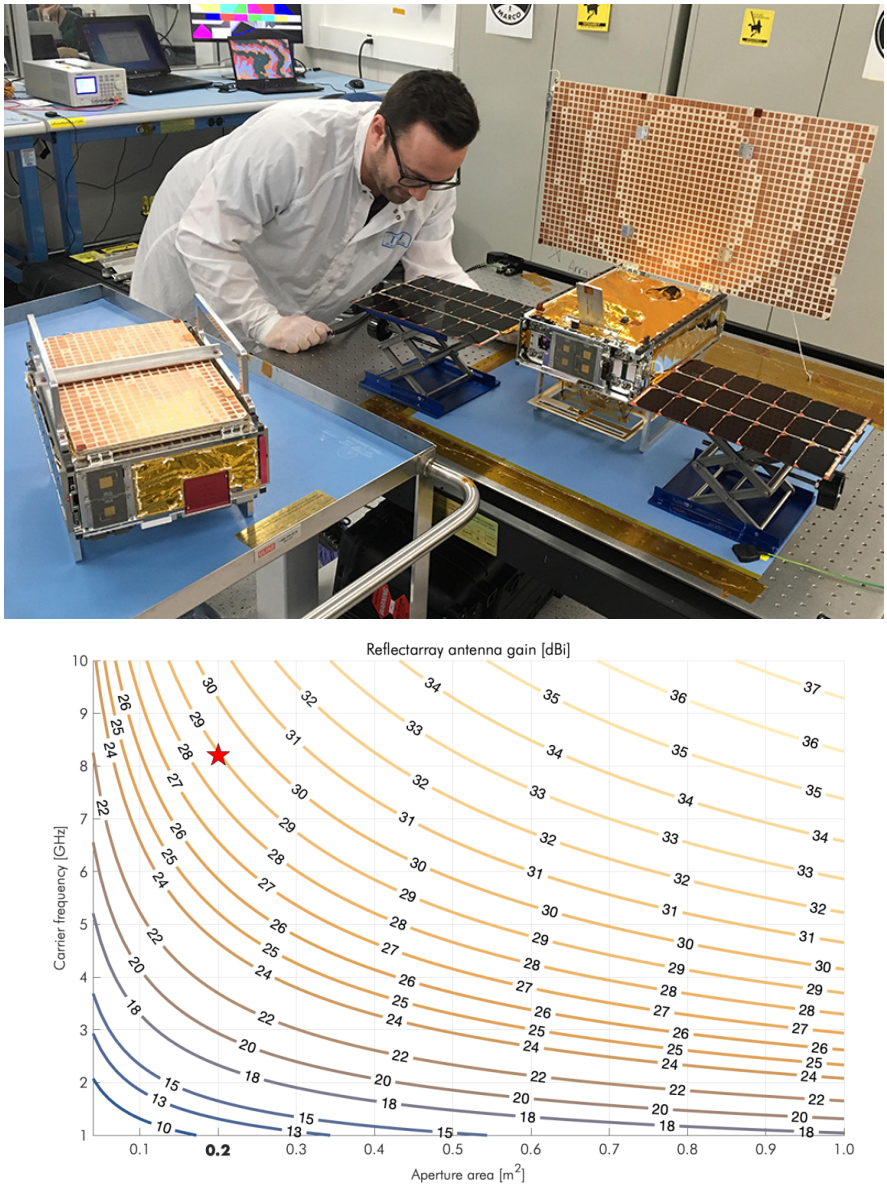


Figure 6.9: *Top*: The MarCO pair in stowed and deployed configuration. The reflectarray shown in this image was used for beyond Earth-orbit communications. The mission showed that CubeSats are capable of deep-space communications and served for inspiration of SURROUND's main technology challenge. *Bottom*: The maximum gain expected from a reflectarray antenna (Crisp et al., 2023), the red star shows the performance of MarCO for context. Credit: NASA/JPL-Caltech

(see Section 3.7), which was launched in 2018 and successfully communicated back to Earth until 2020. MarCO and the rest of the aforementioned spacecraft, make use of reflectarray antennas to communicate. Figure 6.9 shows the maximum indicative gain for a reflectarray antenna assuming a pointing loss of 3 dB, however it was noted that with high performance attitude control and a steerable antenna, these losses can be mitigated. For context, the

performance of MarCO was included as a red star in the figure. MarCO operated with a 4 W transmitter, however in the engineering study, a 15 W transmitter was also considered. The Phase-0 study showed that in order to meet the data requirements using the current technologically available equipment would require an unfeasible amount of time to download the data; 30 days at 1 au, and 90 days at 2 au assuming a 13 m antenna ground segment. This problem could be mitigated by the usage of the 70 m antenna available by the DSN. This solution would cut down the times to 44 mins at 1 au and 2 hrs at 2 au. However, the extended usage of the largest DSN antenna poses practical and political challenges that are outside of the scope of this thesis but have to be considered in the case of a Phase A and Phase B studies. These challenges show that SURROUND would be a more practical mission as a scientific mission, as opposed to a solar monitoring mission.

6.4.5 Frequency of downlinks

The frequency of downlinks depends on the type of SW being monitored. Electrons generating Type III bursts travel at approximately 0.3 c, resulting in a Sun-Earth travel time of about 30 min. To effectively forecast Type III bursts, data needs to be collected more frequently than this travel time. Acquiring data at a cadence of 10 min would provide enough time to derive the burst's propagation direction and still allow a 5-minute window for processing and issuing a forecast within 15 minutes, well before the typical propagation time. The requirements for nowcasting Type III bursts are lower, requiring data acquisition approximately every 15 min.

For Type II bursts, associated with the shock front of a CME, the required lead time is shorter. These events can reach a maximum propagation velocities of around $3500\,\mathrm{km\,s^{-1}}$, resulting in a minimum Earth travel time of about 12 hours. To make a reliable forecast, at least four position samples are needed, equating to a cadence of 3 hours. Similarly, nowcasting Type II bursts requires a cadence on the order of 6 hours.

To estimate data file sizes, the Solar Orbiter Archive (SOAR) was consulted. The SUR-

ROUND mission's spectrometer will have characteristics similar to the HFR module of the SolO/RPW instrument. Typically, the average daily data file size for Level-2 data (L2: processed data) at a cadence of 5 s or 6 s ranges between 130 MB to 240 MB. Level-0 data (L0: raw data) was not considered because it includes data from the entire RPW instrument, which is not relevant to SURROUND. Level-1 data (*L*1: uncalibrated data) were comparable to the data file sizes of L2. A conservative estimate for a 10 s cadence data set from each SURROUND spacecraft is around 150 MB per day. This is explored further in Crisp et al. (2023) and Macario-Rojas, A. et al., (in review).

Assuming 256 spectral channels with 12-bit resolution, a 1 s cadence results in a daily data rate of approximately 30 MB for a single antenna suitable for multilateration. GP methods require data from three antennas or their cross-correlation, yielding a daily data rate of about 90 MB. Including a 35% margin for overheads and housekeeping, the total daily data rate is estimated to be around 120 MB, consistent with the RPW data analysis.

6.5 Conclusion

The SURROUND mission is an ESA-funded Phase-0 mission developed for the purpose of monitoring hazardous SW events using a constellation of low-cost CubeSats. By strategically positioning these spacecraft equipped with radio spectrometers, the mission aims to detect, localise, and track SRBs associated with CMEs and SEPs. This section was part of a much larger study that also aimed to address the different technological challenges and mission analysis required to make a mission like this feasible. These topics are outside the scope of this thesis, as they were not directly my work. Furthermore, the reader might have noticed that throughout this study, SC6 was not included. The reason for this is that, very quickly during the development of SURROUND mission analysis, it became apparent that although the feasibility of a CubeSat being transferred to a non-ecliptic orbit was not impossible, it was certainly not practical, as it would take approximately 16 years to reach an inclination of 30 °, and was very quickly discarded.

Overall, the simulations have shown that the optimal configuration is the proposed *L*1-*L*4-*L*5-*A*-*B* setup, based solely on the accuracy of utilising multilateration techniques (TOA). Alternative configurations such as *L*1-*L*4-*L*5-(*A* or *B*) or *L*1-*L*4-*L*5 would offer acceptable results for radio bursts travelling along the Sun-Earth line; however, deviations from this position will lead to less accurate results. The feasibility of these configurations from a Mission Analysis perspective is addressed in Macario-Rojas, A. et al., (in review). Additionally, the importance of a high cadence radio spectrometer was highlighted, showing that in certain cases, a low cadence spectrometer is capable of outperforming a larger number of spacecraft with lower cadence.

Finally, it should also be considered that CubeSats are relatively low-cost at the expense of durability and the risks associated with a small platform (e.g., loss of communications). Therefore, it is important to consider that the true benefit of using the 5-spacecraft configuration, knowing that the 4 and 3-spacecraft configurations would also work, is that the redundancy ensures the success of the overall mission.

7 Measuring Radio Wave Propagation Effects

7.1 Introduction

The abundance of Type IIIs observed by ground-based telescopes in the low corona at metric to decametric wavelengths (e.g., Ndacyayisenga et al., 2021) and by space-based telescopes in the decametric to kilometric wavelength range (e.g., Reid & Vilmer, 2017) has resulted in numerous studies about the location of the radio sources (e.g., Krupar et al., 2012; Morosan et al., 2014; McCauley et al., 2018; Chen et al., 2023). This suggests that theoretically, there should be an abundance of studies showing the paths of the electron beam exciters travelling from low in the solar corona to interplanetary distances. Unfortunately, with a few exceptions (e.g., Badman et al., 2022), this is not the case.

One reason for the lack of low corona to interplanetary localisation studies is the limited fleet of solar-dedicated spacecraft. As will be shown in Section 7.4, there is a lack of understanding regarding the effects of spacecraft configuration on the localisation of Type III sources. Simulations from Chapter 5 and Chapter 6 demonstrated that this can result in significant uncertainties, leading to discrepancies between ground and space-based observations.

In addition, a lack of accurate and precise localisations makes the measurement of radio scattering at the interplanetary range a challenging task, further contributing to the unexplained discrepancies between the two.

In this chapter (Cañizares et al. (in review)), a Type III SRB was investigated from the low corona ($\sim 0.25\ R_\odot$) to interplanetary distances ($\sim 100\ R_\odot$) using the NRH to image the burst at 150 MHz and five spacecraft (PSP, STEREO A, SolO, Wind and MEX) to multilaterate the path of the electron beam exciters. This allowed in Section 7.4 for a detailed analysis of the effects of spacecraft configuration on localisation methods, Section 7.5 presents the results of the first multilateration performed with five spacecraft, Section 7.6 discusses how the location of the true radio sources was modelled and Section 7.7 focuses on the observed scattering shifts based on the modelled true source locations and the measured locations.

7.2 Observations of a Type III with five spacecraft

On 4 December 2021 at $\sim$ 13:00 UT a double Type III was detected by PSP/FIELDS, STEREO/WAVES, Wind/WAVES, SolO/RPW and MEX/MARSIS (see Figure 7.1). The Type III pair is believed to be two separate events and not a fundamental-harmonic pair as they are separated by $\sim$ 5 min and there is no evidence of fundamental-harmonic frequency ratios in their morphology. The bursts were identified as bright and well defined.

Given the current fleet of solar spacecraft, a five spacecraft observation of a Type III event would have been unfeasible without MEX. However, it is understandable that MARSIS comes with a series of limitations for solar observations. As discussed in Section 3.6.1, MARSIS' operational window is limited to $\sim$ 40 minutes, and as shown in Figure 7.1, the window of operation of AIS was of $\sim$ 10 min for this particular observation. As a result, MARSIS missed one of the two bursts, and in order to confirm which burst was detected, all spectra were light-travel shifted to 1 au and stacked vertically (see Figure 7.2). This process confirmed that the MARSIS burst is the earlier burst and therefore the following study will focus on this particular burst.

Despite MARSIS being operational between 5.5 and 0.1 MHz, Figure 7.1 shows that the burst is weakly observed at frequencies larger than 3 MHz. This could be a consequence of the antennas being directional, thus affecting sensitivity. The narrow operational window of

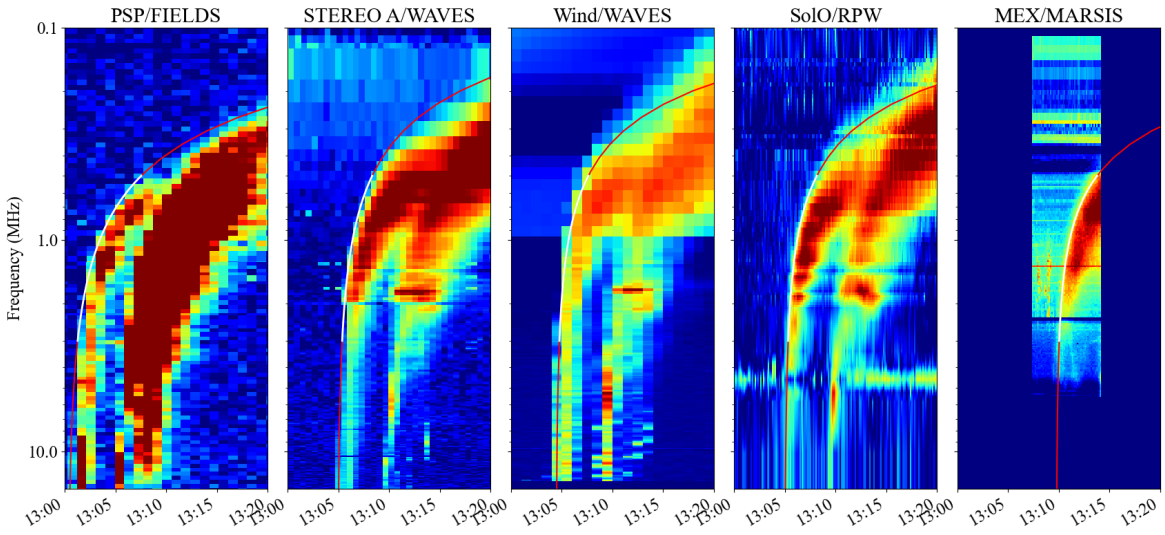


Figure 7.1: Double Type III radio burst observed, from *left* to *right*, by PSP/FIELDS, STEREO A/WAVES, Wind/WAVES, SolO/RPW, and MEX/MARSIS on 4 December 2021. Since MEX/MARSIS was unable to detect the later event, only the earlier burst was considered for this study. The multilateration was performed on the leading edge (red line) in the 0.5–3 MHz frequency range (white line). The leading edge was extracted by following the Section 4.1.2 procedure using manually selected rise times. Source: Cañizares et al. (in review).

MARSIS, also resulted in the truncation of the data at less than 0.5 MHz. Because of this, the five spacecraft multilateration was limited to 3 MHz as a high frequency limit and 0.5 MHz as a low frequency limit. The latter being inevitable, as FIELDS was also unable to capture emission at less than 0.5 MHz and the bursts merged at $\sim$ 0.3 MHz.

Regardless of all the limitations imposed by MARSIS, the martian probe had the advantage of providing spectrograms at the highest cadence of the five spacecraft. The 7.38 s resolution provided by MARSIS was followed by RPW at 7.6/9.2 s (HFR/TNR), SWAVES at 34.98 s, FIELDS at 55.92 s, and WAVES at 60 s.

As shown in Chapter 5, performing BELLA's Bayesian Multilateration (Cañizares et al., 2024) requires time information from the same frequency channels, and in order to mitigate this mismatch in frequency channels, an inverse polynomial function is fitted to the leading edge of the Type III (see Equation 4.11). However, unlike in Chapter 5, the rise times were extracted manually and not using the GH procedure shown in Section 4.1.1. This is because

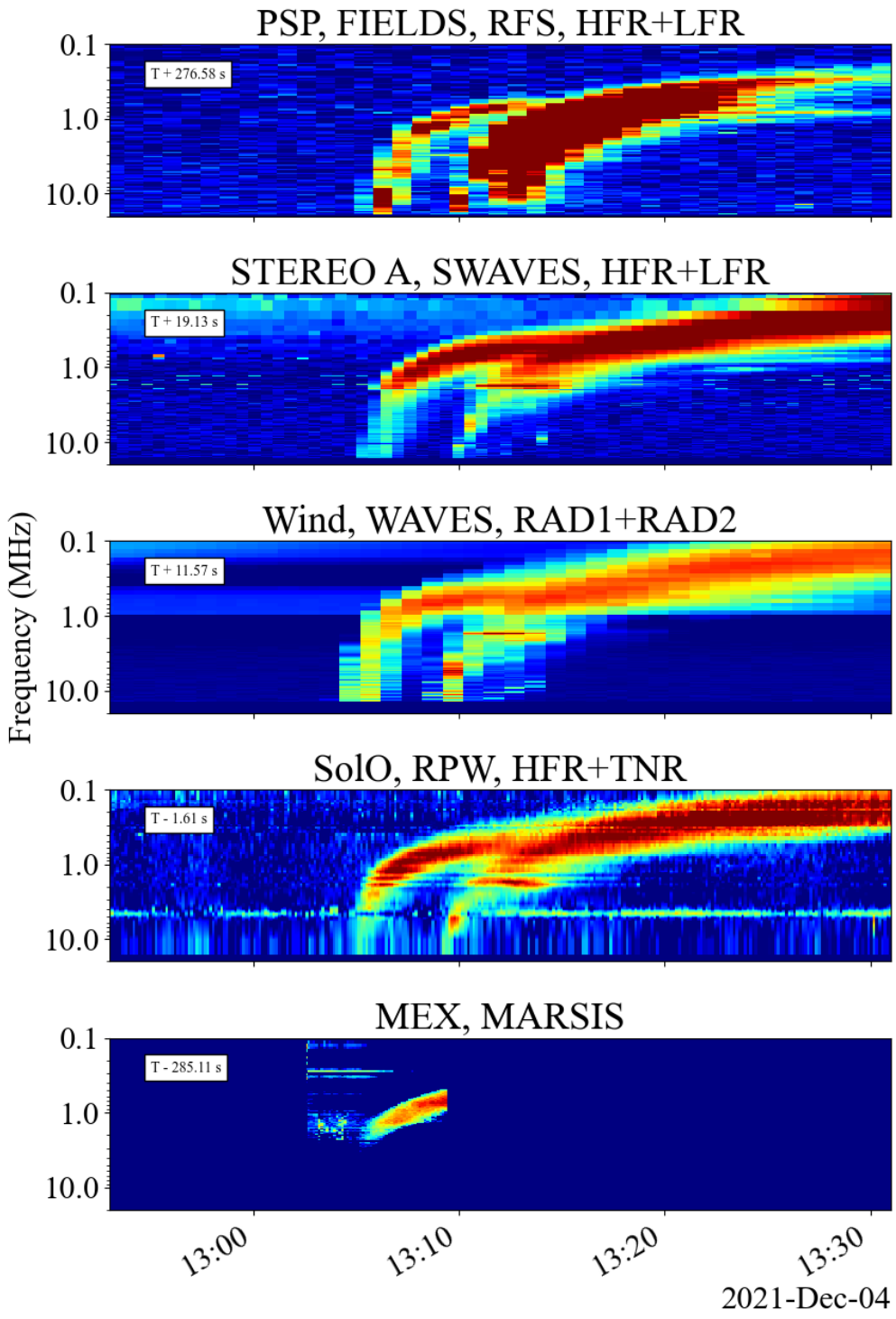


Figure 7.2: Light travel adjusted and vertically stacked plot of the double Type III radio burst observed, from *top* to *bottom*, by PSP/FIELDS, STEREO A/WAVES, Wind/WAVES, SolO/RPW, and MEX/MARSIS on 4 December 2021. The vertical light travel adjusted alignment allowed to confirm that MEX detected the earlier burst and not the later one.

the GH method assumes a single Type III and this is not the case. The fit was plotted as a red line in Figure 7.1, ensuring that the physical characteristics explained in Section 4.1.2 were considered. The segment of the red-fitted function used for the multilateration is shown as white, which corresponds to the overlapping frequency range of all the spectrograms, i.e., the 3 MHz to 0.5 MHz range.

7.3 Onset location of the Type III sources

At approximately the same time as the Type III emission observed in Figure 7.1, NRH detected a moving source in the 150 MHz and 173 MHz frequency channels. Unfortunately, the burst was too weak to be observed by Observations Radio pour Fedome et l'Etude des Eruptions Solaires (ORFEES; Hamini et al., 2021). Additionally, Figure 7.4 shows RPW data together with e-CALLISTO spectra from Birr, Glasgow, and Humain (Benz et al., 2004). Emission from both Type IIIs was detected in the range of 20 MHz to 80 MHz. Considering that on that day, only the active region 12898 was active[1], it is likely that the NRH imaged burst is the Type III, however, it is to be noted that RFI obscured the 100 MHz to 150 MHz frequency range.

Figure 7.3 shows NRH imaging (courtesy of Shilpi Bhunia) at 150 MHz overlaid on a Potential-Field Source-Surface (PFSS; Stansby et al., 2020) and an image taken by AIA at 171 Å at 13:04:14 UT. The 150 MHz source was consistently imaged over an 8 s period at approximately 0.25 $R_\odot$, observed over the western limb, and aligned with the solar equator along a large group of open magnetic field lines. The 173 MHz source was too unstable and was therefore not included in the figure. The only stable source detected by NRH was at 150 MHz, moving in the east-west direction.

Figure 7.5 shows, with the aid of a vertical red line, that, at approximately the same time as NRH, GOES and STIX detected a B-class flare, however the 10–15 keV channel of STIX

[1]AR 12898 produced 10 flares on 4 Dec 2021 `https://solarmonitor.org/index.php?date=20211204&region=12898`

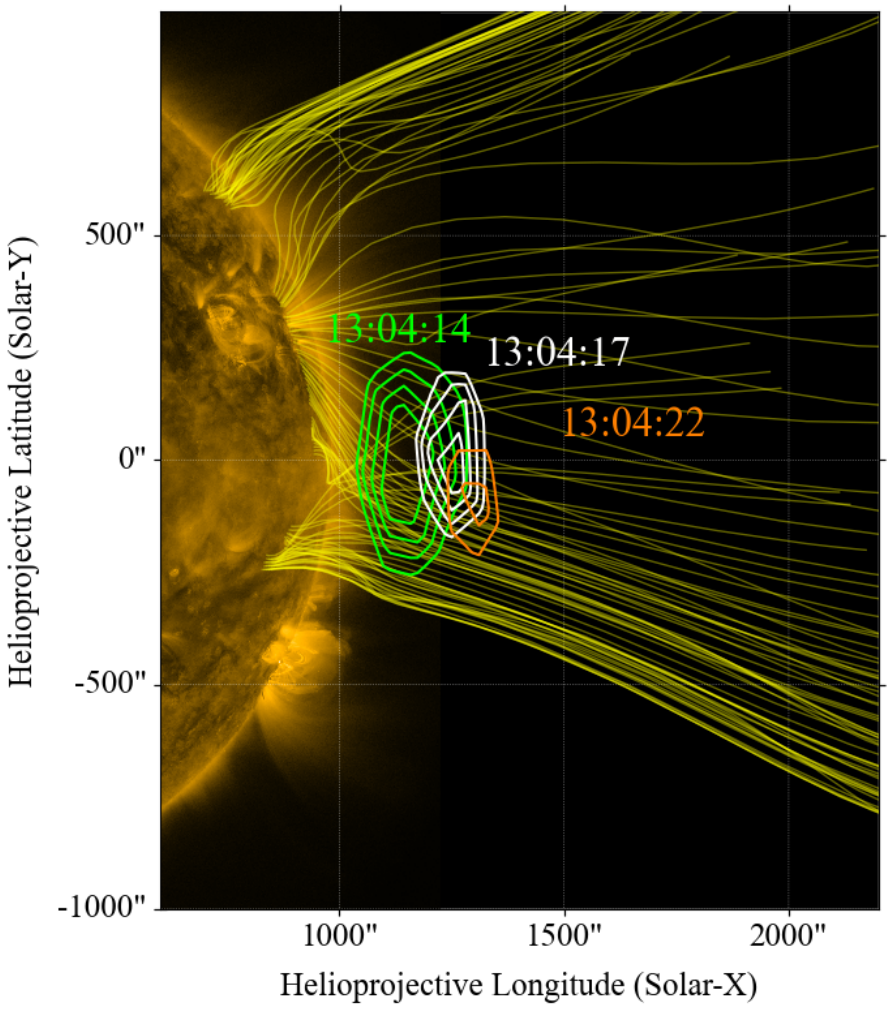


Figure 7.3: NRH imaging (courtesy of Shilpi Bhunia) of the Type III radio burst sources at 150 MHz, overlaid on an AIA 171 Å image, along with a PFSS derived from GONG data. The 150 MHz sources were consistently observed for ∼8 s at approximately ∼ 0.25 $R_{\odot}$ and aligned with the multilateration results. Additionally, the PFSS reveals a large group of open magnetic field lines at the 150 MHz location, consistent with the Parker Spiral derived from the multilateration results. Source: Cañizares et al. (in review).

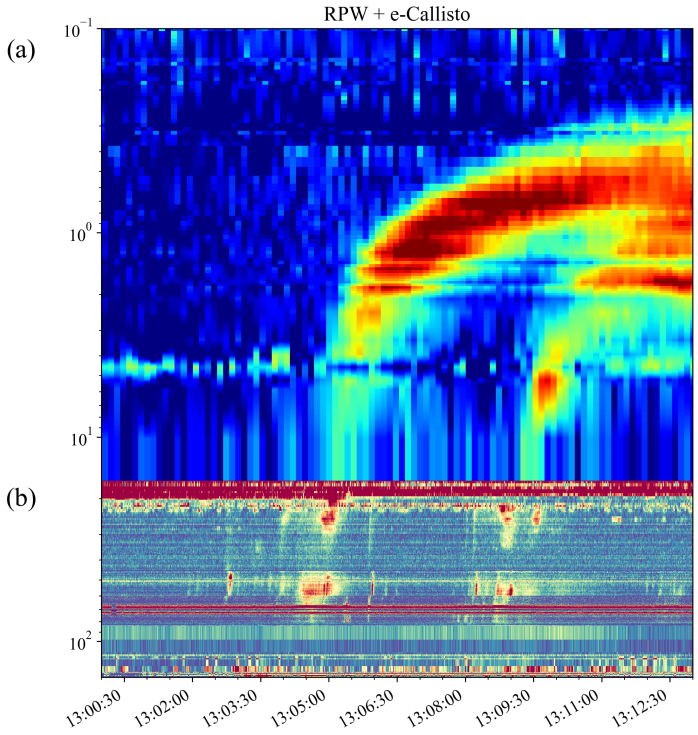


Figure 7.4: Combined dynamic spectra from (a) SolO/RPW and (b) e-Callisto stations in Birr, Humain, and Glasgow displaying the burst radio emission within the 20 MHz to 80 MHz frequency range. Unfortunately, radio interference obscured the results at 150 MHz. NRH imaging at 13:04:17.98 reveals the Type III radio source, which is believed to be a very faint emission and difficult to detect by ORFEES. Source: Cañizares et al. (in review).

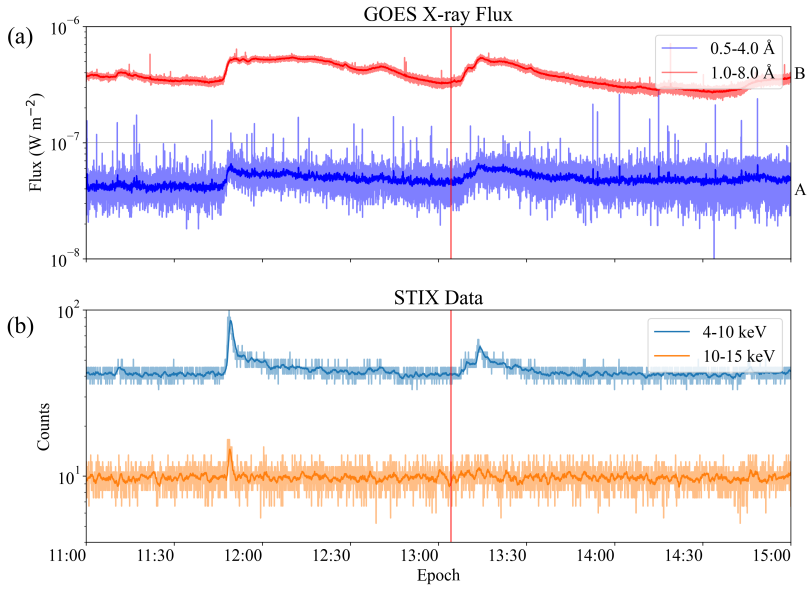


Figure 7.5: GOES (1.0–8.0 Å) and SolO/STIX (4–10 keV) detection of the B class flare at $\sim$ 13:04 UT that is associated with the Type III radio burst (Figure 7.1). The timing of the flare is consistent with the NRH imaging of the Type III shown as a red vertical line. Source: Cañizares et al. (in review).

did not record any activity suggesting that the x-ray emission is on-loop and not from the foot-points. No major events were recorded an hour previous to the Type III event, therefore suggesting that the small B-class flare could be the triggering mechanism through which the electron beams got accelerated. Furthermore, the location of the NRH imaging will later be shown to be consistent with the apparent location of the Type III. Additionally, the PFSS shows open magnetic field lines forming a streamer over the western limb. Section 7.5 will show that this is consistent with the onset location of a Parker Spiral derived from multilaterating the burst.

7.4 Spacecraft configuration assessment

Section 4.2 showed that the minimum number of spacecraft required for 2D multilateration is three. However, this does not mean that any three spacecraft will be capable of multilaterating a source accurately. The use of simulations in Chapter 5 and Chapter 6, showed that the position of spacecraft had major implications on the localisation uncertainties. This section, will empirically validate this hypothesis through the utilisation of real observations.

The five different spacecraft that detected the SRB in Figure 7.1 were located at various points around the inner heliosphere, where PSP was closest to the Sun at $\sim$ 0.5 au and MEX was furthest from the Sun at $\sim$ 1.5 au. This unique observation allows for up to 10 different combinations of three spacecraft, which were used to test spacecraft configuration. A selection of four of the ten possible combinations of spacecraft is shown in Figure 7.6. The confidence maps were produced by following the procedure in Section 5.3.1, and the electron beams paths were localised using the BELLA multilateration procedure (Section 5.2).

The selection shown in Figure 7.6 shows that the confidence maps can be classified into four different categories of spacecraft configurations:

- **Failed**: Ill-defined configurations or configurations that are mostly dominated by areas with uncertainties above the upper tolerance limit.

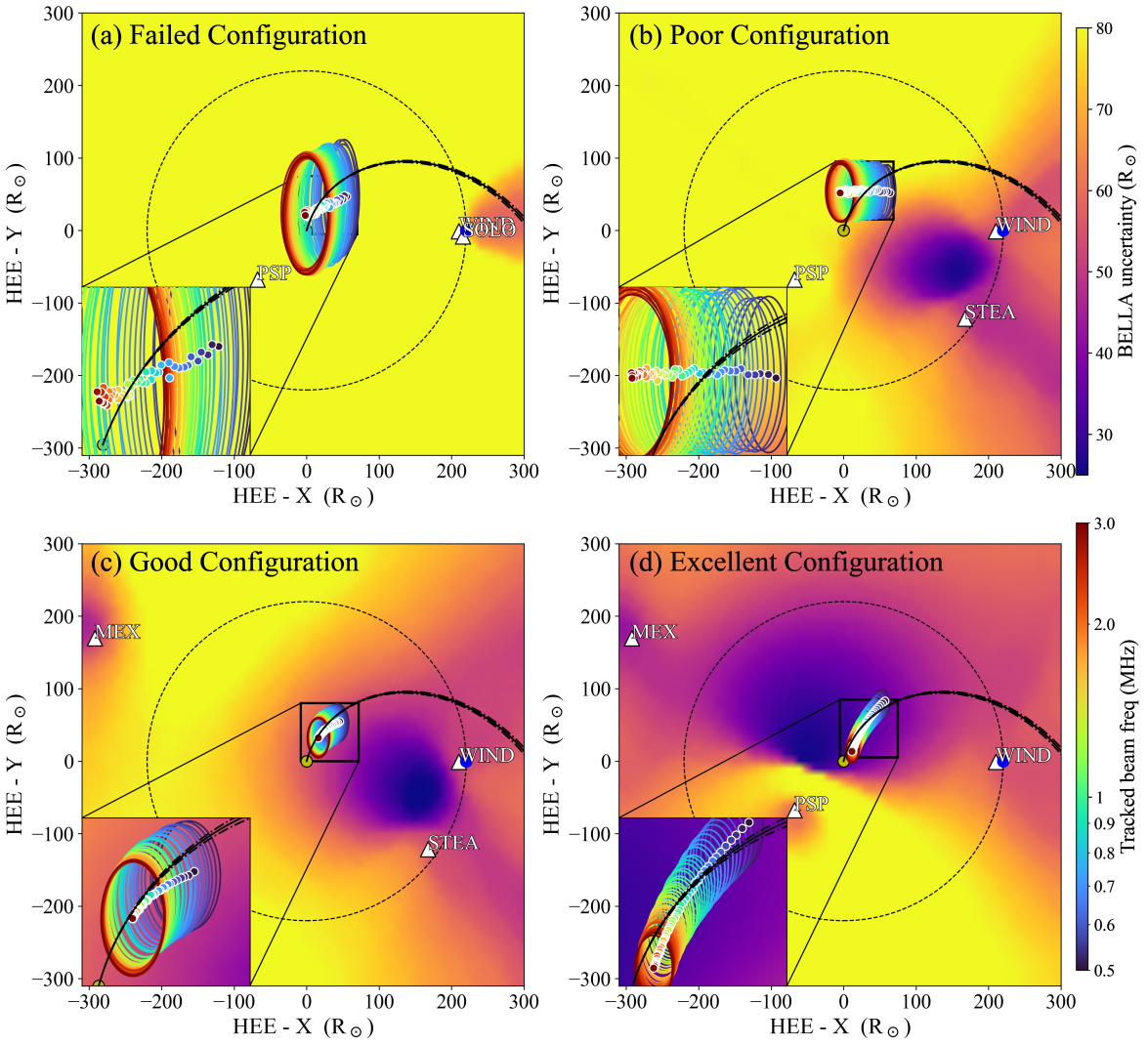


Figure 7.6: Radio burst source positions obtained by multilaterating different spacecraft configurations using BELLA with three spacecraft. The background maps show regions of low confidence (yellow) and high confidence (blue). Spacecraft configurations for the given event were classified as (a) **Failed**, (b) **Poor**, (c) **Good**, and (d) **Excellent**. A Parker Spiral was fitted to the five spacecraft multilateration shown in Figure 7.8 and plotted over all combinations of spacecraft for reference. Looking at this comparison it is evident that the accuracy of the multilateration is heavily dependent on the sparsity of the spacecraft. The cadence of the spacecraft will determine the lower uncertainty threshold that is accepted, thereby impacting the precision of the source locations. Source: Cañizares et al. (in review).

- **Poor**: Areas of high confidence are present but the region is dominated by areas of low confidence. Electron beam likely to appear on a region of low confidence.
- **Good**: Areas of high confidence are present, areas of moderate confidence dominate the region around the Sun.
- **Excellent**: Areas of confidence dominate the region around the Sun, the electron beam will likely be localised in a region of high confidence.

Taking the multilateration results into account, Figure 7.6 shows that the four cases are congruent with the confidence maps classification. The Type III (Figure 7.1) was multilaterated in all cases with identical multilateration parameters in the range of 3 MHz to 0.5 MHz. Figure 7.6 (a) shows an example of the **Failed** spacecraft configuration where all spacecraft are in a line and Wind and SolO are at approximately the same location. As a result, the uncertainties observed are in the order of $\sim$65 $R_\odot$ in the HEE-X direction and $\sim$160 $R_\odot$ in the HEE-Y direction showing an improvement in the uncertainties of the HEE-X direction thanks to the separation between PSP and the SolO/Wind pair. Figure 7.6 (b) shows an example of a **poor** spacecraft configuration. In this case the spacecraft are sparsely distributed but the multilaterated sources are located outside of the region formed by the spacecraft. This results in uncertainties of the order $\sim$40 $R_\odot$ in HEE-X and $\sim$80 $R_\odot$ in HEE-Y. The third case shown in Figure 7.6 (c) is an example of a **Good** combination of spacecraft where the spacecraft are distributed around the sources but the separation is not sparse. In this case the beam path is located in an area of moderate confidence showing uncertainties of approximately $\sim$30 $R_\odot$ in HEE-X and $\sim$60 $R_\odot$ in HEE-Y. The last case study, Figure 7.6 (d), is an example of an **Excellent** spacecraft configuration where the spacecraft positions are well separated and well distributed around the Sun, and as a consequence, the sources are located in a region of high confidence. In this case scenario the sources are located within an uncertainty of $\sim$18 $R_\odot$ in HEE-X and $\sim$31 $R_\odot$ in HEE-Y.

Throughout these four case studies, a Parker Spiral is shown. This spiral was obtained from the five spacecraft multilateration, the process of obtaining this spiral will be shown in Sec-

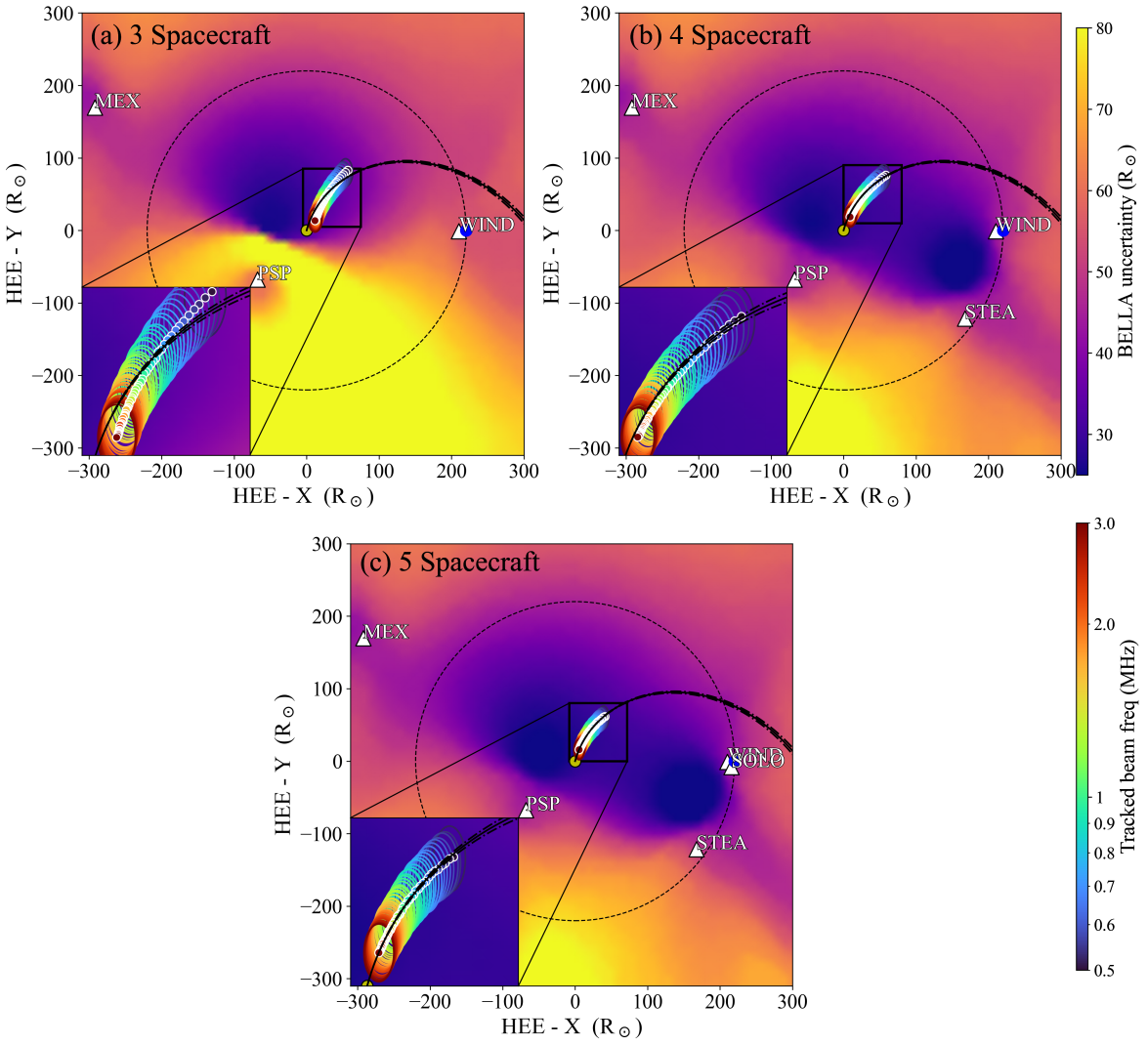


Figure 7.7: Multilateration of the Type III compared with the number of spacecraft: (a) three spacecraft (as shown in Figure 7.6 (d)), (b) four spacecraft, and (c) five spacecraft (as shown in Figure 7.8 (a)). Each spacecraft configuration was sparse, with the beam path situated in regions of high confidence. It was observed that, unlike the configuration (refer to Figure 7.6), the number of spacecraft had a relatively minor effect on precision (i.e., small changes in the uncertainty ellipses). Nevertheless, there was an enhancement in accuracy (i.e., the burst aligns itself with the Parker Spiral), indicating that an increased number of spacecraft can help mitigate errors from the data extraction process. Source: Cañizares et al. (in review).

tion 7.6. Given that this five spacecraft multilateration is the most confident case, the Parker Spiral is assumed to be ground truth, exclusively for the purposes of assessing accuracy with respect to the other spacecraft configurations. The precision on the other hand is measured by the uncertainty ellipses. Figure 7.6 shows how both the precision and accuracy are affected by the spacecraft configuration, showing that as the spacecraft are located sparsely and around the burst, the burst aligns itself with the Parker Spiral (i.e., the multilateration becomes more accurate) and with smaller uncertainties (i.e., the multilateration becomes more precise). This is consistent with Chapter 5 and Chapter 6 simulation results. This implies that a multilateration result, should always use background confidence maps, for the purpose of understanding if the results obtained are physical or altered by the localisation method.

Fortunately, this five spacecraft observation also allows to compare the impact of spacecraft number to the multilateration results. Figure 7.7, shows a comparison of three, four and five spacecraft. Considering that adding an additional spacecraft changes the configuration of spacecraft, an improvement is to be expected regardless. However, in order to asses the impact of spacecraft number, only the **Excellent** configurations were taken into account. Therefore, Figure 7.7 shows a small but noticeable improvement in precision ($\sim$15 $R_\odot$ in HEE-X and $\sim$28 $R_\odot$ in HEE-Y for the five spacecraft case) and a notable improvement in accuracy assuming a Parker Spiral as the ground truth. Comparing the three, four and five spacecraft multilateration, one can notice a small change in the angle of the sources path showing that with an increase in spacecraft number the source's path aligns itself with the Sun's Parker Spiral. This apparent rotation is a consequence of extracting data from a relatively low cadence instrument. BELLA being a statistical method, uses the redundant number of spacecraft to cancel out any errors derived from the data extraction. This highlights the importance of multi-spacecraft missions such as SURROUND for the localisation accuracy. However, it must be emphasised that the spacecraft location with respect to each other is far more important than the number of spacecraft.

7.5 Propagation of the Type III sources

Figure 7.8 shows the results of performing multilateration with five spacecraft. Figure 7.8 (a) shows a bird's eye view of the ecliptic, showing the **Excellent** spacecraft configuration, with a relatively large area of confidence. Unfortunately, there was no spacecraft in the +/+ quadrant and therefore the Y-coordinate shows a larger uncertainty than the X-coordinate. However, the multilaterated beam path is located in the large area of confidence and therefore the lack of a spacecraft in the +/+ quadrant did not appear to have a significant impact on the multilateration.

Figure 7.8 (b) shows a zoomed in view of Figure 7.8 (a) showing that the localised sources are all enclosed within the low uncertainty limit. This implies that the bulk of the uncertainty in this multilateration is dominated by either the instrumental uncertainty (i.e., cadence) and physical uncertainties such as the source size. BELLA assumes the source is point source, therefore if the sources are larger than the light-travel scale size corresponding to the cadence, the multilateration would likely show larger uncertainties than expected. The current observation shows that the uncertainties are as expected given the confidence map and therefore, it is likely that cadence is the major contributor to the uncertainties.

In agreement with the results from Chapter 5 (Cañizares et al., 2024), the measured beam path also shows a curved trajectory, which, as will be shown in Section 7.6, is consistent with a Parker Spiral. This further confirms previous studies (Reiner et al., 1998; Reiner et al., 2009) that showed this behaviour from Type III exciters.

The onset location of this spiral is observed in Figure 7.8 (c), which shows a zoomed in view of Figure 7.8 (b). Figure 7.8 (c) shows a clear view of the deprojected location of the NRH 150 MHz interferometric imaging shown in Figure 7.3. The deprojection was obtained by constraining the angles derived from the interferometric imaging with a Newkirk density model (Newkirk Jr, 1961) at one to four fold. This resulted in a series of intercepts, which were collected in the area of uncertainty. The average value of all these intersections is

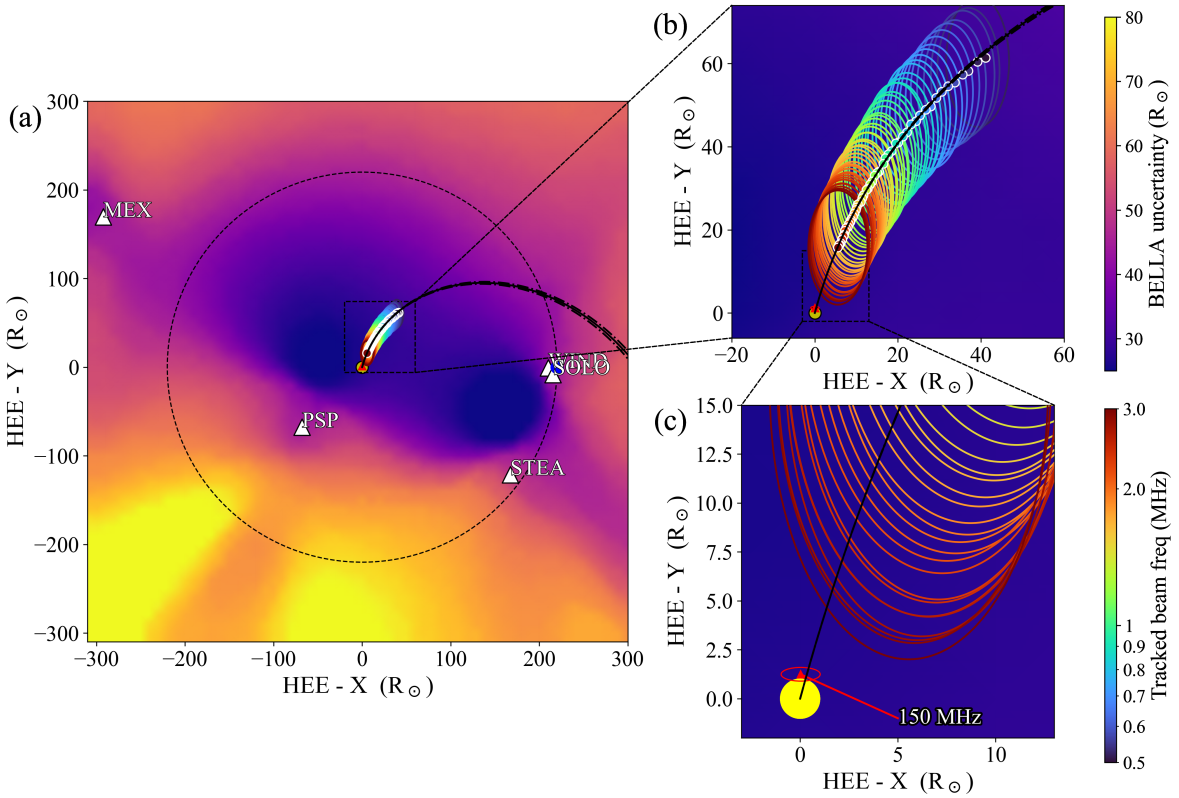


Figure 7.8: BELLA Multilateration of a Type III leading edge with five spacecraft. (a) A top-down view of the ecliptic plane showing the spacecraft configuration. This sparse configuration produced a large area of high confidence where the BELLA sources were detected. (b) A closer inspection of (a) revealing the apparent locations of the sources within the 0.5 MHz to 3 MHz frequency range. The centroids of the BELLA sources were used to fit a Parker Spiral. (c) Zoom of (b) presents a detailed comparison between the NRH 150 MHz interferometric imaging results and the BELLA sources. The Parker Spiral derived from the BELLA data was found to align well with the uncertainty region of the interferometric imaging. Source: Cañizares et al. (in review).

shown as the centroid. The 150 MHz location was observed to be consistent with the Parker Spiral derived from the BELLA sources.

7.6 Modelling the True location of Type III sources

Chapter 5 showed that the BELLA propagation velocity prior to converging at $v \approx c$ is evidence of the localisation being a reconstruction of the apparent source location and not the true source location. This is an important physical consideration as it is in agreement with Chrysaphi et al. (2018) and Kontar et al. (2019), which state that radio waves from a radio source will scatter until they reach a point of optical thinness, after which the radio waves propagate freely. This will result in a larger apparent source located further from the Sun than the true source.

Similarly to Chapter 5, the evidence of scattering is also present in this event. Figure 7.9 shows the electron densities and frequency of emission as a function of the distance from the Sun for the locations of the five spacecraft multilateration. Comparing the BELLA measurements with the Parker (Parker, 1958), Saito (Saito et al., 1977) and Leblanc (Leblanc et al., 1998) density models, the BELLA sources appear much further from the Sun than expected. These density models were previously calibrated using data from the Advanced Composition Explorer (ACE) spacecraft at 1 au (Figure 7.10 *left*). The higher-than-expected density measurement was anticipated, as it is a well documented observation when localising radio sources (Steinberg et al., 1984; Cecconi et al., 2008; Chen et al., 2023; Cañizares et al., 2024). As it was shown in Chapter 5 the most likely physical interpretation of this apparent increase in density is that an inhomogeneous turbulent corona affects the radio source Kontar (2001) and causes severe radio wave propagation effects (Chrysaphi et al., 2018; Kontar et al., 2019; Musset et al., 2021).

Before being able to quantify the effects of radio wave scattering, the expected 'true' location of Type III exciters is modelled via the assumption that these Type III photons are scattered along the path of an Archimedean Parker Spiral. Equation 5.6 (Section 5.5) showed that an

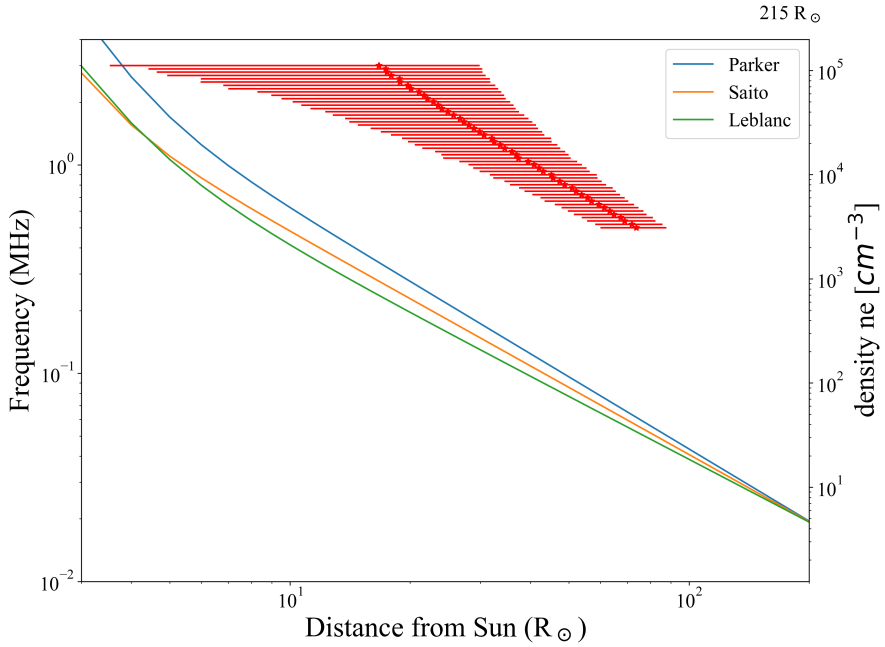


Figure 7.9: Parker, Saito and Leblanc density models compared to the results obtained by BELLA. The density models were calibrated using ACE in-situ data at 1 au (see Fig. 7.10 *left*). The electron density trend shows an approximate negative $1/R^2$ slope consistent with the slope of interplanetary density models. However, the density models showed to be one order of magnitude closer to the Sun than those measured by BELLA. This is consistent with studies (Chrysaphi et al., 2018; Chen et al., 2023) that showed that radio scattering makes the apparent source location appear further from the Sun than their true location. Source: Cañizares et al. (in review).

Archimedean Parker Spiral depends on the velocity of the solar wind v_{sw} and the footpoint longitude ϕ_0. Therefore, the fitted spiral from Equation 5.6 is used to model the expected location of the Type III exciters, using the Parker density model along the the Parker Spiral.

7.7 Measurements of Radio Wave Scattering

Fig. 7.11 shows the positions of the BELLA sources in (a) cartesian coordinates and (b) polar coordinates. As shown in Cañizares et al. (2024), I make the assumption that the Parker Spiral is Archimedean, which is linear in polar coordinates and the velocity of the solar wind is obtained from the slope and the spiral source longitude ϕ_0 is evaluated at the

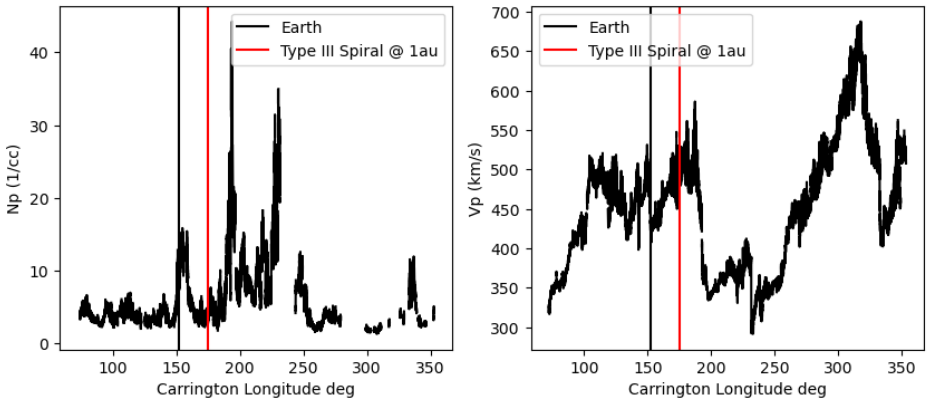


Figure 7.10: In situ data obtained by the ACE spacecraft. The *left* plot shows the proton density and the *right* plot shows the measured velocity of the solar wind. Black vertical lines corresponds to the location of the spacecraft along the Carrington longitude on the date of the event. The red vertical line corresponds to the measurements made when the spacecraft is at the Carrington longitude determined by the BELLA derived Parker Spiral at 1 au.

intercept $r = 0$:

$$\phi(r) = \frac{\Omega}{v_{sw}}(r - r_0) + \phi_0 \tag{7.1}$$

Taking the centroids of the ellipses to fit an Archimedean Parker Spiral results in a $v_{sw} = 492.98 \pm 6.19$ km s^{-1} and $\phi_0 = 74.62 \pm 1.25$ deg with a correlation coefficient $\rho^2 = 0.992$. These results were later compared with the solar wind velocity measured by the ACE spacecraft in-situ at the corresponding Carrington longitude. ACE's measurements of the solar wind (see Fig. 7.10 *right*) were found to be approximately 500 km s^{-1}, in excellent agreement with the BELLA estimation.

Studies have shown (Kontar et al., 2019; Kuznetsov et al., 2020; Chen et al., 2023) that the density inhomogeneities are distributed anisotropically and aligned along the magnetic field line. This means that in order to correct for scattering, we start from the assumption that the sources are shifted along the BELLA derived Parker Spiral. This assumption was supported by the location of the NRH interferometric imaging and the consistency of the inferred spiral with the 1 au solar wind speed. Therefore, by using a Parker model along the spiral we obtain the theoretical location of the sources. Fig. 7.11 shows the theoretical source location as dots, which can be compared to the BELLA localised sources shown as crosses. It is evident that a very large discrepancy exists between the model-expected source

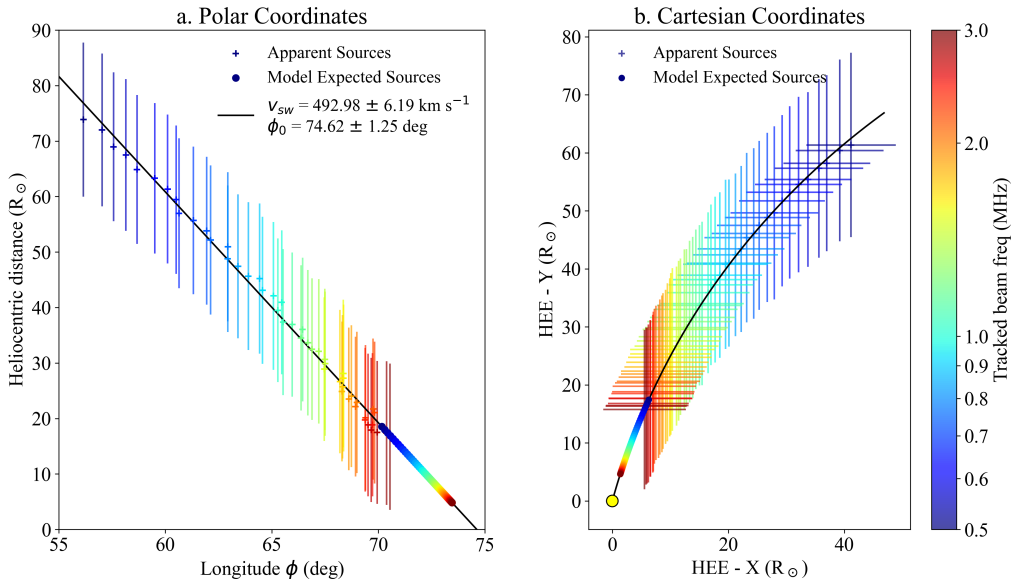


Figure 7.11: The positions of the apparent sources localised by BELLA compared to the expected scattering-free positions determined by the Parker density model. The localisations are shown in (a) in polar coordinates and (b) cartesian coordinates for the readers' convenience. An Archimedean Parker spiral is a linear function in polar coordinates, the linear trend in (b) shows that the BELLA localised sources are consistent with the path of a Parker Spiral. The fitted spiral results in a velocity of the solar wind of $V_{sw} = 492.98 \pm 6.19$ km s^{-1} and a source longitude of $\phi_0 = 74.62^\circ \pm 1.25^\circ$. Source: Cañizares et al. (in review).

locations and the BELLA-estimated (observed) locations, in line with previous quantitative estimations of the scattering-induced source shifts (Chrysaphi et al., 2018; Chen et al., 2023). Therefore, a comparison of the model-expected and BELLA-estimated locations provides an approximate quantification of the scattering-induced shift that impacts the analysed radio emissions.

Fig. 7.12 shows the estimated shifts as a function of frequency in the radial direction. These shifts were quantised by subtracting the heliocentric location of the theoretical 'expected' sources and the heliocentric coordinate of the BELLA sources. These heliocentric shifts showed, as it was anticipated from theory, that scattering is more pronounced at the lower frequencies than at higher frequencies. By fitting a power law to these shifts, we analyse the nature of the estimated scattering. The power law was found to be:

$$\Delta r = 32.48 \cdot f^{-0.88} + 0.09 \tag{7.2}$$

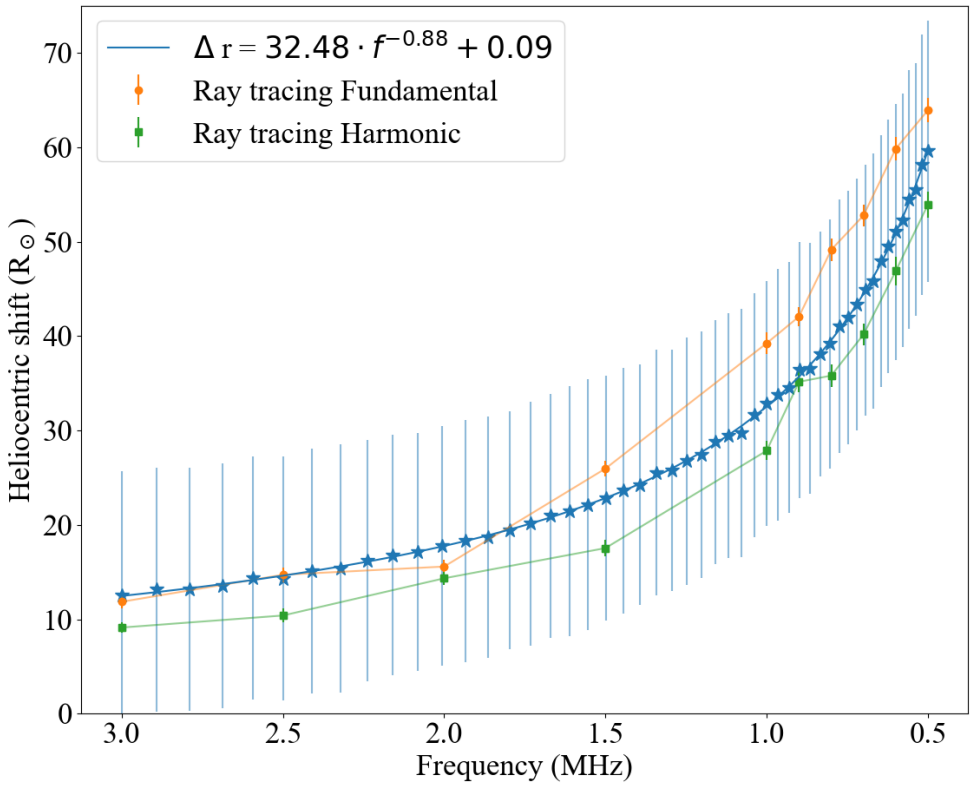


Figure 7.12: Scattering shifts estimated by comparing the BELLA positions to the expected positions along the Parker Spiral given by the Parker density model. Note the frequency axis is inverted as a proxy for distance from the Sun. The results from ray-tracing simulations (Kontar et al., 2019) are shown as orange dots (for fundamental emissions) and green squares (for harmonic emissions). BELLA was found to be in significant agreement with the ray-tracing simulations regardless of whether the emission is fundamental or harmonic. The agreement between the BELLA estimates and the ray-tracing simulations is evidence of the powerful effects that radio-wave scattering induces on the apparent position of radio sources, and validates the descriptions of the anisotropic nature of scattering in the solar corona. Source: Cañizares et al. (in review).

This power law shows that there is a large amplitude coefficient, suggesting a strong sensitivity to changes in frequency. The negative power law coefficient indicates, as expected, an inverse relationship between scattering shifts and frequency. Additionally the power law coefficient is close to -1 which indicates a nearly inversely proportional relationship between the two. It is worth noting that this $\sim f^{-1}$ relationship is also found in measurements of the source size (Kontar et al., 2019), the decay time (Vecchio et al., 2024), and the rise time (Chrysaphi et al., 2024). Furthermore, the offset coefficient of the power law is close to 0, implying that as the frequency approaches infinity, the scattering shift approaches a negligible asymptotic limit, which is also expected from theory.

Fig. 7.12 also shows the expected scattering-induced shifts obtained from 3D ray-tracing simulations of radio-wave propagation in a medium of anisotropic density fluctuations, presented in Kontar et al. (2019). Simulations were performed for both fundamental and harmonic emissions, taking the Parker Spiral as the configuration of the magnetic field.

The ray-tracing simulation outputs are in agreement to the estimates obtained by BELLA. The fundamental ray-tracing simulations are particularly in close agreement with the BELLA estimates at the higher frequency range, whereas the lower-frequency observations are between the simulated fundamental and harmonic source locations. Nevertheless, both the fundamental and harmonic simulations are consistent with the observations and their uncertainties.

The significant agreement between the two independent methods, BELLA and ray-tracing simulations, serves as confirmation of the recent advancements in our theoretical understanding and modelling of anisotropic radio-wave propagation effects (e.g. Kontar et al., 2019; Kuznetsov et al., 2020; Chen et al., 2023). Moreover, it also suggests that density inhomogeneities, which are aligned with the Parker Spiral, have a very strong effect on the path radio-burst photons take from emission to receipt.

7.8 Conclusion

In conclusion, the observations and analyses presented in this chapter (Cañizares et al. (in review)) highlight the intricate dynamics of radio wave propagation through the solar corona, specifically through phenomena such as scattering. The use of BELLA as a multilateration technique with five spacecraft (PSP, SolO, STEREO A, Wind, and MEX) has provided unprecedented detail into the propagation characteristics of Type III radio bursts at the interplanetary frequency range.

The study highlighted the crucial role of spacecraft configuration in the precise localisation of Type III radio sources, with the inclusion of MEX/MARSIS data proving essential for enhancing accuracy and reducing uncertainties. Confidence maps were used in multilateration to ensure the robustness of the results.

The localisation methods included interferometric imaging at 150 MHz by NRH and BELLA at 3 MHz to 0.5 MHz, which were found to be consistent, confirming the reliability of the Parker Spiral model through the imaging's uncertainty region.

Additionally, the effects of radio wave scattering on the apparent positions of the Type III sources was investigated. A solar wind velocity of $\sim 493 \pm 6$ km s^{-1}, was estimated by BELLA and found in excellent agreement with in-situ ACE measurements suggesting ~ 500 km s^{-1}. By comparing the observed positions with the modelled theoretical locations of Type III exciters, scattering shifts were quantified as approximately 12 $R_\odot$ at 3 MHz to 65 $R_\odot$ at 0.5 MHz. Finally, the strong inverse relationship between frequency and scattering was shown, predominantly in the radial direction, following a power law of index -0.88 and in agreement with established scattering models.

8 Conclusions

The work presented in this thesis aimed to further our understanding of the physical phenomena presented in Chapter 1 and Chapter 2 by developing a novel method of localisation, developing a conceptual solar monitoring mission and presenting two in-depth analysis of Type III SRBs, localised in the inner heliosphere.

The main purpose of this thesis was to answer a series of Research Questions:

- Research Question 1: How do electron beams propagate from the Sun to the Earth?
- Research Question 2: How do instrumental effects affect the apparent location of electron beam drivers?
- Research Question 3: How does turbulence affect electron beam propagation and radio emission in the heliosphere?

This thesis covered various aspects of solar radio bursts, localisation methods, spacecraft configurations, and radio wave propagation effects for the purposes of answering the Research Questions. This chapter summarises the key findings and conclusions drawn from the studies presented in Chapters 5, 6, and 7.

8.1 BELLA: Bayesian Localisation and Tracking of Type III Solar Radio Bursts

In Chapter 5, a novel method of localisation known as BELLA was introduced and utilised for the localisation and tracking of a Type III SRB. This chapter gives a in-depth description of the localisation method and focuses on its validation via the usage of simulations and also by comparison to other methods of localisation when analysing a Type III observed by STEREO A, STEREO B and Wind. The main conclusions of this chapter were:

- BELLA was developed as a method of multilateration that uses Bayesian statistics to provide statistically derived source positions which inherently provides an analysis of the uncertainties.
- BELLA successfully demonstrated its ability to provide accurate localisations under a simulated environment of known source locations and known propagation speeds.
- BELLA successfully demonstrated its ability to provide accurate localisation of a Type III radio burst using data from STEREO A, STEREO B and Wind. The results were compared to other established methods of localisation, validating the method.
- Confidence maps were generated and allowed to understand the contribution of spacecraft configuration to the uncertainties of the results. The simulations highlighted the importance of spacecraft configuration in achieving precise localisation. Configurations with well-distributed and sparse spacecraft provided the best results.
- The localisations obtained by BELLA showed that the Type III driver followed the path of a Parker Spiral consistent with the morphology shown by the HUXt solar wind model. It was found that the magnitude of the solar wind was much slower than the speed suggested by the HUXt model.
- The analysis confirmed that the derived electron densities followed an expected $-1/R^2$ slope, although the measured densities were higher than what theoretical models pre-

dict, indicating the presence of radio wave scattering effects.

Overall, BELLA proved to be a robust method for solar radio burst localisation, offering significant improvements over traditional techniques which lacked the ability to inherently produce an analysis of the uncertainties. This work was published in:

> Cañizares, L.A., Badman, S.T., Maloney, S.A., Owens, M.J., Weigt, D.M., Carley, E.P. and Gallagher, P.T., 2024. *Tracking solar radio bursts using Bayesian multilateration.* Astronomy & Astrophysics, 684, p.A182.

8.2 SURROUND: A Constellation of CubeSats around the Sun

Chapter 6 discussed the SURROUND mission concept at Phase-0, which proposes a constellation of CubeSats positioned around the Sun to monitor potentially hazardous space weather events. The main conclusions from this chapter are:

- A 5-spacecraft configuration (*L*1-*L*4-*L*5-*Ahead*-*Behind*) was identified as the most effective for accurate tracking and localisation of solar radio bursts. This configuration benefits from a wide angular separation and stability relative to the Sun-Earth line.
- The originally proposed out-of-ecliptic spacecraft, also known as SC6, was deemed unpractical for a mission of this nature and was discarded from the analysis.
- High cadence data collection (e.g., 10 s to 20 s) was found to be crucial for reducing positional uncertainties in burst localisation.
- Simulations demonstrated that even a 4-spacecraft configuration could achieve acceptable results, providing a viable fallback in case of spacecraft loss. However, the 5-spacecraft configuration offers redundancy, enhancing the mission's reliability and robustness.

The SURROUND mission concept represents a promising approach to improving space

weather monitoring and forecasting, leveraging low-cost CubeSats for comprehensive solar observations. The work from this chapter was accepted for publication as a shared first author publication, a preprint of this work is available as:

> Weigt, D.M.*, Canizares, L.A.*, Maloney, S.A., Murray, S.A., Carley, E.P., Gallagher, P.T., Macario-Rojas, A., Crisp, N. and McGrath, C., 2023. *The science behind SURROUND: a constellation of CubeSats around the Sun.* arXiv preprint arXiv:2308.04194. *these authors contributed equally to this work

Additionally, work from this chapter was submitted for publication and it is pending review:

> Macario-Rojas, A., Crisp, N. H., McGrath, C. N., Cañizares, L. A., Weigt, D. M., Maloney, S. A., Murray, S. A., Gallagher, P. T. *Mission Concept for SURROUND: Operational Space Weather Detection and Tracking using Small Spacecraft* Submitted to: Acta Astronautica (in review)

8.3 Measuring Radio Wave Propagation Effects

Chapter 7 focused on the detailed study of radio wave propagation effects, particularly scattering, using the first observation of a Type III from five spacecraft; PSP, STEREO A, SolO, Wind and MEX. The addition of MEX data to this study was found to be critical. It was shown that without it, the multilateration errors would have dominated the results. The major conclusions from this study were:

- The study successfully employed BELLA for the multilateration of a Type III radio burst using five spacecraft. This provided unprecedented detail into the propagation characteristics of the burst at interplanetary distances.
- Similarly to Chapter 5, the BELLA results were found to follow the path of Parker Spiral.
- NRH interferometric imaging showed evidence of the onset location of the multilaterated Type III. The location of the NRH imaging was consistent with the BELLA

derived Parker Spiral.

- The analysis highlighted the significant impact of spacecraft configuration on localisation accuracy. Configurations that were well-distributed and sparse were classified as **Excellent** and provided the most reliable results. Configurations that were clustered were classified as **Failed** and resulted in high uncertainties. **Good** and **Poor** classifications were intermediate cases, which were dependent on the size and location of the computed area of confidence.

- Comparing the BELLA multilaterated sources with theoretically modelled sources showed evidence of radio wave scattering revealing a lensing-like effect that caused apparent source locations to differ significantly from true locations, as well as changing the apparent velocity of the solar wind. The scattering was found to be predominantly radial, with a strong inverse relationship between scattering shifts and frequency.

This work shows the importance of considering spacecraft configuration in solar radio burst localisation and highlights the potential of multi-spacecraft missions for advancing our understanding of space weather phenomena. The usage of this five-spacecraft measurement allowed for a detailed analysis of radio scattering which showed significant agreement with leading scattering models.

This work is currently under preparation:

> Cañizares, L. A., Badman, S. T., Chrysaphi, N.,Bhunia, S., Sanchez-Cano, B., Maloney, S. A., and Gallagher, P. T., *Electron Beam Propagation and Radio-Wave Scattering in the Inner Heliosphere using Five Spacecraft.* In review, submitted to Astronomy & Astrophysics.

8.4 Final Remarks

This thesis has demonstrated the value of advanced localisation techniques, innovative mission concepts, and detailed analyses of radio wave propagation, improving our understanding

of space weather phenomena and unlocking the possibility of using BELLA for further more detailed studies. BELLA is available open source and I personally would like to encourage the reader to use it for scientific studies, and help develop it further. BELLA can be found via Zenodo,

> Canizares, L. A. (2023). canizarl/solarmap: Release v0.0.7 (v0.0.7). Zenodo. https://doi.org/10.5281/zenodo.10262602

or GitHub,

> https://github.com/TCDSolar/BELLA

9 Future Work

The research outlined in this thesis focused on the usage of a new method to localise the SRB drivers based on Bayesian statistics. BELLA was developed with the intention of providing confident results, giving accurate and precise localisations. Currently, BELLA was released and is available at Canizares (2023). However, this method was simplified as a 2D tool, making the verification of BELLA a manageable task. Additionally, the development of BELLA during this PhD was strictly the responsibility of a single individual, and therefore there are numerous tasks that have to be addressed, such as a number of libraries that require attention, given that updates might result in some incompatibilities. BELLA still has a lot of room for improvement.

Furthermore, the development of the SURROUND mission via the usage of simulations answered a number of questions, which should induce a number of changes in the conceptual design of the mission. In this chapter, these changes will be addressed.

Finally, there are a number of potential studies that can result by utilising BELLA, these further studies could help us further our understanding of the propagation of electron beams, shock-driven CMEs or propagation effects, however, some of these studies might have to wait for the next generation of solar dedicated spacecraft.

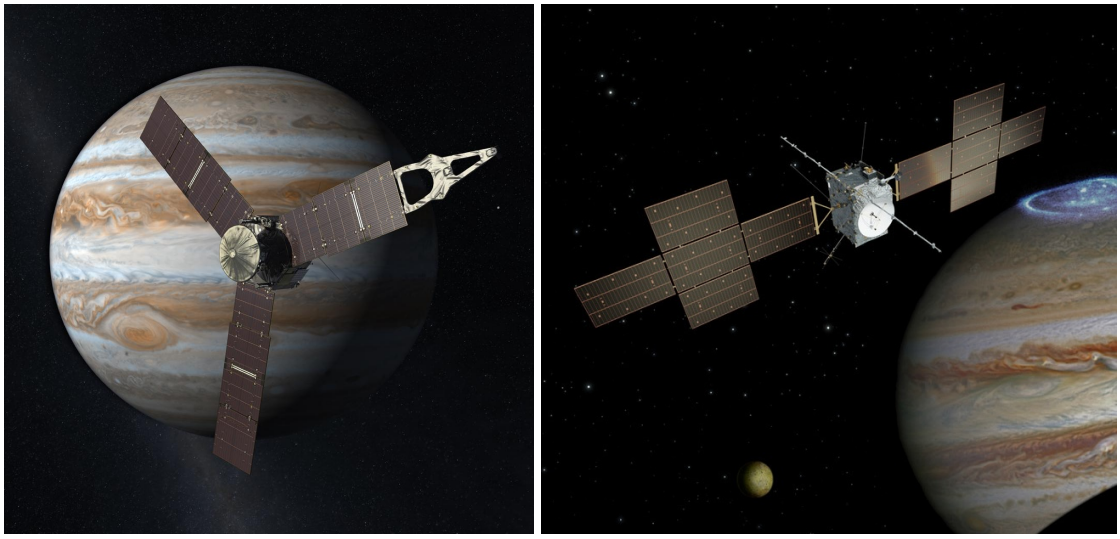


Figure 9.1: Artist impressions of the (*left*) Juno and (*right*) JUICE missions to Jupiter. Despite not being solar dedicated missions, both spacecraft are equipped with radio instruments that could detect SRBs. Credit: ESA/NASA

9.1 Making solar observations with eight spacecraft

The addition of MEX to the fleet of spacecraft used for solar observations was a relatively unexpected revelation. This spacecraft made the analysis from Chapter 7 possible. Additional spacecraft could unlock the potential of BELLA and while Figure 6.6 showed that more spacecraft does not mean a radical improvement on the results performance, the true benefit of additional spacecraft is that new 'Excellent' configurations could emerge, giving rise to larger windows of opportunity to observe SRBs.

9.1.1 The Juno Waves investigation

The Juno spacecraft (Bolton et al., 2010) (see Figure 9.1 *left*), a NASA mission to Jupiter, was launched in 2011 with an initial mission duration of seven years; however, its mission has since been extended through 2025. Among Juno's suite of instruments is Waves (Kurth et al., 2017) the radio instrument designed to study Jupiter's magnetosphere and understand the origins of the auroral activity observed on the poles of the jovian planet.

Juno has a number of frequency receivers, the most relevant for this thesis is the high fre-

quency receiver (HFR), with a range of 0.1 MHz to 45 MHz. At this frequency range, the data from this spacecraft would be compatible with all the spectrograms used in this thesis. The cadences used by Juno/Waves range from 1 s at perijove to 30 s at apojove with periods of 10 s in between. The impressive 1 s cadence at periapsis would make Juno/Waves the fastest cadence of all the space-based spectrograms used for solar observations. Furthermore, the high frequency limit of the spectrogram opens the door at observing Type II radio bursts.

9.1.2 JUICE's Radio Plasma Waves Investigation

If Juno is not enough for observing SRBs, the JUpiter ICy moons Explorer (JUICE; Grasset et al., 2013) could be an alternative. JUICE (see Figure 9.1 *right*), is an ESA mission that is focused on the investigation of the jovian planet and its three largest galilean moons; Ganymede, Callisto and Europa. JUICE was launched in April of 2023 and its orbit injection is expected to be completed by July of 2031[1]. Fortunately, the antennas and solar panels have already been deployed and the radio instruments are collecting data on its journey to Jupiter. Unfortunately, the data is not public yet.

The Radio Plasma Waves Investigation (RPWI; Wahlund et al., 2013) is JUICE's radio instrument designed to investigate radio and plasma waves using four receivers, GANDALF, MIME, FRODO, and JENRAGE. The receiver that is most similar to the receivers used by BELLA is JENRAGE with a frequency range of 80 kHz to 45 MHz, a frequency range that is well within the ranges of all the spectrograms used in this Thesis. Additionally, the cadence of the instrument is of 0.2 s to 30 s depending on the different modes. This makes RPWI a suitable candidate to contribute data to a future BELLA study.

[1]JUICE timeline: `https://www.cosmos.esa.int/web/juice/timeline`

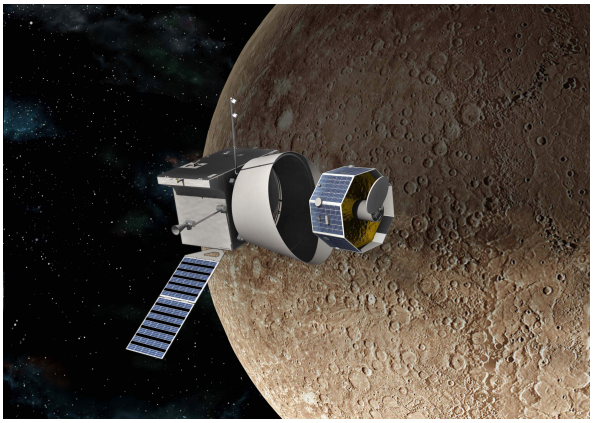


Figure 9.2: BepiColombo is mission developed by ESA and JAXA to study the planet Mercury. BepiColombo consists of two spacecraft, the Mercury Planetary Orbiter (MPO) and the Mercury Magnetospheric Orbiter (Mio). The Plasma Wave Investigation (PWI) on board Mio was designed for solar monitoring of SRBs and could potentially be used in conjunction with other radio instruments for BELLA multilateration. Credit: ESA/JAXA

9.1.3 BepiColombo's Plasma Wave Investigation

BepiColombo (Benkhoff et al., 2021) is a joint mission between ESA, and the Japanese Aerospace Exploration Agency (JAXA) launched on October of 2018 with the purpose of investigating Mercury. BepiColombo is not one, but two spacecraft, the Mercury Planetary Orbiter (MPO) and the Mercury Magnetospheric Orbiter (Mio) spacecraft. Of all the instruments on board Mio, the Plasma Wave Investigation (PWI; Kasaba et al., 2010) is the most relevant for this thesis.

PWI is a radio instrument designed to studying in-situ and remote-sensing observations of electric fields, plasma waves, and radio waves in the Hermean magnetosphere and exosphere. Similar to other space-based radio instruments, PWI has a number of radio receivers tuned to different frequency ranges. The receiver that could potentially be of benefit to BELLA is Spectroscopie des Ondes Radio and du Bruit Electrostatique Thermique which means The radio waves and thermal electrostatic noise spectroscopy (SORBET; Moncuquet et al., 2006) which operates in the 2.5 kHz to 10.2 MHz range. The cadence is reported to vary between 16 s at apohermion and 4 s at perihermion.

It should be noted that despite being a Mercury mission, one of SORBET's requirements is:

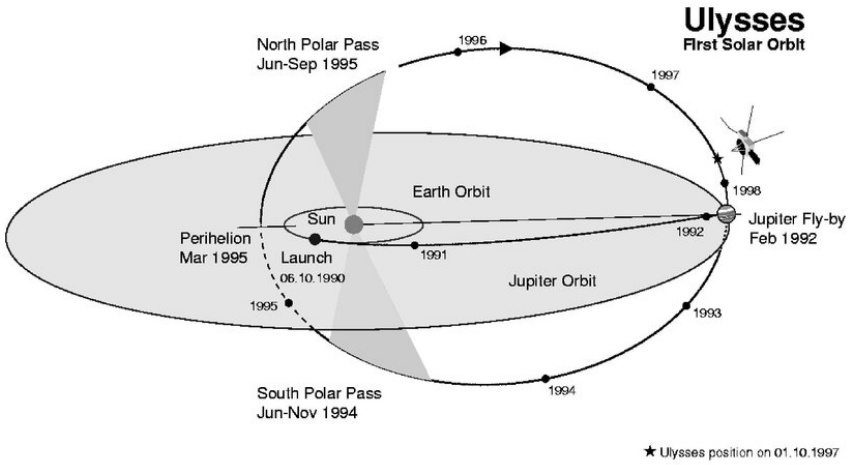


Figure 9.3: Ulysses was launched into a highly elliptical orbit located at approximately 90° from the ecliptic with an aphelion of 5 au and 1 au perihelion. The spacecraft is equipped with a radio spectrometer tuned to the DC to 1 MHz frequency range and was operational between 1990 and 2009. The last three years of this period coincides with the launch of the STEREO mission making this three year period a candidate for five spacecraft observations of SRBs if including MEX and Wind. The out-of-ecliptic configuration of the Ulysses orbit makes this configuration of spacecraft particularly attractive for the development of 3D BELLA and investigation of SRB sources in 3D.

> *Monitoring of solar radio emissions up to 10 MHz in order to create a solar activity index from the view point of Mercury, allowing to correlate it with the Hermean magnetospheric response.*

This mission statement implies that SORBET was designed for the purposes of detecting solar activity, includying Type IIs and Type IIIs making this spectrometer a good candidate of becoming the sixth spacecraft in a future BELLA study.

9.1.4 Ulysses' Unified Radio and Plasma Wave Instrument

The Ulysses mission (Marsden et al., 1986; Wenzel et al., 1992) was launched in 1990 and decommissioned in 2009, given that Wind was launched in 1994, MEX was launched in 2003, and STEREO was launched in 2006, there is a 3 year period in which the five spacecraft were simultaneously observing radio waves.

On board Ulysses was the Unified Radio and Plasma Wave Instrument (URAP; Stone et al., 1992) a radio spectrometer equipped with a 72.5 m electric field antenna and a 7.5 m monopole antenna. URAP was capable of detecting in the DC to 1 MHz frequency range making it ideal for the investigation of interplanetary Type IIIs.

Ulysses was launched into a relatively highly elliptical orbit with perihelion at 1 au and aphelion at 5 au. The orbit is in an out-of-ecliptic configuration at approximately 90°. This out-of-ecliptic configuration makes the potential five-spacecraft configuration an ideal candidate for 3D multilateration.

9.2 BELLApy

Currently, BELLA is nothing more than a number of Python scripts that are available for download at GitHub. These scripts require a number of installed dependencies and it is currently the responsibility of the new user to install these dependencies correctly and set up the correct environment. The aim, is to turn BELLA into a Python package, however, there are a number of milestones that have to be addressed first.

Setting up the BELLA environment is possible and has been tested on a number of new machines. However, for reasons that I do not fully understand, this is a relatively easy task in some machines and near impossible in other machines. BELLA uses by default the PyMC3 package, which is the older version of PyMC (Abril-Pla et al., 2023). One of the reasons BELLA is hard to install is that PyMC3 (and PyMC) are dependent on a Python package known as Theano (Al-Rfou et al., 2016), in particular Theano-PyMC. Theano is a Python library that allows to define, optimise, and evaluate mathematical expressions involving multi-dimensional arrays efficiently. It essentially, helps the Python interpreter convert processes that would be used by the computers central processing unit (CPU), into graphics processing unit (GPU) processes. In plain language, this allows to make a larger number of computations faster. It also allows for the dynamic generation of C code, which accelerates each process. This package is notably difficult to install on Windows machines, often failing due

to C-compiler incompatibilities. While there are internet instructions on how to do this, and testimonials of people saying that they have been able to install it, I personally have never been able to install Theano on a Windows machine and there is a relative large number of frustrated people on these forums. Installing Theano is possible, and strict guidelines and instructions need to be addressed, but this will require time to explore all the different errors. Furthermore, BELLA will be updated so that it uses the latest stable version of PyMC and not PyMC3.

The next package that needs to be addressed before turning BELLA into a Python package is Kapteyn (Terlouw & Vogelaar, 2016). BELLA makes use of the kmpfit module on Kapteyn in order to fit the GH polynomial as the lightcurve of a Type III. The package was developed before Astropy (Robitaille et al., 2013; Price-Whelan et al., 2018, 2022) and therefore most of the functionality of Kapteyn was considered redundant after the release of Astropy. Because of this, the Kapteyn team stopped the development of Kapteyn and only updates the package sporadically, in order to maintain the functionalities that are still not addressed by Sunpy or Astropy. This means that Kapteyn was restricted to the usage of Python 3.8 (at the time when BELLA was being developed) and only recently was made compatible with Python 3.10 and Matplotlib 3.7. For context, Python 3.12 is the current version of Python, and 3.8 will stop being supported in October of this year[2]. Matplotlib is also outdated, as the current release of Matplotlib is 3.9.1. With each of these new releases incompatibilities appear and while it is possible to restrict BELLA to old releases, it is also not recommended and sometimes very difficult to achieve, as installing one package wrong might interfere with the BELLA environment and ruin it. The solution is to make BELLA agnostic to Kapteyn. Taking the relevant functions from the module and making them compatible with newer Python versions.

HDF5 and h5py (Collette, 2013) are packages used for the manipulation of data. Installing these have also caused problems in the past during installation. Most of the problems during installation were caused due to incompatibilities with older versions of packages required

[2] `https://devguide.python.org/versions/`

for Kapteyn, PyMC3 and Theano. There is a very thin range of compatible package versions and it is hard to find this range. It is expected that after addressing the updates of PyMC, Theano and the deletion of Kapteyn, the installation of HDF5 and h5py will be streamlined.

Finally, the last process before turning BELLA into a Python package is to modify all the relevant scripts according to the required and recommended pythonic architecture[3]. This is not necessarily difficult but rather time consuming. The most time consuming procedure will be the development of the required documentation for a Python package. BELLA is currently available for researchers to use, and in this thesis I have presented evidence that it is objectively better than the current alternatives. However, unless the process of using BELLA is user-friendly and accessible, it will never be used by the scientific community.

9.2.1 BELLA 3D

One of the advantages of GP over multilateration is that GP allows for 3D localisation intrinsically. However, multilateration requires at least four spacecraft for three dimensional capabilities. This is because in 3D, one spacecraft leads to a sphere, two spacecraft constrain both spheres at a circular area, three spacecraft will constrain the area into two points and the fourth spacecraft will find the solution (see Figure 9.4 for schematic). Given that, as discussed in chapters 5–7, the instrumental cadence will lead to an uncertainty, these points will be in fact spheroids of uncertainty, analogous to the ellipses of uncertainty shown in this thesis.

Chapters 5–7 also showed the importance of spacecraft separation and distribution around the source for the minimisation of uncertainties, giving rise to uncertainties in the order of 1 au if all spacecraft are close to each other. Assuming that this conclusion extends to the 3-dimensional coordinate system, a three dimensional version of BELLA would not offer much value if the uncertainty in the Z-coordinate is in the order of 1 au. However, this is about to change. As it was mentioned in Chapter 3, it is expected that by the year 2028, SolO will

[3] `https://packaging.python.org/en/latest/tutorials/packaging-projects/`

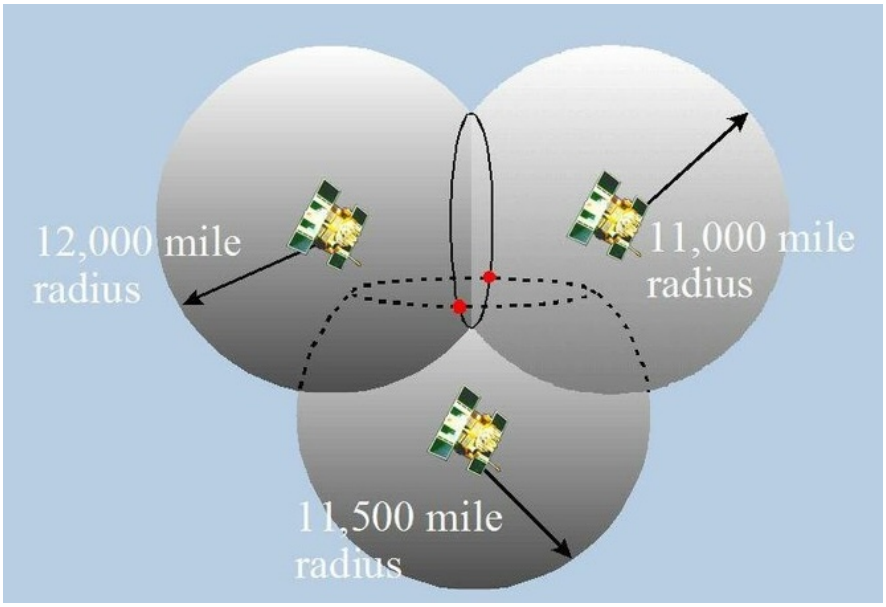


Figure 9.4: In 3D, multilateration forms spheres of uncertainty at each spacecraft. The intersection of three multilateration spheres results in two points. In order to obtain a single solution in 3D multilateration, a fourth spacecraft is required. Source: Bektas et al. (2018)

observe the Sun from 30 ° to 35 ° at perihelion (Müller et al., 2020). Chapters 5–7 showed that at 30 ° the separation is not 'Excellent' but it will certainly give better results than what it is currently possible, likely around 50 $R_{\odot}$ (estimate based on Figure 5.4). However, this number will depend on the location of the rest of the spacecraft.

Figure 9.5 (a) shows the configuration of all the spacecraft used in this thesis as well as the potential spacecraft introduced in this chapter on 26 June 2028. During this date SolO will be located at $\sim$ 30 ° outside of the ecliptic, making 3D multilateration possible. Figure 9.5 (b) shows that during this date, the solar activity will likely be comparable to that of 2023, which was a relatively active year. The location of STEREO A is not shown because the ephemerides were not available for dates after October 2024, however, based on a 22 °/year approximation of its orbit, a back of the envelop calculation positions STEREO A at approximately 90 ° and 1 au, in the XY plane. Wind is also not shown in the diagram for the same reason but it is known that Wind is at L1, which at the scale of the figure is approximately the location of Earth. This date and this spacecraft configuration offers a unique opportunity for the first 8-spacecraft observation of a Type III. Furthermore, the location of

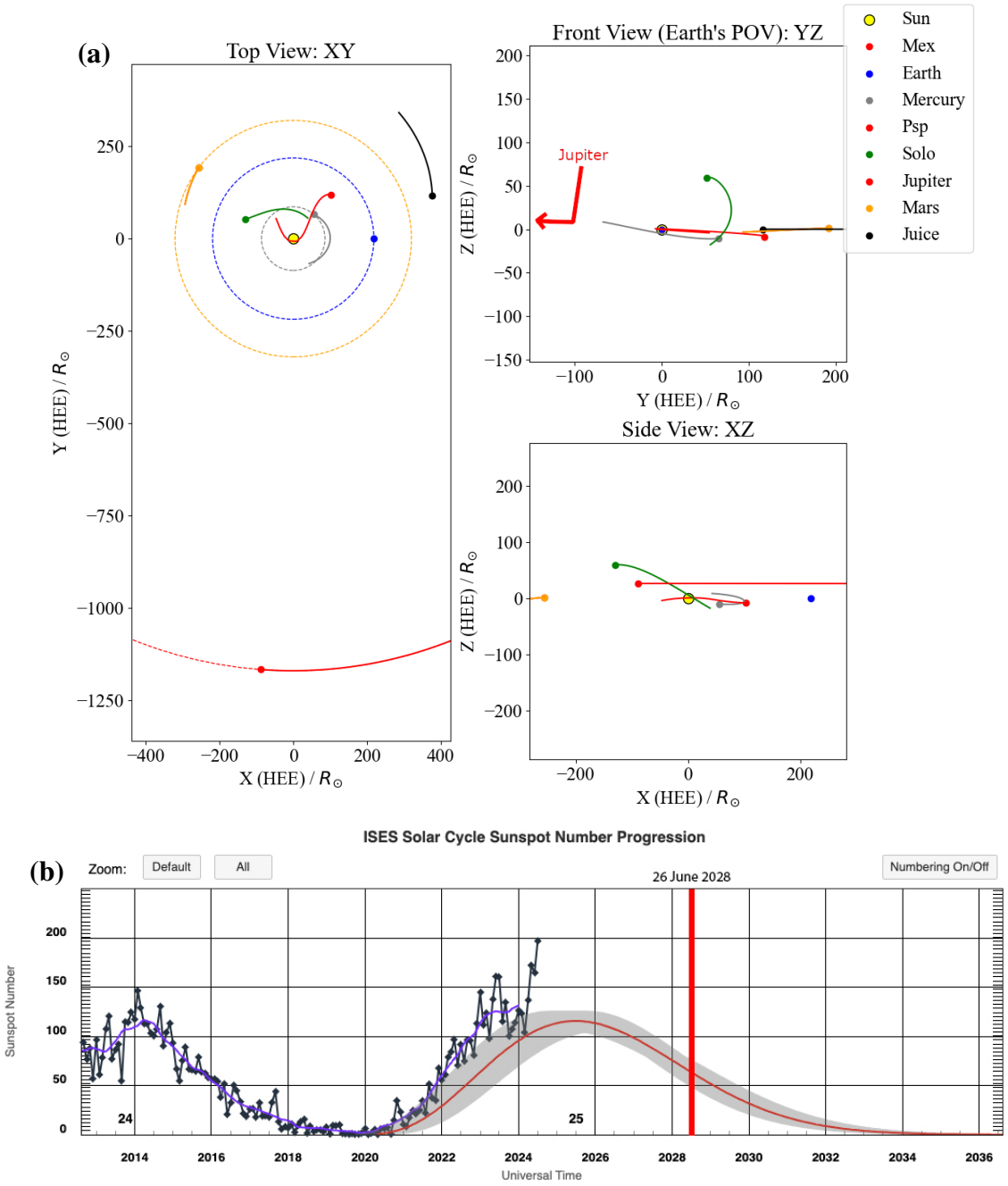


Figure 9.5: (a) Orthographic projections showing the locations of a potential 8-spacecraft configuration. These spacecraft would be PSP, SolO, Wind, STEREO A, MEX, JUICE, JUNO and BepiColombo-Mio. No ephemerides were available for STEREO A and Wind and therefore are not visible in the plot, however based on a 22 °/year it is estimated that it will be located at 90 ° at approximately 1 au and confined to the ecliptic. Wind's location is at L1, which at this scale is approximately the location of Earth. This date offers a unique opportunity where SolO is located at $\sim$ 30 ° outside of the ecliptic, making possible a 3D multilateration. (b) Projection of the solar cycle showing that 2028 will have an activity level comparable to that of 2023. Source of (b): NOAA

Juno and Juice as well as Earth would make for an interesting case in the event of a Type II occurring at less than 45 MHz.

Fortunately, BELLA allows for a relatively quick transition to 3D, and only minor changes have to be implemented to the main code. Now that the 2D version has been validated, developing BELLA 3D is the logical next step. Given that no current spacecraft is available outside of the ecliptic, this development will require validation through simulations. Subsequently, a suitable Type III candidate will need to be identified. However, until SolO reaches its maximum latitude, the uncertainties are expected to remain relatively large.

9.2.2 BELLA+

BELLA has an additional advantage that has not been discussed yet. Currently, BELLA uses multilateration as its sole form of localising the source of the emission. However, BELLA exploits the multilateration equations as a likelihood function. This means that BELLA, in theory, is not restricted by the usage of TOA multilateration. Additional priors and physical models can be added to the BELLA engine. This includes GP and the intensity method shown in Reiner et al. (2009) and Musset et al. (2021) as well as density models and other advanced physics models. Adding additional priors and models could revolutionise our current understanding of BELLA, potentially making spacecraft configurations that were considered unusable for multilateration, into configurations that do not affect the localisation process and reducing the uncertainties further than the limits established by instrumental cadence.

9.3 SURROUND 2.0

Chapter 6 showed the benefits of a well distributed constellation of spacecraft. SURROUND would allow for constant monitoring of solar activity, and would provide invaluable data to the scientific community. One of the disadvantages of using the current fleet of spacecraft for scientific observations is the notable difficulty to find suitable 'Excellent' configurations. This is because all the spacecraft are injected into completely different orbits. The results

from developing SURROUND showed how the *L*1-*L*4-*L*5 configuration provided a solid backbone that would allow constant monitoring supported with the *Ahead* and *Behind* spacecraft supporting enhancement support for performance reasons. However Chapter 6 focused on my work for the ESA Phase-0 mission and did not address other aspects of the project such as Mission Analysis or Spacecraft System Design. Table 9.1 shows the estimates for the transfer velocity, transfer time and maintenance requirements given by the Mission Analysis analysis simulations performed in Macario-Rojas, A. et al., (in review). This table shows, that the *L*4/*L*5 spacecraft are notoriously costly to inject into their corresponding orbit.

Table 9.1: Mission Analysis of the Phase-0 SURROUND mission showing the estimated transfer velocities, transfer time and maintenance. Source: Macario-Rojas, A. et al., (in review).

Location	**Transfer time [months]**	**Transfer** ΔV **[m s^{-1}]**	**Maintenance** ΔV **[m s^{-1}]**	**Total** ΔV **[m s^{-1}]**
L1	4	30	30	330
L4	15–23	1500–900	0	1500–900
L5	15–23	1500–900	0	1500–900
Ahead	0	200	20	220
Behind	5	30	20	50

Knowing that SURROUND is a budget mission, the associated additional costs of inserting two spacecraft into L4 and L5 give rise to the following new concept. SURROUND 2.0 is an alternative mission where instead of launching spacecraft to L4 and L5, the spacecraft constellation will now consist of 3 pairs of *Ahead/Behind* spacecraft and one single spacecraft located at L1. Each of the *Ahead/Behind* pairs will get inserted into orbit in 60 $^\circ$ increments in order to cover a full orbit. By using three pairs of *Ahead/Behind* spacecraft, there is not a constant *L*1-*L*4-*L*5 backbone, but its guaranteed that at least 3 spacecraft are located in the Earth-side quadrants. The mission can operate in two modes, scientific and monitoring.

The monitoring mode will make use of the *L*1 spacecraft and the nearest two spacecraft, thus allowing for constant monitoring and quick response. If needed, the remaining spacecraft can be used accordingly for support observations.

The scientific mode can make use of all spacecraft with the difference that the data is sent

back to Earth at full resolution. In order to do this, each spacecraft will have on-board computers that make use of artificial intelligence algorithms capable of distinguishing between useful events and noise. Once the on-board computers have decided which events are worth investigating, the spacecraft will proceed a full data dump towards ground control. This will only be done when two spacecraft are near Earth, and the rest of spacecraft will proceed to transmit their data in the direction of Earth, following the path of nearest spacecraft, thus creating a network of connected spacecraft.

9.4 Firefly

Firefly (Raouafi et al., 2023b) is a proposed mission currently funded by NASA. The mission consists of four spacecraft which orbit in two planes (see Figure 9.6). The first pair of spacecraft would be located in the ecliptic at approximately 1 au. These spacecraft would initiate their journey as an Ahead/Behind spacecraft pair but will be parked at 120 ° from Earth once they have reached this point. The other spacecraft pair would be injected into an out-of-ecliptic orbit at 70 ° with respect to the ecliptic plane. This polar orbit was designed to observe both poles of the Sun simultaneously.

The mission objective of Firefly is to study the Sun in detail (Harra et al., 2023), from the interior to the surface, covering science objectives such as the study of the internal structure, meridional flows, solar dynamo, magnetic fields, coronal physics, solar activity, the solar wind, space weather and the solar cycle. To do this, each spacecraft would be equipped with a series of in-situ instruments as well as remote instruments capable of studying the Sun at visible to EUV wavelengths. Table 9.2 shows a list of the currently proposed instruments showing that not all spacecraft would necessarily be equipped with all the instruments. This decision was reported to be a cost savings decision (Raouafi et al., 2024). However, in order to prevent cross-calibration issues, any instrument mounted on different spacecraft would be identical. This list of instruments is a preliminary list of instruments considered during their Phase-A study and is not a final list of instruments.

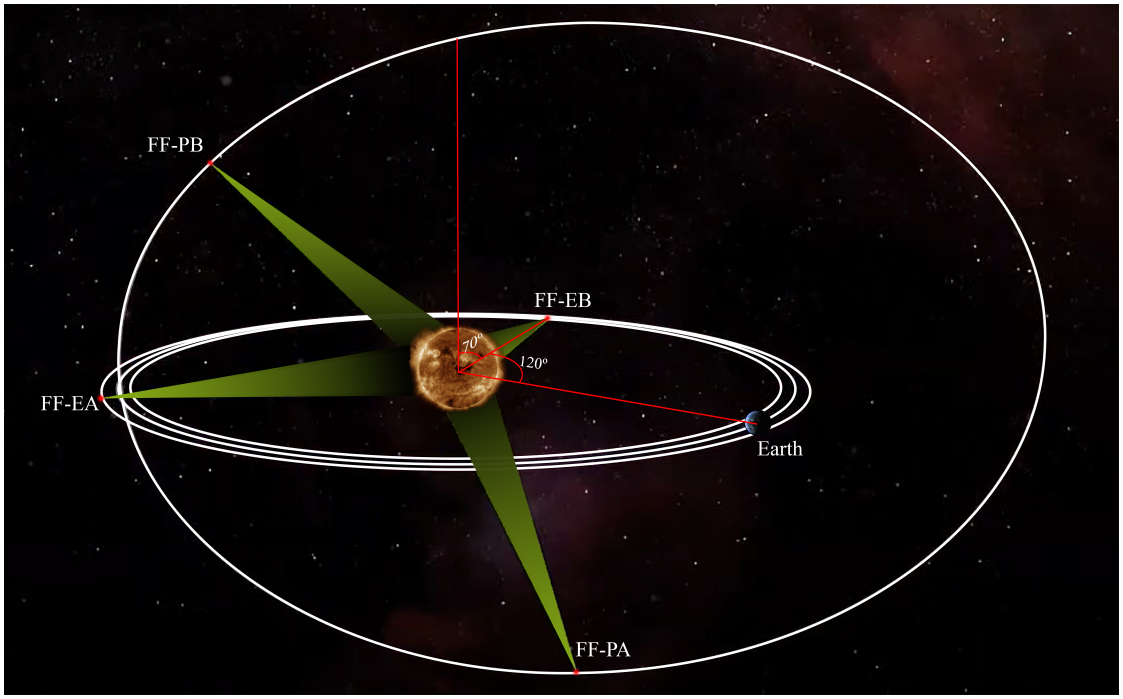


Figure 9.6: The proposed spacecraft configuration of the Firefly mission. The Firefly mission is composed of two pairs of spacecraft, two confined to the ecliptic at 120 ° from Earth and two in a polar configuration where the orbital plane is at 70 ° with respect to the ecliptic. This spacecraft configuration combined with solar observations from Earth would make a potential candidate for Excellent configurations capable of 3D multilateration. Source: Adapted from Raouafi et al. (2024).

Given the spacecraft configuration of Firefly where two spacecraft are located in a polar orbit and two spacecraft are in an ecliptic orbit with an intrinsic large angular separation between all spacecraft, Firefly would make an excellent candidate for a mission designed to perform 3D multilateration. The addition of radio spectrometers to the suite of instruments would be complementary towards the study of Type IIs and Type IIIs which are key diagnostic tools for the study of particle acceleration, shock dynamics, and plasma wave interactions. The SURROUND mission originally considered an out-of-ecliptic spacecraft which was discarded because injecting CubeSats into a polar orbit is impractical from a time perspective, but work from Chapters 5–7 have provided substantial evidence of the benefits of large angular separation towards the localisation uncertainties. A mission of this nature, where the spacecraft are capable of reaching high latitudes, would certainly pose a leap forward in the study of the solar corona, complementing the other suite of instruments.

Instrument	**FF-EA**	**FF-EB**	**FF-PA**	**FF-PB**
Doppler Vector Magnetograph (DVM)	✓	✓	✓	✓
EUV Imager/Solar Spectral Irradiance (EUV/SSI)	✓	✓	✓	
White Light Coronagraph (WLC)	✓	✓	✓	✓
White Light Heliospheric Imager (WL HI)	✓			
Fluxgate Magnetometer (FGM)	✓	✓	✓	✓
Faraday Cup (FC)	✓	✓	✓	✓
Solar Wind Composition (SWC)			✓	
Solar Energetic Particle Suite (EPS)	✓	✓	✓	

Table 9.2: List of the proposed instruments for the Firefly mission and checkmarks showing which spacecraft will carry each instrument. To prevent cross-calibration issues, any instrument carried by multiple spacecraft will be of identical specification. A radio instrument was not considered for this study. However, the addition of a radio instrument could complement the mission are a key diagnostic towards the study of shock driven CMEs, particle accelerations and plasma waves interactions. Source: Adapted from Raouafi et al. (2024).

Radio spectrometers such as Juice/RPWI or SolO/RPW have demonstrated that radio spectrometers are available at a high technology readiness level (TRL) which would suppose a relatively low developmental cost. This makes the consideration of a radio spectrometer an attractive option.

In this chapter, given the large form factor of each Firefly spacecraft, I propose to include a radio spectrometer of similar specification to the radio instrument on board Juice which has a frequency range of 80 kHz to 45 MHz with cadences capable of 0.2 s. The combination of these four spectrometers with the support of SolO, PSP, Wind, STEREO A, and the occasional support of Juno, Juice, and BepiColombo, would make an exceptional suite of spacecraft capable of performing highly accurate and precise multilaterations and triangulations.

Bibliography

Abril-Pla, O., Andreani, V., Carroll, C., Dong, L., Fonnesbeck, C. J., Kochurov, M., Kumar, R., Lao, J., Luhmann, C. C., Martin, O. A., Osthege, M., Vieira, R., Wiecki, T., & Zinkov, R. (2023). Pymc: a modern, and comprehensive probabilistic programming framework in python. *PeerJ Computer Science*, 9, e1516. Cited on page 158.

Acuña, M., Ogilvie, K., Baker, D., Curtis, S., Fairfield, D., & Mish, W. (1995). The global geospace science program and its investigations. *Space Science Reviews*, 71, 5–21. Cited on pages 39 and 40.

Al-Rfou, R., Alain, G., Almahairi, A., Angermueller, C., Bahdanau, D., Ballas, N., Bastien, F., Bayer, J., Belikov, A., Belopolsky, A., et al. (2016). Theano: A python framework for fast computation of mathematical expressions. *arXiv e-prints*, (pp. arXiv–1605). Cited on page 158.

Alcock, B. T. (2018). *Solar electron and radio propagation in the turbulent solar corona*. PhD thesis, University of Glasgow, UK. Cited on pages 21, 68, and 69.

Anderson, M., Appourchaux, T., Auchère, F., Cuadrado, R. A., Barbay, J., Baudin, F., Beardsley, S., Bocchialini, K., Borgo, B., Bruzzi, D., et al. (2020). The solar orbiter spice instrument-an extreme uv imaging spectrometer. *Astronomy & Astrophysics*, 642, A14. Cited on page 51.

Antiochos, S. & Sturrock, P. (1978). Evaporative cooling of flare plasma. *Astrophysical*

Journal, Part 1, vol. 220, Mar. 15, 1978, p. 1137-1143., 220, 1137–1143. Cited on page 10.

Antonucci, E., Romoli, M., Andretta, V., Fineschi, S., Heinzel, P., Moses, J. D., Naletto, G., Nicolini, G., Spadaro, D., Teriaca, L., et al. (2020). Metis: the solar orbiter visible light and ultraviolet coronal imager. *Astronomy & Astrophysics*, 642, A10. Cited on page 51.

Aptekar, R., Frederiks, D., Golenetskii, S., Ilynskii, V., Mazets, E., Panov, V., Sokolova, Z., Terekhov, M., Sheshin, L., Cline, T., et al. (1995). Konus-w gamma-ray burst experiment for the ggs wind spacecraft. *Space Science Reviews*, 71, 265–272. Cited on page 42.

Arge, C. & Pizzo, V. (2000). Improvement in the prediction of solar wind conditions using near-real time solar magnetic field updates. *Journal of Geophysical Research: Space Physics*, 105(A5), 10465–10479. Cited on page 95.

Aschwanden, M. (2004). *Physics of the Solar Corona*. Springer. Cited on page 35.

Badman, S. (2023). *STBadman/Radio-Public: Initial Release*. Cited on page 69.

Badman, S. T., Carley, E., Cañizares, L. A., Dresing, N., Jian, L. K., Lario, D., Gallagher, P. T., Oliveros, J. C. M., Pulupa, M., & Bale, S. D. (2022). Tracking a beam of electrons from the low solar corona into interplanetary space with the low frequency array, parker solar probe, and 1 au spacecraft. *The Astrophysical Journal*, 938(2), 95. Cited on pages xvii, 17, 21, 22, 69, 73, 88, 91, 106, 107, and 125.

Bale, S. D., Goetz, K., Harvey, P. R., Turin, P., Bonnell, J. W., Dudok de Wit, T., Ergun, R. E., MacDowall, R. J., Pulupa, M., Andre, M., Bolton, M., Bougeret, J.-L., Bowen, T. A., Burgess, D., Cattell, C. A., Chandran, B. D. G., Chaston, C. C., Chen, C. H. K., Choi, M. K., Connerney, J. E., Cranmer, S., Diaz-Aguado, M., Donakowski, W., Drake, J. F., Farrell, W. M., Fergeau, P., Fermin, J., Fischer, J., Fox, N., Glaser, D., Goldstein, M., Gordon, D., Hanson, E., Harris, S. E., Hayes, L. M., Hinze, J. J., Hollweg, J. V., Horbury, T. S., Howard, R. A., Hoxie, V., Jannet, G., Karlsson, M., Kasper, J. C., Kellogg, P. J.,

Kien, M., Klimchuk, J. A., Krasnoselskikh, V. V., Krucker, S., Lynch, J. J., Maksimovic, M., Malaspina, D. M., Marker, S., Martin, P., Martinez-Oliveros, J., McCauley, J., McComas, D. J., McDonald, T., Meyer-Vernet, N., Moncuquet, M., Monson, S. J., Mozer, F. S., Murphy, S. D., Odom, J., Oliverson, R., Olson, J., Parker, E. N., Pankow, D., Phan, T., Quataert, E., Quinn, T., Ruplin, S. W., Salem, C., Seitz, D., Sheppard, D. A., Siy, A., Stevens, K., Summers, D., Szabo, A., Timofeeva, M., Vaivads, A., Velli, M., Yehle, A., Werthimer, D., & Wygant, J. R. (2016). The FIELDS Instrument Suite for Solar Probe Plus. Measuring the Coronal Plasma and Magnetic Field, Plasma Waves and Turbulence, and Radio Signatures of Solar Transients. *Space Science Reviews*, 204, 49–82. Cited on page 48.

Barnard, L. & Owens, M. (2022). Huxt—an open source, computationally efficient reduced-physics solar wind model, written in python. *Frontiers in Physics*, (pp. 1062). Cited on page 93.

Barnes, W. T., Community, S., Christe, S., Freij, N., Hayes, L. A., Stansby, D., Ireland, J., Mumford, S. J., Ryan, D. F., & Shih, A. Y. (2023). The sunpy project: An interoperable ecosystem for solar data analysis. *Frontiers in Astronomy and Space Sciences*, 10, 1076726. Cited on page 59.

Barnes, W. T., The SunPy Community, Bobra, M. G., Christe, S. D., Freij, N., Hayes, L. A., Ireland, J., Mumford, S., Perez-Suarez, D., Ryan, D. F., Shih, A. Y., Chanda, P., Glogowski, K., Hewett, R., Hughitt, V. K., Hill, A., Hiware, K., Inglis, A., Kirk, M. S. F., Konge, S., Mason, J. P., Maloney, S. A., Murray, S. A., Panda, A., Park, J., Pereira, T. M. D., Reardon, K., Savage, S., Sipőcz, B. M., Stansby, D., Jain, Y., Taylor, G., Yadav, T., Rajul, & Dang, T. K. (2020). The sunpy project: Open source development and status of the version 1.0 core package. *The Astrophysical Journal*, 890, 68–. Cited on page 59.

Baumback, M., Kurth, W., & Gurnett, D. (1976). Direction finding measurements of type iii bursts in both elevation and azimuth. *Solar Physics*, 46, 475–475. Cited on page 19.

Bektas, S., Karaahmetoglu, N., Yildirm, R., Uyar, A., Yildirim, U., & Pakel, E. (2018). Three point resection in 3d with distances. *International Journal of Research-GRANTHAALAYAH*, 6(2), 2394–3629. Cited on page 161.

Benkhoff, J., Murakami, G., Baumjohann, W., Besse, S., Bunce, E., Casale, M., Cremosese, G., Glassmeier, K.-H., Hayakawa, H., Heyner, D., et al. (2021). Bepicolombo-mission overview and science goals. *Space science reviews*, 217(8), 90. Cited on page 156.

Benz, A. O., Monstein, C., & Meyer, H. (2004). Callisto-a new concept for solar radio. *arXiv preprint astro-ph/0410437*. Cited on page 129.

Berghmans, D., Auchère, F., Long, D. M., Soubrié, E., Mierla, M., Zhukov, A. N., Schühle, U., Antolin, P., Harra, L., Parenti, S., et al. (2021). Extreme-uv quiet sun brightenings observed by the solar orbiter/eui. *Astronomy & Astrophysics*, 656, L4. Cited on page 49.

Beşliu-Ionescu, D., Mariş Muntean, G., Lăcătuş, D. A., Paraschiv, A. R., & Mierla, M. (2014). Detailed analysis of a ge oeffective icme triggered by the march 15, 2013 cme. *Revue Roumaine de Geophysique*, 56, 41–47. Cited on page 11.

Bishop, A. N., Fidan, B., Doğançay, K., Anderson, B. D., & Pathirana, P. N. (2008). Exploiting geometry for improved hybrid aoa/tdoa-based localization. *Signal Processing*, 88(7), 1775–1791. Cited on page 69.

Blake, S. P., Gallagher, P. T., McCauley, J., Jones, A. G., Hogg, C., Campanyà, J., Beggan, C. D., Thomson, A. W., Kelly, G. S., & Bell, D. (2016). Geomagnetically induced currents in the irish power network during geomagnetic storms. *Space Weather*, 14(12), 1136–1154. Cited on page 12.

Blinnikov, S. & Moessner, R. (1998). Expansions for nearly gaussian distributions. *Astronomy and Astrophysics Supplement Series*, 130(1), 193–205. Cited on page 61.

Bolton, S., Team, J. S., et al. (2010). The juno mission. *Proceedings of the International Astronomical Union*, 6(S269), 92–100. Cited on page 154.

Bonnin, X., Hoang, S., Cecconi, B., & Issautier, K. (2023). Wind/waves/rad1 lesia l3 df data collection. Cited on page 42.

Bonnin, X., Maksimovic, M., & Members, R. T. (2024). *RPW Antenna 3 Nov. 13, 2023, Operation Anomaly Report*. Technical Report ROC-OPS-NMP-RPT-00158-LES, CNRS-Observatoire de PARIS, Section de MEUDON – LESIA, 5, place Jules Janssen, 92195 Meudon Cedex – France. Prepared by: RPW Team, Approved by: Milan Maksimovic, For application: Desi Raulin. Cited on page 22.

Boteler, D. (2006). The super storms of august/september 1859 and their effects on the telegraph system. *Advances in Space Research*, 38(2), 159–172. Cited on page 1.

Boteler, D. H. (2019). A 21st century view of the march 1989 magnetic storm. *Space Weather*, 17(10), 1427–1441. Cited on page 1.

Bougeret, J. L., Goetz, K., Kaiser, M. L., Bale, S. D., Kellogg, P. J., Maksimovic, M., Monge, N., Monson, S. J., Astier, P. L., Davy, S., Dekkali, M., Hinze, J. J., Manning, R. E., Aguilar-Rodriguez, E., Bonnin, X., Briand, C., Cairns, I. H., Cattell, C. A., Cecconi, B., Eastwood, J., Ergun, R. E., Fainberg, J., Hoang, S., Huttunen, K. E. J., Krucker, S., Lecacheux, A., MacDowall, R. J., Macher, W., Mangeney, A., Meetre, C. A., Moussas, X., Nguyen, Q. N., Oswald, T. H., Pulupa, M., Reiner, M. J., Robinson, P. A., Rucker, H., Salem, C., Santolik, O., Silvis, J. M., Ullrich, R., Zarka, P., & Zouganelis, I. (2008). S/WAVES: The Radio and Plasma Wave Investigation on the STEREO Mission. *Space Science Reviews*, 136(1-4), 487–528. Cited on page 45.

Bougeret, J. L., Kaiser, M. L., Kellogg, P. J., Manning, R., Goetz, K., Monson, S. J., Monge, N., Friel, L., Meetre, C. A., Perche, C., Sitruk, L., & Hoang, S. (1995). Waves: The Radio and Plasma Wave Investigation on the Wind Spacecraft. *Space Science Reviews*, 71(1-4), 231–263. Cited on page 42.

Bougeret, J.-L. H., MacDowall, R. J., Goetz, K., & Kellogg, P. J. (2021). Wind radio/plasma wave, (waves) hi-res parameters cdf. Cited on page 59.

Cane, H. V., Erickson, W., & Prestage, N. (2002). Solar flares, type iii radio bursts, coronal mass ejections, and energetic particles. *Journal of Geophysical Research: Space Physics*, 107(A10), SSH–14. Cited on page 109.

Canizares, L. A. (2023). Tcdsolar/bella: Release v0.0.1. Cited on page 153.

Carrington, R. C. (1858). On the distribution of the solar spots in latitudes since the beginning of the year 1854, with a map. *Monthly Notices of the Royal Astronomical Society, Vol. 19, p. 1-3*, 19, 1–3. Cited on page 5.

Carrington, R. C. (1859). Description of a Singular Appearance seen in the Sun on September 1, 1859. *Monthly Notices of the Royal Astronomical Society*, 20(1), 13–15. Cited on page 1.

Cañizares, L. A., Badman, S. T., Maloney, S. A., Owens, M. J., Weigt, D. M., Carley, E. P., & Gallagher, P. T. (2024). Tracking solar radio bursts using bayesian multilateration. *A&A*, 684, A182. Cited on pages v, 64, 67, 73, 78, 82, 83, 85, 86, 88, 89, 92, 94, 95, 96, 106, 107, 127, 137, 139, and 140.

Cecconi, B., Bonnin, X., Hoang, S., Maksimovic, M., Bale, S. D., Bougeret, J.-L., Goetz, K., Lecacheux, A., Reiner, M., Rucker, H. O., et al. (2008). Stereo/waves goniopolarimetry. *Space Science Reviews*, 136, 549–563. Cited on pages 19, 45, and 139.

Cecconi, B. & Zarka, P. (2005). Direction finding and antenna calibration through analytical inversion of radio measurements performed using a system of two or three electric dipole antennas on a three-axis stabilized spacecraft. *Radio Science*, 40(3), 1–20. Cited on page 20.

Chen, X., Kontar, E. P., Chrysaphi, N., Zhang, P., Krupar, V., Musset, S., Maksimovic, M., Jeffrey, N. L., Azzollini, F., & Vecchio, A. (2023). Source positions of an interplanetary type iii radio burst and anisotropic radio-wave scattering. *arXiv preprint arXiv:2306.09160*. Cited on pages 21, 22, 36, 71, 91, 96, 107, 125, 139, 140, 141, 142, and 144.

Chen, Y., Przybylski, D., Peter, H., Tian, H., Auchère, F., & Berghmans, D. (2021). Transient small-scale brightenings in the quiet solar corona: A model for campfires observed with solar orbiter. *Astronomy & Astrophysics*, 656, L7. Cited on page 49.

Chicarro, A., Martin, P., & Trautner, R. (2004). The mars express mission: an overview. *In: Mars Express: the scientific payload. Ed. by Andrew Wilson, scientific coordination: Agustin Chicarro. ESA SP-1240, Noordwijk, Netherlands: ESA Publications Division, ISBN 92-9092-556-6, 2004, p. 3-13*, 1240, 3–13. Cited on pages 39 and 53.

Chrysaphi, N., Kontar, E. P., Holman, G. D., & Temmer, M. (2018). Cme-driven shock and type ii solar radio burst band splitting. *The Astrophysical Journal*, 868(2), 79. Cited on pages 36, 38, 139, 140, and 142.

Chrysaphi, N., Maksimovic, M., Kontar, E. P., Vecchio, A., Chen, X., & Pesini, A. (2024). First determination of the angular dependence of rise and decay times of solar radio bursts using multi-spacecraft observations. *Astronomy & Astrophysics*, 687, L12. Cited on page 144.

Cintra, M., Fernandes, F., Rosa, R., & Sodré, Z. (2020). Studying the stochasticity of type i solar storms with gradient spectra. *Boletim da Sociedade Astronômica Brasileira*, 31(1), 39–40. Cited on page 15.

Collette, A. (2013). *Python and HDF5: unlocking scientific data*. " O'Reilly Media, Inc.". Cited on page 159.

Crisp, N. H., Macario Rojas, A., McGrath, C. N., Maloney, S., Cañizares, L. A., Weigt, D. M., Murray, S., Carley, E., & Gallagher, P. (2023). Technology challenges of surround: A constellation of small satellites around the sun for tracking solar radio bursts. SSC23-WII-04. Cited on pages 56, 110, 119, 120, and 122.

Dabrowski, B., Krankowski, A., Blaszkiewicz, L., & Rothkaehl, H. (2016). Prospects for solar and space weather research with polish part of the lofar telescope. *Acta Geophysica*, 64. Cited on page 15.

Dhungana, G., Kehoe, R., Staten, R., Vinko, J., Wheeler, J., Akerlof, C., Doss, D., Ferrante, F., Gibson, C., Lasker, J., et al. (2024). Cosmological distance measurement of twelve nearby supernovae iip with rotse-iiib. *The Astrophysical Journal*, 962(1), 60. Cited on page 61.

Dikpati, M. & Gilman, P. A. (2009). Flux-transport solar dynamos. *Space science reviews*, 144(1), 67–75. Cited on pages 3, 5, and 6.

Dunham, D. W., Guzmán, J. J., & Sharer, P. J. (2009). Stereo trajectory and maneuver design. *Johns Hopkins APL Technical Digest*, 28(1), 104–125. Cited on page 43.

Edlén, B. (1943). Die deutung der emissionslinien im spektrum der sonnenkorona. mit 6 abbildungen. *Zeitschrift für Astrophysik, Vol. 22, p. 30*, 22, 30. Cited on page 3.

Emslie, A., Kucharek, H., Dennis, B., Gopalswamy, N., Holman, G., Share, G., Vourlidas, A., Forbes, T., Gallagher, P., Mason, G., et al. (2004). Energy partition in two solar flare/cme events. *Journal of Geophysical Research: Space Physics*, 109(A10). Cited on page 8.

Fainberg, J., Evans, L. G., & Stone, R. (1972). Radio tracking of solar energetic particles through interplanetary space. *Science*, 178(4062), 743–745. Cited on page 20.

Fainberg, J., Hoang, S., & Manning, R. (1985). Measurements of distributed polarized radio sources from spinning spacecraft-effect of a tilted axial antenna-isee-3 application and results. *Astronomy and Astrophysics, Vol. 153, NO. 2/DEC, P. 145, 1985*, 153, 145. Cited on page 40.

Farrell, W., Thompson, R., Lepping, R., & Byrnes, J. (1995). A method of calibrating magnetometers on a spinning spacecraft. *IEEE Transactions on Magnetics*, 31(2), 966–972. Cited on page 40.

Fisk, L., Schwadron, N., & Zurbuchen, T. (1998). On the slow solar wind. *Space science reviews*, 86, 51–60. Cited on page 8.

Fox, N., Velli, M., Bale, S., Decker, R., Driesman, A., Howard, R., Kasper, J. C., Kinnison, J., Kusterer, M., Lario, D., et al. (2016). The solar probe plus mission: humanity's first visit to our star. *Space Science Reviews*, 204, 7–48. Cited on pages 39, 46, 47, and 48.

Galvin, A. B., Kistler, L. M., Popecki, M. A., Farrugia, C. J., Simunac, K. D., Ellis, L., Möbius, E., Lee, M. A., Boehm, M., Carroll, J., et al. (2008). The plasma and suprathermal ion composition (plastic) investigation on the stereo observatories. *The STEREO Mission*, (pp. 437–486). Cited on page 45.

Ganse, U., Kilian, P., Vainio, R., & Spanier, F. (2012). Emission of type ii radio bursts–single-beam versus two-beam scenario. *Solar Physics*, 280, 551–560. Cited on page 15.

Garton, T. M., Gallagher, P. T., & Murray, S. A. (2018). Automated coronal hole identification via multi-thermal intensity segmentation. *Journal of Space Weather and Space Climate*, 8, A02. Cited on page 85.

Gary, G. A. (2001). Plasma beta above a solar active region: rethinking the paradigm. *Solar Physics*, 203, 71–86. Cited on pages 31 and 32.

Gaunt, C. & Coetzee, G. (2007). Transformer failures in regions incorrectly considered to have low gic-risk. In *2007 IEEE Lausanne power tech* (pp. 807–812).: IEEE. Cited on page 12.

Ginzburg, V. & Zhelezniakov, V. (1958). On the possible mechanisms of sporadic solar radio emission (radiation in an isotropic plasma). *Soviet Astronomy*, 2, 653. Cited on page 33.

Ginzburg, V. & Zhelezniakov, V. (1959). On the mechanisms of sporadic solar radio emission. In *Symposium-International Astronomical Union*, volume 9 (pp. 574–582).: Cambridge University Press. Cited on page 35.

Gloeckler, G., Balsiger, H., Bürgi, A., Bochsler, P., Fisk, L. A., Galvin, A. B., Geiss, J., Gliem, F., Hamilton, D., Holzer, T., et al. (1995). The solar wind and suprathermal ion

composition investigation on the wind spacecraft. *Space Science Reviews*, 71, 79–124. Cited on page 42.

Gopalswamy, N. (2011). Coronal mass ejections and solar radio emissions. *Planetary Radio Emissions*, 7, 325–342. Cited on page 16.

Gopalswamy, N., Yashiro, S., Michalek, G., Stenborg, G., Vourlidas, A., Freeland, S., & Howard, R. (2009). The soho/lasco cme catalog. *Earth, Moon, and Planets*, 104, 295–313. Cited on pages 12 and 105.

Grasset, O., Dougherty, M., Coustenis, A., Bunce, E., Erd, C., Titov, D., Blanc, M., Coates, A., Drossart, P., Fletcher, L., et al. (2013). Jupiter icy moons explorer (juice): An esa mission to orbit ganymede and to characterise the jupiter system. *Planetary and Space Science*, 78, 1–21. Cited on page 155.

Grotian, W. (1939). Zur frage der deutung der linien im spektrum der sonnenkorona. *Naturwissenschaften*, 27(13), 214–214. Cited on page 3.

Guillon, S., Toner, P., Gibson, L., & Boteler, D. (2016). A colorful blackout: The havoc caused by auroral electrojet generated magnetic field variations in 1989. *IEEE Power and Energy Magazine*, 14(6), 59–71. Cited on page 1.

Hale, G. E., Ellerman, F., Nicholson, S. B., & Joy, A. H. (1919). The magnetic polarity of sun-spots. *Astrophysical Journal, vol. 49, p. 153*, 49, 153. Cited on page 5.

Hamini, A., Auxepaules, Gabriel, Birée, Lionel, Kenfack, Guy, Kerdraon, Alain, Klein, Karl-Ludwig, Lespagnol, Patrice, Masson, Sophie, Coutouly, Lucile, Fabrice, Christian, & Romagnan, Renaud (2021). Orfees - a radio spectrograph for the study of solar radio bursts and space weather applications. *J. Space Weather Space Clim.*, 11, 57. Cited on page 129.

Harra, L., Fletcher, L., Gizon, L., Solanki, S., Romoli, M., Kusano, K., Hotta, H., Katsukawa,

Y., Harrison, R., Owen, C., et al. (2023). Firefly: the science case for a full view of the solar sphere. *Heliophysics 2024 Decadal Whitepapers*, 55(3). Cited on page 165.

Harten, R. & Clark, K. (1995). The design features of the ggs wind and polar spacecraft. *Space Science Reviews*, 71(1-4), 23–40. Cited on page 41.

Hathaway, D. H. (2015). The solar cycle. *Living reviews in solar physics*, 12(1), 4. Cited on pages 4 and 5.

Hayakawa, H., Bechet, S., Clette, F., Hudson, H. S., Maehara, H., Namekata, K., & Notsu, Y. (2023). Magnitude estimates for the carrington flare in 1859 september: As seen from the original records. *The Astrophysical Journal Letters*, 954(1), L3. Cited on page 1.

Heidt, H., Puig-Suari, J., Moore, A., Nakasuka, S., & Twiggs, R. (2000). Cubesat: A new generation of picosatellite for education and industry low-cost space experimentation. *Proceedings of the Small Satellite Conference*. Cited on page 54.

Henney, C., Keller, C., & Harvey, J. (2006). Solis-vsm solar vector magnetograms. *arXiv preprint astro-ph/0612584*. Cited on page 85.

Hewish, A. (2002). James stanley hey, mbe 3 may 1909–27 february 2000. Cited on page 14.

Hiesinger, H., Landgraf, M., Carey, W., Karouji, Y., Haltigin, T., Osinski, G., Mall, U., & Hashizume, K. (2019). Returning to the moon with heracles: An esa-jaxa-csa joint study. In *Geophysical Research Abstracts*, volume 21. Cited on page 99.

Hoang, S., Maksimovic, M., Bougeret, J.-L., Reiner, M., & Kaiser, M. L. (1998). Wind-ulysses source location of radio emissions associated with the january 1997 coronal mass ejection. *Geophysical research letters*, 25(14), 2497–2500. Cited on page 20.

Hodges, R. E., Chahat, N. E., Hoppe, D. J., & Vacchione, J. D. (2016). The mars cube one deployable high gain antenna. In *2016 IEEE International Symposium on Antennas and Propagation (APSURSI)* (pp. 1533–1534).: IEEE. Cited on page 56.

Hodgson, R. (1859). On a curious appearance seen in the sun. *Monthly Notices of the Royal Astronomical Society, Vol. 20, p. 15-16*, 20, 15–16. Cited on page 1.

Hoffman, M. D., Gelman, A., et al. (2014). The no-u-turn sampler: adaptively setting path lengths in hamiltonian monte carlo. *J. Mach. Learn. Res.*, 15(1), 1593–1623. Cited on page 76.

Hoffman, R. & Hesse, M. (1996). Global geospace science (ggs) program and the polar satellite. In *International Conference on Substorms*, volume 389 (pp. 721). Cited on page 40.

Horbury, T., O'brien, H., Blazquez, I. C., Bendyk, M., Brown, P., Hudson, R., Evans, V., Oddy, T., Carr, C., Beek, T., et al. (2020). The solar orbiter magnetometer. *Astronomy & Astrophysics*, 642, A9. Cited on page 51.

Hou, Y., Yu, M., Wang, J., Liu, C., Chen, M., & Wu, B. (2024). Evolution of the electron phase space of the two-stream and bump-on-tail instabilities in collisional plasma. *Physics of Plasmas*, 31(4). Cited on pages xvii and 34.

Howard, R. A., Moses, J., Vourlidas, A., Newmark, J., Socker, D. G., Plunkett, S. P., Korendyke, C. M., Cook, J., Hurley, A., Davila, J., et al. (2008). Sun earth connection coronal and heliospheric investigation (secchi). *Space Science Reviews*, 136, 67–115. Cited on page 45.

Howard, R. A., Vourlidas, A., Colaninno, R., Korendyke, C., Plunkett, S., Carter, M., Wang, D., Rich, N., Lynch, S., Thurn, A., et al. (2020). The solar orbiter heliospheric imager (solohi). *Astronomy & Astrophysics*, 642, A13. Cited on pages 49 and 51.

Inan, U. S. & Gołkowski, M. (2010). *Principles of plasma physics for engineers and scientists*. Cambridge University Press. Cited on pages 29, 30, 32, and 33.

Jebaraj, I. C., Krasnoselskikh, V., Pulupa, M., Magdalenic, J., & Bale, S. D. (2023).

Fundamental–harmonic pairs of interplanetary type iii radio bursts. *The Astrophysical journal letters*, 955(1), L20. Cited on page 61.

Jebaraj, I. C., Magdalenić, J., Podladchikova, T., Scolini, C., Pomoell, J., Veronig, A., Dissauer, K., Krupar, V., Kilpua, E., & Poedts, S. (2020). Using radio triangulation to understand the origin of two subsequent type ii radio bursts. *Astronomy & Astrophysics*, 639, A56. Cited on pages 19, 106, and 107.

Jordan, R., Picardi, G., Plaut, J., Wheeler, K., Kirchner, D., Safaeinili, A., Johnson, W., Seu, R., Calabrese, D., Zampolini, E., et al. (2009). The mars express marsis sounder instrument. *Planetary and Space Science*, 57(14-15), 1975–1986. Cited on page 53.

Kaiser, M. L. & Adams, W. J. (2007). Stereo mission overview. In *2007 IEEE Aerospace Conference* (pp. 1–8).: IEEE. Cited on pages 43 and 44.

Kaiser, M. L., Kucera, T., Davila, J., St Cyr, O., Guhathakurta, M., & Christian, E. (2008). The stereo mission: An introduction. *Space Science Reviews*, 136, 5–16. Cited on pages 39, 43, and 45.

Kalaivani, P. P., Prakash, O., Shanmugaraju, A., Feng, L., Lu, L., Gan, W., & Michalek, G. (2021). Analysis of type ii and type iii radio bursts associated with seps from non-interacting/interacting radio-loud cmes. *Astrophysics*, 64, 327–344. Cited on page 109.

Kasaba, Y., Bougeret, J.-L., Blomberg, L. G., Kojima, H., Yagitani, S., Moncuquet, M., Trotignon, J.-G., Chanteur, G., Kumamoto, A., Kasahara, Y., et al. (2010). The plasma wave investigation (pwi) onboard the bepicolombo/mmo: First measurement of electric fields, electromagnetic waves, and radio waves around mercury. *Planetary and Space Science*, 58(1-2), 238–278. Cited on page 156.

Kasper, J., Lazio, J., Romero-Wolf, A., Lux, J., & Neilsen, T. (2021). The sun radio interferometer space experiment (sunrise) mission. In *2021 IEEE Aerospace Conference (50100)* (pp. 1–11).: IEEE. Cited on page 56.

Kasper, J. C., Abiad, R., Austin, G., Balat-Pichelin, M., Bale, S. D., Belcher, J. W., Berg, P., Bergner, H., Berthomier, M., Bookbinder, J., et al. (2016). Solar wind electrons alphas and protons (sweap) investigation: Design of the solar wind and coronal plasma instrument suite for solar probe plus. *Space Science Reviews*, 204, 131–186. Cited on page 48.

Kataoka, R., Shiota, D., Fujiwara, H., Jin, H., Tao, C., Shinagawa, H., & Miyoshi, Y. (2022). Unexpected space weather causing the reentry of 38 starlink satellites in february 2022. *Journal of Space Weather and Space Climate*. Cited on page 99.

Kaune, R. (2012). Accuracy studies for tdoa and toa localization. In *2012 15th International Conference on Information Fusion* (pp. 408–415).: IEEE. Cited on page 91.

Kellogg, P. J. (1976). Tracking of kilometric-wave type iii solar bursts in elevation and elongation and apparent source sizes. *Solar Physics*, 46, 449–458. Cited on page 19.

Kerdraon, A. & Delouis, J.-M. (2007). The nançay radioheliograph. In *Coronal Physics from Radio and Space Observations: Proceedings of the CESRA Workshop Held in Nouan le Fuzelier, France, 3–7 June 1996* (pp. 192–201).: Springer. Cited on page 57.

Klein, K.-L. & Posner, A. (2005). The onset of solar energetic particle events: prompt release of deka-mev protons and associated coronal activity. *Astronomy & Astrophysics*, 438(3), 1029–1042. Cited on page 108.

Kontar, E. P. (2001). Dynamics of electron beams in the inhomogeneous solar corona plasma. *Solar Physics*, 202(1), 131–149. Cited on pages 33 and 139.

Kontar, E. P., Chen, X., Chrysaphi, N., Jeffrey, N. L., Emslie, A. G., Krupar, V., Maksimovic, M., Gordovskyy, M., & Browning, P. K. (2019). Anisotropic radio-wave scattering and the interpretation of solar radio emission observations. *The Astrophysical Journal*, 884(2), 122. Cited on pages 36, 37, and 38.

Kontar, E. P., Chen, X., Chrysaphi, N., Jeffrey, N. L. S., Emslie, A. G., Krupar, V., Maksimovic, M., Gordovskyy, M., & Browning, P. K. (2019). Anisotropic Radio-wave Scatter-

ing and the Interpretation of Solar Radio Emission Observations. *apj*, 884(2), 122. Cited on pages 22, 70, 139, 141, 143, and 144.

Kontar, E. P., Emslie, A. G., Clarkson, D. L., Chen, X., Chrysaphi, N., Azzollini, F., Jeffrey, N. L. S., & Gordovskyy, M. (2023). An anisotropic density turbulence model from the sun to 1 au derived from radio observations. Cited on pages 91 and 96.

Kosovichev, A.-a., Schou, J., Scherrer, P., Bogart, R., Bush, R., Hoeksema, J., Aloise, J., Bacon, L., Burnette, A., De Forest, C., et al. (1997). Structure and rotation of the solar interior: initial results from the mdi medium-l program. *The first results from SOHO*, (pp. 43–61). Cited on page 3.

Kou, Y. K., Jing, Z. C., Cheng, X., Pan, W. Q., Liu, Y., Li, C., & Ding, M. D. (2020). What determines solar flares producing interplanetary type III radio bursts? *The Astrophysical Journal*, 898(1), L24. Cited on page 18.

Krucker, S., Hurford, G. J., Grimm, O., Kögl, S., Gröbelbauer, H.-P., Etesi, L., Casadei, D., Csillaghy, A., Benz, A. O., Arnold, N. G., et al. (2020). The spectrometer/telescope for imaging x-rays (stix). *Astronomy & Astrophysics*, 642, A15. Cited on page 51.

Krupar, V., Eastwood, J., Kruparova, O., Santolik, O., Soucek, J., Magdalenić, J., Vourlidas, A., Maksimovic, M., Bonnin, X., Bothmer, V., et al. (2016). An analysis of interplanetary solar radio emissions associated with a coronal mass ejection. *The Astrophysical Journal Letters*, 823(1), L5. Cited on page 20.

Krupar, V., Kruparova, O., Szabo, A., Pinto, R. F., Maksimovic, M., & Oliveros, J. C. M. (2024). Enhancing triangulation of interplanetary type iii bursts through wavevector correction. *The Astrophysical Journal*, 960(2), 101. Cited on page 20.

Krupar, V., Maksimovic, M., Kontar, E., Zaslavsky, A., Santolik, O., Soucek, J., Kruparova, O., Eastwood, J., & Szabo, A. (2018). Interplanetary type iii bursts and electron density fluctuations in the solar wind. *The Astrophysical Journal*, 857(2), 82. Cited on page 36.

Krupar, V., Nguyen, Q. N., Bonnin, X., Cecconi, B., & Maksimovic, M. (2022). Stereo/waves/lfr-hfr l3 df data collection. Cited on pages 46, 59, 89, and 91.

Krupar, V., Santolik, O., Cecconi, B., Maksimovic, M., Bonnin, X., Panchenko, M., & Zaslavsky, A. (2012). Goniopolarimetric inversion using svd: An application to type iii radio bursts observed by stereo. *Journal of Geophysical Research: Space Physics*, 117(A6). Cited on pages 21 and 125.

Krupar, V., Szabo, A., Maksimovic, M., Kruparova, O., Kontar, E. P., Balmaceda, L. A., Bonnin, X., Bale, S. D., Pulupa, M., Malaspina, D. M., Bonnell, J. W., Harvey, P. R., Goetz, K., de Wit, T. D., MacDowall, R. J., Kasper, J. C., Case, A. W., Korreck, K. E., Larson, D. E., Livi, R., Stevens, M. L., Whittlesey, P. L., & Hegedus, A. M. (2020). Density fluctuations in the solar wind based on type III radio bursts observed by parker solar probe. *The Astrophysical Journal Supplement Series*, 246(2), 57. Cited on page 36.

Kurth, W., Hospodarsky, G., Kirchner, D., Mokrzycki, B., Averkamp, T., Robison, W., Piker, C., Sampl, M., & Zarka, P. (2017). The juno waves investigation. *Space Science Reviews*, 213, 347–392. Cited on page 154.

Kuznetsov, A. A., Chrysaphi, N., Kontar, E. P., & Motorina, G. (2020). Radio Echo in the Turbulent Corona and Simulations of Solar Drift-pair Radio Bursts. *The Astrophysical Journal*, 898(2), 94. Cited on pages 141 and 144.

LaBelle, J., Treumann, R. A., Yoon, P. H., & Karlicky, M. (2003). A model of zebra emission in solar type IV radio bursts. *The Astrophysical Journal*, 593(2), 1195–1207. Cited on page 16.

Lam, H.-L., Boteler, D., Burlton, B., & Evans, J. (2012). Anik-e1 and e2 satellite failures of january 1994 revisited. *Space Weather*, 10(10). Cited on page 12.

Lamy, P., Floyd, O., Boclet, B., Wojak, J., Gilardy, H., & Barlyaeva, T. (2019). Coronal mass ejections over solar cycles 23 and 24. *Space Science Reviews*, 215, 1–129. Cited on pages 105 and 108.

Lang, K. R. (2001). *The Cambridge Encyclopedia of the Sun*. Cambridge University Press. Cited on pages 4 and 9.

Lang, M. & Owens, M. J. (2019). A Variational Approach to Data Assimilation in the Solar Wind. *Space Weather*, 17(1), 59–83. Cited on page 93.

Lang, M., Witherington, J., Turner, H., Owens, M. J., & Riley, P. (2021). Improving Solar Wind Forecasting Using Data Assimilation. *Space Weather*, 19(7), e2020SW002698. Cited on page 93.

Leblanc, Y., Dulk, G. A., & Bougeret, J.-L. (1998). Tracing the Electron Density from the Corona to 1au. *Solar Physics*, 183(1), 165–180. Cited on pages 95, 101, 110, and 139.

Lepping, R., Acũna, M., Burlaga, L., Farrell, W., Slavin, J., Schatten, K., Mariani, F., Ness, N., Neubauer, F., Whang, Y., et al. (1995). The wind magnetic field investigation. *Space Science Reviews*, 71, 207–229. Cited on page 40.

Lin, R., Anderson, K., Ashford, S., Carlson, C., Curtis, D., Ergun, R., Larson, D., McFadden, J., McCarthy, M., Parks, G., et al. (1995). A three-dimensional plasma and energetic particle investigation for the wind spacecraft. *Space Science Reviews*, 71, 125–153. Cited on page 40.

Luhmann, J., Curtis, D., Schroeder, P., McCauley, J., Lin, R., Larson, D., Bale, S., Sauvaud, J. A., Aoustin, C., Mewaldt, R., et al. (2008). Stereo impact investigation goals, measurements, and data products overview. *The STEREO Mission*, (pp. 117–184). Cited on page 45.

Macario-Rojas, A., Crisp, N. H., McGrath, C. N., **Cañizares, L. A.**, Weigt, D. M., Maloney, S. A., Murray, S. A., Carley, E. P., & Gallagher, P. T. (202X). Mission concept for surround: Operational space weather detection and tracking using small satellites. Cited on pages 56, 100, 122, 123, and 164.

MacDowall, R., Lara, A., Manoharan, P., Nitta, N., Rosas, A., & Bougeret, J.-L. (2003). Long-duration hectometric type iii radio bursts and their association with solar energetic particle (sep) events. *Geophysical research letters*, 30(12). Cited on page 109.

Magdalenić, J., Marqué, C., Krupar, V., Mierla, M., Zhukov, A., Rodriguez, L., Maksimović, M., & Cecconi, B. (2014). Tracking the cme-driven shock wave on 2012 march 5 and radio triangulation of associated radio emission. *The Astrophysical Journal*, 791(2), 115. Cited on pages 19 and 20.

Maguire, C. A., Carley, E. P., Zucca, P., Vilmer, N., & Gallagher, P. T. (2021). Lofar observations of a jet-driven piston shock in the low solar corona. *The Astrophysical Journal*, 909(1), 2. Cited on pages 19 and 105.

Maksimovic, M., Bale, S., Chust, T., Khotyaintsev, Y., Krasnoselskikh, V., Kretzschmar, M., Plettemeier, D., Rucker, H., Souček, J., Steller, M., et al. (2020). The solar orbiter radio and plasma waves (rpw) instrument. *Astronomy & Astrophysics*, 642, A12. Cited on pages 50 and 52.

Maksimovic, M., Bale, S., Chust, T., Khotyaintsev, Y., Krasnoselskikh, V., Kretzschmar, M., Plettemeier, D., Rucker, H., Souček, J., Steller, M., et al. (2021). The solar orbiter radio and plasma waves (rpw) instrument (corrigendum). *Astronomy & Astrophysics*, 654, C2. Cited on page 52.

Malandraki, O. E. & Crosby, N. B. (2018). Solar energetic particles and space weather: Science and applications. *Solar particle radiation storms forecasting and analysis: the HESPERIA HORIZON 2020 project and beyond*, (pp. 1–26). Cited on page 108.

Mallette, L. (1982). Geostationary operational environmental satellite/goes/-a multifunctional satellite. In *9th Communications Satellite System Conference* (pp. 536). Cited on page 10.

Malone-Leigh, J., Campanyà, J., Gallagher, P. T., Hodgson, J., & Hogg, C. (2024). Mapping

geoelectric field hazards in ireland. *Space Weather*, 22(2), e2023SW003638. Cited on page 12.

Manning, R. & Fainberg, J. (1980). A new method of measuring radio source parameters of a partially polarized distributed source from spacecraft observations. *Space Science Instrumentation*, 5, 161–181. Cited on pages 20 and 21.

Marsden, R., Wenzel, K., & Smith, E. (1986). The ulysses mission. Cited on page 157.

Mayer, F., Freij, N., Pérez-Suárez, D., Mumford, S., Christe, S., Sipőcz, B., Ireland, J., Earnshaw, M., Hewett, R. J., Modi, S., Maloney, S., Panda, A., Chatterjee, A., Rajul, derdon, Shih, A. Y., Bray, E. M., Hughitt, K., Lim, P. L., & Hayes, L. (2024). sunpy/radiospectra: v0.5.0. Cited on page 59.

McCauley, P. I., Cairns, I. H., & Morgan, J. (2018). Densities probed by coronal type iii radio burst imaging. *Solar Physics*, 293, 1–25. Cited on page 125.

McComas, D., Elliott, H., Schwadron, N., Gosling, J., Skoug, R. M., & Goldstein, B. (2003). The three-dimensional solar wind around solar maximum. *Geophysical research letters*, 30(10). Cited on pages 7 and 8.

McComas, D. J., Alexander, N., Angold, N., Bale, S., Beebe, C., Birdwell, B., Boyle, M., Burgum, J. M., Burnham, J. A., Christian, E. R., Cook, W. R., Cooper, S. A., Cummings, A. C., Davis, A. J., Desai, M. I., Dickinson, J., Dirks, G., Do, D. H., Fox, N., Giacalone, J., Gold, R. E., Gurnee, R. S., Hayes, J. R., Hill, M. E., Kasper, J. C., Kecman, B., Klemic, J., Krimigis, S. M., Labrador, A. W., Layman, R. S., Leske, R. A., Livi, S., Matthaeus, W. H., McNutt, R. L., Mewaldt, R. A., Mitchell, D. G., Nelson, K. S., Parker, C., Rankin, J. S., Roelof, E. C., Schwadron, N. A., Seifert, H., Shuman, S., Stokes, M. R., Stone, E. C., Vandegriff, J. D., Velli, M., von Rosenvinge, T. T., Weidner, S. E., Wiedenbeck, M. E., & Wilson, P. (2014). Integrated science investigation of the sun (isis): Design of the energetic particle investigation. *Space Science Reviews*, 204(1–4), 187–256. Cited on page 48.

Meléndez, J., Sawant, H., Fernandes, F., & Benz, A. (1999). Statistical analysis of high-frequency decimetric type iii bursts. *Solar Physics*, 187, 77–88. Cited on page 19.

Melrose, D. (1987). Plasma emission: A review. *Solar Physics*, 111, 89–101. Cited on page 33.

Melrose, D. (1991). Collective plasma radiation processes. *IN: Annual review of astronomy and astrophysics. Vol. 29 (A92-18081 05-90). Palo Alto, CA, Annual Reviews, Inc., 1991, p. 31-57.*, 29, 31–57. Cited on pages 33 and 34.

Mercier, C. & Trottet, G. (1997). Coronal radio bursts: A signature of nanoflares? *The Astrophysical Journal*, 474(1), L65–L68. Cited on page 15.

Miesch, M. S. (2005). Large-scale dynamics of the convection zone and tachocline. *Living Reviews in Solar Physics*, 2(1), 1. Cited on page 3.

Milligan, R. O., Gallagher, P. T., Mathioudakis, M., Bloomfield, D. S., Keenan, F. P., & Schwartz, R. A. (2006a). Rhessi and soho cds observations of explosive chromospheric evaporation. *The Astrophysical Journal*, 638(2), L117. Cited on page 10.

Milligan, R. O., Gallagher, P. T., Mathioudakis, M., & Keenan, F. P. (2006b). Observational evidence of gentle chromospheric evaporation during the impulsive phase of a solar flare. *The Astrophysical Journal*, 642(2), L169. Cited on page 10.

Moncuquet, M., Matsumoto, H., Bougeret, J.-L., Blomberg, L. G., Issautier, K., Kasaba, Y., Kojima, H., Maksimovic, M., Meyer-Vernet, N., & Zarka, P. (2006). The radio waves and thermal electrostatic noise spectroscopy (sorbet) experiment on bepicolombo/mmo/pwi: Scientific objectives and performance. *Advances in Space Research*, 38(4), 680–685. Cited on page 156.

Morosan, D. E., Gallagher, P. T., Zucca, P., Fallows, R., Carley, E., Mann, G., Bisi, M., Kerdraon, A., Konovalenko, A., MacKinnon, A., et al. (2014). Lofar tied-array imaging

of type iii solar radio bursts. *Astronomy & astrophysics*, 568, A67. Cited on pages 19 and 125.

Mueller, J., Maldonado, H., & Driesman, A. (2003). Stereo: The challenges. *Acta Astronautica*, 53(4-10), 729–738. Cited on page 43.

Müller, D., Cyr, O. S., Zouganelis, I., Gilbert, H. R., Marsden, R., Nieves-Chinchilla, T., Antonucci, E., Auchère, F., Berghmans, D., Horbury, T., et al. (2020). The solar orbiter mission-science overview. *Astronomy & Astrophysics*, 642, A1. Cited on pages 39, 49, 50, and 161.

Munro, R., Gosling, J., Hildner, E., MacQueen, R., Poland, A., & Ross, C. (1979). The association of coronal mass ejection transients with other forms of solar activity. *Solar Physics*, 61, 201–215. Cited on page 10.

Murphy, P. C., Carley, E. P., Ryan, A. M., Zucca, P., & Gallagher, P. T. (2021). Lofar observations of radio burst source sizes and scattering in the solar corona. *Astronomy & Astrophysics*, 645, A11. Cited on page 36.

Musset, S., Maksimovic, M., Kontar, E., Krupar, V., Chrysaphi, N., Bonnin, X., Vecchio, A., Cecconi, B., Zaslavsky, A., Issautier, K., Bale, S. D., & Pulupa, M. (2021). Simulations of radio-wave anisotropic scattering to interpret type iii radio burst data from solar orbiter, parker solar probe, stereo, and wind. *Astronomy & Astrophysics*, 656, A34. Cited on pages 21, 71, 139, and 163.

Ndacyayisenga, T., Uwamahoro, J., Raja, K. S., & Monstein, C. (2021). A statistical study of solar radio type iii bursts and space weather implication. *Advances in Space Research*, 67(4), 1425–1435. Cited on page 125.

Nelson, G. J. & Melrose, D. B. (1985). Type II bursts. In D. J. McLean & N. R. Labrum (Eds.), *Solar Radiophysics: Studies of Emission from the Sun at Metre Wavelengths* (pp. 333–359). Cambridge University Press. Cited on page 15.

Newkirk Jr, G. (1961). The solar corona in active regions and the thermal origin of the slowly varying component of solar radio radiation. *Astrophysical Journal, vol. 133, p. 983*, 133, 983. Cited on page 137.

Ogilvie, K., Chornay, D., Fritzenreiter, R., Hunsaker, F., Keller, J., Lobell, J., Miller, G., Scudder, J., Sittler, E., Torbert, R., et al. (1995). Swe, a comprehensive plasma instrument for the wind spacecraft. *Space Science Reviews*, 71, 55–77. Cited on page 40.

Oliveros, J. C. M., Raftery, C. L., Bain, H. M., Liu, Y., Krupar, V., Bale, S., & Krucker, S. (2012). The 2010 august 1 type ii burst: A cme–cme interaction and its radio and white-light manifestations. *The Astrophysical Journal*, 748(1), 66. Cited on page 20.

Owen, C., Bruno, R., Livi, S., Louarn, P., Al Janabi, K., Allegrini, F., Amoros, C., Baruah, R., Barthe, A., Berthomier, M., et al. (2020). The solar orbiter solar wind analyser (swa) suite. *Astronomy & Astrophysics*, 642, A16. Cited on page 51.

Owens, A., Baker, R., Cline, T., Gehrels, N., Jermakian, J., Nolan, T., Ramaty, R., Seifert, H., Shephard, D., Smith, G., et al. (1995). A high-resolution ge spectrometer for gamma-ray burst astronomy. *Space Science Reviews*, 71, 273–296. Cited on page 42.

Owens, M., Lang, M., Barnard, L., Riley, P., Ben-Nun, M., Scott, C. J., Lockwood, M., Reiss, M. A., Arge, C. N., & Gonzi, S. (2020). A computationally efficient, time-dependent model of the solar wind for use as a surrogate to three-dimensional numerical magnetohydrodynamic simulations. *Solar Physics*, 295(3), 43. Cited on page 93.

Palmer, C. (2021). Spacex starship lands on earth, but manned missions to mars will require more. Cited on page 99.

Parker, E. (1969). Theoretical studies of the solar wind phenomenon. *Space Science Reviews*, 9(3), 325–360. Cited on page 7.

Parker, E. N. (1958). Dynamics of the interplanetary gas and magnetic fields. *Astrophysical Journal, vol. 128, p. 664*, 128, 664. Cited on pages 7, 101, 110, and 139.

Parnell, C. E. & De Moortel, I. (2012). A contemporary view of coronal heating. *Philosophical Transactions of the Royal Society A: Mathematical, Physical and Engineering Sciences*, 370(1970), 3217–3240. Cited on page 3.

Picardi, G., Biccari, D., Seu, R., Marinangeli, L., Johnson, W., Jordan, R., Plaut, J., Safaenili, A., Gurnett, D., Ori, G. G., et al. (2004). Performance and surface scattering models for the mars advanced radar for subsurface and ionosphere sounding (marsis). *Planetary and Space Science*, 52(1-3), 149–156. Cited on page 53.

Poquerusse, M. (1994). Relativistic type 3 solar radio bursts. *Astronomy and Astrophysics (ISSN 0004-6361), vol. 286, no. 2, p. 611-625*, 286, 611–625. Cited on page 18.

Price-Whelan, A. M., Lim, P. L., Earl, N., Starkman, N., Bradley, L., Shupe, D. L., Patil, A. A., Corrales, L., Brasseur, C., Nöthe, M., et al. (2022). The astropy project: sustaining and growing a community-oriented open-source project and the latest major release (v5. 0) of the core package. *The Astrophysical Journal*, 935(2), 167. Cited on page 159.

Price-Whelan, A. M., Sipőcz, B., Günther, H., Lim, P., Crawford, S., Conseil, S., Shupe, D., Craig, M., Dencheva, N., Ginsburg, A., et al. (2018). The astropy project: Building an open-science project and status of the v2. 0 core package. *The Astronomical Journal*, 156(3), 123. Cited on page 159.

Puig-Suari, J., Schoos, J., Turner, C., Wagner, T., Connolly, R., & Block, R. P. (2000). Cubesat developments at cal poly: the standard deployer and polysat. In *Small Payloads in Space*, volume 4136 (pp. 72–78).: SPIE. Cited on page 54.

Pulupa, M., Bale, S. D., Bonnell, J. W., Bowen, T. A., Carruth, N., Goetz, K., Gordon, D., Harvey, P. R., Maksimovic, M., Martínez-Oliveros, J. C., Moncuquet, M., Saint-Hilaire, P., Seitz, D., & Sundkvist, D. (2017). The solar probe plus radio frequency spectrometer: Measurement requirements, analog design, and digital signal processing. *Journal of Geophysical Research: Space Physics*, 122(3), 2836–2854. Cited on page 48.

Raouafi, N., Matteini, L., Squire, J., Badman, S., Velli, M., Klein, K., Chen, C., Matthaeus, W., Szabo, A., Linton, M., et al. (2023a). Parker solar probe: Four years of discoveries at solar cycle minimum. *Space Science Reviews*, 219(1), 8. Cited on page 46.

Raouafi, N. E., Berger, T., Hoeksema, J. T., Vourlidas, A., Upton, L. A., Gibson, S. E., Newmark, J. S., Lepri, S. T., Hassler, D. M., Kinnison, J., Georgoulis, M., Ho, G. C., Viall, N. M., Harra, L., Velli, M., Szabo, A., Casti, M., Bourouaine, S., Jagarlamudi, V. K., Vievering, J. T., Mason, J. P., Solanki, S. K., Fletcher, L., Harrison, R. A., Katsukawa, Y., Kusano, K., Owen, C. J., Romoli, M., Wimmer-Schweingruber, R. F., Leibacher, J. W., Appourchaux, T., & Boumier, P. (2024). The firefly (4π) constellation: Going above and beyond in the heliosphere exploration. Presented at IAUS 390 A Multi-Point view of the Sun: Advances in Solar Observations and in Space Weather Understanding. Cited on pages 165, 166, and 167.

Raouafi, N. E., Hoeksema, J. T., Newmark, J. S., Gibson, S., Berger, T. E., Upton, L. A., Vourlidas, A., Hassler, D. M., Kinnison, J., Ho, G. C., Mason, G. M., Vievering, J. T., Viall, N. M., Szabo, A., Casti, M., Case, A. W., Lepri, S. T., Velli, M., Georgoulis, M. K., Bourouaine, S., Jagarlamudi, V. K., Laming, J. M., Mason, J. P., Harra, L., Madjarska, M., Chitta, L. P., Castellanos Duran, J. S., Korpi-Lagg, A., Badman, S., Chifu, I., Lario, D., Wing, S., Bale, S., Paouris, E., Narayanamurthy, S., Sinjan, J., Bernasconi, P., Krivova, N., Gizon, L., Leamon, R. J., Gosain, S., Kazachenko, M., Petrie, G., Martinez Pillet, V., Jain, K., Luhmann, J., Bertello, L., Toriumi, S., Jiang, C., Vasko, I., Harvey, J. W., Schad, T. A., Jebaraj, I. C., Scherrer, P., Hofmeister, S., Tiwari, S., Wang, H., Roth, M., Panesar, N., Sekii, T., Magyar, N., Guglielmino, S. L., Parenti, S., Tremblay, B., Tziotziou, K., de Toma, G., Chen, B., Katsukawa, Y., de Pontieu, B., Cheng, X., Cheung, M., Kosovichev, A., Jiang, J., Schunker, H., Kawabata, Y., Oba, T., Cameron, R., Mathew, S. K., de la Cruz Rodriguez, J., Kusano, K., Temmer, M., Andretta, V., Sven, W., Samara, E., Heinemann, S. G., Warmuth, A., Jafarzadeh, S., Mackay, D. H., Fludra, A., Bellot Rubio, L., Orozco Suárez, D., Chen, T. Y., Kontogiannis, I., Yardley, S., Veronig, A., Joshi, J.,

Spadaro, D., Kubo, M., Bose, S., Bello González, N., Solanki, S., Denker, C., Verma, M., Vocks, C., Borrero, J. M., Mathews, N. H., Cury, S., Sasso, C., Stenborg, G., Tibebu, G., Battams, K., Wijsen, N., Bruno, A., Peter, H., Mason, E. I., Caplan, R. M., Martinez-Sykora, J., Seaton, D., Airapetian, V., Jian, L., Thompson, W. T., Ofman, L., Wallace, S., Kucera, T., Desai, R., Richardson, I., Burkepile, J., Cranmer, S., Strauss, R. D. T., Murabito, M., Alfred, d. W., Xie, H., Rempel, M., Hess Webber, S., Reeves, K. K., Hurlburt, N., Berrilli, F., Deluca, E., Egeland, R., Ko, Y.-K., Kee, N. D., Mahajan, S. S., Craig, D., Wood, B. E., Chris, C., Nigro, G., Shaik, S. B., Gosic, M., Shimizu, T., Zuccarello, F., Nitta, N., Chatzistergos, T., Fan, Y., Zhang, J., Fehlmann, A., Palmerio, E., Ishikawa, R. T., Danilovic, S., Skan, M., Froment, C., Díaz Baso, C. J., Liang, Z.-C., Dudok de Wit, T., Barczynski, K., Johnston, C., Pariat, E., Hadid, L., Aulanier, G., Brun, A. S., Athanasios, K., Cauzzi, G., Dredger, P., French, R., Christian, D., Linton, M., Ireland, J., Tarr, L., Strugarek, A., Uritsky, V., Derosa, M., Kretzschmar, M., García, R. A., Monteiro, M. J. P. F. G., Mathur, S., Breton, S. N., Pinto, R. F., Martinez Oliveros, J. C., Loper, R., Auchère, F., Wang, T., Reginald, N., Cunha, M. S., Teriaca, L., Chintzoglou, G., Lynch, B. J., Linker, J., Beck, P., Shannon, J., Clare, B., Krupiarz, C., Whiting, I. D., Byerly, A., Bushman, S., Carrelli, D., Kijewski, S., Englander, J., Mizes, A., Porter, J., O'Neill, M., Chattopadhyay, D., Albers, J., Rast, M., Ermolli, I., Tzeng, N., Hudson, J. F., Giunta, A., Buchlin, É., Bommier, V., Duncan, N., Janvier, M., Strecker, H., Siu, A., Perri, B., Maksimovic, M., Vilmer, N., Toledo-Redondo, S., Kuckein, C., Alberti, T., Antolin, P., Aznar Cuadrado, R., Berghmans, D., Brigitte, S., Bucik, R., Calchetti, D., Caspi, A., Cohen, C., Corbard, T., Cremades, H., Cummings, A., Dhakal, S., Dolla, L., Dominique, M., Emslie, G., Ferrente, F., Finley, A. J., Fletcher, L., Fraschetti, F., Gafeira, R., Gissot, S., Hegde, D., Hu, Q., Innocenti, M. E., Jin, M., Klein, K., Kumar, P., Lacatus, D., Magdalenic, J., Mandal, S., Mandrini, C. H., Mierla, M., Miralles, M. P., Moore, R., Neville, J., Niembro, T., Nikou, E., Nindos, A., Papaioannou, A., Rajaguru, S. P., Reville, V., Rochus, P., Rodriguez, L., Romoli, M., Shestov, S., Shi, C., Sorriso-Valvo, L., St. Cyr, O. C., Sterling, A., Stevens, M. L., Susino, R., Swisdak, M., Thompson, B. J., Valliap-

pan, S. P., Verbeeck, F., Bothmer, V., Xudong, S., Zhukov, A., Katsiyannis, T., Owen, C., Karna, N., Janssens, J., Khomenko, E., Gary, D., Bandyopadhyay, R., Chhiber, R., Tenerani, A., Rouillard, A., Patsourakos, S., Anastasiadis, A., Bocchialini, K., Moraitis, K., Rivera, Y., Drake, J., Baudin, F., Chandran, B., Dayeh, M., Reardon, K., Cairns, I., Bizien, N., Wexler, D., Bahauddin, S., Rodriguez-Pacheco, J., Yu, S., Lee, J., Gontikakis, C., Koukras, A., Le Contel, O., Pezzi, O., Kintziger, C., Boumier, P., Balasis, G., Dikpati, M., Pesnell, W. D., Chai, Y., Nandy, D., Charles, A., Corti, C., Zhao, L., Matthaeus, W. H., Gilly, C. R., Erlandson, R. E., Derouich, M., Zhao, L., Poedts, S., Shi, C., Vieira, L., Adhikari, L., Buitrago-Casas, J. C., Huang, J., Moestl, C., Liu, M., Oloketuyi, J., Zhuang, B., Alberti, T., Rodríguez-García, L., Perez, J. C., Xu, Z., Kooi, J., Woodham, L. D., Tripathi, D., Young, P., López-Portela, C., Cuesta, M. E., & Wilson, L. (2023b). Firefly: The Case for a Holistic Understanding of the Global Structure and Dynamics of the Sun and the Heliosphere. Cited on page 165.

Ratcliffe, H., Bian, N. H., & Kontar, E. P. (2012). Density fluctuations and the acceleration of electrons by beam-generated langmuir waves in the solar corona. *The Astrophysical Journal*, 761(2), 176. Cited on page 33.

Ravishankar, A. & Michałek, G. (2019). Estimation of arrival time of coronal mass ejections in the vicinity of the earth using solar and heliospheric observatory and solar terrestrial relations observatory observations. *Solar Physics*, 294(9), 1–21. Cited on page 108.

Reames, D. V., Tylka, A. J., & Ng, C. K. (2001). Solar energetic particles and space weather. In *AIP Conference Proceedings*, volume 552 (pp. 1185–1190).: American Institute of Physics. Cited on page 14.

Reid, H. A. & Kontar, E. P. (2018). Solar type iii radio burst time characteristics at lofar frequencies and the implications for electron beam transport. *Astronomy & Astrophysics*, 614, A69. Cited on page 61.

Reid, H. A. & Kontar, E. P. (2021). Fine structure of type iii solar radio bursts from langmuir wave motion in turbulent plasma. *Nature Astronomy*, 5(8), 796–804. Cited on page 18.

Reid, H. A. & Vilmer, N. (2017). Coronal type iii radio bursts and their x-ray flare and interplanetary type iii counterparts. *Astronomy & Astrophysics*, 597, A77. Cited on page 125.

Reid, H. A. S. & Ratcliffe, H. (2014). A review of solar type iii radio bursts. *Research in Astronomy and Astrophysics*, 14(7), 773. Cited on pages 16, 18, 33, and 34.

Reiner, M. J., Fainberg, J., Kaiser, M. L., & Stone, R. G. (1998). Type III radio source located by Ulysses/Wind triangulation. *Journal of Geophysical Research: Space Physics*, 103(A2), 1923–1932. Cited on pages 19, 20, 93, and 137.

Reiner, M. J., Goetz, K., Fainberg, J., Kaiser, M. L., Maksimovic, M., Cecconi, B., Hoang, S., Bale, S. D., & Bougeret, J.-L. (2009). Multipoint observations of solar type iii radio bursts from stereo and wind. *Solar Physics*, 259, 255–276. Cited on pages 21, 93, 137, and 163.

Reinwald, M., Moseley, B., Szenicer, A., Nissen-Meyer, T., Oduor, S., Vollrath, F., Markham, A., & Mortimer, B. (2021). Seismic localization of elephant rumbles as a monitoring approach. *Journal of the Royal Society Interface*, 18(180), 20210264. Cited on page 69.

Riffel, R. A. (2010). Profit: A new alternative for emission-line pro file fit ting. *Astrophysics and Space Science*, 327, 239–244. Cited on page 61.

Robitaille, T. P., Tollerud, E. J., Greenfield, P., Droettboom, M., Bray, E., Aldcroft, T., Davis, M., Ginsburg, A., Price-Whelan, A. M., Kerzendorf, W. E., et al. (2013). Astropy: A community python package for astronomy. *Astronomy & Astrophysics*, 558, A33. Cited on page 159.

Rochus, P., Auchere, F., Berghmans, D., Harra, L., Schmutz, W., Schühle, U., Addison, P., Appourchaux, T., Cuadrado, R. A., Baker, D., et al. (2020). The solar orbiter eui instrument: the extreme ultraviolet imager. *Astronomy & Astrophysics*, 642, A8. Cited on page 51.

Rodríguez-Pacheco, J., Wimmer-Schweingruber, R., Mason, G., Ho, G., Sánchez-Prieto, S., Prieto, M., Martín, C., Seifert, H., Andrews, G., Kulkarni, S., et al. (2020). The energetic particle detector-energetic particle instrument suite for the solar orbiter mission. *Astronomy & Astrophysics*, 642, A7. Cited on page 51.

Sabroff, A. E. (1968). Advanced spacecraft stabilization and control techniques. *Journal of Spacecraft and Rockets*, 5(12), 1377–1393. Cited on page 43.

Saito, K., Poland, A. I., & Munro, R. H. (1977). A study of the background corona near solar minimum. *Solar Physics*, 55(1), 121–134. Cited on pages 95, 101, 110, and 139.

Salvatier, J., Wiecki, T. V., & Fonnesbeck, C. (2016). Probabilistic programming in python using pymc3. *PeerJ Computer Science*, 2, e55. Cited on page 74.

Sanchez-Cano, B. et al. (202X). Type-iii solar radio bursts at mars: 16 years of observations from the mars express-marsis instrument between 0.1 and 5.5 mhz. *To be submitted to Space Weather*. Cited on page 53.

Sanpechuda, T. & Kovavisaruch, L.-o. (2008). A review of rfid localization: Applications and techniques. In *2008 5th international conference on electrical engineering/electronics, computer, telecommunications and information technology*, volume 2 (pp. 769–772).: IEEE. Cited on page 69.

Schoolcraft, J., Klesh, A., & Werne, T. (2017). Marco: interplanetary mission development on a cubesat scale. *Space Operations: Contributions from the Global Community*, (pp. 221–231). Cited on page 56.

Schwabe, H. (1844). Sonnenbeobachtungen im jahre 1843. von herrn hofrath schwabe in dessau. *Astronomische Nachrichten, volume 21, issue 15, p. 233*, 21, 233. Cited on page 3.

Simnett, G. M. (2017). Energetic particle acceleration. *Energetic Particles in the Heliosphere*, (pp. 21–44). Cited on page 108.

Smith, M., Craig, D., Herrmann, N., Mahoney, E., Krezel, J., McIntyre, N., & Goodliff, K. (2020). The artemis program: an overview of nasa's activities to return humans to the moon. In *2020 IEEE Aerospace Conference* (pp. 1–10).: IEEE. Cited on page 99.

Solanki, S. K., del Toro Iniesta, J., Woch, J., Gandorfer, A., Hirzberger, J., Alvarez-Herrero, A., Appourchaux, T., Pillet, V. M., Pérez-Grande, I., Kilders, E. S., et al. (2020). The polarimetric and helioseismic imager on solar orbiter. *Astronomy & Astrophysics*, 642, A11. Cited on page 51.

Speagle, J. S. (2019). A conceptual introduction to markov chain monte carlo methods. *arXiv preprint arXiv:1909.12313*. Cited on page 69.

Spicer, D., Benz, A., & Huba, J. (1981). Solar type i noise storms and newly emerging magnetic flux. *Astronomy and Astrophysics*, 105, 221–228. Cited on page 15.

Spiegel, E. & Zahn, J.-P. (1992). The solar tachocline. *Astronomy and Astrophysics (ISSN 0004-6361), vol. 265, no. 1, p. 106-114.*, 265, 106–114. Cited on page 3.

Stansby, D., Yeates, A., & Badman, S. T. (2020). pfsspy: A python package for potential field source surface modelling. *Journal of Open Source Software*, 5(54), 2732. Cited on page 129.

Steinberg, J., Aubier-Giraud, M., Leblanc, Y., & Boischot, A. (1971). Coronal scattering, absorption and refraction of solar radiobursts. *Astronomy and Astrophysics, Vol. 10, p. 362 (1971)*, 10, 362. Cited on page 38.

Steinberg, J. L., Hoang, S., Lecacheux, A., Aubier, M. G., & Dulk, G. A. (1984). Type III radio bursts in the interplanetary medium - The role of propagation. *aap*, 140, 39–48. Cited on pages 20, 96, and 139.

Stewart, R. et al. (1965). Solar radio bursts of spectral type v. *Australian Journal of Physics*, 18(2), 143–166. Cited on page 16.

Stone, R., Bougeret, J., Caldwell, J., Canu, P., De Conchy, Y., Cornilleau-Wehrlin, N., Desch, M., Fainberg, J., Goetz, K., & Goldstein, M. (1992). The unified radio and plasma wave investigation. *Astronomy and Astrophysics Supplement Series (ISSN 0365-0138), vol. 92, no. 2, Jan. 1992, p. 291-316. Research supported by CNES and CNRS.*, 92, 291–316. Cited on page 158.

Swartwout, M. (2013). The first one hundred cubesats: A statistical look. *Journal of small Satellites*, 2(2), 213–233. Cited on page 54.

Terlouw, J. & Vogelaar, M. (2016). Kapteyn package: Tools for developing astronomical applications. *Astrophysics Source Code Library*, (pp. ascl–1611). Cited on page 159.

Terlouw, J. P. & Vogelaar, M. G. R. (2014). *Kapteyn Package, version 2.3b3*. Kapteyn Astronomical Institute, Groningen. Available from `http://www.astro.rug.nl/software/kapteyn/`. Cited on page 61.

Thejappa, G. & MacDowall, R. J. (2010). Localization of a type iii radio burst observed by the stereo spacecraft. *The Astrophysical Journal*, 720(2), 1395. Cited on page 70.

Tonks, L. & Langmuir, I. (1929). Oscillations in ionized gases. *Physical Review*, 33(2), 195. Cited on page 35.

Topputo, F., Wang, Y., Giordano, C., Franzese, V., Goldberg, H., Perez-Lissi, F., & Walker, R. (2021). Envelop of reachable asteroids by m-argo cubesat. *Advances in Space Research*, 67(12), 4193–4221. Cited on page 56.

Tousey, R. (1973). The solar corona. In *Space research conference*, volume 2 (pp. 713–730). Cited on page 10.

Van Der Marel, R. P. & Franx, M. (1993). A new method for the identification of non-gaussian line profiles in elliptical galaxies. *The Astrophysical Journal*, 407, 525–539. Cited on page 61.

van Haarlem, M. P., Wise, M. W., Gunst, A. W., Heald, G., McKean, J. P., Hessels, J. W. T., de Bruyn, A. G., Nijboer, R., Swinbank, J., Fallows, R., Brentjens, M., Nelles, A., Beck, R., Falcke, H., Fender, R., Hörandel, J., Koopmans, L. V. E., Mann, G., Miley, G., Röttgering, H., Stappers, B. W., Wijers, R. A. M. J., Zaroubi, S., van den Akker, M., Alexov, A., Anderson, J., Anderson, K., van Ardenne, A., Arts, M., Asgekar, A., Avruch, I. M., Batejat, F., Bähren, L., Bell, M. E., Bell, M. R., van Bemmel, I., Bennema, P., Bentum, M. J., Bernardi, G., Best, P., Bîrzan, L., Bonafede, A., Boonstra, A. J., Braun, R., Bregman, J., Breitling, F., van de Brink, R. H., Broderick, J., Broekema, P. C., Brouw, W. N., Brüggen, M., Butcher, H. R., van Cappellen, W., Ciardi, B., Coenen, T., Conway, J., Coolen, A., Corstanje, A., Damstra, S., Davies, O., Deller, A. T., Dettmar, R. J., van Diepen, G., Dijkstra, K., Donker, P., Doorduin, A., Dromer, J., Drost, M., van Duin, A., Eislöffel, J., van Enst, J., Ferrari, C., Frieswijk, W., Gankema, H., Garrett, M. A., de Gasperin, F., Gerbers, M., de Geus, E., Grießmeier, J. M., Grit, T., Gruppen, P., Hamaker, J. P., Hassall, T., Hoeft, M., Holties, H. A., Horneffer, A., van der Horst, A., van Houwelingen, A., Huijgen, A., Iacobelli, M., Intema, H., Jackson, N., Jelic, V., de Jong, A., Juette, E., Kant, D., Karastergiou, A., Koers, A., Kollen, H., Kondratiev, V. I., Kooistra, E., Koopman, Y., Koster, A., Kuniyoshi, M., Kramer, M., Kuper, G., Lambropoulos, P., Law, C., van Leeuwen, J., Lemaitre, J., Loose, M., Maat, P., Macario, G., Markoff, S., Masters, J., McFadden, R. A., McKay-Bukowski, D., Meijering, H., Meulman, H., Mevius, M., Middelberg, E., Millenaar, R., Miller-Jones, J. C. A., Mohan, R. N., Mol, J. D., Morawietz, J., Morganti, R., Mulcahy, D. D., Mulder, E., Munk, H., Nieuwenhuis, L., van Nieuwpoort, R., Noordam, J. E., Norden, M., Noutsos, A., Offringa, A. R., Olofsson, H., Omar, A.,

Orrú, E., Overeem, R., Paas, H., Pandey-Pommier, M., Pandey, V. N., Pizzo, R., Polatidis, A., Rafferty, D., Rawlings, S., Reich, W., de Reijer, J. P., Reitsma, J., Renting, G. A., Riemers, P., Rol, E., Romein, J. W., Roosjen, J., Ruiter, M., Scaife, A., van der Schaaf, K., Scheers, B., Schellart, P., Schoenmakers, A., Schoonderbeek, G., Serylak, M., Shulevski, A., Sluman, J., Smirnov, O., Sobey, C., Spreeuw, H., Steinmetz, M., Sterks, C. G. M., Stiepel, H. J., Stuurwold, K., Tagger, M., Tang, Y., Tasse, C., Thomas, I., Thoudam, S., Toribio, M. C., van der Tol, B., Usov, O., van Veelen, M., van der Veen, A. J., ter Veen, S., Verbiest, J. P. W., Vermeulen, R., Vermaas, N., Vocks, C., Vogt, C., de Vos, M., van der Wal, E., van Weeren, R., Weggemans, H., Weltevrede, P., White, S., Wijnholds, S. J., Wilhelmsson, T., Wucknitz, O., Yatawatta, S., Zarka, P., Zensus, A., & van Zwieten, J. (2013). LOFAR: The LOw-Frequency ARray. *Astronomy & Astrophysics*, 556, A2. Cited on page 19.

Vasanth, V., Umapathy, S., Vršnak, B., Žic, T., & Prakash, O. (2014). Investigation of the coronal magnetic field using a type ii solar radio burst. *Solar physics*, 289(1), 251–261. Cited on page 105.

Vecchio, A., Maksimovic, M., Chrysaphi, N., Kontar, E. P., & Krupar, V. (2024). Temporally resolved Type III solar radio bursts in the frequency range 3-13 MHz. *The Astrophysical Journal Letters*. Cited on page 144.

Villela, T., Costa, C. A., Brandão, A. M., Bueno, F. T., Leonardi, R., et al. (2019). Towards the thousandth cubesat: A statistical overview. *International Journal of Aerospace Engineering*, 2019. Cited on page 54.

Vogelaar, M. (1999). A gipsy program to fit parameters of a gauss function, the gauss-hermite series or a voigt line-shape to data from gipsy sets or ascii files. Cited on page 61.

Von Rosenvinge, T., Barbier, L., Karsch, J., Liberman, R., Madden, M., Nolan, T., Reames, D., Ryan, L., Singh, S., Trexel, H., et al. (1995). The energetic particles: acceleration,

composition, and transport (epact) investigation on the wind spacecraft. *Space Science Reviews*, 71, 155–206. Cited on page 42.

Vourlidas, A., Howard, R. A., Plunkett, S. P., Korendyke, C. M., Thernisien, A. F., Wang, D., Rich, N., Carter, M. T., Chua, D. H., Socker, D. G., et al. (2016). The wide-field imager for solar probe plus (wispr). *Space Science Reviews*, 204, 83–130. Cited on page 48.

Vršnak, B., Sudar, D., & Ruždjak, D. (2005). The cme-flare relationship: Are there really two types of cmes? *Astronomy & Astrophysics*, 435(3), 1149–1157. Cited on page 11.

Wahlund, J. et al. (2013). The radio & plasma wave investigation (rpwi) for juice. In *European Planetary Science Congress* (pp. EPSC2013–637). Cited on page 155.

Watanabe, K., Masuda, S., & Segawa, T. (2012). Hinode flare catalogue. *Solar Physics*, 279, 317–322. Cited on page 8.

Watkins, L., Stinco, P., Tesei, A., & Meyer, F. (2024). A probabilistic focalization approach for single receiver underwater localization. Cited on page 69.

Weber, R., Fitzenreiter, R., Novaco, J., & Fainberg, J. (1977). Interplanetary baseline observations of type iii solar radio bursts. *Solar Physics*, 54, 431–439. Cited on page 20.

Weigt, D., Cañizares, L., Maloney, S., Murray, S., Carley, E., Gallagher, P., Macario-Rojas, A., Crisp, N., & McGrath, C. (2023). The science behind surround: a constellation of cubesats around the sun. *arXiv preprint arXiv:2308.04194*. Cited on pages 56 and 100.

Wenzel, K., Marsden, R., Page, D., & Smith, E. (1992). The ulysses mission. *Astronomy and Astrophysics Supplement, Vol. 92, NO. 2/JAN, P. 207, 1992*, 92, 207. Cited on page 157.

Widdison, E. & Long, D. G. (2024). A review of linear multilateration techniques and applications. *IEEE Access*, 12, 26251–26266. Cited on page 66.

Wiecki, T., Salvatier, J., Vieira, R., Kochurov, M., Patil, A., Osthege, M., Willard, B. T., Engels, B., Carroll, C., Martin, O. A., Seyboldt, A., Rochford, A., Paz, L., rpgoldman,

Meyer, K., Coyle, P., Gorelli, M. E., Abril-Pla, O., Kumar, R., Lao, J., Andreani, V., Yoshioka, T., Ho, G., Kluyver, T., Beauchamp, K., Andorra, A., Pananos, D., Spaak, E., Edwards, B., & Ma, E. (2023). pymc-devs/pymc: v5.6.1. Cited on page 74.

Wilson III, L. B., Brosius, A. L., Gopalswamy, N., Nieves-Chinchilla, T., Szabo, A., Hurley, K., Phan, T., Kasper, J. C., Lugaz, N., Richardson, I. G., et al. (2021). A quarter century of wind spacecraft discoveries. Cited on page 40.

Zhang, P., Wang, C., Ye, L., & Wang, Y. (2019). Forward modeling of the type iii radio burst exciter. *Solar Physics*, 294(5), 1–20. Cited on pages 21, 60, 88, 91, and 107.

Zhou, J. & Shi, J. (2009). Rfid localization algorithms and applications—a review. *Journal of intelligent manufacturing*, 20, 695–707. Cited on page 69.